

https://dspace.org/

An implantable sensor for disease detection and treatment

Ngoepe, Mpho Phehello

2014-08-25
http://hdl.handle.net/10539/15242

Downloaded from a DSpace repository. https://dspace.org/

AN IMPLANTABLE SENSOR FOR DISEASE DETECTION AND TREATMENT

MPHO PHEHELLO NGOEPE

A dissertation submitted to the Faculty of Health Sciences,
University of the Witwatersrand, in fulfillment of the requirements for the degree of Master of Science in Medicine



Supervisor:
Professor Viness Pillay, Department of Pharmacy and Pharmacology,
University of the Witwatersrand, South Africa

Co-Supervisor:
Associate Professor Yahya Essop Choonara, Department of Pharmacy and Pharmacology,
University of the Witwatersrand, South Africa

Co-Supervisor:
Dr. Lisa Claire du Toit, Department of Pharmacy and Pharmacology,
University of the Witwatersrand, South Africa

Johannesburg, 2014

DECLARATION

I, Mpho Phehello Ngoepe declare that this dissertation is my own work. It is being submitted for the degree of Master of Science in Medicine in the field of Pharmaceutics in the Faculty of Health Sciences at the University of the Witwatersrand, Johannesburg, South Africa. It has not been submitted before for any degree or examination at this or any other University.

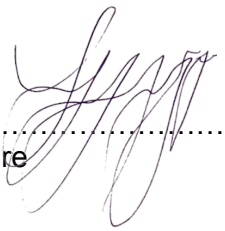

……
Signature

14-05-2014
……
Date

RESEARCH PUBLICATION

Review: Integration of Biosensor and Drug Delivery Systems for Early Detection and Chronic Illness Management. Mpho P. Ngoepe, Yahya E. Choonara, Lisa C. Du Toit, Pradeep Kumar, Valence M.K. Ndesendo and Viness Pillay. Sensors 2013, 13(6), 7680-7713.

Research Paper I: Anti-β-LDL-Conjugated Solid Lipid Nanoparticles: Ideal immunoaffinity absorbents and targeted drug delivery system for lipophilic drugs. Mpho P. Ngoepe, Yahya E. Choonara, Lisa C. Du Toit, Pradeep Kumar, Valence M.K. Ndesendo and Viness Pillay. To be submitted to Targeted Drug Delivery.

Research Paper II: Characterization of viscoelastic hydrogel plasticizer effect on linear viscoelastic region. Mpho P. Ngoepe, Yahya E. Choonara, Lisa C. Du Toit, Pradeep Kumar and Viness Pillay. To be submitted to Progress in Polymer Science.

Research Paper III: An implantable sensor for diet induced atherosclerosis prevention and treatment in Large White Pigs. Mpho P. Ngoepe, Yahya E. Choonara, Lisa C. Du Toit, Pradeep Kumar and Viness Pillay. To be submitted to Journal of Controlled Release.

PATENT FILLED

An implantable sensor for disease prevention and treatment. Mpho P. Ngoepe, Yahya E. Choonara, Lisa C. Du Toit, Pradeep Kumar and Viness Pillay. Application number: 2013/03981.

ABSTRACT

Current sensors employed in medicine are used to detect chemical and biochemical abnormalities. Their applications range from biopsy (brain), enzyme-linked immunosorbent assay (ELISA) (spinal fluid), blood (bio-barcode), and sweat and urine bio-diagnostics where the primary focus is the selection of biomarkers that can pinpoint the occurrence of the disease. Emerging sensors for cholesterol detection are based on enzymatic functions, which degrade these molecules, where the signal can be visualized optically by using a transducer. Cholesterol is a steroid metabolite that is employed for the synthesis of steroid hormones, and the establishment of proper membrane permeability and fluidity. Since cholesterol is insoluble in blood, it is transported in the circulatory system within lipoproteins, complex spherical particles which have an exterior comprising of amphiphilic proteins and lipids with outward-facing surfaces that are water-soluble and inward-facing surfaces that are lipid-soluble. Low-density lipoprotein (LDL) is known as 'bad' cholesterol. High-density lipoprotein (HDL) is known as 'good' cholesterol. LDL is linked to cardiovascular conditions such as atherosclerosis and hypertension, which ultimately lead to coronary heart disease, myocardial and cerebral infarction (stroke). An appropriate therapeutic response to a sensor system for cholesterol, specifically LDL, detection implicates the design of an implantable system for stimuli-responsive drug release. The proposed system was designed to detect specific biochemical changes by employing nanoparticles made of glyceryl behenate, polyoxyethylene-polyoxypropylene block copolymer, avidin, biotin and anti-beta lipoprotein antibodies as sensors. This was achieved by coating nanoparticles with antibodies specific to the antigen (i.e. LDL) to create an antibody-conjugated antibody conjugated solid lipid nanoparticles (henceforth known as 'antibody conjugated SLN). Fenofibrate was used as a model drug due to its low water solubility and to its lipophilic properties similar to statins. The antibody conjugated SLNs were of 150nm in size and had a zeta potential of -28mV. Their drug entrapment efficacy was 86%, with a drug release of 16mg/day due to Fickian diffusion and erosion mechanism. The slow release was due semi-crystalline structure determined by XRD and DSC. Antigen responsive hydrogel was designed by incorporation of thiolated antibody conjugated SLN via Traut's reagents, polyethylene glycol diacrylate, methyl acrylic acid and polyethylene glycol 200. The osmotic pump was designed from polyethylene oxide, ethyl cellulose and mannitol. The drug reservoir was synthesized from ethyl cellulose coated gelatin capsule via coacervation phase separation method. The polymeric tube synthesized from ethyl cellulose, methyl cellulose and castor oil was coated with antigen responsive hydrogel. *Ex vivo* studies evaluating intravascular stability of the implant in correlation with mechanical analysis indicated the polymeric tube unstable. An 18-gauge catheter was used for forming an infusion tube as a substitute for the polymeric tube. The implant showed a correlation of Korsmeyer-Peppas drug release during *in vivo* and *in vitro* studies. A constant drug release of 881µg/day was observed during *in vivo*. This played a role in reduction of total cholesterol by means of reduction in LDL sub-fractions by 30%; in correlation with LDL particle enhance clearance from the plasma due to SLN-LDL uptake. An increase by 46% in HDL was observed, which correlated to fenofibrate therapeutic effect. Pharmacokinetic analysis indicated improved mean residence time and efficacy. This indicated that the device could be used for delivery of lipophilic drugs and detection of circulating biomarkers.

ACKNOWLEDGEMENTS

I would like to acknowledge and express appreciation to all those without whom the completion of this work would not have been possible. I express my gratitude to the following people:
I wish to thank, first and foremost my parents Lucy Ngwepe and Victor Nengovhela for their support and sacrifice to see me achieve my goals. Thank you for your understating and investing in my future. Special thanks to my siblings, Baleseng Ngwepe, Tshegofatso Ngwepe, Dennis Ngwepe and Patricia Ngwepe for their support.

It is with immense gratitude that I acknowledge the support and help of my Professor Viness Pillay. Thank you for giving me an opportunity to better my career path. Through his great mentorship and guidance has made all accomplishments possible.

I owe my deepest gratitude to my co-supervisor Associate Professor Yahya E. Choonara for his ideas and contributions made this study a success. His input has truly expanded my knowledge and skills.

This dissertation would not have been possible without help from my co-supervisor Dr. Lisa C. Du Toit. Thank you for your patience, guidance, support and valuable input. I am truly indebted to you for your help.

It gives me great pleasure in acknowledging my friends/closest colleagues - Maluta Steven Mufamadi, Felix Mashingaidze, Angus Hibbins, Sunaina Indermun, Bafana Themba and Derusha Frank. Without their motivation and support, I would not have accomplished anything.
I am indebted to my many colleagues who supported me: Pradeep Kumar, Ahmed Seedat, Kealeboga Mokolobate, Nonhlanhla Masina, Jonathan Pantshwa, Olufemi Akilo, Tebogo Kgesa, Martina Manyikana, Latavia Singh, Tasneem Rajan, Pierre Kondiah, Naeema Mayet, Famida Ghulam-Hoosain, Fatema, Mia, Khuphukile Madida, Mershen Govender, Dr. Lomas Kumar Tomar, Dr. Charu Tyagi and Dr. Divya Bijukumar.

I will also like to express my gratitude to Mr. Sello Ramarumo always being there to help.
I would like to thank Central Animal Services staff of Wits University and Professor Kennedy Erlwanger for assistance and input.

Thank you to the National Research Foundation (NRF), University of the Witwatersrand Staff Bursary and Department of Education Clinical training (DoE) for the research grants.

DEDICATION

This dissertation is dedicated to my late grandparents Josephine Ngoepe and Samuel Ngoepe. Thank you for your wisdom and love.

ANIMAL ETHICS DECLARATION

I, Mpho Ngoepe hereby confirm that the study entitled 'An implantable sensor for disease prevention and treatment' received the approval from the Animal Ethics Screening Committee (AESC) of the University of the Witwatersrand with Ethics Clearance Number 2011/52/05 (Appendix B).

TABLE OF CONTENTS

		Page
DECLARATION		i
RESEARCH PUBLICATION AND PRESENTATIONS		ii
PUBLICATIONS		ii
PATENT FILLED		iii
ABSTRACT		iv
ACKNOWLEDGEMENTS		v
DEDICATION		vii
ANIMAL ETHICS DECLARATION		viii
TABLE OF CONTENTS		ix
LIST OF FIGURES		xv
LIST OF TABLES		xviii
1. Introduction and Motivation for Study		
1.1.	Background of this Study	1
1.2.	Rationale for this Study	3
1.3.	Aim and Objectives of this Study	5
1.4.	Novelty of this Study	6
1.5.	Overview of this Dissertation	6
2. Literature Review		
2.1.	Introduction	8
2.2.	Biomarkers as Indicators of Disease Progression and Occurrence	10
2.3.	Biosensors for Disease Detection and Monitoring	12
2.3.1.	Immunosensor and other Affinity Biosensor	13
2.3.2.	Amperometric Immunosensors	14
2.3.3.	Label Free Immunosensors	14
2.3.4.	Bioreporter Type Biosensor	15
2.3.5.	Enzyme-based Biosensors (Electrochemical Biosensors)	15

2.3.6. Cholesterol Biosensor 16
2.4. Drug Delivery Systems Design and Applications 16
2.5. Factors Affecting Implantable Medical Devices 20
2.6. Current Methods used in Medical Diagnosis and Management 21
2.7. Concluding Remarks 24

3. Development and Characterization of Antibody Conjugated Nanoparticles

3.1. Introduction 25
3.2. Materials and Methods 27
3.2.1. Materials 27
3.2.2. Preparation of solid lipid nanoparticles 27
3.2.3. Determination of nanoparticle size and stability 28
3.2.4. Modification of antibodies and nanoparticle avidin coating 28
3.2.5. Analysis of biotinylated antibody structural integrity 29
3.2.6. Antibody and Apolipoprotein B100 concentration analysis 30
3.2.7. Oxidation of Low Density Lipoprotein 30
3.2.8. Confirmation of biotinylation of the fragment crystallizable region of the antibody 31
3.2.9. Microscopic analysis of antibody conjugated solid lipid nanoparticles 31
3.2.10. Thermodynamic and molecular interaction analysis of solid lipid nanoparticles 32
3.2.11. Structural crystallinity analysis of antibody conjugated nanoparticles 32
3.2.12. Structural transformations analysis of solid lipid nanoparticles 33
3.2.13. Drug entrapment efficacy and loading capacity 33
3.2.14. *In vitro* drug release analysis from antibody-conjugated nanoparticles 34
3.3. Results and Discussion 35
3.3.1. Higher magnification of solid lipid nanoparticles 35
3.3.2. Molecular modeling of antibody conjugation to avidin coat 36
3.3.3. Surfactant concentration impact on particle size and stability 38
3.3.4. Impact of drug incorporation on nanoparticle size and stability 39
3.3.5. Solid lipid nanoparticle stability and size prior after avidin coating 41
3.3.6. Thermodynamic properties of antibody conjugated nanoparticles 42
3.3.7. Confirmation of antibody conjugated nanoparticle crystallinity 44

3.3.8. Structural transformations analysis of antibody conjugated nanoparticles 46
3.3.9. Confirmation of low-density lipoprotein oxidation 47
3.3.10. Determination of antibody structural integrity after modification 48
3.3.11. Characterization of drug loading capacity and encapsulation efficiency 49
3.3.12. *In vitro* drug release studies 50
3.4. Concluding Remarks 54

4. Synthesis and Characterization of Antigen Responsive Interpenetrating Network for Controlling Drug Infusion Rate

4.1 Introduction 55
4.2. Materials and Methods 57
4.2.1. Materials 57
4.2.2. Fabrication of the viscoelastic hydrogel via thermal polymerization 57
4.2.3. Analysis of hydrogel viscoelastic properties and flow behavior 58
4.2.4. Determination of hydrogel membrane rigidity and resilience under mechanical strain 58
4.2.5. Hydrogel pore size distribution analysis 59
4.2.6. Formulated hydrogels swelling kinetics and dynamics 60
4.2.7. Hydrolytic degradation of viscoelastic hydrogel 61
4.2.8. Thermodynamic stability analysis of viscoelastic hydrogel 61
4.2.9. Hydrogel thermal degradation analysis at various heating rates 62
4.2.10. Structural transformations analysis of viscoelastic hydrogel 62
4.2.11. Hydrogel molecular weight characterization 63
4.2.12. Pore size and hydrogel surface microscopic evaluation 63
4.2.13. Hydrogel thermal decomposition kinetics characterization 64
4.2.14. Cytotoxicity analysis of viscoelastic hydrogel biocompatibility 65
4.3. Results and Discussion 66
4.3.1. Viscoelastic hydrogel microscopic analysis 66
4.3.2. Porosity analysis of viscoelastic hydrogel 68
4.3.3. Hydrogel molecular modeling 69
4.3.4. Molecular weight determination of the synthesized hydrogel 71
4.3.5. Rheological analysis of hydrogels for determination of shear response 72
4.3.5.1. Formulated hydrogel flow behavior characterization 72

4.3.5.2. Characterization of viscoelastic behavior 76
4.3.5.3. Evaluation of hydrogel elastic strength and structural recovery under constant strain 78
4.3.6. Swelling behavior and kinetics of formulated hydrogels 80
4.3.7. Hydrogel mechanical analysis for matrix resilience and rigidity 81
4.3.8. Evaluation of structural changes after polymerization 82
4.3.9. Hydrogel thermodynamic analysis 83
4.3.9.1. Thermodynamic stability and molecular interaction analysis 83
4.3.9.2. Thermal degradation analysis of viscoelastic hydrogel at various heating rate 86
4.3.10. Lifetime prediction of hydrogel stability 87
4.3.11. Cytotoxicity analysis of viscoelastic hydrogel 88
4.4. Concluding Remarks

5. Implant design procedure, mechanical characterization and *ex vivo* evaluation

5.1 Introduction 91
5.2. Materials and Methods 93
5.2.1. Materials 93
5.2.2. Reservoir fabrication from gelatin capsule 93
5.2.3. Characterization of modified gelatin capsule hardness and resilience 93
5.2.4. Antigen responsive hydrogel synthesis and characterization 94
5.2.5. Antigen responsive hydrogel viscoelasticity determination 95
5.2.6. Porous polymeric tube synthesis 95
5.2.7. Mechanical analysis of polymeric tube 95
5.2.8. Osmotic pump fabrication 96
5.2.9. Implant fabrication and characterization 97
5.2.10. Implant Optimization using Design of Experiments 98
5.2.11. Porosity analysis on Design of Experiments formulations 99
5.2.12. *In vitro* dissolution tests on Design of Experiments formulations 99
5.2.13. Swellability studies and hydrolysis degradation studies 100
5.2.14. Evaluation of implant components thermal stability under various heating rates 101
5.2.15. Kinetics and lifetime prediction of implant components 101

5.2.16.	Thermodynamic evaluation of implant components	103
5.2.17.	Structural transformations analysis of implant components	103
5.2.18.	Implant *Ex vivo* experimentation for evaluation of intravascular stability	103
5.2.19.	Quantitative determination of fenofibrate in plasma from *ex vivo* studies	105
5.3.	Results and Discussion	106
5.3.1.	Implant design and characterization	106
5.3.2.	Determination of antigen responsiveness	107
5.3.3.	Determination of the Infusion rate from the osmotically driven implant	109
5.3.4.	Optimized formulation responses	111
5.3.4.1.	Influence of pore size changes on drug release	111
5.3.4.2.	Optimized drug delivery system characterization	113
5.3.5.	Polymeric tube mechanical strength analysis	114
5.3.6.	Thermal degradation measurements of polymeric tube and modified capsule at various heating rates	115
5.3.7.	Analysis of thermal decomposition of polymeric tube and modified capsule	116
5.3.8.	Thermal degradation kinetics analysis	117
5.3.9.	Activation energy of polymeric tube and modified capsule	120
5.3.10.	Hydrolytic degradation of modified capsule, antigen responsive hydrogel and polymeric tube	121
5.3.11.	Mechanical properties of polymeric tube and modified capsule	122
5.3.12.	Analysis of the implant intermolecular properties	123
5.3.13.	*In vitro* dissolution of optimized antigen responsive drug delivery system	126
5.3.14.	Implant mechanical stability in circulating plasma	126
5.4.	Concluding Remarks	129

6. *In Vivo* Evaluation of the Drug Delivery Device

6.1	Introduction	131
6.2.	Materials and Methods	133
6.2.1.	Materials	133
6.2.2.	Use of experimental animals	133
6.2.3.	Experimental procedures conducted on Large White pig model	133
6.2.5.	Catheter and Implant implantation	136
6.2.5.	Chromatographic qualitative assay of fenofibrate concentration in Large	138

White pig model
6.2.6. Total cholesterol and Lipoprotein levels quantification and characterization 139
6.2.7. Data statistical analysis 140
6.3. Results and Discussion 140
6.3.1. Post-surgical examination 140
6.3.2. Implant induced inflammatory response analysis 140
6.3.3. Cholesterol level evaluation 143
6.3.4. Validation of fenofibrate concentration chromatographic assay 148
6.3.5. Capsule *in vivo* biodegradation 152
6.3.6. Pharmacokinetics analysis 153
6.4. Concluding Remarks 154

7. Conclusion and Recommendations

7.1 Conclusion 156
7.2. Recommendations 157

8. References 158

9. Appendix 178

LIST OF FIGURES

		Page
Figure 1.1:	Flow diagram depicting experimental procedure for design of IVISDDD and infusion device.	4
Figure 2.1:	Biomarkers based on site of extraction and major illness association.	11
Figure 2.2:	Schematic depicting functional principles of a biosensor.	13
Figure 2.3:	Various techniques of drug delivery system formulation.	18
Figure 2.4:	Reversible antigen responsive hydrogel.	23
Figure 3.1:	TEM (a and b) and SEM images (c and d) of native SLN (a and c) and antibody-conjugated SLN (b and d) interacting with LDL particles.	36
Figure 3.2:	Schematic depicting anti β-LDL antibody-biotin-avidin interaction.	38
Figure 3.3:	Scatter plot of solid lipid nanoparticle size and stability at varying surfactant concentration, whereby F1 = 0.8%, F2 = 0.4%, F3 = 0.2% and F4 = 0.1% surfactant concentration.	40
Figure 3.4:	Scatter plot of SLN size and stability in response to increase in drug concentration.	41
Figure 3.5:	Plot indicating the size, zeta potential and electrophoretic mobility changes before and after avidin coating.	42
Figure 3.6:	Conventional DSC thermograms showing temperature transition of drug loaded solid lipid nanoparticles.	43
Figure 3.7:	Bar graph showing changes in glass transition and enthalpy in response to drug incorporation.	44
Figure 3.8:	XRD diffractogram confirming semi-crystalline structure of the antibody conjugated SLN.	46
Figure 3.9:	FTIR spectrum of (a) antibody biotinylation and (a) SLN avidin coating.	47
Figure 3.10:	Oxidation of LDL particles by $CuSO_4$ 10mM PBS, pH 7.4 at 37°C for 3 hours	48
Figure 3.11:	SDS-PAGE and radial immunodiffusion characterization of antibodies.	49
Figure 3.12:	Cumulative fenofibrate drug release from antibody-conjugated SLN in PBS (pH 7.4, 0.2% Tween 80)	51
Figure 3.13:	*In vitro* drug release kinetics models, Zero-order, First-order, Higuchi, Hixson Crowell and Korsmeyer-Peppas.	53

Figure 4.1:	Scanning Electron Microscopy (SEM) images of hydrogels after hydrolysis. (a) Hydrogel surface, (b) pore grooves, (c) Pore distribution and (d) pore diameter variation.	67
Figure 4.2:	Isotherm log plot of polymerized hydrogel	69
Figure 4.3:	Polymerization schematics generated using HyperChem for molecular modeling.	71
Figure 4.4:	Debye plot of viscoelastic hydrogel indicating molecular weight	72
Figure 4.5:	Yield stress test showing a plot of viscosity (η) versus strain (τ) versus shear rate ($\dot{\gamma}$).	
Figure 4.6:	Characterization of viscoelastic polymer flow based on Newtonian and non-Newtonian flow	76
Figure 4.7:	Frequency sweep showing storage (G") and loss (G') modulus versus frequency (ω)	77
Figure 4.8:	Stress Sweep of H1 ($-$), H2 (x), H3 (Δ), H4 ($\circ$) and H5 ($*$).The linear viscoelastic limits are defined as the strains and stresses at which the complex modulus decreases to 95 % of its value. ($\lvert\eta^*\rvert - \text{complex dynamic viscosity and } \lvert G^*\rvert - \text{complex modulus}$).	79
Figure 4.9:	FTIR spectra of the viscoelastic hydrogel after polymerization	83
Figure 4.10:	DSC curve of viscoelastic hydrogel showing glass transition, melting temperature and crystallization peaks.	85
Figure 4.11:	TGA characteristic of viscoelastic hydrogel showing different melting points of H2	87
Figure 4.12:	Logistic model determining cytotoxicity of viscoelastic hydrogel	89
Figure 5.1:	A lateral view (with magnification) of the intravascular implantable sensor and drug delivery device	98
Figure 5.2:	*Ex vivo* studies setup using peristaltic pump (a) *Ex vivo* step on the peristaltic apparatus, (b) Insertion of the implant into a peristaltic tube, sheep's blood maintained at 37±0.5°C.	105
Figure 5.3:	Schematic of the IVISDDD. (a) Indicates the layout of coating of the porous polymeric tube with the antigen responsive IPN (b) indicates formation of the IVISDDD using osmotic pump, modified gelatin capsule and coated polymeric tube and (c) indicates the assembled IVISDDD using an 18Ga. catheter for infusion of anti-LDL SLN.	107
Figure 5.4:	Scatter plot showing the effects of the free antigen concentration on the	109

hydrogel swelling ratio.
Figure 5.5: Graphical depiction of the increasing rigidity of the osmotic pump with swelling (photographic image of osmotic pump as inset at 60 minutes) 110
Figure 5.6: Correlation of cumulative drug release to pore size of the IVISDDD 113
Figure 5.7: Optimized antigen responsive drug delivery system 114
Figure 5.8: TGA and DTG curves under 6°C, 8°C and 10°C heating rate for modified gelatin capsule (a) and polymeric tube (b). 116
Figure 5.9: Timebase FTIR spectrum showing immergence of carbon dioxide due to carbon based materials. 117
Figure 5.10: Kinetic analysis to determine activation energy of polymeric tube 118
Figure 5.11: Kinetic analysis to determine activation energy of modified gelatin capsule 119
Figure 5.12: Scatterplot depicting the change in E_a with mass loss 121
Figure 5.13: Hydrolytic degradation of the gelatin capsule, the polymeric tube and the hydrogel. 122
Figure 5.14: FTIR spectra of the (a) polymeric tube, (b) antigen responsive IPN and (c) modified gelatin capsule. 125
Figure 5.15: A typical UPLC chromatogram indicating the separation and retention time of fenofibrate (1.905 min) and the internal standard nicotinic acid (0.233 min) 127
Figure 5.16: Standard calibration curve generated for quantifying fenofibrate in plasma samples employing a UPLC (N=3, S.D = 0.3). 128
Figure 5.17: *Ex vivo* drug release from implant (N=3). 129
Figure 6.1: A schematic illustrating the study design for the *in vivo* experimentation in the Large White pig model 135
Figure 6.2: Catheterization and implant insertion surgical procedure. (a) The surgical procedure for the jugular vein catheterization of experimental pigs depicting surgical incision into the jugular area, (b) insertion of the catheter, (c) subcutaneous tunneling, (d) insertion of the drug delivery device, (e) suturing of the catheter external injection ports and site of implantation sutured. 137
Figure 6.3: Histological micrographs showing representative sections of subcutaneous tissue following implantation of the gelatin reservoir 143
Figure 6.4: Cholesterol standard curve 145

Figure 6.5: LDL concentration profiles for the 25-day study (N=3). 146
Figure 6.6: HDL concentration profiles obtained in 25-day (N=3). 147
Figure 6.7: Diet induced hypercholesterolemia, reduction of total cholesterol (N=3). 148
Figure 6.8: Standard curve of fenofibrate obtained by UPLC (N=3, S.D=0.03). 149
Figure 6.9: *In vivo* drug release profiles in all experimental pigs obtained using UPLC (N=3). 151
Figure 6.10: Adjusted R^2 of drug release for determination of drug release 153

LIST OF TABLES

		Page
Table 3.1:	Formulations for assessing the stability and size of SLN based on ($\%^{w/}_{v}$) ratio between solid lipid and non-ionic stabilizer.	28
Table 3.2:	Release kinetics data of fenofibrate loaded SLN for targeted drug delivery.	52
Table 4.1:	Formulations of viscoelastic hydrogel based on changes in plasticizer and crosslinker concentration.	57
Table 4.2:	Method parameters for yield test, stress sweep and frequency sweep tests.	58
Table 4.3:	Textural Profiling Parameters Settings Employed for Physicochemical Characterization of viscoelastic hydrogels.	59
Table 4.4:	Evacuation and Heating Phase Parameters Employed for Porositometric Analysis.	60
Table 4.5:	BJH surface pore volume and pore size of viscoelastic hydrogel responsive to hemodynamic forces (1nm = 10 Angstrom).	69
Table 4.6:	Creep test analysis of viscoelastic hydrogel for structural recovery evaluation.	80
Table 4.7:	Equilibrium swelling ratio, equilibrium water content and swelling exponent.	81
Table 4.8:	Mechanical analysis of polymer strength and structural recovery.	82
Table 4.9:	Determination of heat of fusion and melting temperatures affected by plasticizer concentration.	86
Table 4.10:	Interaction energy and density changes caused by plasticizer concentration.	86
Table 4.11:	Determination of activation energy for prediction of polymer lifetime under inert atmosphere.	88
Table 4.12:	Predicted viscoelastic hydrogel lifetime at varying temperatures.	88
Table 5.1:	Design of Experiments for antigen responsive polymeric tube.	99
Table 5.2:	Mathematical models to be used to describe drug dissolution curves.	100
Table 5.3:	UPLC instrumental settings for the determination of Fenofibrate in	106

plasma samples.
Table 5.4: Design of Experiments response, in vitro drug release correlation to change in porosity. 112
Table 5.5: Nanotensile tests to determine mechanical strength of polymeric tube strands. 115
Table 5.6: Thermal degradation kinetic parameters of a modified gelatin capsule (reservoir) and a polymeric tube at a mass loss of 5%. 119
Table 5.7: Lifetime prediction of capsule and polymeric tube at varying temperatures. 121
Table 5.8: Textural analysis for determination of mechanical strength of the reservoir and polymeric tube. 123
Table 5.9: Determination of the most favorable drug release kinetics of IVISDDD. 126
Table 6.1: Atherogenic swine diet composition. 134
Table 6.2: UPLC analysis parameters. 139
Table 6.3: Histological analysis of implantation sites based on grading immune response (Scaling 1-5). 143
Table 6.4: Pharmacokinetic parameters of anti-LDL SLN and antibody free SLN 155

CHAPTER ONE
INTRODUCTION AND MOTIVATION FOR THE STUDY

1.1. Background of this Study

Current sensors employed in medicine are used to detect chemical and biochemical abnormalities. Their applications include use in; brain biopsies, enzyme-linked immunosorbent assays (ELISA) for spinal fluid, bio-barcode in blood and diagnostics using sweat and urine where the primary focus is the selection and detection of biomarkers that can pinpoint the occurrence of a disease (Giljohann and Mirkin, 2009). Genetically modified bio-substances such as enzymes, receptors and antibodies have been designed and immobilized on different kinds of polymers/substrates to allow efficient biomarker detection (Hock et al., 2002; Miyata et al., 2002). Other sensing procedures of great interest consider the formation of a complex between functional monomers and the analyte (target molecule) in an appropriate solution (Parmpi and Kofinas, 2004). This complex is then made rigid by polymerization in the presence of a high concentration of a crosslinker (Bergmann and Peppas, 2008). Thereafter, the analyte is removed by washing, which leaves an imprint (intact binding site) specific to the analyte (Caldorera-Moore and Peppas, 2009).

Novel sensors for cholesterol detection are based on the enzymatic functions (hydrolysis of sterol esters by cholesterol esterase) which degrade cholesterol, where the signal can be visualized optically by using a transducer (Arya et al., 2008; Erickson et al., 2008; Gerard et al., 2002; Sethi, 1994; Vo-Dinh, 2008). Current hyperlipidemia sensors utilize cholesterol esterase, cholesterol oxidase seperatelty or in combination on various platforms for immobolisation of enzymes (Pundir et al., 2012). This aids in determination of total plasma cholesterol. However, there are currently no integrated biosensor-drug delivery systems, and the use of enzymes requires restrictive physciochemial conntions that facilitate enzymatic activity. Cholesterol is a steroid metabolite that is employed in the manufacture of steroid hormones, and the establishment of membrane permeability and fluidity. Since cholesterol is insoluble in blood, it is transported in the circulatory system within lipoproteins, complex spherical particles, which have an exterior composed of amphiphilic proteins and lipids whose outward-facing surfaces are water-soluble and inward-facing surfaces are lipid-soluble. Low-density lipoprotein (LDL) cholestrol is known as ‘bad’ cholesterol. High-density lipoprotein (HDL) cholesterol is known as ‘good’ cholesterol. LDL is linked to cardiovascular conditions such as atherosclerosis and

hypertension, which ultimately lead to coronary heart disease, myocardial and cerebral infarction (stroke) (Tymoczko et al., 2002). It occurs due to oxidized LDL molecules, which are present in atherosclerotic lesions that play a key role in atherosclerosis (Calara et al., 1998). An appropriate sensor system for cholesterol, specifically constant LDL detection warrants the design of an implantable system for stimuli-responsive drug release. The design of an implantable system, which responds by releasing a drug on detection of the antigen (LDL), involves consideration of the same drug release mechanism, which applies to other 'smart-release' systems such as pH and temperature-sensitive hydrogels. An effective system that has been deployed in other implantable constant drug release requirement has been the development of osmotic pump.

Osmotic pump research has moved from applications in laboratory animals only, to usage in reliable controlled-release systems for humans. Osmotically controlled drug-delivery systems use osmotic pressure to modulate the release of the active agent. Drug delivery from these systems, largely is independent of the physiological factors. Good examples are Alzet® osmotic pumps. These are miniature infusion pumps currently used in laboratory animals for continuous drug dosing. Miniature pumps like these offer advantages such as helping researchers/medical practitioners save critical time by eliminating the need for frequent monitoring and repetitive injection schedules. This improves patient compliance and reduces side effects profile caused by frequent dosing by ensuring that continuous levels of compounds be maintained at therapeutic levels. The foremost advantages of osmotic pumps are that they allow continuous infusion of solutions at a continuous rate, do not restrict patient's movement, and are therefore, less stressful. However, the foremost disadvantage is that the infusion rate or infusion solution cannot be altered during infusion procedures (Abe et al., 2009). The main reason for changing the infusion rate is dose dependent. A change in the infusion rate affects the pharmacokinetics and pharmacodynamics of the drug.

In this study, the primary focus would be to design a composite polymeric system, which will function as an Intra-Vascular Implantable Sensor and Drug Delivery Device (IVISDDD). The IVISDDD will thus comprise of two components, namely a biosensor component based on antibody conjugated solid lipid nanoparticles (SLN); and a response (drug delivery) component comprising a polymer tube contained within an antigen responsive hydrogel system for implanting. Should high levels of LDL be detected, the implant will responsively release

lipophilic drug fenofibrate, the model drug, which will in turn lower the circulating LDL concentration to a desirable level.

1.2. Rationale for this Study

There are ranges of medical disorders, including those of lipoprotein metabolism, that are associated with varied biochemical changes. The proposed system would function to detect specific biochemical changes by employing nanoparticles as sensors. This would be achieved by coating nanoparticles with antibodies specific for the antigen (i.e. LDL) to create an antibody-conjugated anti-LDL SLN. Once the antigen is detected following binding to the anti-LDL SLN, the anti-LDL SLN-antigen (anti-LDL SLN-LDL) complex would induce a change in the implant promoting the release of therapeutic compounds that would ultimately lower the level of the antigen. A response in the anti-LDL SLN-antigen complex would be achieved by designing an antigen responsive interpenetrating network (IPN) hydrogel for recognition of the antigen complex. This allows the creation of specificity of the imprint region to the nanoparticle-antigen complex based on its structural characteristics. Figure 1.1 shows a simplified flowchart giving a breakdown of how the implant was designed and the types of analysis for assessing its performance.

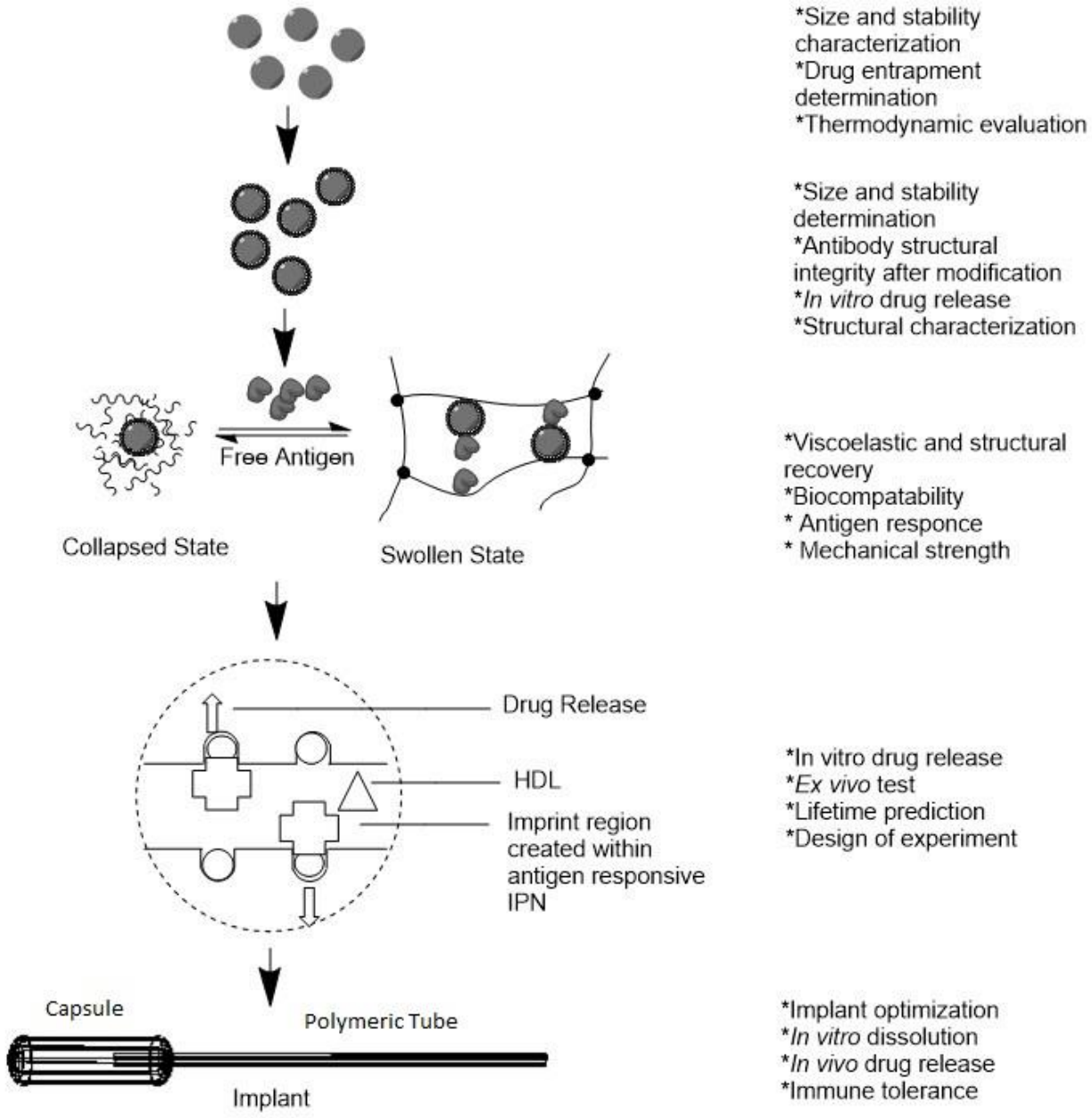

Figure 1.1: Flow diagram depicting experimental procedure for design of IVISDDD and infusion device.

The interaction of the nanoparticles within the hydrogel was due to covalent or non-covalent forces. The anti-LDL SLN-LDL complex would then bind to the imprint regions created within the tubule. Progressive binding would cause pressure within the tubule, exacerbated by hemodynamic forces as blood flows through the tubule lumen, which in turn would exert pressure on the neighboring drug-loaded hydrogel, causing disruption of the polymeric network, thus promoting a drug release from the neighboring hydrogel. Consequently, drug release would

occur due to antigen recognition and implant stimulation, allowing responsive drug delivery (Bayer and Peppas, 2008; Meilander et al., 2001). This presents a biochemically-activated mode of drug delivery in contrast to pH and temperature-dependent systems (Bajpai et al., 2008). The system could be adapted to detect diverse antigens thus having application in:

1. Detection and removal of toxins e.g. bacteriocins and mycotoxins.
2. Stimuli-response due to elevated molecules – hypercholesterolemia.
3. Detection and treatment of bacteremia e.g. Meningococcus.
4. Mutant protein detection.
5. Allergy-inducing compound detection followed by responsive treatment of the allergic reaction.
6. Detection of antigens specific to infectious diseases and subsequent treatment e.g. tuberculosis.

1.3. Aim and Objectives of this Study

The aim of this study was to design an IVISDDD that would detect hyperlipidemia before it manifests through recognition of a high levels of LDL concentrations and respond by the release of fenofibrate in order to address the chemical imbalance. The objectives of the study include;

1. To identify suitable biodegradable polymers for anti-LDL SLN design and identify monoclonal antibodies specific to the antigen (LDL), followed by their immobilization onto the sensor to form an antibody-conjugated anti-LDL SLN.
2. To design antigen responsive interpenetrating network (IPN) hydrogel specific to the antibody-conjugated anti-LDL SLN.
3. To create a polymeric tube to incorporate hydrogel for loading of the anti-LDL SLN.
4. To monitor the binding activity of the anti-LDL SLN and the release levels of the drug from the IVISDDD in response to the antigen *in vitro.*
5. To undertake thorough physicochemical and physicomechanical characterization of the IVISDDD.
6. To define variables for optimization of the sensorial and responsive behavior of the IVISDDD employing Design of Experiments.
7. To ascertain tolerance of the IVISDDD via *in vivo* investigations and to ascertain the level of drug release in relation to stimulation.

1.4. Novelty of this Study

- A biodegradable, nano-enabled, implantable system for the simultaneous detection and treatment of elevated blood cholesterol levels has not been designed to date.
- Embedding antibody conjugated nanoparticles in a viscoelastic hydrogel responsive to hemodynamic forces
- Intravenous infusion of anti-LDL solid lipid nanoparticles for management of hyperlipidemia
- This system has the potential for application in the detection of changes in the circulating blood levels of diverse substances e.g. neurotoxins, pathogens and chemical imbalances.

1.5. Overview of this Dissertation

Chapter 1 introduces and outlines the background to the study. Factors affecting diagnosis and management of hyperlipidemia are discussed. The chapter also discusses the use of implantable drug delivery system such as osmotic pumps and focuses on its advantages, disadvantages, and ways to improve the infusion rate of therapeutic compounds. It outlines the rationale, motivation, aim and objectives of the study and the potential benefits of the study.

Chapter 2 presents a literature review focusing on integration of biosensors in drug delivery. It entails the use of biosensors in diagnosis of diseases; characterization of different types of biomarkers and modes of detection; categorize different types of drug delivery systems, how they are synthesized for a variety of disease and duration of use and discuss factors affecting implantable medical devices. It further details how to incorporate the integration of biosensor technology with drug delivery systems in order to manage chronic diseases such as diabetes and hyperlipidemia by detection and controlling high levels of glucose and cholesterol, respectively.

Chapter 3 describes the development and characterization of anti-LDL SLN solid lipid nanoparticles. Synthesis of anti-LDL SLN for detection of low-density lipoprotein is discussed. Drug entrapments, antibody biotinylation and conjugation are discussed. Radial immunodiffusion and sodium dodecyl sulfate polyacrylamide gel electrophoresis (SDS-PAGE) are used for characterization of the modified antibodies to assess their affinity for oxidized and un-oxidized LDL particles known as atherogenic biomarkers. Drug release was assessed using dissolution, whilst microscopy is used to confirm nanoparticle morphology and formation of LDL-nanoparticle complex.

Chapter 4 describes synthesis and characterization of antigen responsive interpenetrating network (IPN) hydrogel. In this Chapter, viscoelastic hydrogel was synthesized and cross-linked with thiolated anti-LDL SLN via avidin thiol-groups and acrylate groups found on methyl acrylic acid and polyethylene glycol diacrylate. Rheology was used to characterize mechanical strength of the polymer to withstand hemodynamic force, whilst texture analysis was used for measuring resilience. Hydrogel swelling and cytotoxicity were analyzed to determine possibility of toxicity during implantation and level of swelling after implantation.

Chapter 5 describes implant fabrication procedure; implant mechanical characterization and *ex vivo* studies for evaluation of implant intravascular performance. An implant was fabricated using a polymeric tube to stabilize the antigen responsive interpenetrating network (IPN) hydrogel for intravenous implantation; osmotic pump and drug reservoir designed for subcutaneous implantation and infusion of drug into the polymeric tube, whereby the antigen responsive interpenetrating network (IPN) hydrogel will aid in controlling rate of diffusion. TGA and hydrolysis were used to determine the lifetime of the IVISDDD components, whilst *ex vivo* studies were conducted to determine how blood flow would affect the implant drug release rate.

Chapter 6 describes the *in vivo* animal studies undertaken on the device. This Chapter entails the use of Large White pig model for determination of implant response to diet induced hypercholesterolemia. Pigs were fed a high cholesterol diet for the duration of the study. UPLC analytical methods developed validated and applied for the quantification of the model drug fenofibrate, whilst pathology was conducted to determine the tolerance of IVISDDD by the animals.

Chapter 7 provides the conclusions and recommendations for further study in this field.

CHAPTER TWO
LITERATURE REVIEW

2.1. Introduction

Management of chronic illnesses such as diabetes and cardiovascular disorders require maintenance of glucose and cholesterol levels. For better health management, biological sensors or biosensors have been used in diagnostics. Biosensors are analytical devices that utilize biological recognition elements such as antibodies and receptors for the detection of disease biomarkers, followed by the quantification of biomarkers by means of transducers (Sethi, 1994; Vo-Dinh, 2008). Once the state and level of disease/illness is assessed, it is then followed by prognosis and finally illness management with intervention of suitable therapeutics. Drug delivery systems offer illness management by means of utilizing sustainable responsive and targeted drug delivery vehicles. These procedures followed by illness management are expensive, as they require highly skilled personnel and expensive equipment. In many cases, medical intervention efficiency is reduced when the most high-risk (susceptible) patients are not diagnosed at an early stage such as in the case of cancer and cardiovascular diseases. Biomarkers which are measurable and quantifiable biological parameters such as macromolecule concentration, volatile compounds and genetic variation (single nucleotide polymorphism), found in the presence of biological material, serve as indicators for health and physiology-related assessments (Colburn, 2000). Selection of biomarkers is therefore the key to illness management before they manifests. In this chapter various biomarkers, biosensors and drug delivery systems will be discussed in order to discuss improvements for diagnostics and therapeutic intervention by integrating biosensors with drug delivery system. This can help improve chronic illness caused by glucose and cholesterol.

The diagnosis of profound disease such as cancer generally requires a biopsy to be performed. This is however an invasive procedure where prognosis is limited. Accurate analysis requires technologies such as micro arrays in order to trace susceptibility and level of severity. The analysis of proteomics and genomics require sophisticated instruments and highly trained personnel for data analysis in relation to the high number of people diagnosed with cancer. As an alternative, physiochemical changes that occur during illness can be analyzed making use of noninvasive procedures. Lung cancer is one of the illnesses that can be diagnosed by means of analyzing exhaled volatile organic compounds (Di Natale et al., 2003; Machado et al., 2005).

Volatile organic compounds such as hexane, methylpentane and benzene derivatives such as *o*-toluidine and aniline have been used as lung cancer biomarkers (Phillips et al., 2006; Phillips et al., 1999). These technologies will replace the use of X-rays, which does not show illness manifestation until a tumor has formed. After diagnosis, medical intervention is required for illness management. This is where drug delivery plays an important role since proper mode of delivery contributes substantially to the efficiency of illness management.

Advances in drug delivery systems and technologies aim at overcoming limitations of conventional drug delivery using traditional dosage forms by achieving enhanced bioavailability and therapeutic index, reduced side effects, and improved patient acceptance or compliance. The purpose of modern drug delivery systems is to improve the pharmacokinetics and pharmacodynamics that often play very important roles in therapeutic efficacy and overall functioning of the body systems. Pharmacokinetics deals with drug delivery inside the body, which involves absorption, distribution, metabolism and elimination; while pharmacodynamics deals with the physiological effects of drugs on the body and the mechanisms of drug action. The relationship between drug concentration and effects require efficient formulation to meet optimum illness management. The use of responsive polymers, microtubules and nanoparticles has allowed targeting sites of illness and controlling the drug release profile. Factors exerting crucial role in drug delivery system design are biocompatibility, controlled drug release and degradation.

Integration of diagnosis and therapeutics into a single system can improve illness management. The combination of biosensors and drug delivery system vehicles does not only allow self-regulated therapeutics but is a protective means against biohazard agents as well (Cao et al., 2001). Detection of biohazards levels, chemical and biochemical substances require selection of a marker which can be used as direct or indirect indicator. As in environmental applications pollution can be determined by detecting the level of elevated foreign compounds and chemical by-products, this same mode of detection can be applied for illness management. Biochemical imbalances, such as those of glucose and cholesterol levels, are indicative of different illness. Hypercholesterolemia and hyperglycemia signify elevated levels of cholesterol and glucose, whereas hypercholesterolemia and hypoglycemia indicate their low levels.

The identification of a chemical, biochemical or pathogen organism is generally been done employing common technologies of enzyme-linked immunosorbent assay (ELISA), polymerase

chain reaction (PCR), flow cytometry and spectroscopy. These are time consuming, require specialized training, and involve complicated processing steps to culture or extract the analyte from samples. In relation to drug delivery, conventional modes of delivery such as oral, rectal, transdermal, subcutaneous, or sublingual administration have shown lower bioavailability (depends on the chemical nature of the administered compound such as hydrophilic or hydrophobic), whereas intravenous and intramuscular routes of administration have shown to reduce patient compliance (Kwon and Kim, 2005). Implantable and portable biosensors for drug delivery offer self-monitoring and increased patients' compliance (Sershen and West, 2002).Integrated biosensors and drug delivery devices can offer a continuous diagnosis, prognosis and efficient therapeutic management through targeting disease specific biomarkers.

2.2. Biomarkers as Indicators of Disease Progression and Occurrence

The term biomarker (i.e. biological marker) was introduced in 1989 (Mayeux, 2004). This was defined as measurable and quantifiable biological parameters such as specific enzyme concentration, specific hormone concentration, specific gene phenotype distribution in a population, presence of biological substances. These serve as indices for health and physiology-related assessments, such as disease risk, psychiatric disorders, and environmental exposure and its effects, disease diagnosis, metabolic processes, substance abuse, pregnancy, cell line development and epidemiologic studies (Vasan, 2006). This was further clarified as a characteristic that is objectively measured and evaluated as an indicator of normal biological processes, pathogenic processes, or pharmacologic responses to a therapeutic intervention. Biomarkers can indicate a variety of health or illness characteristics, including the level or type of exposure to an environmental factor, genetic susceptibility, genetic responses to exposures, markers of subclinical or clinical illness, or indicators of response to therapy. Thus, a simplistic way to think of biomarkers is as indicators of disease trait (risk factor or risk marker), disease state (preclinical or clinical), or disease progression rate. Figure 2.1 depicts the "biomarkers" basing most on site of extraction and major illness association.

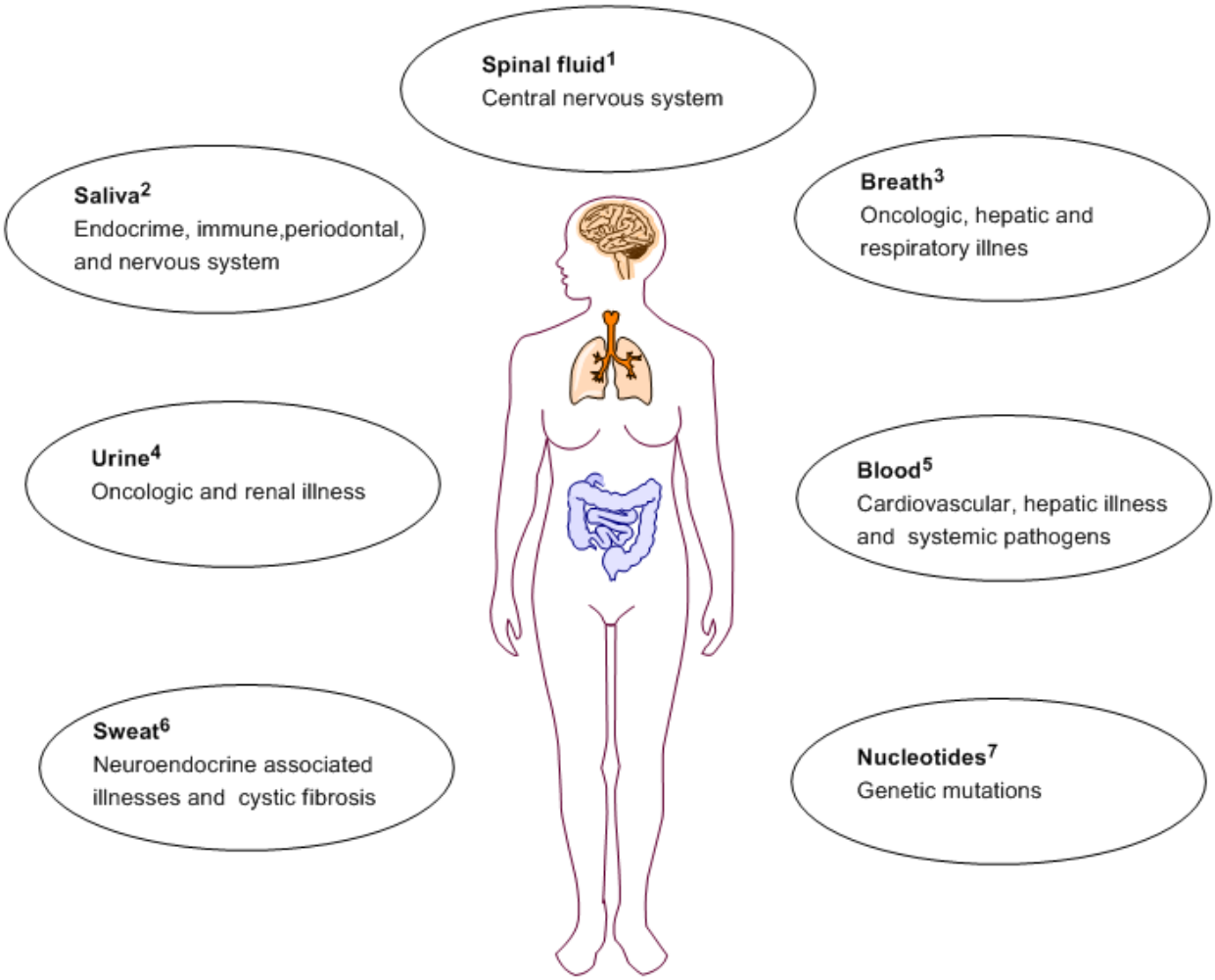

Figure 2.1: Biomarkers based on site of extraction and major illness association. (Adapted from (Belluzo et al., 2008; Chambers and Vanderhyden, 2006; Di Francesco et al., 2005; Gonzalo-Ruiz et al., 2009; Huang et al., 2006; Miekisch et al., 2001; Wong, 2006).

Accordingly, biomarkers can be classified as antecedent biomarkers (identify the risk of developing an illness), screening biomarkers (screen for subclinical disease), diagnostic biomarkers (recognize overt disease), staging biomarkers (categorize disease severity), or prognostic biomarkers (predict future disease course, including recurrence and response to therapy, and monitoring efficacy of therapy). Defining abnormal values is a critical step before the clinical use of a biomarker. It is important to characterize the distribution of the markers in people in the community and in patient samples on whom the biomarker will be tested. At least three potential approaches exist for defining abnormal biomarker levels and these are, reference, discrimination and threshold defining risk. The reference limits uses a comparison of normal and disease individuals. However, this varies in terms of sex, age and ethical background in different disease.

Chronic illnesses such as diabetes, lupus, osteoarthritis, rheumatoid arthritis, cancer, Cystic fibrosis, asthma, Parkinson's disease, coronary heart diseases and AIDS require continuous monitoring. Cancer is an illness that requires early detection and accurate diagnostics for efficient treatment. Lupus and AIDS affect the immune system, making the body susceptible to pathogenic invasion; usage of microchips with biosensors can allow the release of multiple drugs based on the pathogen being detected. Therefore, continuous monitoring of biomarkers is required for defensive measures and illness management. Parkinson's disease is an illness that affects the central nervous system, which requires drug passing through the blood brain barrier. In Parkinson's disease patients, continuous conventional drug usage is affected when a patient has lost control of their motor skills. Therefore, the use of implants that can release a continuous supply of drugs at a specified time interval would allow better illness management without any denting intervention. Four other illnesses such as diabetes, coronary heart disease, asthma, and arthritis will require a responsive treatment to the physiochemical changes that may occur at any given time by means of using biosensors.

2.3. Biosensors for Disease Detection and Monitoring

Chemical sensors and biosensors are of interest within the field of modern analytical chemistry and pharmaceutics. There is a number of published research works which show the diversity of approaches and techniques applied. This is due to new demands and opportunities that are appearing particularly in clinical diagnostics, environmental analysis, food analysis and production monitoring (Berna, 2010; Ivnitski et al., 1999; Ou et al., 2004). A sensor is a device which functions by producing a signal which is proportional to the concentration of a specific (bio) chemical or a set of (bio) chemicals in the presence of a number of interfering species (Thévenot et al., 2001). This is accomplished by means of using biological recognition elements such as enzymes, antibodies, receptors, tissues and microorganisms as sensitive materials because of their excellent selective functionality for target substances. Figure 2.2 is a schematic depicting functional principles of a biosensor. Sensors can be divided into various groups based on the mode of function in terms of sensing region and transduction.

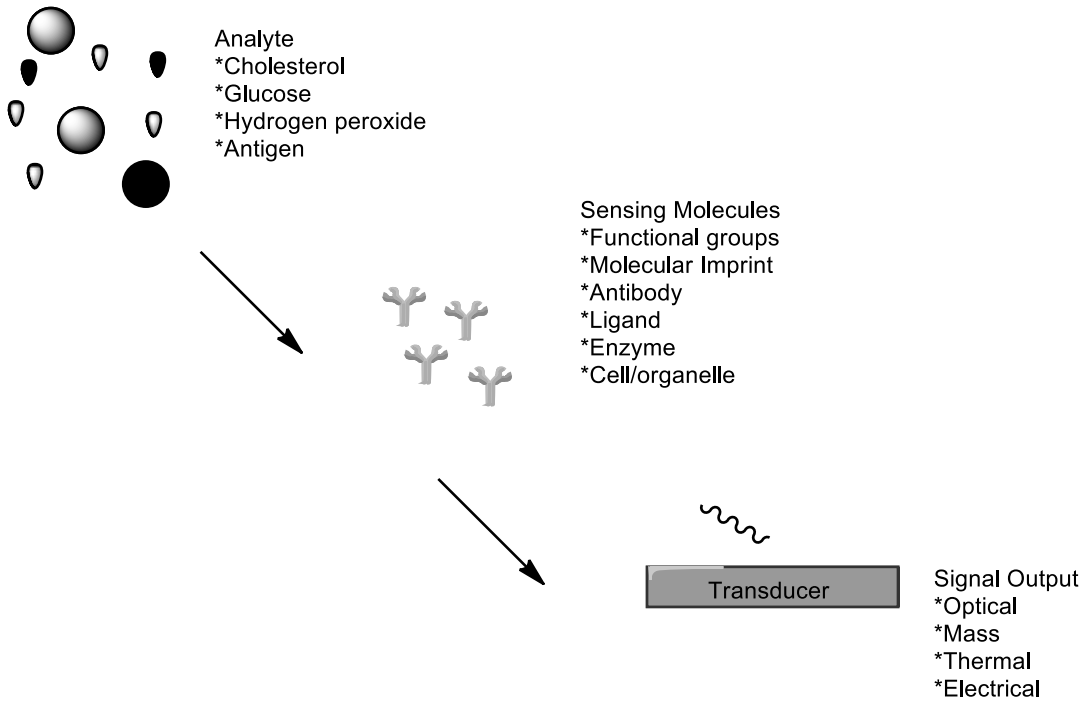

Figure 2.2: Schematic depicting functional principles of a biosensor.

2.3.1. Immunosensor and other Affinity Biosensors

Immunosensors and Affinity Biosensors constitute immobilized biological recognition elements such as antibodies, antigen, receptor protein and short oligonucleotide sequences for detection of biomarkers (Byrne et al., 2009; Killard et al., 1995). Once the analyte binds to the sensing element, the signal is converted by the transducer into a measurable unit. The mode of quantification can be achieved by measuring the specific activity of a label, such as its radioactivity, enzyme activity, fluorescence, chemi-luminescence or bioluminescence (Bhattacharyya and Klapperrich, 2007; Li et al., 2007). Immunosensors use antibodies or antibody fragments as biological recognition fragments which generate a signal during physical changes as they mimic antibody properties. Single-stranded oligonucleotide sequences known as aptamers are also considered immunosensors as they mimic antibodies properties by being folded into order to form structures that allow binding to target analytes (Byrne et al., 2009)]. Contrary to aptamers, genome sensors use probes (nucleic acid fragments) which specifically recognize and bind to a complementary/target nucleic acid strand. The recognition is dependent upon the formation of stable hydrogen bonds between the two nucleic acid strands due to nucleotides hybridization. Hydrophobic, ionic and hydrogen bonds play a role in both genome sensors and immunosensors (Levicky and Horgan, 2005). Both these applications can be used to detect degree of viral infection and forms of cancer (microarray-mRNA) whereby the

immunosensor would detect structural components of the virus, whereas genome sensors would detect the genomic fingerprint (Shan et al., 2003). Depending on the method of signal transduction, sensors can further be divided into four basic groups: optical (bioreporter), mass (cantilever), electrochemical (amperometric), and thermal sensors (Martin-Palma et al., 2009). Electrochemical biosensors can thus be classified as either being biocatalytic (enzyme) or affinity (antibody) devices (Ronkainen et al., 2010).

2.3.2. Amperometric Immunosensors

Enzyme-linked immunosorbent assay (ELISA) represents an amperometric immunosensor where the enzymes undergo redox reactions to generate an electrochemically active product. Current amperometric immunosensors use antibodies or antigens due to their high sensitivity. They can be immobilized onto polymer membrane, Langmuir-Blodgett film, sol-gel and self-assemble monolayers. Unlike enzymes, the antibodies and antigens lack electrochemical activity, therefore for functionality in biosensing they have to be labeled or use a probe molecule such as ferricyanide in the solution (Vestergaard et al., 2007). Carcinoembryonic antigens (CEA) are extensively studied biomarker for tumor. An amperometric biosensor was designed for detection of the antigen by means of immobilization of anti-CEA monoclonal antibody on a self-assembled monolayer (Wu et al., 2009). There are two different kinds of immunoassays, the homogeneous immunoassay which involves a mixture of antibodies, antigens and labeled antigens. The antigens can be distinguished by a change of activity of the marker when coupled during competitive binding. Heterogeneous immunoassays have antibody or antigen immobilized on a solid support where the immune-complex forms when a solution containing the other immune-agent is added (Laboria et al., 2010). The disadvantage is that labeling is a complicated and time-consuming process that often leads to physiologically irrelevant binding information and the denaturation of the modified proteins (Ramirez et al., 2009).

2.3.3. Label Free Immunosensors

Cantilevers are an example of label free biosensors, which offer a simple, rapid, reliable, minimal cost and low limit of analyte detection. Due to its label free detection principle and small size, this type of biosensor has applicable advantages in diagnostic applications, disease monitoring and research in genomics and proteomics (Vollmer and Arnold, 2008). A cantilever biosensor functions by means of transduction of the molecular interaction between analyte and capturing molecule, immobilized as a layer on one surface of a cantilever. Biomolecular interactions taking place on a solid-state interface leads to an increase in mass (Backmann et

al., 2005). This process results in bending of the cantilever. The capturing molecules are immobilized onto the cantilever by means of direct absorption or by means of covalent attachment to the surface modified with functional groups (Wu et al., 2008). Other label-free immunosensors include optical label free detectors such as venerable surface plasmon resonance sensors that can obtain quantitative data on intermolecular binding (Çağlayan et al., 2009). Label-free voltammetric immunosensors use electro-active residues in the antibody structure to give specific current response during immune complex formation (Vestergaard et al., 2007). Carbon nanotubes and self-assembled monolayer (SAM) represent some of label free biosensors. Apart from label-free measurements that utilize detection of refractive index with surface plasmon resonance, mass change with quartz crystal microbalance and change in conductivity, viscosity and mass with surface acoustic wave; a novel method that utilizes the use changes in ion channels current can be used. By means using a mesoporous polymer, when an analyte of interest enters into the polymer nanopore, this will transiently block the ion current, resulting in a downward current-pulse. Through this mechanism, analytes detection can be achieved by monitoring the blockage of nanopores before and after an immunological reaction as the current-pulse frequency is proportional to the concentration of the analyte (Alvarez and Lechuga, 2010).

2.3.4. Bioreporter Type Biosensors

Bioreporters is a fusion of genome biosensors and cell based sensors. Genetically modified microbes can be used to produce a measurable signal in response to a specific chemical or physical agent in their environment (Lin et al., 2011). Cell-based biosensors have been used in various fields such as biomedicine, environmental monitoring and pharmaceutical screening. They offer high sensitivity, excellent selectivity and rapid response. In pharmaceutics, these biosensors are useful in analyzing the effect of pharmaceutical compounds on a given physiological system. Enzyme-based biosensor can also be classified with genome and cell-based sensors and can be used to convert the analyte into a quantifiable substance exhibiting fluorescence or conductivity. The reporter proteins range from green fluorescent protein, aequorin, firefly luciferase, and/or bacterial luciferase (Ripp et al., 2008).

2.3.5. Enzyme-Based Biosensors (Electrochemical Biosensors)

Enzymatic activities tend to either produce or consume protons and/or electroactive species (Wilson and Hu, 2000). The use an electrode as the transducer can be utilized to quantify the amount analytes during enzymatic reaction. Biosensors constituting enzymes usually employ a

class of enzymes known as oxidoreductases, whilst in some case oxidases and dehydrogenases can also be used. When direct transfer of electron between the electrode and enzyme redox center cannot be accomplished, this requires the use of a mediator (must be non-toxic, independent of the pH, stable in both the oxidized and reduced forms) such as ferrocene which can aid in promoting the relay of electron transfer to an electrode (Badia et al., 1993). In another study it was found that dopamine and daunomycin can improve the relay (Battaglini et al., 1994). Other mediators involve the use of organometal compounds (Zhao et al., 2010). In enzyme-based biosensor, the presence of oxygen affects the activity of the mediator. Therefore the use of mediators improves biosensor performance by eliminating the oxygen dependence and improves the ability to control the concentration of the oxidizing agent in the biosensor (Chaubey and Malhorta, 2002). The use of enzyme electrodes as biosensors will continue to increase because they are simple and inexpensive to manufacture, and they provide rapid analysis with the possibilities of being easily regenerated and reusable (Garcia et al., 2011).

2.3.6. Cholesterol Biosensor

Cholesterol oxidase contains flavin adenine dinucleotide (FAD) as the active redox center. During enzymatic reaction, oxygen acts as a physiological mediator on the electrode surface which undergoes electrochemical oxidation and leads to formation of cholest-4-enone and hydrogen peroxide (Aoun et al., 2004). The increase in H_2O_2 or reduction in O_2 can be used to determine the amount of cholesterol. This however has a disadvantage as the variation in oxygen tension of the sample leads to fluctuations in electrode response while reoxidation of hydrogen peroxide leads to increased interference from metabolites such as ascorbate and uric acid (Ahn and Sampson, 2004). To overcome this disadvantage a combination of two or more enzymes is used which offer more selectivity for the analyte (primary enzyme cholesterol oxidase acts on cholesterol, generated hydrogen peroxide caught by a secondary enzyme peroxidase or hemoglobin) of interest and reduce chances of interference (Cass et al., 1984). A disposable biosensor has been developed that can determine total cholesterol. The total cholesterol is determined by disposable strips immobilized with Fe_3O_4, cholesterol oxidase (ChOx) and cholesterol esterase (ChE) (Zhao et al., 2009). The enzyme combination allows the detection of both esterified and free cholesterol.

2.4. Drug Delivery Systems Design and Applications

Drug delivery system platform is a rapidly expanding market for pharmaceutical and biomedical engineering. In terms of pharmaceuticals, the need for drug carriers that will offer targeted drug

delivery is of vital importance. This is of great value as it reduces the side effect profile by allowing usage of low dosage drugs, site-specific activity and increased bioavailability. Non-targeted systemic drug administration leads to the bio-distribution of pharmaceuticals across the entire body (Sijja et al., 2009). This distribution causes toxicity effects on non-target tissues and wastage of pharmaceutical compounds since they are used by non-target tissues. For biomedical engineering, design of devices that will offer better diagnosis and therapeutics is required to ensure better illness management. Biomedical engineering will aid in targeted drug delivery, selective targeting of imaging contrast agents, delivery of nucleic acid and genetic therapies, and prediction of pharmacokinetics and pharmacodynamics patterns of the drug (Pierigè et al., 2008).

Biomaterials are needed to design a stable and biocompatible drug delivery system. These can vary from natural polymers, metals compound, modified and synthetic polymers. Biocompatibility and biodegradation of these play a vital role in the toxicity effect of the system and its mode of action. A beneficial drug delivery system must have an effect on drug absorption, distribution, and metabolism levels (Deo et al., 2003). This can be achieved by controlling drug delivery system. Controlled drug delivery system functions by means of controlling where and when the therapeutic agent will be released. The major features of controlled drug delivery system include the rate of drug release and mode of activation. Drug release may be rapid or may occur over a prolonged period of time depending on the required action and the location of the device in the body. Figure 2.3 is a schematic depicting the different modes of drug delivery system synthesis.

The mode of release and the rate is related to the biomaterial constituting the major part of the system. Depending on the location where the system is directed to release the drug, the biomaterial that make up the system play a role in terms of reacting with the physiochemical compounds to protect the therapeutics, sense the activator and also allow binding to the target site for localized drug release. Targeted drug delivery can be done by means of using natural organic compounds. These natural compounds interact with surface of the synthetic/modified polymers and peptides. The use of sugar molecules which can be mucoadhesive allows targeting of the intestine. These will be stimulated by temperature (e.g., poly (*N*-isopropylacrylamide)) and pH level (polyacrylic acid and chitosan) for drug release. There are different kinds of polymers that can be used for this purpose; anionic (polyacrylic acid), cationic

(chitosan), non-ionic (polyethylene glycols) and thiolated polymers (cysteine conjugates) (Inzelt et al., 2000).

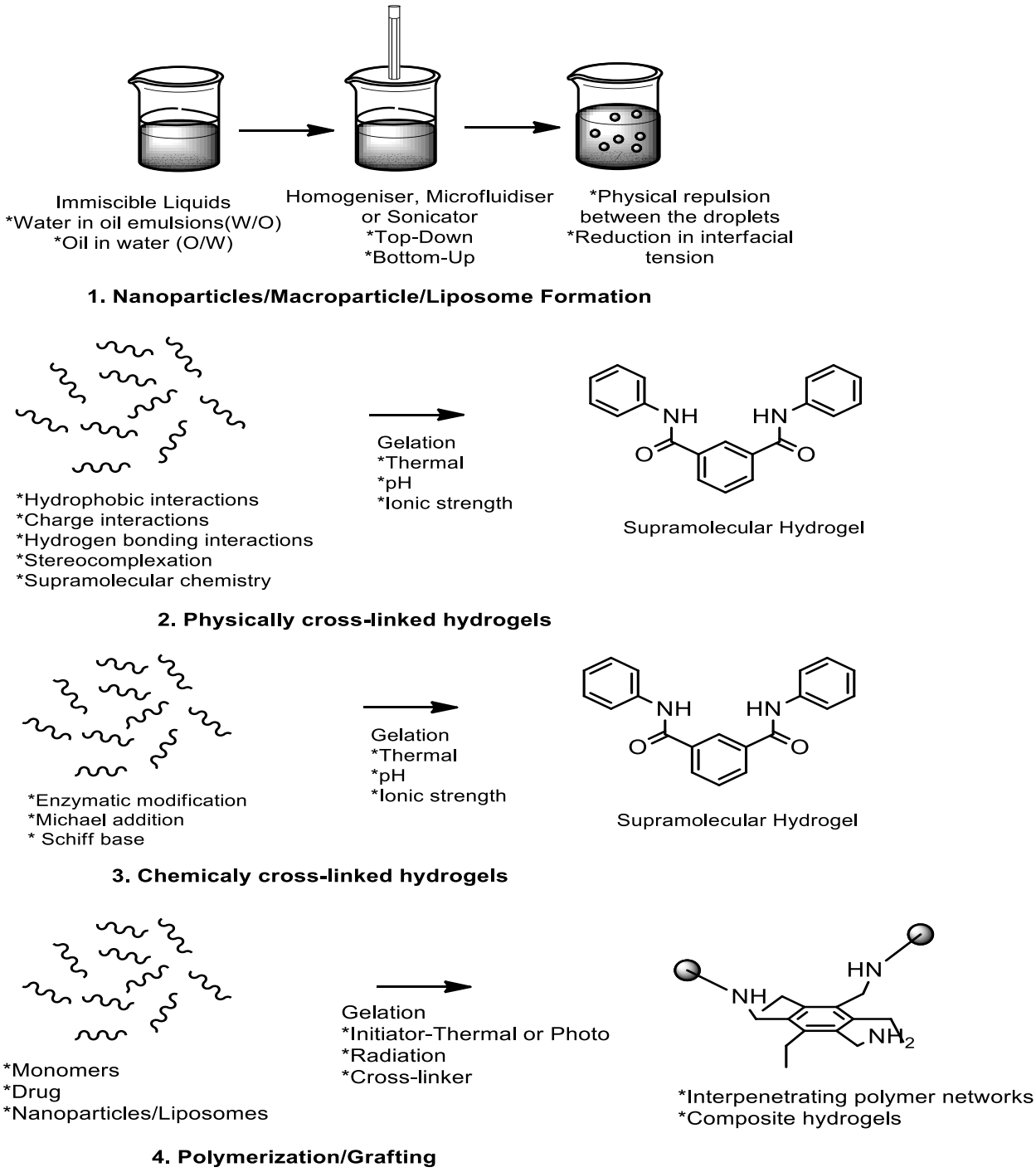

Figure 2.3: Various techniques of drug delivery system formulation. (Adapted from (Bhattacharya and Misra, 2004; Hoare and Kohane, 2008; Malam et al., 2009).

Depending on the mode of action required for the drug delivery system, these biomaterials could be modeled into different forms such as spheres for carrying therapeutics and film/hydrogels layers for physiochemical response. For therapeutic implication, nanoparticles and liposomes are primarily used to adsorb and absorb drugs of interest and even for encapsulating the sensitive therapeutics. Targeted drug delivery requires binding of biochemical molecules which offer directed control of therapeutic action. For continuous and responsive drug delivery system, thin films and even nanoparticles may be used as they can respond to the physiochemical changes that may occur in the body. Hydrogels form a three-dimensional structure consisting of cross-linked networks of water-soluble polymers, which can undergo conformational changes once they interact with water (Deligkaris et al., 2010). They can further be modified to react at a certain temperature, detection of analyte based on interaction with functional groups or pH in relation to their mode of action and target site. Upon reaching a certain site of action, the swelling dynamics will change, allowing for the diffusion of a therapeutic from the network matrix.

The fabrication of these systems relates to their chemical properties. If a system is designed for targeting the gastric intestinal tract, it must withstand physiochemical changes such as pH and temperature before it reaches its required site of action. Polymers such as chitosan, polyvinyl alcohol and ethylene glycol, can be used for both targeted and responsive action. Chitosan as a drug carrier has been used for various administration routes such as oral, bucal, nasal, transdermal, parenteral, vaginal, cervical, intrauterine and rectal (Denkbas and Odabasi, 2000). As a responsive or targeted drug delivery vehicle, these biomaterials can be cross-linked or conjugated to other compounds to offer a responsive and improved targeting. Synthesis can be conducted by means of modifying temperature, ionic strength and pH during formulation. Physiochemical interactions such as hydrophobic/hydrophilic interactions, charge condensation, and hydrogen bonding have effects on the physiological interactions of the device.

Biodegradation relates to biocompatibility as the byproducts must be excreted or recycled by the body. Degradation and drug release kinetics are dependent on the concentration of the polymers and the cross linkers used. Cross linkers affects the drug release due to changes in porosity and viscosity. This can be changed by means of chemical modification, employing other compounds such as salts and metals. Salts can affect the tolerance of the physiochemical environment by changing the ionic strength of the device and act as cofactors for enzymatic action (Gil and Hudson, 2004). Different forms of drug delivery systems are designed based on

mode of action. More focus has been directed towards responsive and target drug delivery towards organs. The brain and spinal cord are protected by the blood brain barrier (Qin et al., 2008). This barrier affects the treatment of the neurological illness. By having different forms of drug delivery systems which may though have advantages and disadvantages, will offer a chance to design new therapeutic treatment methods.

A drug delivery system has a number of benefits such as reduced toxicity, reduced side effects profile, controlled drug release, targeted drug delivery and usage of biocompatible (nonpathogenic such as viral vectors and additives for drug stabilization) substances. Nanoparticles are the most widely used since they can offer a number of benefits. The main benefits of nanoparticles being high surface to mass ratio, quantum properties (conductivity), and ability to absorb and carry a variety of therapeutics (Frasco and Chaniotakis, 2009). Nanoparticles based on their mode of synthesis can have two major applications; imaging and carriers. All forms of drug delivery must take into consideration and fulfill basic requisites such as knowledge of drug incorporation and release, formulation stability, shelf life, biocompatibility, biodistribution, targeting and functionality before they can be declared fit for medical.

2.5. Factors Affecting Implantable Medical Devices

The conventional oral and intravenous routes of drug administration do not provide ideal pharmacokinetic profiles especially for drugs which display high toxicity and/or narrow therapeutic windows. For such drugs, the ideal pharmacokinetic profile will be one wherein the drug concentration reaches therapeutic levels without exceeding the maximum tolerable dose and maintains these concentrations for extended periods of time until the desired therapeutic effect is reached. One of the ways such a profile can be achieved in an ideal case scenario would be by encapsulating the drug in a polymer matrix. Implantable drug delivery has a number of advantages in relation to conventional drug delivery such as localized delivery of drug. The product can be implanted directly at the site where drug action is needed and hence systemic exposure of the drug can be reduced. This becomes especially important for toxic drugs which are related to various systemic side effects (such as the chemotherapeutic drugs). In sustained delivery of drugs, the drug encapsulated is released over extended periods and hence eliminates the need for multiple injections. This feature can improve patient compliance especially for drugs for chronic indications, requiring frequent injections. Stabilization of the drug is an important aspect in implantable drug delivery systems. The polymer can protect the drug

from the physiological environment and hence improve its stability *in vivo*. This particular feature makes this technology attractive for the delivery of labile drugs such as proteins.

The development of long-term implantable biosensors has been seriously impeded by the deleterious effects of biofouling and lack of poor *in vivo* biocompatibility. Biofouling is a major drawback in biosensor technology as the process reduces sensing capacity of the sensors. Biofouling is the process whereby biomolecules are adsorbed on the sensor when there is an inflammatory response to the foreign body. These molecules are usually of less than 15kDa in size. Proteins, peptides, lipids, phospholipids and other small molecules can adhere to the surface by integrating into the polymer matrix. Apart from disrupting sensing capability in drug delivery integrated systems, biofouling may lead to reduction in drug diffusion. Therefore, it is necessary to have polymers that resist protein adsorption such as polyethylene glycol and polyethylene oxide.

Most of the microfabricated implants are in the form of biosensors. There is a time limit in the use of microfabricated implantable biosensors due to their short functional duration. By designing an implantable biosensor that has a long term functionality this can be a critical component of the ideal closed-loop drug delivery or monitoring system, without considering the issue of implant biocompatibility and biofouling which must be addressed in order to achieve long-term *in vivo* sensing (Grayson et al., 2004). By using a thermal, pH, ionic strength or biomolecular sensitive hydrogel as a transducer which can be used in the integration of drug delivery system and biosensor, better biocompatibility and reduced biofouling may be achieved. A cantilever can be used, such as a lid on a reservoir whereby a sensing molecule embedded in a responsive hydrogel can stimulate the opening and closing of the lid in relation to analyte quantity. Furthermore, the use of an electrically responsive hydrogel can also be used as components of MEMS-based sensors or drug delivery devices whereby the external electrical current can be applied on an implant to stimulate drug release intramuscularly. The drug delivery MEMS technology has been applied to formulate microparticles and microreservoirs.

2.6. Current Methods used in Medical Diagnosis and Management

Using chemical biosensors to determine the levels of important marker molecules may serve to guide therapeutic regimens, thereby improve drug safety and efficacy (Nadeau, 2009). Determination of biomarkers in a non-invasive manner and diagnosis at point of care is the key to improving illness management in pharmaceutical intervention and patient compliance.

Biosensors are tools that can shape illness treatment by increasing accuracy of diagnosis, illness monitoring and prognosis. The advantages of biosensors are that they are easy to use, inexpensive, rapid and robust and also allow analysis of different biomarkers simultaneously (Tothill, 2009). The other main advantage is that there is no sample preparation since the biosensor can detect the biomarker within a pool of contaminated bimolecular substances. Current drug delivery systems can be integrated with biosensors. Microneedles are minimally invasive drug delivery systems which are painless and have no blood contact which reduces infection and risk of device contamination. In drug delivery, they are used to inject a therapeutic agent transdermal whilst in biomedical sensing they are useful for fluid extraction for analysis.

Smart polymers may function in the same manner as biological systems. Stimuli responsive hydrogels can undergo structural changes when exposed to external stimuli such as pH, temperature and ionic changes. The polymers are divided into three groups based on their physical form. Linear free chain polymers in solutions undergo reversible collapse after a stimulus is applied, covalently cross-linked reversible hydrogels swell/shrink when triggered by environmental changes and chain adsorbed/surface-grafted form polymers experience reversible swelling/collapse on the surface once a trigger is set off (Kumar and Mishra, 2007). Like affinity biosensors, a hydrogel was designed by grafting an antigen-antibody complex to a polymer network. This led to competitive binding of the free antigen which triggered a change in the network structure of the hydrogel (Miyata et al., 1999). Figure 2.4 indicates that the hydrogel was also found to retain its primary structure due to shape memory behavior after reversible binding (Roy et al., 2010).

This behavior allows long-term use of the system unlike affinity biosensors that are saturated over time as reversible binding is not favored. In terms of usage of enzymes, the entrapment of glucose oxidase within a pH responsive hydrogel (gluconic acid increase due to oxidation of glucose) and attachment of insulin allowed the smart polymers to act as both drug delivery vehicles for insulin and biosensors of glucose concentration (Traitel et al., 2000). Other reversible systems include biotin/desthiobiotin (analogue of biotin) and Concanavalin A (Con A) immobilized systems. Desthiobiotin/biotin-binding protein complex can also be dissociated under physiological conditions by either biotin or desthiobiotin (Hirsch et al., 2002). Since biotin can be used to label a variety of proteins, this can be conjugated to either antibodies or antigens to serve as a reversible biosensor. Immobilization of Con A has been shown to lead to a

reversible sol-gel phase when in the presence of free glucose and due to competitive binding with insulin conjugated with glucose (Qiu and Park, 2001).

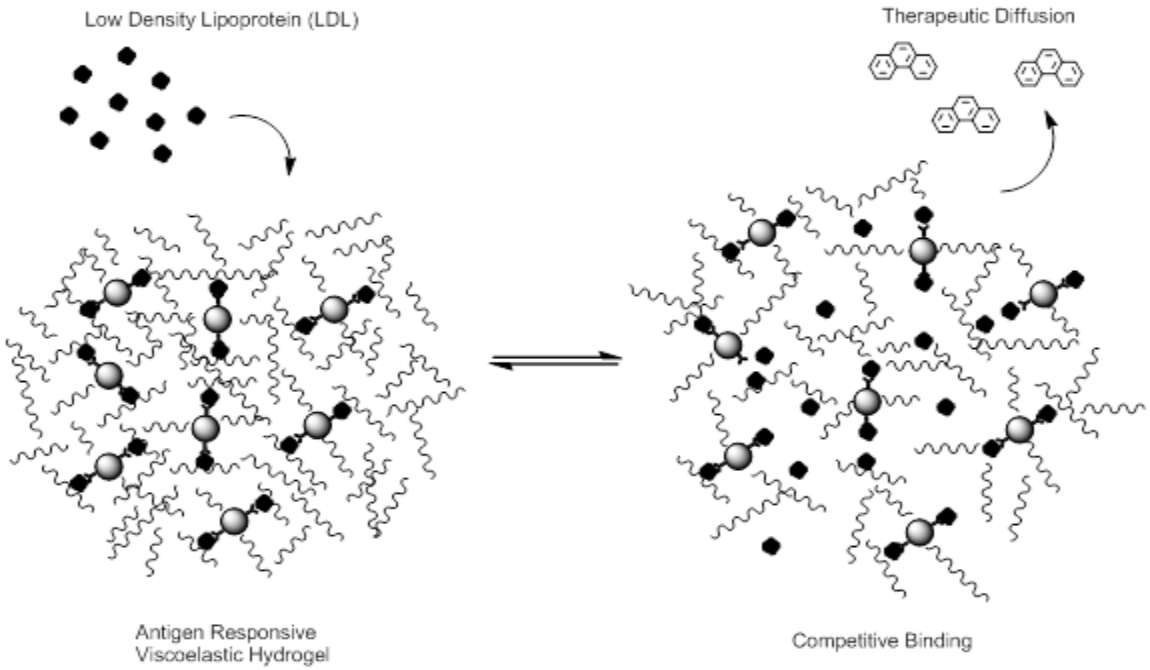

Figure 2.4: Reversible antigen responsive hydrogel. (Adapted from (Miyata et al., 1999)).

Responsive controlled treatment will reduce the side effect profile as this will reduce continuous accumulation of active pharmaceutical ingredients (APIs) in the body, which may lead to toxicity. In general, integration of biosensors and drug delivery systems offers patients a chance for self-monitoring which will improve illness management since all information in relation to their medical problems may be continuously monitored and maintained. Early detection of chronic illnesses such as cancer will therefore offer better and effective therapeutic treatments, while illness monitoring is applicable to common chronic illness such as diabetes (hyperglycemia) and cardiovascular diseases (hypercholesterolemia) which are increasing at an alarming rate in developing countries. By designing an implantable biosensor which will function as a “lap on a chip” will facilitate rapid illness management since the patients are in control of the health status. This may further be optimized by including multiple drugs in the implant reservoir for better illness management, thus preventing any further complication that may occur during self-regulatory therapeutic treatment.

2.7. Concluding Remarks

According to the World Health Organization, cardiovascular diseases are the leading cause of death around the world with an estimating 17.3 million deaths in 2008 which will be followed by 23.3 million deaths in 2030 (WHO, 2013). Diabetes mellitus, however, is categorized on a pandemic level where its prevalence in Africa ranges between 1 and 20%. Other diseases such as chronic respiratory diseases are also on the increase as they are often underdiagnosed due to limited diagnostic resources. The cause of respiratory in children is mainly allergens and pollutants which can be monitored and controlled. Due to low availability and accessibility of drugs and diagnostic tools, these diseases continue to increase in prevalence. Integration of biosensors and drug delivery offers the design of an 'implantable pharmacy' which can operate as a closed loop system. This will offer continuous diagnosis, treatment and prognosis without vast data processing and specialist intervention.

Implantable sensors are expected to interface with the body's biochemistry to provide a critical link between diagnosis and therapeutics. However, the creation of biosensors with integration of drug delivery system requires a closed loop monitoring of the device. The use of implants such as biomedical (or biological) microelectromechanical systems (BioMEMS) can release a continuous supply of drugs at a specified time interval to allow better illness management without any serious intervention. For illnesses such as diabetes, coronary heart diseases, asthma, and arthritis will require a responsive treatment since physiochemical changes may occur anytime. In general, integration of the biosensor and the drug delivery system offers patients a chance for self-monitoring which will improve illness management since all information in relation to their medical problems may be continuously monitored and managed. Early detection of chronic illnesses such as cancer will therefore offer better and effective therapeutic treatments, while illness continuous monitoring is applicable to common chronic illnesses such as diabetes and cardiovascular diseases which are increasing at an alarming rate in developing countries (Gaziano and Pagidipati, 2013).

CHAPTER THREE
DEVELOPMENT AND CHARACTERIZATION OF ANTIBODY CONJUGATED NANOPARTICLES

3.1. Introduction

Combined hyperlipidemia is an atherogenic lipid disorder characterized by high levels of Low Density Lipoproteins (LDL) and Triglycerides (TGs), and low levels of High Density Lipoprotein (HDL) (Athyros et al., 2002). Patients with type 2 diabetes are more susceptible to this disorder (Rabbani et al., 2011). Although dietary and medical interventions can aid in combating hypercholesterolemia, this can further be enhanced by means of extracorporeal elimination of LDL particles from the plasma and improving bioavailability of lipophilic drugs. Statins (Lovastatin, simvastatin, atorvastatin, fluvastatin and pravastatin) and fibrates (Clofibrate, fenofibrate and Gemfibrozil) have been used for treatment of combined hyperlipidemia and are capable of reducing atherosclerosis related morbidity and mortality in patients with diabetes in combination with diet (Athyros et al., 2002). They function by inhibiting the rate-limiting step of cholesterol synthesis in the liver (Vaughan et al., 1996). This reduction further results in increased synthesis of LDL receptors and consequently an increased LDL removal from plasma (Hopkins, 2010). Fenofibrate, a third-generation fibric acid derivative lipophilic drug is a highly effective agent for the treatment of atherogenic dyslipidemias, producing significant increases in HDL-C, reduction in levels of apolipoprotein B (protein component of LDL particles) and reducing in LDL-C. Fenofibrate therapy produces substantial reductions in the level of very-low-density lipoprotein cholesterol (VLDL-C), triglyceride-rich lipoproteins and it has a beneficial effect on lipoprotein(a) and several non-lipid risk factors that include; plasma fibrinogen, C-reactive protein, and platelet activity.

Poor water solubility of compounds with therapeutic value has always been of concern in pharmaceutics and novel formulation strategies are being designed to circumvent this shortcoming. In order to pass across the biological membrane, for efficient absorption coefficient, such compounds with low water solubility need to possess certain hydrophilic-lipophilic-balance (HLB) (Merisko-Liversidge and Liversidge, 2008). Administration of poorly water soluble drugs, such as fibrates, with lipids is a highly effective mechanism of enhancing their absorption with lipid based formulations such as solid lipid nanoparticles (SLN) therefore, can have a major impact in improving bioavailability of such drug (Gokce et al., 2010). These

particles can be used to deliver hydrophilic and hydrophobic drug via oral as well as intravenous administration (Freitas and Müller, 1998).

SLN can be formulated from lipids such as triglycerides, complex glyceride mixtures or even waxes which can form the lipid core (Parveen et al., 2012), that can be stabilized using a variety of surfactants. To ascertain the effectiveness of SLN as drug carriers, loading capacity has to be evaluated by analyzing solubility and miscibility of the target drug with lipid melt which can affect the amount of drug entrapped (Muller et al., 2000). The drug release rate is profoundly governed by formulation components and the procedure adopted for SLN preparation. The concentration of surfactant, apart from playing a major role in SLN stabilization, also plays a role in drug release rate as low concentrations leads to a minimal burst and prolonged drug release (Uner and Yener, 2007). Additionally, the surface of SLN allows electrostatic interaction with macromolecules such as peptides, nucleotides and proteins (Bondi et al., 2007; Goppert and Muller, 2003), and this facet of SLN can be harnessed for conjugating SLN to LDL specific antibodies which will then target LDL, allowing apheresis of LDL by means of increasing LDL uptake during SLN phagocytosis. Such immunoaffinity techniques are considered most efficient for significantly reducing LDL levels without hampering HDL levels (Blaha et al., 2005), and SLN binding to streptavidin, DNA and biotinylated ligands is previously documented (Pedersen et al., 2005).

The aim of the present study was to prepare SLN as carriers of lipophilic drugs; fenofibrate and specifically target against LDL for management of combined hyperlipidemia. Incorporation of fenofibrate in SLN and further conjugation of these particles to anti-LDL antibodies will generate a system that detects and binds LDL particles along with providing increased bioavailability of the fenofibrate, both of which are important aspects for combating hyperlipidemia. Such system will facilitate in LDL plasma clearance during SLN clearance and allow therapeutic management of high LDL particles through drug eluding SLN. Furthermore, slow release of fenofibrate will aid in reducing myopathy, thus improving patient compliance due to targeted delivery (Tiwari and Pathak, 2011). Antibody conjugated SLN are synthesized and used for detection of LDL particles by means of targeting the Apo-B100 protein found on LDL particles.

3.2. Materials and Methods

3.2.1. Materials

Gattefossé (Lyon, France) gave the lipid component, Compritol 888 ATO (glyceryl behenate), as a gift sample. Pluronic F68 (polyoxyethylene-polyoxypropylene block copolymer), fenofibrate, ethanol, Tween 80, anti-LDL antibodies, Lipoprotein (Low Density from human plasma), Biotin N-hydroxysuccinimide ester, SnakeSkin® pleated dialysis tubing, 3.5kDa, avidin from egg white, sodium deoxycholate, Trizma base, Triton X100, sodium chloride, ammonium persulfate (APS), N,N,N,N–tetramethylethylenediamine (TEMED) and methanol were purchased from Sigma (Sigma-Aldrich, Missouri, USA). Double distilled water (ddH_2O) was obtained from a Milli-Q station. All the other reagents used were of analytical grade.

3.2.2. Preparation of solid lipid nanoparticles

Fenofibrate loaded SLNs were prepared by the oil-in-water ultrasonic-solvent emulsification technique. The composition of various formulations is shown in Table 3.1. A lipid solution was prepared by dissolving Compritol in ethanol at 90˚C, while stabilizer of varying concentrations was prepared by dissolving Pluronic F68 in distilled water at 90˚C. The temperature used represents the temperature above Compritol melting point (70°C). The temperature was maintained during the synthesis process to obtain a system with good characteristics. For drug encapsulation and drug-polymer interaction, various fenofibrate concentrations (0.2, 0.4 and 0.6($\%^{w/}_{v}$)) were dissolved in lipid solution prior to addition of the stabilizer to a formulation that showed better stability. In addition, empty SLN were prepared. The stabilizer solution was then slowly added into the lipid melt solution to create an emulsion. The coarse oil in water emulsion was obtained using the CV18 Vibracell probe sonicator for 20 minutes, whilst the emulsion containing 100mL beaker was submerged in 0°C waterbath (Sonics & Material, Inc., Connecticut, USA). The beaker was then transferred to a sonication bath (SB 5200, Ultrasonic Cleaner,) to break any large unstable particles and to generate a uniform size distribution (Ningbo Hengliang Trading Co. Ltd., Zhejiang, China). A 0.5%$^{w/}_{v}$ sucrose was added to the SLN solution as a cryoprotectant prior to freezing at -80°C for 24 hours. The nanoparticles were then lyophilized for 24 hours (Labconco, Missouri, USA) with a 2 hours condensation phase at −60°C and a 24 hours sublimation phase at 25mm Torr. Each batch was prepared in triplicate, and the average size was evaluated.

Table 3.1: Formulations for assessing the stability and size of SLN based on ($\%^{w/}_{v}$) ratio between solid lipid and non-ionic stabilizer.

Formulation	Compritol ATO 888($\%^{w/}_{v}$)	Pluronic F68($\%^{w/}_{v}$)
F1	0.8	0.8
F2	0.8	0.4
F3	0.8	0.2
F4	0.8	0.1

3.2.3. Determination of nanoparticle size and stability

The average size and stability (zeta potential) was determined by the dynamic light scattering technique. Each measurement was obtained at a 90° fixed-angle for 180 seconds, at 25°C, and the laser light wavelength was set at 678nm. A digital correlator was used to analyze the scattering intensity data under a unimodal analysis mode. Particle size and size distribution of native SLN, drug loaded SLN and avidin coated were analyzed by a Zetasizer NanoZS instrument (Malvern Instruments (Pty) Ltd., Worcestershire, UK). A 10mm quartz cuvette was used. The lyophilized nanoparticles were appropriately diluted with filtered distilled water (0.22μm pore) until the light scattering signal of the particles in suspension was within the instrument's sensitivity range. Prior to analysis, the suspended nanoparticles were further filtered through a 0.22μm pore size polycarbonate membrane filter. Zeta potential was determined by means of transforming the electrophoretic into Z-potential by applying the Smoluchowski approximation using a capillary cell after diluting dispersion by 1:10 using filtered distilled water (0.22μm pore). Each sample was tested in triplicate.

3.2.4. Modification of antibodies and nanoparticle avidin coating

Biotinylation of lysine residue on anti-LDL antibodies Fc region was conducted as per the Pierce Chemical Co. biotinylation protocol (Thermo Fisher Scientific Inc., Massachusetts, USA). Biotinylation was carried out in 50mM phosphate buffer, pH 6.5. The mixture of biotin-NHS and anti-LDL antibody at a ratio of 10:1 was stirred for 30 minutes at room temperature, and then incubated at 4°C for 24 hours. This was then followed by dialysis (SnakeSkin® pleated dialysis tubing, 3.5kDa) purification in PBS (pH 7.4) for 24 hours at 4°C. For avidin coating of SLN, the nanoparticles were immersed in avidin solution prepared in PBS (pH 7.4), stirred for 2 hours at room temperature. The ratio of SLN to avidin was 20:1. Thereafter the coated nanoparticles were dialyzed (SnakeSkin® pleated dialysis tubing, 3.5kDa) using PBS (pH 7.4) at 4°C for 24 hours to remove traces of free avidin. For antibody conjugation to SLN, five molar excess of biotinylated antibodies were mixed with avidin coated nanoparticles in PBS (pH 7.4) while stirring for 30 minutes in a 37°C water bath at 50rpm to form antibody conjugated SLN. They

were then lyophilized and store at -20°C for future studies. The interaction between biotin and biotinylated lysine residue was indicated using ACD/ChemSketch Freeware (ACD/Labs, Toronto, Canada) software.

3.2.5. Analysis of biotinylated antibody structural integrity

SDS-PAGE analysis was performed for confirming biotinylation of antibody on a Bio-Rad vertical electrolysis cell Criterion system (Bio-Rad Laboratories Pty Ltd., California, USA). Gel preparation, apparatus setup, protein loading and gel visualization was conducted in accordance to SDS-PAGE protocol (Bio-Rad Laboratories Pty Ltd., California, USA). A volume of 5µL of unmodified antibody, biotinylated antibody and Takara Broad protein marker (200kDa) were mixed separately with buffer constituted from 4.75µL Laemmli sample buffer (62.5mM Tris-HCL (pH 6.8), 2%$^{w/}_{v}$ SDS, 25% glycerol, 0.01%$^{v/}_{v}$ bromophenol blue and 5%$^{v/}_{v}$ β-mercaptoethanol) and 0.25µL β-mercaptoethanol in respective Eppendorf™ tubes. The samples were heated at 70°C for 10 minutes. A 10% resolving gel was prepared adding ddH_2O (7.8mL), 1.5M Tris-HCL (3.75mL, pH 8.8), 30% acrylamide/bis (3.3mL), 10%$^{w/}_{v}$ APS (75µL) and TEMED (10µL). The gel solution was poured into the gel-casting casing and allowed to polymerize. Isobutanol (100µL) was used to overlay on top of the casted resolving gel and allowed to stand for 3 minutes before removal and rinsing with ddH_2O. A paper towel was used to dry the casing before adding onto the resolving gel, the 4% stacking gel solution comprising of ddH_20 (9mL), 0.5M Tris-HCL (3.78mL, pH 6.8), 30% acrylamide/bis (1.98mL), 10%$^{w/}_{v}$ APS (75µL) and TEMED (20µL). A 10-well comb was inserted into the stacking gel to allow formation of wells during polymerization. A volume of 10µL of each sample was added into respective wells. A Tris-HCl running buffer (25mM Tris, 192mM glycine and 0.1% SDS, pH 8.3) was used. A standard 200 voltage was applied with a combination of an initial current of 100mA and a final 40mA current for 50 minutes. The gels were then removed from the cassettes and washed three times with MilliQ water. A gel fixation solution (50%$^{v/}_{v}$ methanol and 10%$^{v/}_{v}$ glacial acetic acid) was poured to cover the gels and left for 15 minutes, thereafter removed by rinsing with MilliQ water. Gel staining was conducted by immersing the gels in a staining solution (0.1%$^{w/}_{v}$) Coomassie Brilliant Blue, 40%$^{v/}_{v}$ methanol and 10%$^{v/}_{v}$ glacial acetic acid) for 2 hours in an orbital shaker (50rpm, 25°C). After washing out with MilliQ water a destaining solution (10%$^{v/}_{v}$) methanol and 7% glacial acetic acid) was added. MilliQ water was used for rinsing prior gel visualization using a Victor X3 Luminometer (PerkinElmer Inc., Missouri, USA). Each sample was tested in triplicate.

3.2.6. Antibody and Apolipoprotein B100 concentration analysis

Protein concentration was analyzed to determine the concentration of antibodies and the antigen Apo-B100 protein. This was used for determination of appropriated amounts of antibody and LDL concentration for use in oxidation and radial immunodiffusion studies. The Thermo Scientific™ Pierce BSA Protein Assay Standards protocol was used to generate a standard curve to be used for protein concentration analysis. Bovine serum albumin (BSA) was used to generate a standard curve for analysis of unmodified anti-β-LDL antibodies, biotinylated antibodies, unoxidized LDL and oxidized LDL (ApoB) particle concentration. 0.1g of BSA was dissolved in 10mL of water at room temperature. The stock BSA solution was diluted to span the 100-1,500µg/mL range. A Bradford protein reagent was made which constituted final concentrations of 0.01%$^{w/}_{v}$ Coomassie Brilliant Blue G-250, 4.7%$^{v/}_{v}$ ethanol, and 8.5%$^{v/}_{v}$ phosphoric acid. 60µL of each standard and protein samples was mixed with 940µL of Bradford reagent in respective Eppendorf™ tubes. Each concentration was made in triplicate. Each sample was allowed to incubate at room temperature for 10 minutes. The concentrations were determined using an absorbance at 595nm using quartz cuvettes against a blank containing 60µL of water mixed with 940µL of Bradford reagent (Specord 40, AnalytikJena, Jena, Germany). Absorbance was plotted against [BSA] and an equation for the line was generated. Each sample was tested in triplicate.

3.2.7. Oxidation of Low Density Lipoprotein

LDL oxidation was conducted to determine if the antibodies could detect oxidized LDL, which are biomarkers of atherosclerosis. This was also used to illustrate that fenofibrate did not have direct anti-oxidation properties on LDL particles. Oxidation using copper ions was conducted as per the Springer Protocol (Springer Protocols, Methods in Molecular Biology). For oxidation process LDL concentration was adjusted to 100µgmL^{-1} using 10mM PBS, pH 7.4. The oxidative modification of LDL was initiated by addition of freshly prepared 10µM $CuSO_4$ solution at 37°C in a shaker bath (25rpm) and allowed to proceed for 3 hours. Another oxidation solution was prepared with an addition of Captopril, whilst another solution contained fenofibrate and the fourth solution served as a control consisting of LDL only. The kinetics of LDL oxidation was monitored every 15 minutes by measuring solution absorbance at 234nm (Specord 40, AnalytikJena, Jena, Germany). The conjugated dienes concentration was calculated by using extinction coefficient (29mmolL^{-1}cm^{-1}). Susceptibility to oxidation was expressed as the “lag time” determined from an intercept of lines drawn through the linear portion of lag and propagation phases for each sample. To quantify a successful lipid peroxidation, the formation

of thiobarbituric acid reactive substances (TBARS) was analyzed in a spectrophotometer at 532 nm hourly (Specord 40, AnalytikJena, Jena, Germany). The results were recorded as malondialdehyde (MDA) equivalent content ($nmolmg^{-1}$ LDL-protein) from excitation coefficient of $155mmolL^{-1}cm^{-1}$. Each sample was tested in triplicate.

3.2.8. Confirmation of biotinylation of the fragment crystallizable region of the antibody

Change in antigen recognition after modification was tested using radial immunodiffusion. This was also used for confirming the site of modification on the Fc region without affecting the binding affinity (Fab region). Radial immunodiffusion was conducted as per the Imgenex Private Ltd protocol (Imgenex Private Ltd., Bhubaneswar, India). In brief, 0.17g of agarose was heat melted in 17mL 1X Assay buffer. 450µL of biotinylated antibody solution was mixed with the cooled 15mL agorose solution at 37°C. The mixed solution was then poured onto a clean petri dish. The dish was gently swirled for generating a uniform distribution of antibody and allowed to solidify for 15-20 minutes. Wells were then made using the broader back end of a 1mL micropipette tip according to the template printed from Imgenex single radial immunodiffusion kit's user manual. A control consisted of unmodified antibody solution. The wells were then sealed with 20µL of molten agarose solution per well and ensured that the distribution was uniform. Oxidized and unoxidised LDL particles were used in concentrations of 2mg/mL, 1mg/mL, 0.5mg/mL, 0.25mg/mL and 0.125mg/mL. The petri dish was left at room temperature inside a box containing wet cotton wool for 48 hours to allow precipitin rings to form. Each sample was tested in triplicate.

3.2.9. Microscopic analysis of antibody conjugated solid lipid nanoparticles

Transmission electron microscopy (JEM-100S, JOEL Pty Ltd, Tokyo, Japan) was used to visualize the morphology of the nanoparticles and formation of the SLN-LDL complex. Solution of antibody conjugated SLN and SLN-LDL complex were poured onto respective copper grids surface. The samples were allowed to dry prior analysis into TEM. The SEM (JOEL JSM 840, SEMTech Solutions, Inc., Massachusetts, USA) was also used for topological surface analysis of SLN. A layer of gold/palladium was applied onto SEM specimen mounts prior to addition of antibody conjugated SLN powder onto the surface. The samples were allowed to dry for 48 hours prior visualization under SEM.

3.2.10. Thermodynamic and molecular interaction analysis of solid lipid nanoparticles

DSC was performed using DSC 1 (Mettler Toledo, Ohio, USA) instrument using an empty aluminum pan that served as a reference sample for thermodynamic analysis. For conventional DSC measurements, drug loaded SLN with varying drug concentrations were heated from -20°C to 100°C at a heating rate of 10°C/min. This was analyzed to determine the interaction between the drug and the lipid core. Each sample was tested in triplicate. To determine the purity of the sample that can affect the crystalline/amorphous state, the van't Hoff equation (Equation 3.1) was used.

$$T_f = T_0 - \frac{RT_0^2}{\Delta Hf} x_{2.0} \frac{1}{F} \quad (3.1)$$

Where T_f is the melting temperature, T_0 is the melting temperature of the pure substance, R is the gas constant, ΔH_f is the molar heat of fusion, $x_{2.0}$ is the molar concentration to be determined.

3.2.11. Structural crystallinity analysis of antibody conjugated nanoparticles

X-ray powder diffraction analysis was performed to determine changes/presence of crystallinity. Analysis was conducted on a Rigaku MiniFlex600 Benchtop X-ray Diffractometer (Rigaku Corporation, Tokyo, Japan) fitted with; a 600W (40Kv-15mA) X-ray generator, a counter monochromator to cut X-rays other than Cu Kα X-rays and a high intensity D/tex Ultra high speed 1D detector. The diffractometer was operated using the Rigaku MiniFlex Guidance software, version 1.2.0.0 and data was analyzed using the Rigaku PDXL Basis software able to perform integrated intensity calculations. Measurement parameters included a divergence slit (DS) of 1.25º, Scattering slit (SS) of 1.25º, a 0.3mm receiving slit (RS) and a Goniometer radius of 150 mm. Each powder sample of fenofibrate, avidin, Compritol, Pluronic F68, SLN and anti-LDL SLN was pressed flat onto a square grooved glass slide that acted as the sample holder. Measurements were performed by scanning each sample at 0.01-100º/min over a diffraction angle range of 3º-60º 2θ. The XDR diffractograms generated were used to determine the crystallinity and amorphous phases of the respective samples (Santos et al., 2003; Mishra et al., 2008; Kumar et al., 2011; Raviolo and Briñón, 2011).

3.2.12. Structural transformations analysis of solid lipid nanoparticles

Attenuated Total Reflectance-FTIR (ATR-FTIR) analysis of native SLN components (Compritol, avidin, Pluronic F68 and fenofibrate), Biotin-NHS, dehydrated proteins (Biotinylated antibody) and the fabricated SLN was undertaken to evaluate, ascertain and compare the structural transformations. ATR-FTIR spectra were recorded on a Perkin Elmer Spectrum 2000 FTIR spectrometer with a MIRTGS detector (PerkinElmer Spectrum 100, Wales, UK), using an ATR-FTIR cell and a diamond crystal internal reflection element. Samples were analyzed at a wavenumber range of 650–4000cm−^{1} with a resolution of 4cm^{-1} and 100 scans per spectrum.

3.2.13. Drug entrapment efficacy and loading capacity

Different concentrations of fenofibrate were loaded into an emulsion to determine drug entrapment efficiency, loading capacity and drug-polymer interaction. These factors can affect mechanism of drug release and structural properties. After entrapment, the nanoparticles were lyophilized to dry the particles and the free drug. The lyophilized particles were suspended in methanol for 10 minutes to dissolve the free drug. The nanoparticles were centrifuged (4000g) to obtain the supernatant followed by measuring the absorbance of the supernatant using UV instrument (Specord 40, AnalytikJena, Jena, Germany) at 290nm. From the different absorbance readings in relation to drug amount the entrapment efficacy and loading capacity were determined using the equation 3.2 and 3.3, respectively. Each sample was tested in triplicate. To determine interaction between the drug and nanoparticle, Flory-Huggins equation was used (Equation 3.4).

$$Entrapment\ Efficiency(\%) = \frac{Mass\ of\ Initial\ Drug - Mass\ of\ Free\ Drug}{Mass\ of\ Initail\ Drug} \times 100 \quad (3.2)$$

$$Loading\ Capacity(\%) = \frac{Mass\ of\ Initial\ Drug - Mass\ of\ Free\ Drug}{Mass\ of\ Nanoparticles} \times 100 \quad (3.3)$$

$$T_m = T_m^0 + T_m^0 \left(\frac{V_2}{\Delta H_2}\right) B(1-\phi_2)^2 \quad (3.4)$$

Where; T_m^0 and T_m are the melting point of pure fenofibrate and SLN incorporated fenofibrate respectively, while $^{\Delta V_2}/_{H_2}$ was the heat of fusion of pure fenofibrate per unit volume. B represented the interaction energy density.

$$B = X_{12}\, RT/V_1 \tag{3.5}$$

X_{12} represented the interaction parameter for drug incorporated nanoparticle while V_1 was the molar volume of Compritol (lipid core).

3.2.14. *In vitro* drug release analysis from antibody-conjugated nanoparticles

In vitro release studies were performed using dialysis method. Evaluation of drug release from anti-LDL SLN was performed by immersing drug loaded anti-LDL SLN in a dialysis membrane (10kDa cut off) into a six-station dissolution test apparatus (Model 7ST, G.B. Caleva, Dorset, UK). The speed of the paddle was set to 100rpm while the vessels contained 250mL PBS (pH 7.4 at 37±0.5°C). Each sample was tested in triplicate. A sample (5mL) was withdrawn at pre-determined time intervals and 5mL of fresh buffer was replaced to maintain sink conditions. Prior to reading of absorbance, a 0.22µm filter was used to filter the sample (Specord 40, AnalytikJena, Jena, Germany). Release kinetics was calculated from the equations 3.6-3.10. Zero-order kinetics (Equation 3..6) is described as process of constant release based on the observation of the drug dissolution of several types of modified release pharmaceutical dosage forms (Costa and Sousa Lobo, 2001). SigmaPlot 12 (Systat Software, Inc., California, USA) was used for for mathematical and statistical analysis.

$$Q_t \;=\; Q_0 + \; K_0\, t \tag{3.6}$$

First-order kinetics (Equation 3.7) which describes absorption and/or elimination of water-soluble drugs in porous matrices and a drug release independent of drug concentration.

$$In\, Q_t \;= In\, Q_0 \;-\; K_1\, t \tag{3.7}$$

Higuchi describes (Equation 3.8) the drug release from a matrix system where initial drug concentration in the matrix is much higher than drug solubility, where drug diffusion takes place only in one dimension, drug particles are much smaller than system thickness, matrix swelling and dissolution are negligible, drug diffusivity is constant and perfect sink conditions are always attained in the release environment (Shoaib et al., 2006).

$$Q_t = \; K_h t^{1/2} \tag{3.8}$$

For confirming the mechanism of drug release the first 60% of released drug was fitted in Korsmeyer-Peppas equation (Equation 3.9)

$$M_t / M_\infty = K_k t^n \quad (3.9)$$

Where M_t/M_∞ is fraction of drug released at time t, k is the rate constant and n is the release exponent. Due to enlarged particle size after addition of drugs, Hixson-Crowell (Equation 3.10) was used to analyze release based on change in surface area and diameter of the particle size.

$$\sqrt[3]{Q_i} - \sqrt[3]{Q_r} = K_s t \quad (3.10)$$

The model with the highest coefficient of determination (adjusted R^2) was considered the most suitable kinetic model for describing the release of fenofibrate from the SLN. The n value for Korsmeyer-Peppas model was used for determining mode of release (diffusion/erosion).

3.3. Results and Discussion

In the present study, fenofibrate loaded SLN were prepared by an oil-in-water emulsion technique using ultra-sonication methods. The selection and utilization of Compritol 888 ATO was based on earlier reports, which show the lipid offers long-term drug release (Rao et al., 2009). Varying concentrations of Pluronic F68 were used in this study due to surfactant concentration affecting particle size growth and aggregation. The emulsion technique with the utilization of ultra-sonication resulted in consistent production of smaller size nanoparticles (<150nm) with narrow size distribution and good entrapment efficiency. The SLN were synthesized to be coated with avidin, which were then conjugated with biotinylated anti-LDL antibodies.

3.3.1. Higher magnification of solid lipid nanoparticles

Transmission and Scanning electron micrographs of SLN were obtained in order to study the morphology of the particles and visualize their interaction with LDL. Synthesized native SLN and SLN interacting with LDL were visualized. Figure 3.1(a) presents a high magnification TEM image of native SLN and Figure 3.1(b) shows antibody conjugated SLN interaction with LDL particles at a still higher magnification. These images indicate a solid matrix structure without crystal formation. Scanning electron micrographs were also obtained for native SLN (Fig. 3.1(c)) and for the antibody-conjugated SLN interacting with LDL particles (Fig. 3.1(d)). The SEM and

TEM images of antibody conjugated SLN indicated that site specific biotinylation of lysine in the fragment crystallizable region (Fc) were successful. This is due to antibodies affinity to LDL Apo-B100 antigen site, which indicates that the fragment antigen-binding (Fab) region was not interrupted. Both types of micrographs showed rounded morphologies of the nanoparticles with a size ranging between 90-140nm. The particles appear to be aggregated in both TEM and SEM images (Fig. 3.1(a) and 3.1(c)). In the case of antibody conjugated SLN, observation of aggregation was attributed by the presence of avidin-biotin that caused non-specific aggregation of nanoparticles as coating with avidin-biotin complex has been reported to result in self-association of the nanoparticles (Langer et al., 2000). Concentrations of stabilizer and crystalline state of the polymers used also affected level of stability due to interference of cohesion (Keck and Muller, 2006). Although aggregation of nanoparticles was also observed to be dependent on the concentration of nanoparticles used during characterization and application (McNally et al., 2003), at high concentration nanoparticle aggregated whilst small concentration were evenly dispersed.

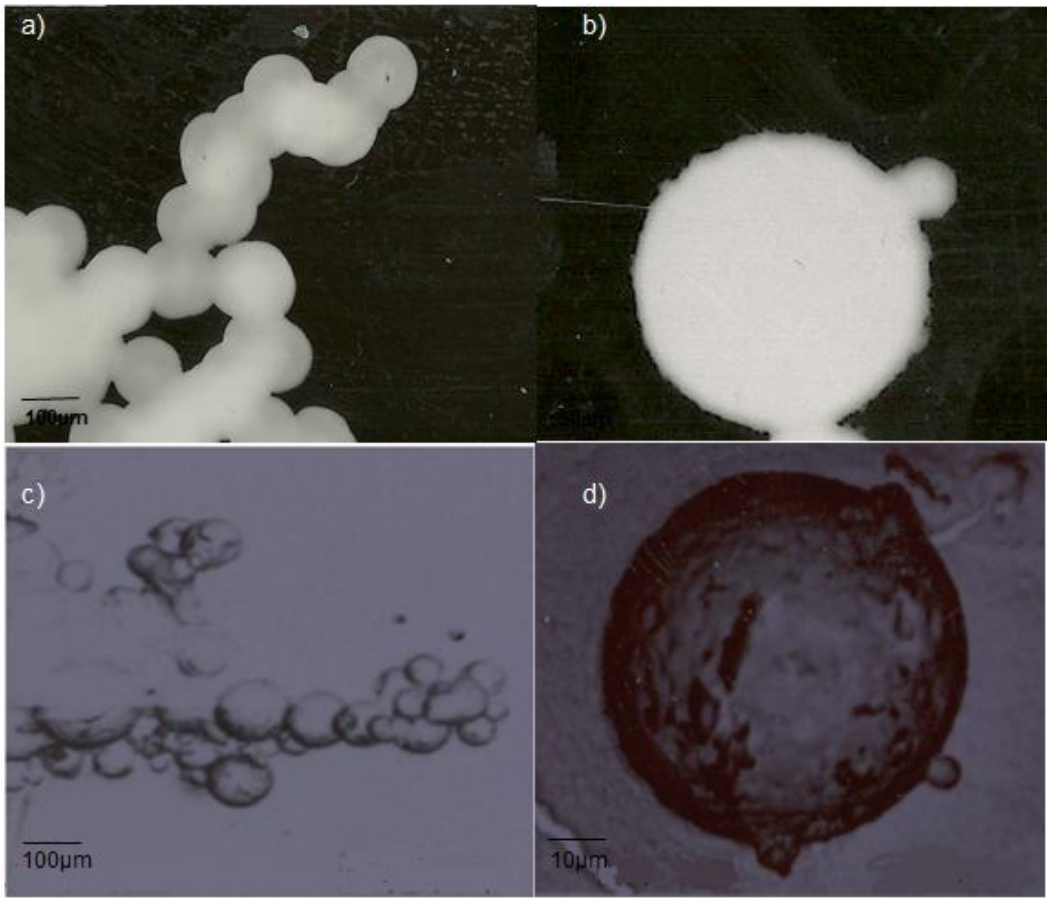

Figure 3.1: TEM (a and b) and SEM images (c and d) of native SLN (a and c) and antibody-conjugated SLN (b and d) is interacting with LDL particles.

3.3.2. Molecular modeling of antibody conjugation to avidin coat

ACD/ChemSketch Freeware (ACD/Labs, Toronto, Canada) software was used to illustrate the interaction between biotin and biotinylated lysine residue. This image was drawn with the aid of referral to the Protein Data Bank (2AVI). Conjugation of anti-LDL-antibody to SLN was undertaken to confer the particles the ability to complex with LDL. This would consequently result in LDL apheresis via enhanced LDL liver degradation *in vivo*. The level of LDL-SLN complex formation was primarily affected by the orientation of antibody on the SLN surface. This was dependent on the antibody biotinylation or modification site. Since the antibody would conjugate with SLN through modified site, the modification aiming Fc region and avoiding antigen binding (LDL binding in this case) Fab region of the antibody was successful. This preserved the functional activity of the antibody. This was done by targeting the lysine residues on the Fc fragment that has ionizable amine side chains. This procedure avoided biotinylation Fab which can cause inaccessibility of Fab fragments by the LDLs Apo-B100 (Figure 3.2) (Yavuz and Denizli, 2005). This ascertained the participation of Fc fragment in binding to the avidin moieties on the SLN while Fab region on the opposite part of the antibody was free and available for LDL binding as indicated in microscopic analysis. Conjugation of anti-LDL antibodies onto nanoparticles has been reported in previous studies to target LDL particles using polylactic acid (PLA) nanoparticles (Maximov et al., 2010). Like PLA nanoparticles previously reported, SLN nanoparticles are expected to be taken up by liver Kupffer cells and macrophages enhancing LDL uptake. Furthermore due to drug loading of biodegradable and biocompatible solid lipid nanoparticles, burst drug release is expected to occur during degradation in the liver by lipase while slow release in plasma during circulation (Müller et al., 1996).

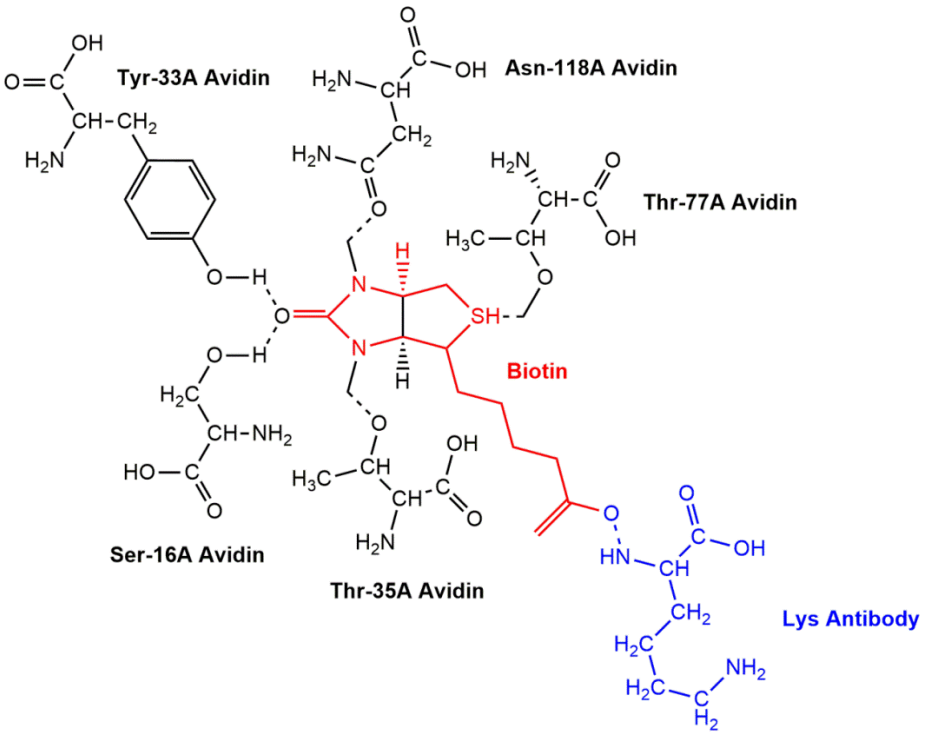

Figure 3.2: Schematic depicting anti β-LDL antibody-biotin-avidin interaction.

3.3.3. Surfactant concentration impact on particle size and stability

All the prepared samples were analyzed in order to determine their particle size distribution, zeta potential, and polydispersity index (PDI) values. Zetasizer was used to evaluate size distribution and stability of nanoparticles consisting of various surfactant concentrations using light scattering technique. Zeta potential of the nanoparticle dispersions was also studied to determine the level of stability, as non-aggregating nanoparticles are ideal for intravenous administration. Size was evaluated as the nanoparticle size ideal for intravenous administration ranges between 50-250nm for distribution to liver, spleen and blood (De Jong and Borm, 2008). The PDI was also used to define the particle size distribution. As seen in Figure 3.3, F1, F2 and F3 had zeta potential of -13.5±1.25mV, -19.7±1.52mV and -20.6±1.73mV, respectively. This showed a zeta potential of less than ±30mV and/or near ±30mV, which indicated less stability. This finding correlated with the microscopic observation, as these formulations showed some level of aggregation during analysis. Such aggregation of particles was due to Pluronic F68 forming an adhesive gel. Pluronic sol-gel transition was caused by colloidal self-assembly which was due to an increase in its concentration (Missirlis et al., 2006). Only F4 had zeta potential of -37.5±2.67mV, which was above ±30mV indicating that these nanoparticle formulations were stable in suspension. This indicated that low Pluronic concentration was favored.

The size of the nanoparticles also varied with varying surfactant concentration. An increase in surfactant concentration resulted in smaller nanoparticles as previously reported in many studies (F1 - 89.92±6.8nm, F2 - 101±5.9nm, F3 - 147±11.37nm and F4 - 107±2.98nm). However once there was a critical concentration of SLN of a certain size, this caused aggregation that correlates to zeta potential analysis. The PDI of the formulations ranged from 0.16-0.36 indicating an even dispersion of low concentration of the stabilizer accounted to the surface charge that would reduce aggregation of the particles. F3 had an increase in size overtime, which was due to either Oswald ripening; excess stabilizer dissolving or redisposition on already formed SLN. However, lower concentrations of stabilizer in F4, generated better surface tension, whereas increased stabilizer concentration impaired surface tension in F3 resulting in a larger unstable size. This indicated that F4 with low surfactant concentration (0.1%$^{w/}_{v}$) was more stable based on zeta potential results and had a size large enough to allow coating with avidin to remain within the 50-250nm size range for intravenous application. This range was used, as aggregation of nanoparticles intravenously would lead to rapid clearance and hinging in nanoparticles structure, which can impair drug release.

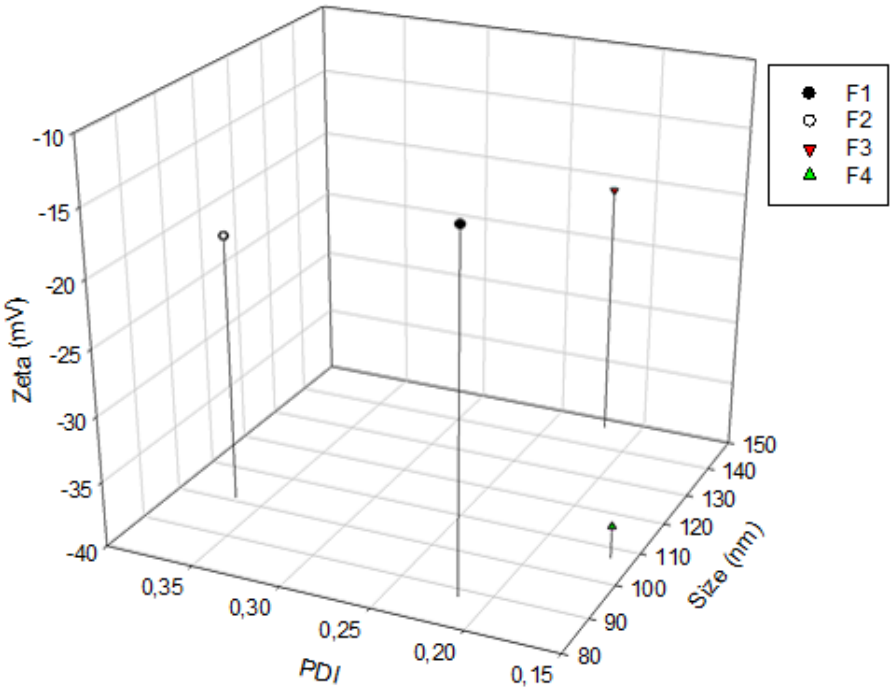

Figure 3.3: Scatter plot of solid lipid nanoparticle size and stability at varying surfactant concentration, whereby F1 = 0.8%, F2 = 0.4%, F3 = 0.2% and F4 = 0.1% surfactant concentration.

3.3.4. Impact of drug incorporation on nanoparticle size and stability

Due to F4 stability and size, this was used for analysis of lipophilic (fenofibrate) drug incorporation impact on the structure of SLNs. Stability of nanoparticles can be affected by drug concentration due to variation in polymer concentration (as drug-polymer ratio changes), drug-polymer interaction and drug solubility (Dhakar et al., 2010). Change in drug: polymer ratio can lead to the formation of smaller particles that will result in drug loss from the surface during preparation. Although, initially the drug will increase with increasing nanoparticle size, the drug-polymer interaction will affect the stability of nanoparticles. In Figure 3.4, this was confirmed by entrapping various fenofibrate concentrations ranging from 0.0-0.6%$^{w/}_{v}$. As observed in Figure 3.4, the size of the particles increased from 107nm to 116nm, relative to increase in drug concentration. The drug free formulation retained the 107±2.98nm size, -37.5±2.67mV zeta potential, and PDI of 0.16±0.02. The 0.2%$^{w/}_{v}$ formulation resulted in an increase in size to 109±2.23nm, zeta potential decreased to -32.1±1.4mV and a PDI of 0.17±0.01. The 0.4%$^{w/}_{v}$ formulation resulted in an increase in size to 117±2.56nm, zeta potential decreased to -29.5±2.32mV and a PDI of 0.18±0.01. The 0.6%$^{w/}_{v}$ formulation resulted in an increase in size to 110±2.66nm, zeta potential decreased to -25.4±1.22mV and a PDI of 0.22±0.02.

This indicated that incorporation of drug could cause changes in size and zeta potential. Due to fenofibrate being a lipophilic drug, interaction with the lipid core led to these variations observed. The 0.2%$^{w/}_{v}$ drug concentration did not have significant change in size due to low drug concentration diffusing during drug incorporation. This was caused by formation of fenofibrate nano-crystals being stabilized by the stabilizer, which was later detected and added to the average size of the SLN during Zetasizer analysis. The stability of the particles, as indicated by the zeta potential recorded with different drug load, was observed to decrease with increasing drug: polymer ratio in SLN. This data shows that an increase in nanoparticles size leads to higher drug entrapment. However, zeta size was gradually decreased as large nanoparticles agglomerate. This indicated that formulation within the range of 0.2-0.4%$^{w/}_{v}$ drug concentration were more stable in size and zeta potential, whereas an increase above this optimum range led to agglomeration and increased possibility of Oswald ripening overtime.

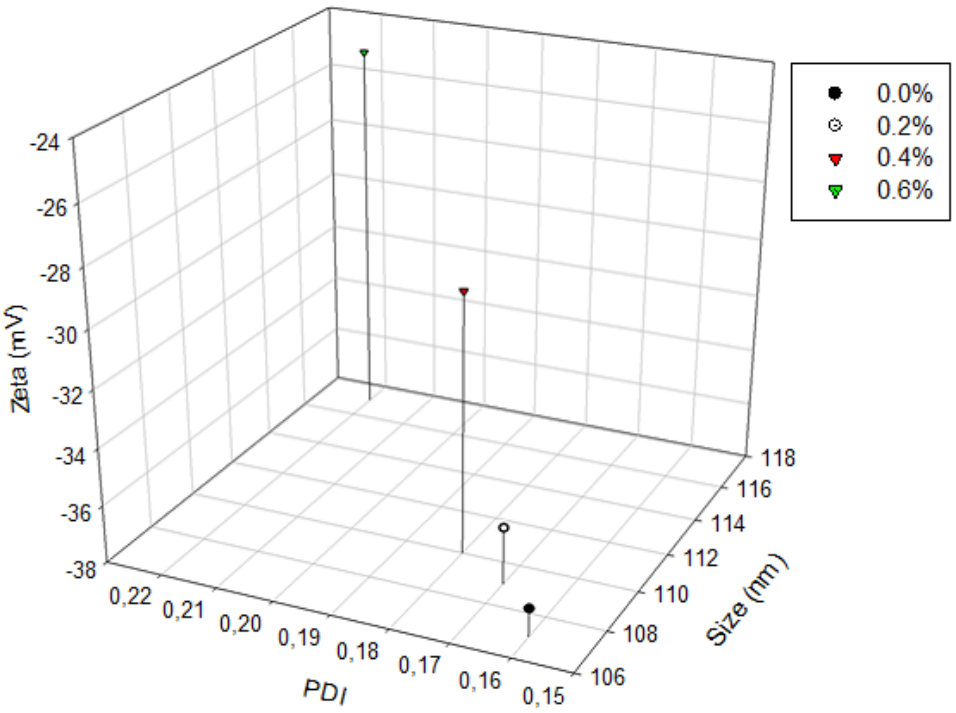

Figure 3.4: Scatter plot of SLN size and stability in response to increase in drug concentration.

3.3.5. Solid lipid nanoparticle stability and size prior after avidin coating

SLN coating was required for conjugation of anti-LDL antibodies via biotin-avidin complex. F4, which showed more stability, was coated with avidin that increased the size of nanoparticles from 107±2.98nm size as observed for native SLN (uncoated), to 135±3.12nm (Figure 3.5). Zeta potential also dropped down from -37.5±2.67mV to -20±2.06mV. The electrophoretic mobility changed from -2.6±0.3μmcm/Vs to -1.6±0.2μmcm/Vs. The change in zeta potential and electrophoretic mobility was due to change in surface tension of SLN, produced by avidin covering the stabilizer Pluronic F68. This changed surfactant interfacial surface tension properties as the surface was not exposed to the media suspending the nanoparticles. Furthermore, due positive charge of surface avidin under neutral pH, this reduced the electrophoretic mobility. Apart from impacts of stabilizer concentration and protein coating of nanoparticles, lyophilisation has been reported to also influence particle size, zeta potential and polydispersity index due to the use of cryoprotectant during lyophilisation (Schwarz and Mehnert, 1997).

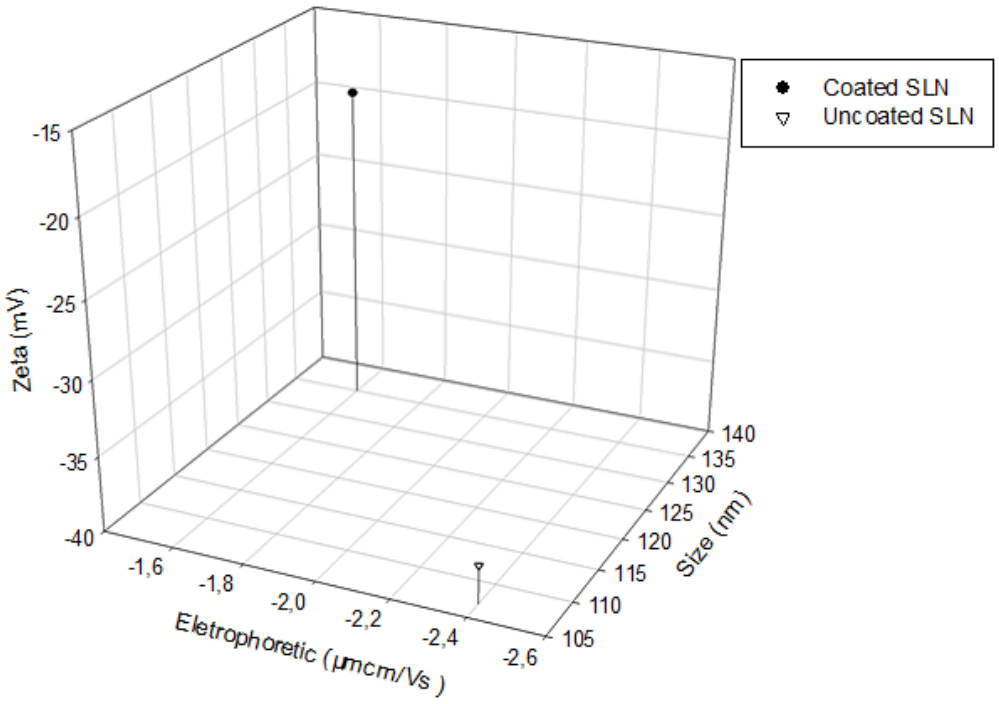

Figure 3.5: Plot indicating the size, zeta potential and electrophoretic mobility changes before and after avidin coating.

3.3.6. Thermodynamic properties of antibody conjugated nanoparticles

Differential scanning calorimeter (DSC) analysis was carried on loaded and unloaded SLNs in order to determine the physical state of the drug and lipid, level of purity and to find out whether there were any interactions between them. DSC was also used to determine the amorphous and crystalline nature of the SLN, which can aid in understanding the release properties of drugs from polymeric systems. Lipids have a crystalline nature whereby multiple polymorphic states: unstable (α), metastable (β') and stable (β) can occur during heating/melting and cooling/recrystallization (Souto et al., 2006). It was essential to have a glass transition that was greater or equal to 40°C, which is required to maintain solid nanoparticles in a solid state at body temperature. The varying drug concentration formulations were analyzed in this study. In Figure 3.6, the thermographs shows two separate peaks indicating a mixture of Pluronic F68 which has a melting temperature of 51°C while Compritol have a melting temperature of 70°C. The addition of drug indicated to further suppress the melting peaks of Compritol and Pluronic F68. This indicated that the drug was interacting with the lipid core due to the drug's lipophilic properties.

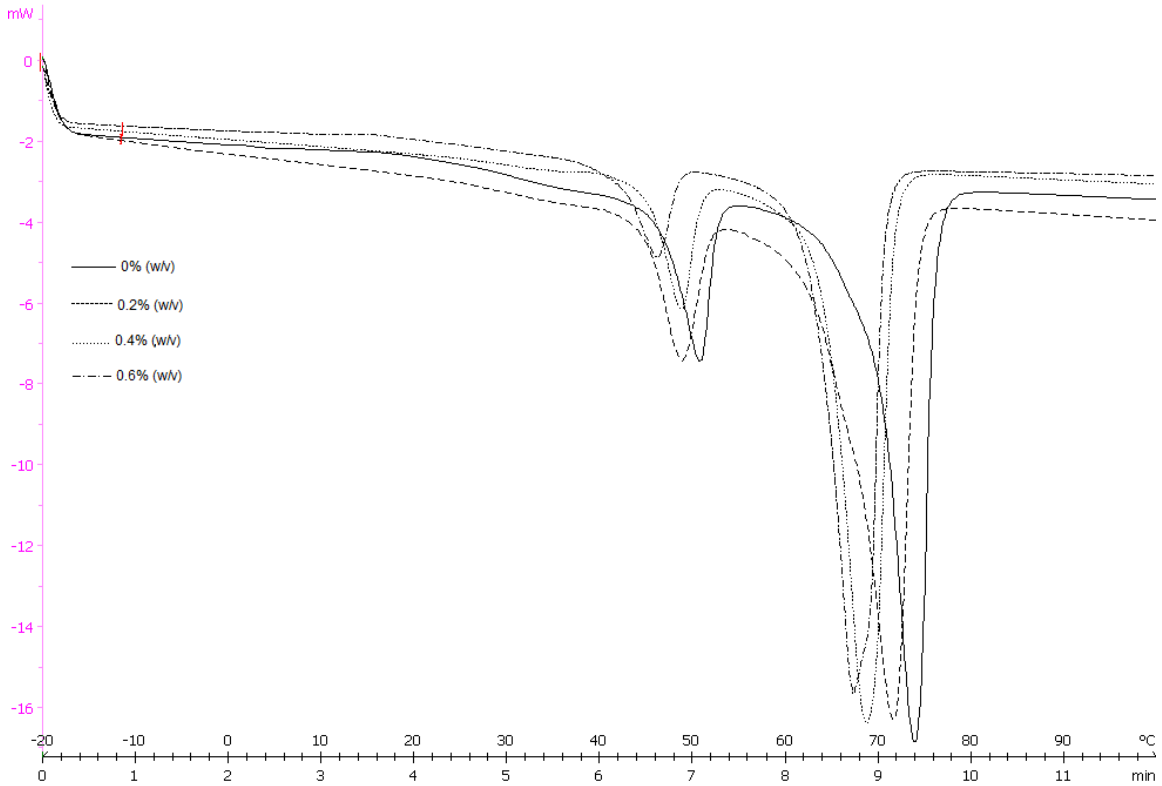

Figure 3.6: Conventional DSC thermograms showing temperature transition of drug loaded solid lipid nanoparticles.

The glass transition temperatures (T_g) determined indicated the region whereby the polymer went from a hard glass-like state to a rubber-like state. In Figure 3.7, native SLN indicated a glass transition of 41.05°C. Addition of fenofibrate shifted T_g to lower temperature, 0.2%$^{w/}_{v}$ drug loaded SLN had a T_g of 40.04°C, 0.4%$^{w/}_{v}$ drug loaded SLN had a T_g of 39.70°C and 0.6%$^{w/}_{v}$ drug loaded SLN had a T_g of 35°C. Furthermore, from the peaks obtained at different drug concentration it can be seen that an increase in drug content led to a reduction in the SLN melting point (Figure 3.6). The integral continued to drop from 24.37mJ (native SLN) to 4.53mJ (0.4%$^{w/}_{v}$ drug loaded SLN). The value increased to 18.09mJ in 0.6%$^{w/}_{v}$ drug loaded SLN. This indicated that the interaction of fenofibrate and SLN that suppressed the glass transition also impaired the enthalpy of fusion and crystallization.

In native SLN, the crystalline polymorphism was induced by Compritol (glyceride), whilst interaction of drugs in 0.2-0.4%$^{w/}_{v}$ drug loaded SLN caused polymer transition. In 0.6%$^{w/}_{v}$ drugs loaded SLN; the increase in integral was due to limit in loading capacity, causing crystallization of free drug. From DSC, melting point depression of the lipid core, the interaction energy density (B/J cm^{-3}) and interaction parameter (X_{12}) were found to be 0.06 and 4.6 x 10^{-6}, respectively.

This indicated a low level of ionic interaction that occurred between the fenofibrate and lipid core. This interaction was due to either the drug interacting with the liquid crystalline phase or drug penetrating into the stabilizer interfacial film (Chambin et al., 2004). Furthermore, lipophilic drugs are known to be lipid soluble, which caused dispersion of fenofibrate within the lipid core. Percentage impurity was found to be 12.6%, which relates to free drug and drug in the stabilizer interfacial film. The excess free drug correlated with the drug: polymer ratio system. This indicated that when the ratio of the drug to polymer was not optimized, the drug would diffuse during formulation. This can impair drug entrapment efficiency. In this study, this indicated the SLN that are more stable would consist of 0.8%$^{w/}_{v}$ lipid, 0.1%$^{w/}_{v}$ surfactant and 0.3%$^{w/}_{v}$ lipophilic drug.

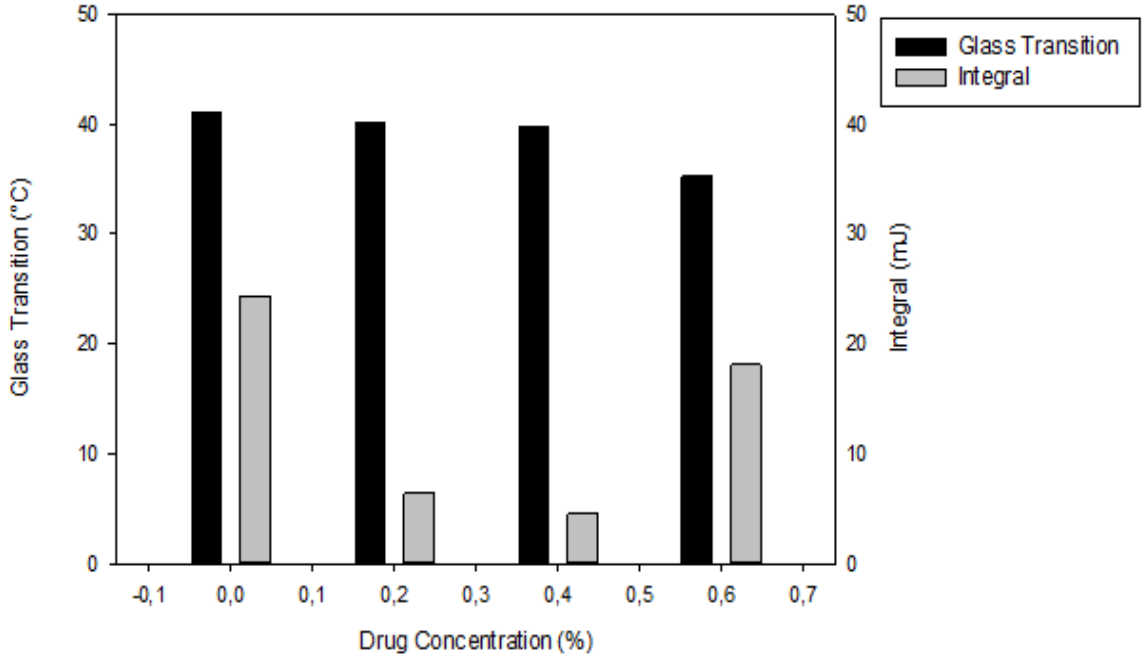

Figure 3.7: Bar graph showing changes in glass transition and enthalpy in response to drug incorporation.

Without optimization of drug loaded SLN drug-polymer ratios, the amount of free drug and drug leaching can affect the stability of the formulation over time due to changing of the amorphous and crystalline characteristic of the SLN. The change in crystalline structure to amorphous state would make the SLN release rate switch from slow to rapid. This occur when the molecular mobility of a glassy amorphous solid is reduced and an increase in the number and magnitude of molecular motions (Hancock et al., 1995).

3.3.7. Confirmation of antibody conjugated nanoparticle crystallinity

XRD was used to evaluate crystallinity of SLN in correlation with data found in DSC. The test was done in triplicates. Crystalline nanoparticles are more stable and facilitate slow drug release whilst amorphous nanoparticles facilitate rapid drug release (Chiu and Prenner, 2011). The XRD pattern was characterized by the interplanar d- spacing and the relative intensities (I/I_0) of the strongest peaks in the pattern. This was used to find out the position of values of product crystallinity or amorphic nature. Data helped in finding out the fingerprinting region of relative intensity with respect to d-spacing values. In Figure 3.8, the diffractogram indicated a semi-crystalline SLN due to suppression of crystallinity by an amorphous avidin layer whilst crystallinity was produced by fenofibrate, Compritol and Pluronic F68. Furthermore, disappearance of some peaks in avidin coated SLN correspond to primary components used to make avidin coated SLN; indicated a change in crystalline phase and/or crystal structure. The change in interplanar spacing of the lipid matrix indicated that the crystallinity was due to orthorhombic β′ form of triglycerides.

This form of polymorphism indicate metastable form which can promote sustained release (Mishra et al., 2008).There was also a presence of α-amorphous phase which explains the ability of the SLN to have high entrapment efficiency. This was also supported by DSC increase in enthalpic relaxation. In correlation to purity levels in DSC, these changes in polymorphism reduced the spaces in the matrix and causing the drug to come out. The shifting of peaks to higher values of the diffraction angle indicated that lattice parameter was decreasing due to structural relaxation. In correlation with DSC scans, XRD confirmed semi crystallinity whereby the amorphous avidin reduced the level of crystallinity and structural relaxation. In relation to fenofibrate crystallinity, the solid lipid nanoparticle dispersion shows a reduction in drug crystallinity was due to drug interaction with polymers and surfactants (Patel et al., 2010). This information confirms drug entrapment was successful and supports DSC drug-polymer interaction. Based on the correlation of DSC and XRD data, this indicated that the expected drug release mechanism would be diffusion, and not through the degradation/erosion of the polymer. Thus drug release would be slow in an aqueous medium because of its semi-crystalline form and possess hydrophobic properties as previously reported (Jeong and Gutowska, 2002).

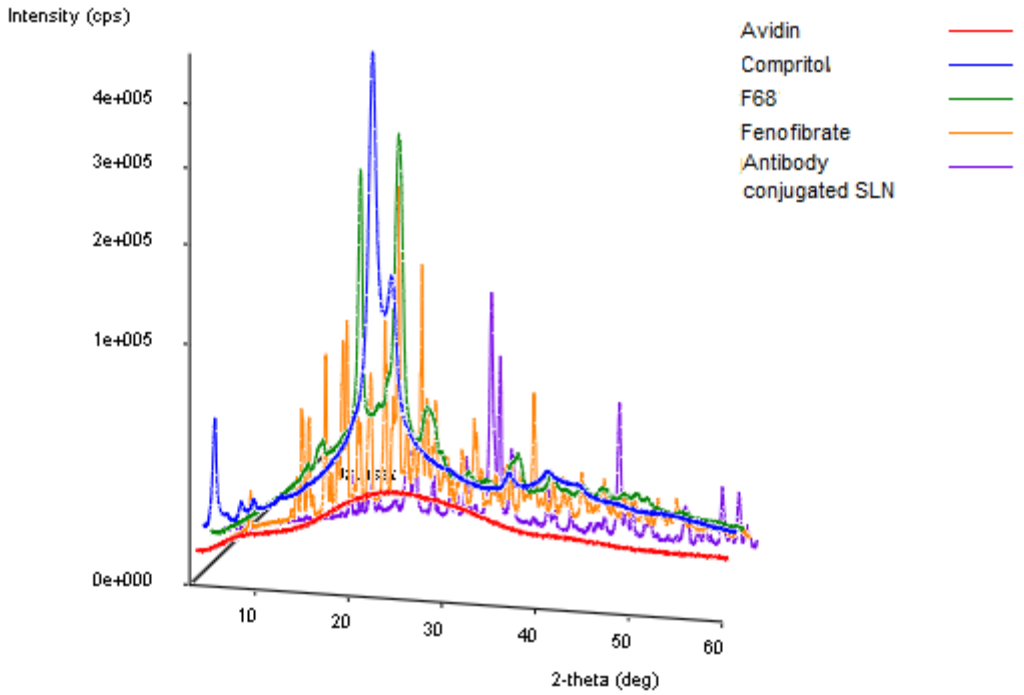

Figure 3.8: XRD diffractogram confirming semi-crystalline structure of the antibody conjugated SLN.

3.3.8. Structural transformations analysis of antibody conjugated nanoparticles

FTIR was used to validate biotinylation of antibodies and validated entrapment of SLN by avidin. Lyophilized avidin coated nanoparticles and biotinylated antibodies were evaluated for their IR absorption of the functional groups. Figure 3.9, indicates that the functional groups give characteristic IR absorption at specific narrow frequency range. Stretching & bending vibrations are also observed to vary after formulation. The biotinylation of anti-Apo-B100 was confirmed due to occurrence of the sharp 1738cm^{-1} (amide I) and 1217cm^{-1} peak that is distinctive in biotin NHS. The peaks represent conjugation due to lowering of absorption (Foerstendorf et al., 2001). Due to the upshift, this indicated that there are conformational changes due to biotin/lysine interaction. The 1011.35cm^{-1} was shifted, which indicated interaction. The biotinylation amine group is represented by the band 1559.90cm^{-1} shows amide II (NH bend + C-N stretch) which indicated amide bond formation between biotin-NHS and antibody lysine residue (Lapin and Chabal, 2009). Avidin coated SLN showed a broad O-H functional group represented around 3262cm^{-1}. This peak is also visible in uncoated SLN. However, the distinctive peaks found in Compritol, 2910cm^{-1} and 2850cm^{-1} are suppressed by avidin broad 2988cm^{-1} peak. This was

due the C-H alkene group. The avidin amine groups (N-H) are seen by the 1644 peakcm^{-1}, the secondary amine groups were imposed by the broad O-H group and the C-H found from 1305cm^{-1} to 1087cm^{-1} that also superimposed the 1200-1000cm^{-1} representing C-O groups distinctive for Pluronic F68. The characteristic peaks of fenofibrate are slightly shifted around 1725cm^{-1} and 1646cm^{-1}. The shift indicates that there was some level of interaction. The interaction was confirmed using DSC and XRD.

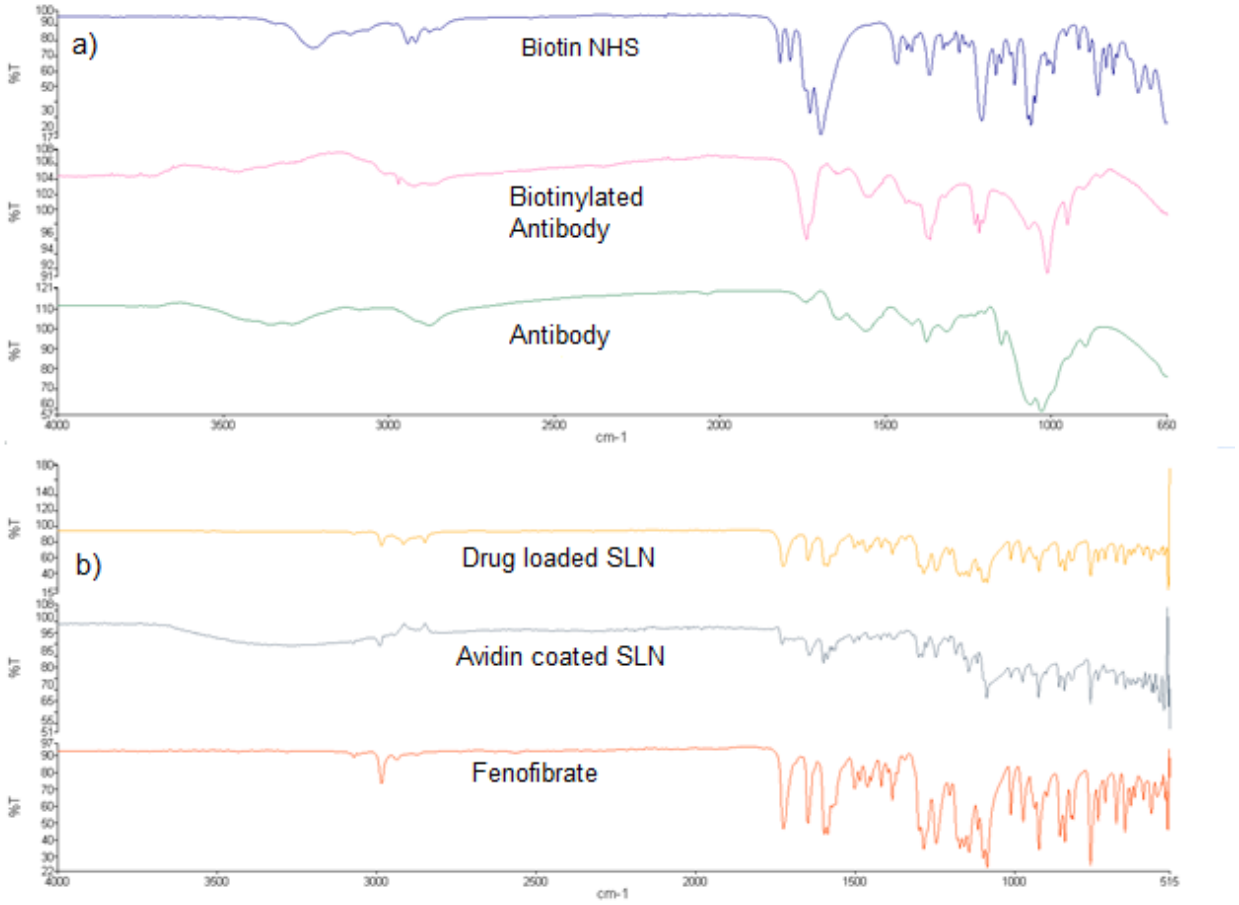

Figure 3.9: FTIR spectrum of (a) antibody biotinylation and (b) SLN avidin coating.

3.3.9. Confirmation of low-density lipoprotein oxidation

LDL particles were oxidized in order to assess change in antibody recognition of the Apo-B100 protein and indicate that fenofibrate does not have direct anti-oxidation effects. Oxidation of LDL by copper ions has been shown to result in free radicals binding to Apo-B100 protein (Pietzsch et al., 2000). The oxidative modification of LDL (ox-LDL) is the major factor that stimulates the development and progress of atherosclerosis. Figure 3.10 indicates successful modification of LDL and that fenofibrate has no direct antioxidant effects on LDL oxidation, when compared to

captopril (Sonoki et al., 2002). Thus, fenofibrate would affect oxidation by means of affecting the size and composition of small dense LDL that are susceptible to oxidation into larger LDL. These LDLs are more affinity for LDL receptors and readily catabolized (Zhu et al., 2010). Ultimately, fenofibrate can reduce the level of peroxidative products without having direct antioxidant effects in the plasma (Beltowski et al., 2002). LDL oxidation began with a lag phase where protective endogenous anti-oxidants are consumed by initiating free radical species. This can be seen by the copper ion free LDL solution. This was then followed by propagation where the polyunsaturated fatty acids contained in the LDL are rapidly oxidized to lipid hydroperoxides (Ghaffari and Ghiasvand, 2010). The ox-LDL particles were then stored in PBS buffer at -20°C prior to use for radial immunodiffusion experiment without further modification.

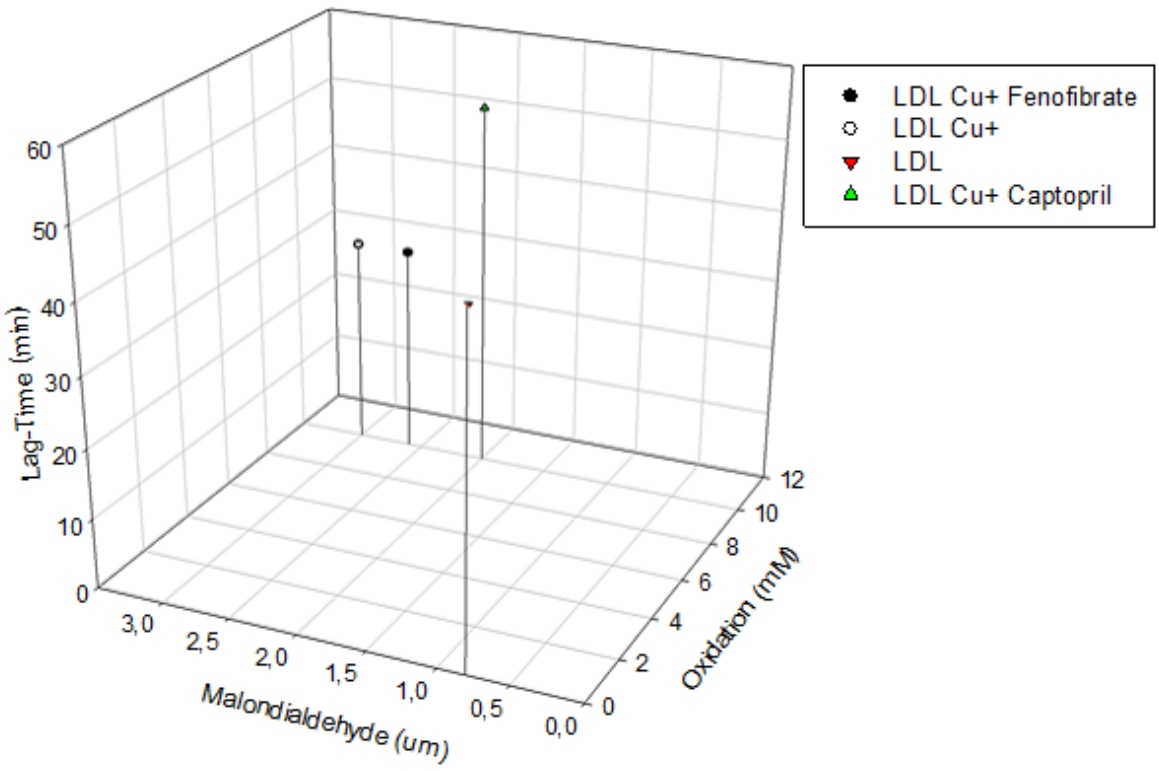

Figure 3.10: Oxidation of LDL particles by $CuSO_4$ 10mM PBS, pH 7.4 at 37°C for 3 hours.

3.3.10. Determination of antibody structural integrity after modification

SDS-PAGE was used to evaluate structural integrity of the antibodies after biotinylation. A 200kDa protein marked was used to identify each of the antibody chains. Both biotinylated and unmodified antibodies were analyzed. The antibody used in this study, falls under IgG antibody

family, which has a molecular weight of 25kDa for the light chain and 50kDa heavy chain. Figure 3.11(a) confirms the presence of these chains when comparing unmodified (Line 1) and biotinylated-antibody (Line 3) to the marker (Line 2). From the SDS-PAGE analysis, it indicates that the biotinylation of the antibody did not change the chain weight due to biotin miniature size. Radial immunodiffusion was also used in validating the biotinylation site of the antibodies as illustrated by Figure 3.11(b). The immunodiffusion studies were also used in validating interaction of antibodies with oxidized LDL particles. The data indicated that antibody biotinylation and LDL oxidation did not impair functionality and selectivity of the antibodies due to antibodies polyclonal activity. This indicated that the antibodies Fab region was not interrupted and that the antibodies can interact with oxidized LDL particles, which are known to lead to atherogenic plaques. This supports the microscopic SLN-LDL complex data. Future studies are however required to assess the epitope regions on the Apo-B100 protein not affected by oxidation.

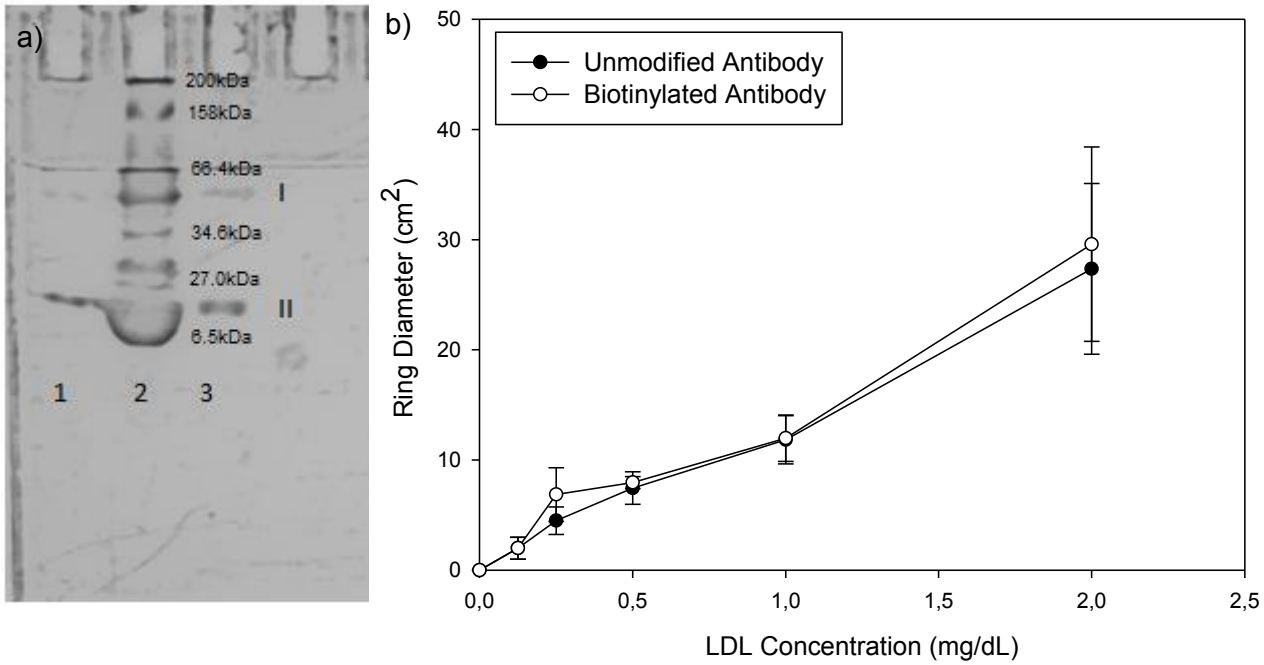

Figure 3.11: SDS-PAGE and radial immunodiffusion characterization of antibodies.

3.3.11. Characterization of drug loading capacity and encapsulation efficiency

Drug loading capacity and encapsulation efficiency were assessed using nanoparticles consisting of 0.8% $^{w/}_{v}$ Compritol and 0.1% $^{w/}_{v}$ Pluronic F68. The drug concentration varying from 0.2-0.6% was added with the lipid solution as described in section 3.2.2 for drug entrapment.

The drug entrapment efficiency was determined to be 86% for 0.4%$^{w/}_{v}$ and 84% for 0.6%$^{w/}_{v}$, which was higher than the 76% found from 0.2%$^{w/}_{v}$ drug concentration formulation. High lipid concentration in relation to drug concentration affected loading due to Compritol precipitating faster on the surface of the dispersed phase and prevented drug diffusion across the phase boundary. The presence of excess drug was also observed in DSC, which affected glass transition. This also increased viscosity of the solution that delayed drug diffusion within the polymer droplets (Dhakar et al. 2010). This also increased in viscous which hampered stability of the nanoparticles, which was seen during zeta potential analysis. Low drug concentration in relation to high polymer concentration can lead to higher drug entrapment, however due to solubility of the drug in the continuous phase this caused drug diffusion during SLN synthesis. Contrary to low drug concentration added as described in section 3.2.2, increase in drug concentration by 0.6%$^{w/}_{v}$ led to increase in size (117nm) but reduction in zeta potential (-25.4±1.22mV) and PDI (0.22) due to maximum drug: polymer ratio. The drug entrapment efficiency also dropped to 84% due to large particles which caused surface bound drug to be removed. The results indicate that an optimum drug concentration of 0.4%$^{w/}_{v}$ in relation to 0.6%$^{w/}_{v}$ polymer was ideal for stable nanoparticles with high entrapment efficiency. Due to fenofibrate being lipid soluble, the interaction with the lipid core also resulted in improvement of drug entrapment efficacy. This was supported by DSC ionic interaction data.

3.3.12. *In vitro* drug release studies

Drug release was monitored for a period of 25 days on a dissolution apparatus (Model 7ST, G.B. Caleva, Dorset, UK) as indicated in Figure 3.12. The study had to be terminated after 25 days due to dissolution media starting to evaporate which can impair sink conditions. This data was then analyzed with SigmaPlot 12 (Systat Software, Inc., California, USA) using student t test. Mean dissolution time (MDT) and mean residence time (MRT) were calculated as they are functions of dose/solubility ratio using equation 3.11 and 3.12, respectively (Rinaki et al., 2003). They were both calculate using a model independent method which uses the amount of the drug substance dissolved in the dissolution medium after several known time intervals (Podczeck, 1993).

$$MDT = \frac{ABC}{a_{tmax}} \tag{3.11}$$

$$MRT = \frac{\int_0^t t.c_t\, dt}{AUC} \tag{3.12}$$

where ABC is the area between the drug dissolution curve and its asymptote and AUC is the area under the residence profile curve. The time for 50% of the drug to appear in solution was used. MDT was found to be 5.49±1.33, whilst MRT was found to be 4.99±1.07. In order for the drug to have therapeutic effect, the MDT has to be below the time it will take the particles to clear from the blood stream. This supports the slow drug release of fenofibrate from SLN. *In vivo* studies are required in order to determine the time for SLN clearance. The nonlinear regression curve ($f = 1.25 + 3.74x$) was generated for the identification of the kinetic model.

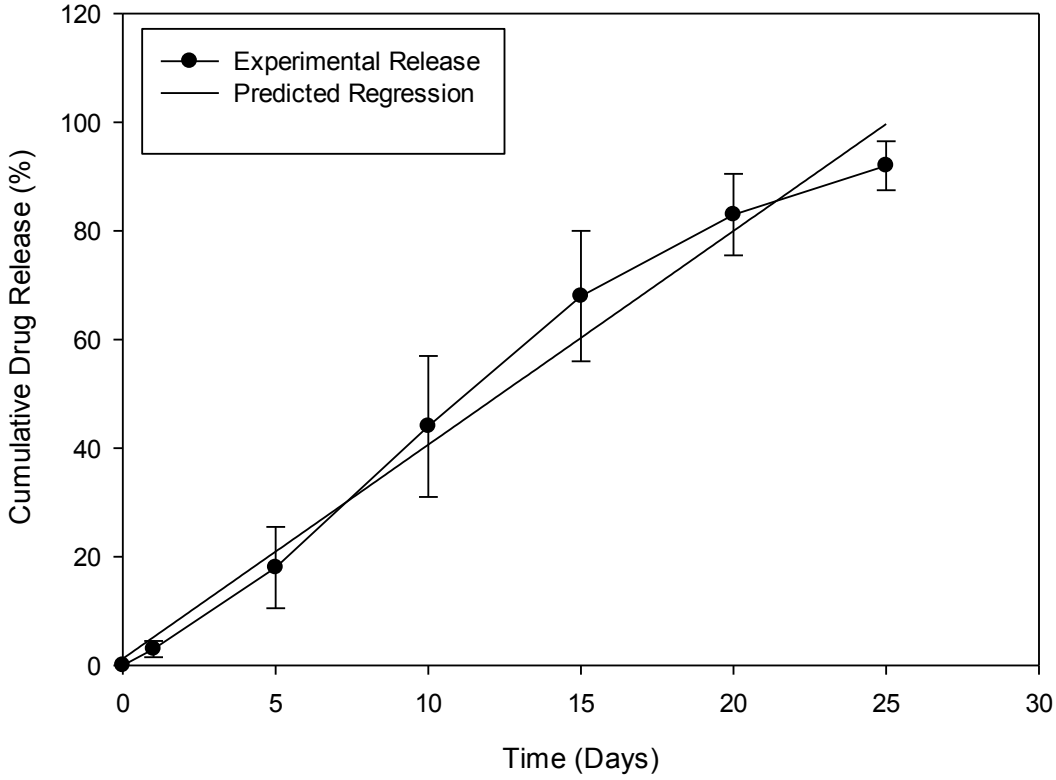

Figure 3.12: Cumulative fenofibrate drug release from antibody-conjugated SLN in PBS (pH 7.4, 0.2% Tween 80).

Table 3.2 shows the rank order for drug release kinetics and drug release mechanism order based on adjusted R^2 values (Equation 3.13): Korsmeyer-Peppas > Zero-order > Hixson-Crowell > First-order > Higuchi Kinetic. The values were determined using the drug release kinetic models illustrated in Figure 3.13. The calculated kinetics were confirmed by means of

using DDsolver excel add-in dissolution data modeling (Zhang et al., 2010). It is expected that the best model would be the one with the highest adjusted coefficient of determination. This is due to R^2 is always expected to increase or at least stays constant when adding new model parameters, whilst a decrease would be giving an indication if the new parameter really improves the model or might lead to over fitting as indicated in equation 3.13 (Costa and Sousa Lobo, 2001).

$$R^2_{adjusted} = 1 - \frac{(n-1)}{(n-p)}(1 - R^2) \quad (3.13)$$

Where, n is the number of dissolution data points and p is the number of parameters in the model. The data indicates sustained and controlled drug release. When n = 0.5, the drug release is controlled by diffusion and is time-dependent, while when n = 1.0, the drug release is controlled by swelling and is time-independent with zero-order kinetics. Values of n between 0.5 and 1.0 indicate superposition of both phenomena, known as anomalous transport (Costa and Sousa Lobo, 2001). n>1.0 shows this super case II transport indicating diffusion and erosion mode of release (Korsmeyer et al., 1983). The n vale of 0.878 indicates that there is Anomalous transport mechanism, which occurs due to a coupling of Fickian diffusion and polymer relaxation. This mode of release is due to Fickian diffusion through the hydrated layers of the matrix and polymer chain relaxation and erosion are both involved (Szepes et al., 2008). This data related to previous study on SLN whereby anomalous transport was also favored which showed constant drug release rate essential for sustained release from a lipid matrix. This was also followed by Hixson-Crowell model indicating that the drug was released by constantly changing surface area. In this study, erosion of the avidin coat led to change in surface area of the SLN that favored anomalous transport. The diffusion rate was further supported by the previously stated DSC semi-crystalline state and relaxation of the lipid core. This indicates that SLN are suitable for entrapment of lipophilic drugs (Bawarski et al., 2008; Wong et al., 2008).

Table 3.2: Release kinetics data of fenofibrate loaded SLN for targeted drug delivery.

Equation	Zero-order	First-order	Higuchi Kinetic	Korsmeyer-Peppas	Hixson-Crowell
R^2 Adjusted	0.9818	0.9609	0.9090	0.9846	0.9815
R^2 Observed	0.9911	0.9873	0.9714	0.9939	0.9942
n	N/A	N/A	N/A	0.878	N/A

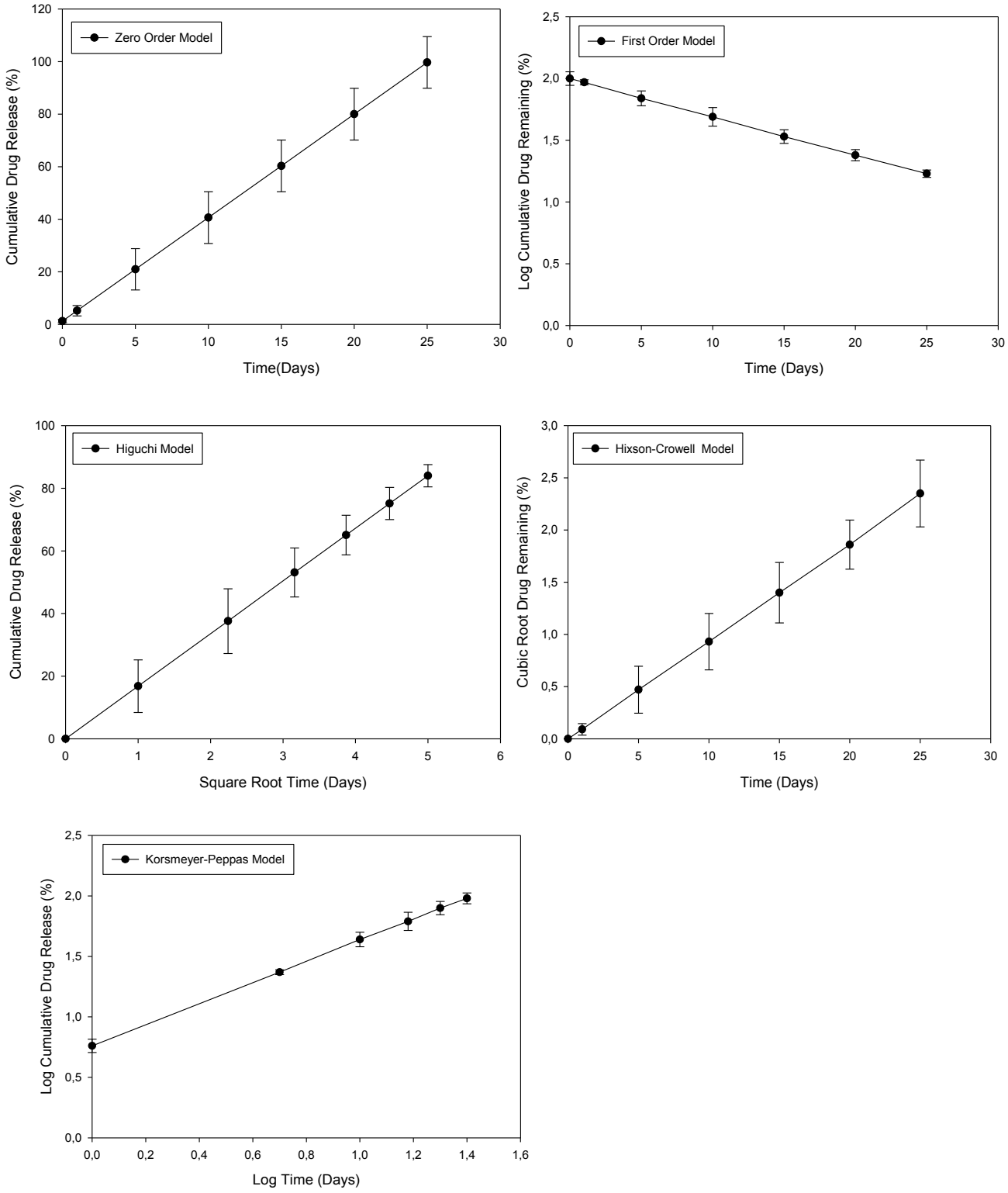

Figure 3.13: *In vitro* drug release kinetics models, Zero-order, First-order, Higuchi, Hixson Crowell and Korsmeyer-Peppas.

3.4. Concluding Remarks

In the present study, the effect of stabilizer on SLN size and stability was analyzed and the use of antibody-conjugated SLN for targeting LDL particles was evaluated. It was found that an increase in stabilizer led to aggregation of the nanoparticles due to Pluronic F68 gel phase transition. This indicated that the use of appropriate ratios of stabilizer to polymer is crucial in synthesizing stable nanoparticles with improved stability. The use of DSC allowed to characterize the ideal storage temperature (<40°C) for the nanoparticles such as to avoid changing between amorphous and crystalline states. The interaction between the drug and polymer indicated that polymer relaxation can play a role during drug diffusion and affect drug entrapment efficiency. This proved that SLN can be used a vehicles for transport of lipophilic drugs such as fenofibrate. Due to drugs interacting with the lipid core, this offered high entrapment efficiency and allowed sustained drug release due to ionic interaction requiring energy to break the drug-polymer interaction bonds during diffusion. This was confirmed by *in vitro* drug release whereby anomalous transport was favored. The use of XRD confirmed the semi-crystalline structure of the SLN which indicated that sustained drug release was favored. XRD also showed structural relaxation which was also observed by favoring of anomalous transport mechanism (polymer relaxation) during drug release.

These nanoparticles have also provided targeting capabilities by binding to both oxidized and unoxidised LDL particles. This can be used is LDL plasma clearance. This shows that the synthesized antibody nanoparticles in this will only target LDL particles due to binding to Apo-B100 which is only located on the surface of LDL particles (Carmena et al., 2004). Therefore by targeting B-100 proteins they can be a direct link to the level of cardiovascular disease as they are discriminating than other plasma lipids and lipoproteins (HDL). Future studies require analysis of antibody conjugated SLN *in vivo*. This will allow analyzing distribution of SLN in variety of tissues and organs and also confirm burst release during degradation of SLN in the liver. In this study, the SLN are used in two different drug delivery devices. The first device involves embedding the antibody conjugated SLN into a viscoelastic hydrogel to form an antigen responsive hydrogel. The hydrogel for embedding SLN has to be stable under fluctuating hemodynamic forces. This is discussed in the following chapters. The second device involves infusion of antibody conjugated SLN directly into the blood stream to elude fenofibrate during circulation and to enhance LDL uptake.

CHAPTER FOUR
SYNTHESIS AND CHARACTERIZATION OF ANTIGEN RESPONSIVE INTERPENETRATING NETWORK HYDROGEL FOR CONTROLLING DRUG INFUSION RATE

4.1. Introduction

Responsive hydrogels can undergo gel-sol phase transitions when exposed to a number of physical and chemical stimuli. This is facilitated by interruption of covalent bonds, hydrogen bonds, van der Waals interaction and physical entanglement (Qiu and Park, 2012). Physical stimuli can range from temperature, electric current, light, pressure, sound and magnetic fields (El-Hamed et al., 2011). Chemical stimuli include pH, ions and specific molecular recognition events such as antigen recognition and enzyme catalysis (Bae et al., 2010; Hoffman, 2002). Temperature sensitive hydrogels consist of hydrophobic groups and lower critical solution temperature which cause temperature phase transition. Electric current sensitive hydrogels consist of polyelectrolytes which cause ionic migration and electrostatic disruption which in turn causes hydrogel shape changes. Photosensitive hydrogels constitute of molecules that can absorb light (chromopore) or dissociate (radiation sensitive) when exposed to light whilst pH sensitive hydrogel contain either pendant acid or basic groups which allow exchange of protons between the gel and the environment (Qiu and Park, 2012). Antigen responsive hydrogel require non-covalent interaction between the biomarker and recognition molecules so that reversible interaction can take place (Miyata et al., 1996; Nakamae et al., 1994). These stimuli responsive phenomena may be adapted in the design of a self-regulated drug delivery system.

The use of an antigen responsive hydrogel will further facilitate the reduction of possible inflammatory response seen in glucose biosensors, where both acute and chronic inflammation and fibrosis around implantation site are often observed (Hickey et al., 2002). By suppressing inflammatory response, implants can have extended lifetime (Wang et al., 2009). Inflammation can have negative impacts on patient compliance and disrupt functions of implants. Other problems that impair implant function are biofilm formation whereby protein accumulates around the implant causing aggregation of cells around the implant which will in turn impair the rate of programmed drug release from a hydrogel based-implant. Using a range of monomers in hydrogel formation, individual properties can affect the structure and biocompatibility of the synthesized hydrogel. Apart from improving chemical properties to enhance biocompatibility, physical properties must also be refined for long-term stability and function.

In this study three different polymers were used for synthesis of viscoelastic hydrogel. Polyethylene glycol diacrylate offers properties such as elasticity, protein adsorption reduction in hydrogels and non-immunogenic properties which imparts both mechanical strength to hydrogels and biocompatibility (Bhattarai et al., 2005; Charles et al., 2009). This is necessary for implant design as the polyether backbone cannot be degraded by mammalian enzymes (Nemir et al., 2010). Methacrylic acid is primarily used in bioadhesive products because it allows the implant to adhere to most target surfaces. This can be used to immobilize implants in the desired location despite motor movements which may cause friction leading to delocalization from implantation site. Polyethylene glycol 200 is an FDA approved polymer which has been shown to be biocompatible and has been used in many drug delivery systems (Jean-Francois and Fortier, 1996).

These polymers are required for intravenous applications as alterations in blood flow together with biomolecular changes of the endothelial cells contribute to the focal distribution of atherosclerotic lesions and might be used as phenomena to target in the implementation of new therapeutic strategies (Cecchi et al., 2011). In the human circulatory system, shear stress ranges from 1-6 dynes/cm^2 in veins, 10-70 dynes/cm^2 in normal arteries, approximately 4 dynes/cm^2 in atherogenic prone arterial regions and 70->100 dynes/cm^2 in high-shear thrombotic regions constituting of plaques, stents and cardiac valves (Malek et al., 1999; Murata et al., 1997; Ruggeri et al., 2006)). The ability of arteries to maintain constant flow and lumen size, in the face of a growing atherosclerotic lesion has been shown to be other forms of adaptive responses of the arterial wall to injury (Korshunov et al., 2007). Turbulent and laminar flow can impair drug release (Emara et al., 2009). Arterial blood flow has been shown to undergo change after stenting and angioplasty (Lu et al., 2003). Fabricating a hemodynamic tolerant device will aid in maintaining predetermined drug release and obtaining optimum *in-vitro*/*in vivo* correlation as the changes caused by shear stress can impair drug release rate. An antigen responsive interpenetrating network (IPN) hydrogel was synthesized, as it was required for controlling the infusion rate of IVISDDD during detection of high levels of LDL particles. The hydrogel would be used for embedding antibody conjugated SLN to allow antigen responsive surface.

4.2. Material and Methods

4.2.1. Materials

Polyethylene glycol diacrylate 750 (cross-linker), polyethylene glycol 200 (plasticizer), Azobisisobutyronitrile (initiator), and methyacrylic acid (monomer) were purchased from Sigma (Sigma Aldrich, Missouri, USA). Caco-2 cells, AAF-Glo™ Substrate, Assay Buffer and Digitonin were purchased from Promega (Promega Corporation, Wisconsin, USA). Dimethyl sulfoxide (aprotic solvent) and liquid paraffin were purchased from Merck (Merck KGaA, Darmstadt, Germany). All the chemical agents were analytic grade and used without further purification.

4.2.2. Fabrication of the viscoelastic hydrogel via thermal polymerization

The viscoelastic PEGDA-PEG200-MAA hydrogel were prepared following thermal initiated free radical polymerization. In brief, appropriate amounts of MAA, PEGDA and PEGDA were mixed with DMSO in a Schlenk flask. The compositions of the various formulations are listed in Table 4.1. The solution was then purged with nitrogen gas while being stirred for 2 hours to completely remove traces of oxygen, which act as free radical scavengers. Liquid paraffin was heated to 50°C prior to immersing the vacuum-sealed Schlenk flask into the bath. AIBN (100µL) was injected into the flask to allow polymerization. After 4 hours of polymerization, the viscoelastic hydrogel was then immersed in toluene to deactivate and remove traces of the thermal initiator. Thereafter, the hydrogel was dialyzed in water-DMSO (8:2) 0.1M NaOH solutions for 24 hours to remove traces of toluene and free methacrylic acid monomers. The hydrogels were then stored in 100mL vials bottles at room temperature for future use.

Table 4.1: Formulations of viscoelastic hydrogel based on changes in plasticizer and crosslinker concentration.

Formulations	PEGDA(% $^{v/}_{v}$)	MAA(% $^{v/}_{v}$)	PEG200(% $^{v/}_{v}$)
H1	1	3	0
H2	1	3	10
H3	1	3	20
H4	3	3	0
H5	3	1	0

Formulations were tested to evaluate their viscous properties and flowing behavior after the polymerization reaction prior to further analysis. Formulations that did not exhibit favorable viscoelastic behavior (brittle) were excluded from further studies. Formulations that are brittle due with high cross-linker/ low plasticizer percentage can damage arterial wall, whilst highly viscous formulations would flow under high flow rate impairing implant physical properties.

4.2.3. Analysis of hydrogel viscoelastic properties and flow behavior

The rheological tests were carried out with a Modular Advanced Rheometer (Thermo Electron Corp., Karlsruhe, Germany). In the oscillatory mode, a parallel plate (40mm diameter, 35Ti) geometry measuring system was employed, and the gap was set to 1mm. The viscoelastic properties were determined by using the frequency sweep method for all formulations using parameters indicated in Table 4.2. The storage modulus (G′), the loss modulus (G″) and the dynamic viscosity (η) were recorded. 0.5mL of polymerized viscoelastic hydrogel was applied on the sample stage. Each test was run in triplicate. During the frequency sweep, a solvent trap polycarbonate cover was used to prevent sample drying and evaporating as this would affect the rheological properties of the sample. The stress sweep test was conducted in order to determine the stress value to be used in the creep test. This value was taken from the point where the loss modulus stated to decrease; which is a value indicating the critical stress, a point where the hydrogel strength correlates with its yield point (G' vs. G"). This test was run to determine the deformation energy and flow. The yield stress was also determined for analysis point of flow and type of flow of the hydrogel. For all the tests, the temperature was set at 37°C.

Table 4.2: Method parameters for yield test, stress sweep and frequency sweep tests.

Parameters	Yield stress	Stress sweep	Frequency sweep
Temperature (°C)	37	37	37
Frequency (Hz)	-	1	0.01-100
Strain (Pa)	0-100	0-100	6.5
Duration (Sec)	200	-	-
Steps	-	20	-

4.2.4. Determination of hydrogel membrane rigidity and resilience under mechanical strain

The texture properties of the PEGDA-MAA-PEG200 were performed using a Texture Analyser TA.XT Plus (Stable Micro System, Surrey, UK) using a P/2-2mm diameter stainless cylinder probe and a 10mm cylindrical delrin probe for testing membrane resilience, deformation energy and membrane rigidity. Texture analyzer parameters employed for deformation energy, rigidity

and resilience testing are shown in Table 4.3. The individual formulation hydrogels were placed on the platform and the respective probe attached to the crosshead of the instrument during analysis. Rigidity was tested using a ¼ spherical stainless probe on hydrogels. The 10 mm cylindrical delrin probe was used to measure membrane resilience and deformation energy of hydrogels. Rigidity was calculated from the force versus distance graph, deformation was calculated from the force versus distance graph and resilience was calculated on a force versus time graph. On the graph resilience was determine using the equation:

$$Membrane\ Resilience\ (\%) = \frac{AUC\ (Anchors\ 2-3)}{AUC(Anchors\ 1-2)} \times 100 \quad (4.1)$$

Table 4.3: Textural Profiling Parameters Settings Employed for Physicochemical Characterization of viscoelastic hydrogels.

Parameters	Resilience	Rigidity	Deformation
Pro-test speed	1mm/s	1mm/s	1mm/s
Test speed	0.5mm/s	0.5mm/s	0.5mm/s
Post-test speed	10mm/s	10mm/s	10mm/s
Trigger type	Auto	Auto	Auto
Load cell	5kg	5kg	5kg
Trigger force	0.05N	0.05N	0.05N
Compression strain	Variable	N/A	N/A
Target mode	Strain (50%)	Force	Force

4.2.5. Hydrogel pore size distribution analysis

Due to formulations consisting of various concentrations of crosslinker and a plasticizer that can also act as a porogen, the porosity of formulation was evaluated. Nitrogen sorption measurements were performed using parameters illustrated in Table 4.4 to determine the surface area and pore size distribution based on Barrett-Joyner-Halenda (BJH) model. The model predicts the presence of pores in the material by means of the use of the adsorption isotherm (Lastoskie & Gubbins, 2001). The porosity analyzer, Micrometrics ASAP 2020 was used to determine the level of porosity as it plays a role during drug release and entrapment (Micrometrics, Georgia, USA). A minimum of 100mg of the lyophilized samples were weighed and placed into the sample holders. Each of the polymerized hydrogel was lyophilized for 24 hours (Labconco, Missouri, USA) with a 2 hours condensation phase at −60°C and a 24 hours sublimation phase at 25mm Torr. The filler rod was used to reduce the free space volume thus improving accuracy in samples with lower total surface area. The heating mantle was used to encapsulate the sample tube during degassing process. The degassing process was run for 15

hours. After the degassing phase, the sample tube was transferred to the analysis holder, where the tube was immersed in liquid nitrogen during analysis; this was run for 6 hours.

Table 4.4: Evacuation and Heating Phase Parameters Employed for Porositometric Analysis.

Parameter	Rate/target
Evacuation phase	
Temperature ramp rate	10°C/min
Target temperature	40°C
Evacuation rate	50.0mmHg/s
Unrestricted evacuation from	30mmHg
Vacuum set point	500μmHg
Evacuation time	60 min
Heating phase	
Temperature ramp rate	10°C/min
Hold temperature	30°C
Hold time	900 min

4.2.6. Formulated hydrogels swelling kinetics and dynamics

Swelling kinetics and dynamics were analyzed on lyophilized hydrogels dispersed in PBS pH 7.4. The swelling tests were conducted in triplicate while keeping hydrogels in 100mL of swelling medium at 37±0.5°C. The time required for equilibrium swelling was noted. The weight of hydrogels was measured every 30 minutes after briefly drying each swollen hydrogel on filtering paper. The swelling ratio was calculated as:

$$SR = \frac{W_t - W_0}{W_0} \quad (4.2)$$

Where, SR, W_t and W_0 are the swelling weight ratio, weight of swollen hydrogel at time t and the hydrogel before swelling, respectively. To determine kinetics of the swelling process, the equation 4.3 was used to determine the rate law where the swelling exponent *n* provided insight into the water sorption mechanism that was in operation. The analysis of the diffusion mechanism in all networks was described by the following equation 4.3.

$$SR = Kt^n \quad (4.3)$$

Where; K was the swelling ratio front factor, *n* represented the swelling exponent. A straight line was obtained by plotting ln (SR) versus ln (t) for the initial 60% of swelling. The gradient of this line was computed as the n value while the intersection showed ln (K)**.** Equilibrium water content was calculated from the equation 4.4.

$$EWC\ (\%) = \frac{W_\infty - W_0}{W_\infty} \times 100 \quad (4.4)$$

Where W_∞ was the weight of hydrogel the gel at equilibrium state and W_0 was regarded as the initial weight of the dry hydrogel.

4.2.7. Hydrolytic degradation of viscoelastic hydrogel

Hydrogels incorporating polythelyne glycol have increased solubility. This makes the formulations containing polyethylene glycol susceptible to hydrolytic degradation over time, which may impair drug delivery system by reducing duration of operation. Hydrolytic degradation was conducted on dry hydrogel pieces of similar shape and weight. The hydrogels were then immersed in 100mL PBS (pH 7.4) at 37±0.5°C for the duration of the study. The used buffer was exchanged with new buffer every week for 16 weeks. The test was conducted in a shaker bath rotating at 20 rpm maintained temperature of 37±0.5°C. Due to polymer hydrolysis following second order reaction kinetics, the rate of hydrolytic reaction was calculated since hydrolysis rate is proportional to water concentration and hydrolytic polymer bonds (Lyu and Untereker, 2009). Mass change was evaluated every week for the duration of the study. Prior weighing, each hydrogel was tapped dry on a paper towel.

4.2.8. Thermodynamic stability analysis of viscoelastic hydrogel

A thermodynamic property of the most stable hydrogel (viscoelastic and high mechanical strength) was evaluated using DSC. The impact of addition of plasticizer, PEG-200 was also evaluated as the plasticizer can have an impact on hydrogel glass transition. The interaction between the plasticizer and PEGDA-MAA was also evaluated. DSC experiments were performed using a Mettler Toledo DSC system (Mettler Toledo, Ohio, USA). Mettler STARe software system, version 9.x, was used for data acquisition and indium were used to calibrate the instrument. The polymers were pulverized into powder form prior to loading into 40µL aluminum pans. A fine powder is more favorable than coarse aggregates of particles and is a better representative of the substance as a whole. The samples (10mg) were then transferred into DSC standard aluminum pans and sealed. Small sample amounts are required as this reduces the temperature gradients within the sample. The samples were analyzed by a conventional method with heating over the temperature range from 0-450 °C at a rate of 10°C/min under a nitrogen (8kPa) atmosphere. For temperature modulated DSC, a heating rate of 2°C/min was used. The thermal history was removed by heating the hydrogels from 0-100°C

and maintained at this temperature for 3 minutes. To determine interaction between the MAA and PEGDA, Flory-Higgins equation was used:

$$T_m = T_m^0 + T_m^0 \left(\frac{V_2}{\Delta H_2}\right) B(1-\phi_2)^2 \quad (4.5)$$

T_m^0 and T_m were regarded as the melting points of MAA and PEGDA respectively, while $^{V_2}/_{\Delta H_2}$ was the heat of fusion of MAA per unit volume. B represents the interaction energy density.

$$B = X_{12}RT/V_1 \quad (4.6)$$

X_{12} represented the Flory-Higgins parameter, while V_1 is the molar volume of MAA.

4.2.9. Hydrogel thermal degradation analysis at various heating rates

The thermogravimetric analysis (TGA) of Perkin-Elmer (PerkinElmer Inc., Massachusetts, USA) was carried out to evaluate the stabilities of the samples as the function of temperature in nitrogen atmosphere under a flow of 30mL/min and heating rate of 10°C/min. The most stable formulation was used for thermogravimetric analysis. TGA was used in combination with Evolved gas analysis (EGA) after pyrolysis was carried out using a TGA 4000 thermogravimetric analyzer (PerkinElmer Inc, Massachusetts, USA) combined with infrared spectrometry (TG-IR) through the TL 8000 transfer line. The Pyris 6 software was used to perform the thermal analysis and to trigger the IR software. The heating was conducted from 30°C to 600°C at a heating rate of 10°C/min. TimeBase software was used for IR data interpretation for designing Gram-Schmidt plot. The formulation that showed stability was evaluated by gridding the hydrogel into fine powder. The thermogravimetric test was conducted in triplicate. Each test consisted of a powder weighing approximately 10-20mg.

4.2.10. Structural transformations analysis of viscoelastic hydrogel

Attenuated Total Reflectance-FTIR (ATR-FTIR) analysis of PEGDA, PEG-200, MAA and synthesized hydrogel was undertaken to evaluate, ascertain and compare the structural transformations. ATR-FTIR spectra were recorded on a Perkin Elmer Spectrum 2000 FTIR spectrometer with a MIRTGS detector (PerkinElmer Spectrum 100, Wales, UK), using an ATR-FTIR cell and a diamond crystal internal reflection element. Samples were analyzed at a wavenumber range of 650-4000cm^{-1} with a resolution of 4cm^{-1} and 100 scans per spectrum.

4.2.11. Hydrogel molecular weight characterization

The Zetasizer Nano series was used to perform molecular weight measurements using static light scattering (Malvern Instruments (Pty) Ltd., Worcestershire, UK). This uses time averaged intensity of scattered light accumulated for a number of sample concentrations. The molecular weight was determined by measuring the sample at different concentration and by applying the Rayleigh equation. The formulation that indicated stable rheological properties (viscoelastic behavior and high structural recovery percentage after deformation), mechanical (can withstand high shear rate > 70 dynes/cm^2) and swelling (low swelling percentage to reduce thrombotic shear effects) was evaluated. This formulation was selected to be used for embedding antibody conjugated SLN.

$$\frac{KC}{R_\theta} = \frac{1}{M} + 2A_2C \tag{4.7}$$

The Debye plot was then generated by means of a linear fit of KC/R_θ versus concentration. The intercept was equal to the inverse of the molecular weight and the slope was twice the 2nd virial coefficient. The 2nd virial coefficient was used to determine polymer interaction strength and sample solubility, which was used to compute polymer molecular weight. Sample concentration was set around a range of 0.25-1g/L to avoid multiple scattering in highly concentrated samples and to prevent undetectable scattered light in lower concentrated samples. All solvents were filtered through a 0.22µm filter to remove traces of contaminants. Prior to analysis, the refractive index of the polymer was measured using a refractometer (Atago Co Ltd., Tokyo, Japan). Ultraviolet absorbance was measured in the range of 190-1000nm using a UV spectrometer (Specord 40, AnalytikJena, Jena, Germany). The experiment was conducted using polyethylene glycol 200 as a control to quantify the accuracy of the procedure.

4.2.12. Pore size and hydrogel surface microscopic evaluation

The lyophilized most stable hydrogel was cut in transverse section and mounted on a double sided tape on aluminum stubs and were sputter coated with gold using the fine coat gold sputter ((SPI-Module Sputter Coater, SPI Supplies, Pennsylvania, USA).) and then micrographs were recorded using the scanning electron microscope (Desktop SEM, Phenom World BV, Eindhoven, Netherlands) to study the porous nature of hydrogels.

4.2.13. Hydrogel thermal decomposition kinetics characterization

Thermogravimetric Analysis (TGA) provides a method for accelerating the lifespan testing of polymers so that short-term experiments can be used to predict lifespan of concerned materials. Thermal degradation kinetics and lifetime prediction were determined using a TGA 400 thermogravimetric analyzer (PerkinElmer Inc, Massachusetts, USA). The materials were heated at several different rates through their decomposition region. From the resultant thermal curves, the temperatures for a constant decomposition level were determined. The kinetic activation energy was then determined from a plot of the logarithm of the heating rate versus the reciprocal of the temperature of the constant decomposition level. This activation energy was then used to calculate estimated lifetime at a given temperature or the maximum operating temperature for a given estimated lifespan. The sample with mass of 10mg was inserted directly into a ceramic crucible and the temperature was increased from 30°C to 600°C under both air (30mL/min) and nitrogen flow (20mL/min) using three heating rates of 6°C/min, 8°C/min and 10°C/min. the conversion rate of reaction was determined as the ratio of actual mass loss to the total mass loss (Equation 4.8) corresponding to the degradation process using Model Free kinetics software.

$$\alpha = \frac{M_0 - M}{M_0 - M_f} \tag{4.8}$$

Where; *M,* M_0 and M_f are the actual, initial and final masses of the sample, respectively. The rate of degradation, (dα/dt), can be expressed as functions of temperature and mass of the sample. Using the selected value of conversion, the temperature (in kelvin) at that conversion level was measured for each thermal curve. A graph of the logarithm of the heating rate versus the corresponding reciprocal temperature at constant conversion was plotted. The plotted data produced a straight line. The next step in the process was the calculation of activation energy (E) from the slope using the method of Flynn and Wall (Equation 4.9).

$$E = \frac{-R}{b}\left[\frac{d\log\beta}{d(1/T)}\right] \tag{4.9}$$

Where; E was the activation energy (J/mol), R was the gas constant (8.134J/molK), T as the temperature at constant conversion (K), β was the heating rate (°C/min) and b was a constant (0.457). The value of the derivative term (d log β)/ [d (1/T)] was the slope of the line (Equation 4.10).

$$\ln t_f = \frac{E}{RT_f} + \ln\left[\frac{E}{\beta R}.P(X_f)\right] \quad (4.10)$$

$$T_f = \frac{E/R}{\ln T_f - \left[\frac{E}{\beta R}.P(X_f)\right]} \quad (4.11)$$

Where; t_f was the Estimated time of failure (min), E_a was the activation energy (J/mol), T_f was the failure temperature (K), R represented the gas constant (8.134 J/molK), $P(X_f)$ as the function whose values depend on E_a at the failure temperature and β was the heating rate (°C/min). The estimated lifetime t_f of a polymer to failure was determined using the time when the mass loss reaches 5wt%, i.e. α = 0.05.

4.2.14. Cytotoxicity analysis of viscoelastic hydrogel biocompatibility

Cytotoxicity studies were conducted to determine biocompatibility of the implant and to assess adequate removal of the free radical initiator from the hydrogel. Caco-2 cells were used in this study. The cells were cultured in RPMI-1640 media (with L-glutamine and sodium bicarbonate) supplemented with 5% fetal bovine serum, 10% horse serum (both heat inactivated) and 1% penicillin/streptomycin (Sigma-Aldrich, Missouri, USA). The cells were then maintained in an incubator (RS Biotech Galaxy, Irvine, UK) with a humidified atmosphere of 5 % CO_2 at 37°C. Cytotoxicity on Caco-2 cells was determined using CytoTox-Glo™ Cytotoxicity assay (Promega Corporation, Wisconsin, USA). This is a single-reagent-addition, homogeneous, luminescent assay that allows measurement of the number of dead cells in cell populations. The cells were seeded at a density of 200,000 cells for 24 hours in a 96-well culture plate. Briefly, Caco-2 cells were incubated with varying hydrogel concentration at 37°C in a CO_2 incubator (RS Biotech Galaxy, Irvine, UK) for 24 hours. 50µL of CytoTox-Glo™ reagent containing the substrate was added to each well as per the Promega Co. protocol. The cytotoxicity assay was performed by incubation of the CytoTox-Glo™ substrate with treated cells at room temperature for 15 minutes. The supernatant was collected through centrifuging (Optima® LE-80 K, Beckman, California, USA) at 1,800rpm for 20 minutes. For cell viability studies, the pellet was further lysed with CytoTox-Glo™ buffer (50µL) which was followed by incubation at room temperature for 15 minutes. Dead and live cell signals were measured by a Victor™X3 luminometer (PerkinElmer Inc., Massachusetts, USA). The percentage of viable cells was calculated using the Equation 4.12.

$$Cell\ Viability = 100 \times \frac{Average\ Luminescnece\ for\ x - Average\ Luinescence\ for\ Blank}{Average\ Luminescence\ for\ Control - Average\ Luminescence\ for\ Blank} \quad (4.12)$$

Where; average Luminescence for X% is the luminescence values of cells treated with the various hydrogel concentrations, average Luminescence for Blank (i.e. the luminescence of 50µL substrate which was added to a 100µL medium in an empty well without cells) and a control is the luminescence of untreated cells incubated with the CytoTox-Glo™ CTCA reagent (i.e. 50µL substrate). Dead cell number and total cytotoxicity were measured.

4.3. Results and Discussion

4.3.1. Viscoelastic hydrogel microscopic analysis

SEM was used to characterize the hydrogel surface and pore size distribution of the synthesized hydrogels. H2 indicated better mechanical, chemical and rheological properties. Microscopic analysis was also used for prediction of mode of drug release based on the pore size and level of distribution. Hydrogels can be categorized as either physical or chemical hydrogels. Physical hydrogels are hydrogels whose network structure is held together by molecular entanglements and secondary forces such as ionic, hydrogen bonds and hydrophobic forces. Chemical hydrogels are formed from crosslinking of polymers (Prestwich et al., 1998). Factors such as type of solvent composition, temperature and monomer concentrations used during hydrogel synthesis play a role in phase separation and formation of pores (Hoffman, 2002). PEG200 has at times been used as a porogen due to high solubility in water. In this study, it was used to improve the viscoelastic properties of the hydrogel. In Figure 4.1, PEG-200 indicated to have also played a role in generating a hydrogel with high pore distribution (C-D). Due to PEG-200 being situated between the cross-linked networks (PEGDA-MAA) forming an interpenetrating network, this interacted with water during water diffusion into the hydrogel. This indicates that water soluble materials such as polyethylene glycol can act as unreactive plasticizers that can affect polymer glass transition and also cause formation of pores (Kabiri et al., 2003). This can also affect swelling behavior and mechanical strength (Uzum and Karadag, 2012).

For polymers cross-linked via polymerization (chemical hydrogel), the rate of polymerization also has an impact on the development of the network structure. The swelling of porous bulk hydrogel resulted in an increase in pore size; which can provide a unique opportunity for the regulation of transport through the film in a very broad diffusivity range from the level in solution

down to a level in solids (Stuart et al., 2010). This indicated that diffusion of therapeutics across the interpenetrating network could be favored. By modulating the amount/type of polymer used in synthesis of hydrogel, generation of a thin responsive hydrogel films can be used as various supports of adhesion or grafting for controlled diffusion of various chemicals, biomolecules and nanoparticles (Tokarev and Minko, 2009). The surface of the hydrogel indicated to have no pores on the surface (A) whist inside there was a large distribution of pores in the form of groves (B). This form of pore distribution was contributed by the crosslinker concentration controlling the mesh size and the plasticizer acting as a porogen.

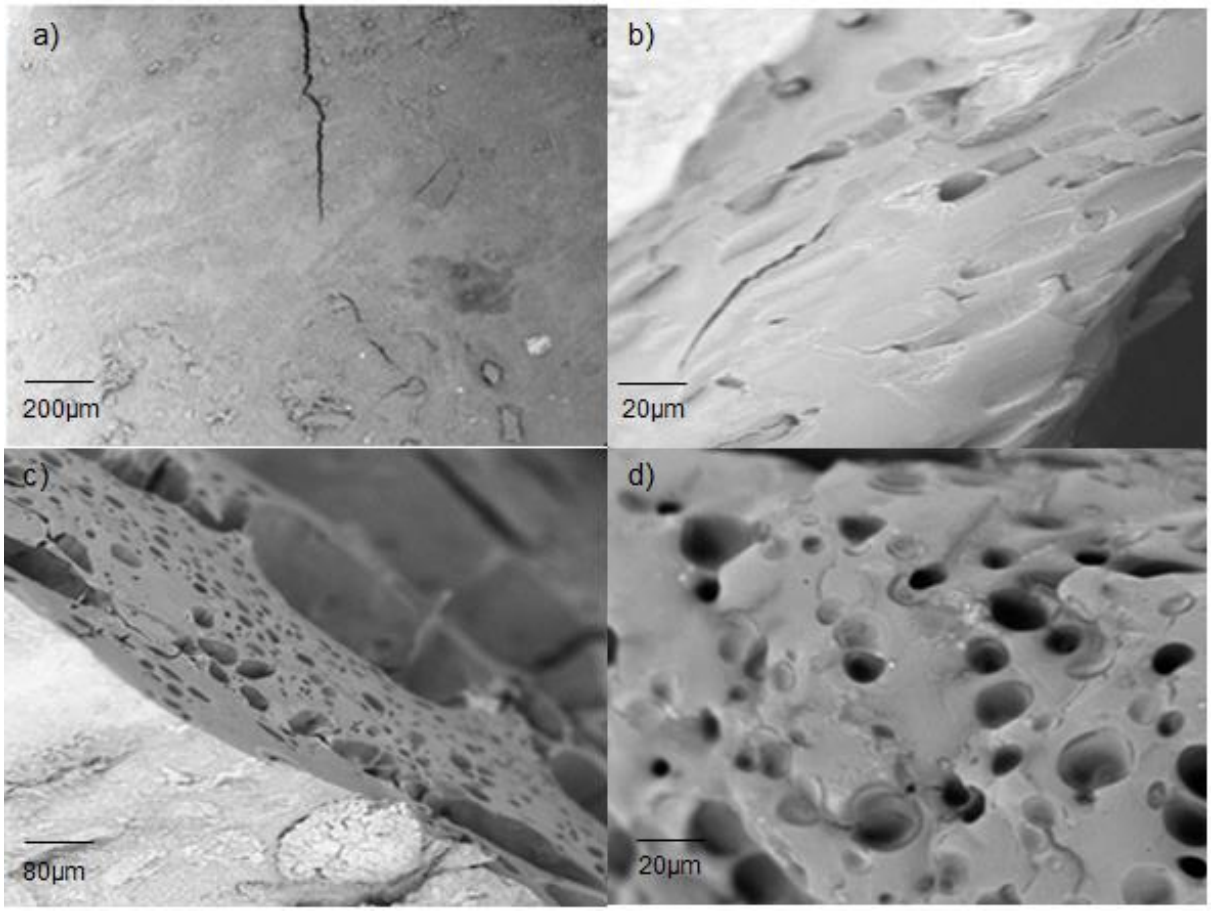

Figure 4.1: Scanning electron microscopy (SEM) images of hydrogels after hydrolysis. (a) Hydrogel surface, (b) pore grooves, (c) Pore distribution and (d) pore diameter variation.

4.3.2. Porosity analysis of viscoelastic hydrogel

Porosity analysis was used to characterize the size of the pores illustrated in SEM images. Presence of large sized pores within hydrogels will likely result in faster swelling rates (Kim et al., 2009). Based on the study, it indicated that increasing the crosslinking agent (PEGDA)

concentration would reduce the pore size due to tighter network structure, thus leading to reduced swelling rate. The amount of plasticizer (PEG200) used also played a role in the network structure by bridging polymer-polymer bonds and associations, thus affecting the level of porosity. An increase in porosity can help increase diffusion gradient, but it can also reduce structural integrity of the hydrogel when under strain. The synthesized hydrogels was observed to have distributed pores according to the isotherm log plot (Figure 4.2). The adsorption and desorption curve is classified as type III based on a classification system developed by de Boer (Condon, 2006). According to the classification system, a material is; not porous or possibly macroporous, and has a low energy of adsorption. A loop in the curve was used to characterize the pores. Nearly vertical and parallel adsorption and desorption branches observed indicated that there are regular even pores with no interconnecting channels (Aranovich and Donohue, 1997). This was supported by SEM micrographs that show no interconnection pores in Figure 4.1(B). Table 4.5 shows that increasing the crosslinker reduced the porosity of the gel because of the increased degree of network linkages. H1 is an inverse of H5, which indicated high crosslinker concentration reduced the hydrogel mesh size. H4 represent a 1:1 ratio of PEGDA: MAA without plasticizer. Due to MAA self-dimerization, this also affected the hydrogel mesh size in combination to PEGDA high concentration. Increasing the plasticizer also reduced the pore size as it causes interpenetration of the gel network structure (H2 and H3). The impact of high porosity on physiochemical properties were then analyzed using rheology and swelling studies.

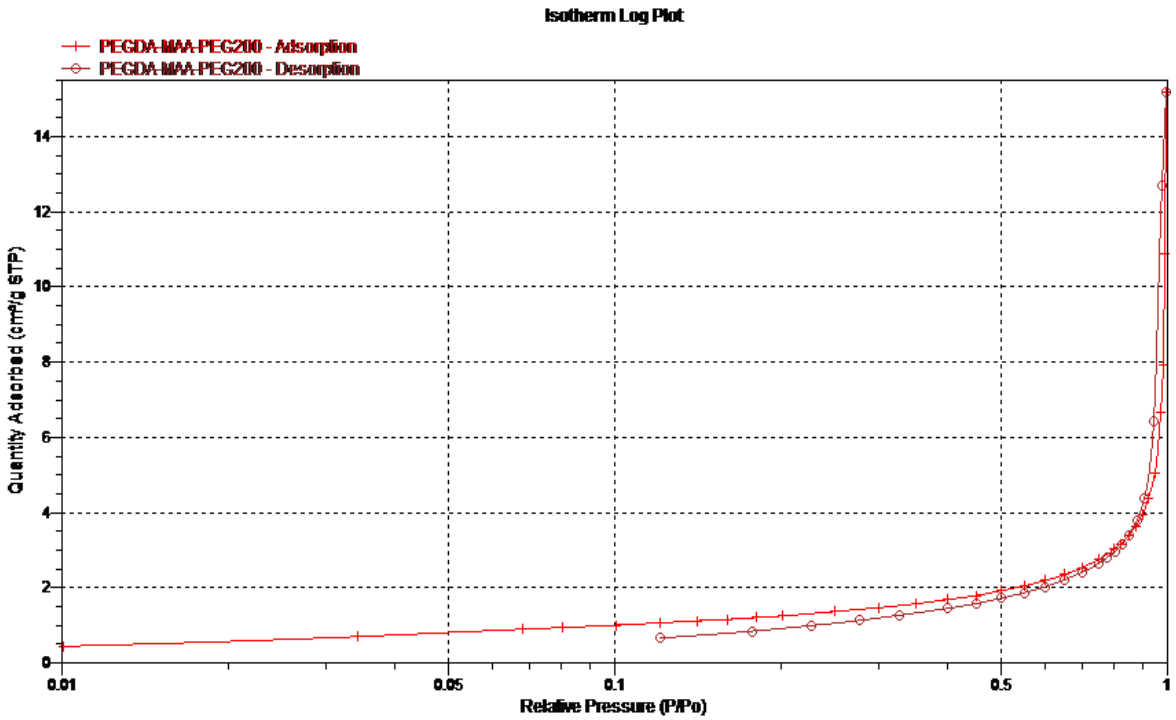

Figure 4.2: Isotherm log plot of polymerized hydrogel.

Table 4.5: BJH surface pore volume and pore size of viscoelastic hydrogel responsive to hemodynamic forces (1nm = 10 Angstrom).

Formulation	Volume (cm^3/g)	Pore Size (Å)
H1	0.010302	86.9339±5.4
H2	0.002239	60.1263±7.3
H3	0.002668	36.0439±4.2
H4	0.001356	23.6133±6.2
H5	0.000094	20.3204±2.3

4.3.3. Hydrogel molecular modeling

HyperChem version 8.0 was used for molecular modeling of the hydrogel (Hypercube, Inc., Florida, USA). The synthesis of covalently crosslinked PEG hydrogels falls into one of three major categories; chain growth or free-radical polymerization, step-growth polymerization, and mixed-mode polymerization which involves a combination of chain and step growth reactions (Papavasiliou et al., 2012). This model indicated that factors that affect polymerization include the; (1) initiator, (2) type of solvent, (3) temperature, (4) free radical scavenger and (5) crosslinker: functional monomer ratio. Free radicals are used to convert the monomer into their active state. Each free radical reacted with a single monomer unit (Braunecker and Matyjaszewski, 2007). However, concentration of initiator added in the solution has to be taken into consideration as high concentrations can result in the formation of short chains making the

solution appear more viscous without gelation. Polymerization reactions consisted of initiation, propagation and termination reactions. Methacrylic acids can occur in different forms depending on the solvent they are in; ranging from being; a monomer, a dimer (self-associate) and as a linear oligomer (self-association), associated with a solvent molecule, or associated with the carboxylic group of a growing polymer chain (Figure 4.3). DMSO is a polar aprotic solvent character with a high boiling point of approximately 188°C. MAA form self-associates (cyclic dimers) when it is bulky. However, when MAA is in DMSO the self-association of the acid has to compete with the formation of monomer-solvent complexes, which will result in increased activation energies for propagation, and thus a reduced rate coefficient of this reaction.

Individual monomers took part in the propagation reaction. By using a thermal initiator, additional energy was present for breaking of the intermolecular hydrogen bonds of the self-associates (Kutchta et al., 2000). The OH group of the methacrylic acid interacted with the sulfur group, S $(CH_3)_2$ of DMSO through hydrogen bonding. When water was added, this interacted with the COOH group. In the presence of water, the hydrophobic nature of the methyl group would affect the packaging of the polymer chain, thus causing swelling of hydrogel. Due to high boiling point of DMSO, porosity was reduced as the separation between the solvent and the polymer was delayed as compared to when solvents with low boiling points are used as these solvents are separated from the polymer at an early stage (Fernández-Garcia et al., 1998). Pore size and total pore volume were dependent on the solvent in combination to monomer and crosslinker ratio. This was due to the solubility coefficient of the monomers in the DMSO. This was due to the phase separation of the solvent from the hydrogel once it has been formed (Sharma and Puri, 2001). Separation occurred early on, followed by the preferential swelling of the cross-linked nuclei in the monomer resulting in bigger pores forming (Beiler and Sáfrány, 2007). Covalent crosslinking and subsequent gelation was induced in the presence of PEG macromers containing multiple acrylate groups found in the crosslinking agent PEG diacrylate (PEGDA). This was followed by PEG-200 interpenetrating the PEGDA-MAA network further stabilizing the hydrogel.

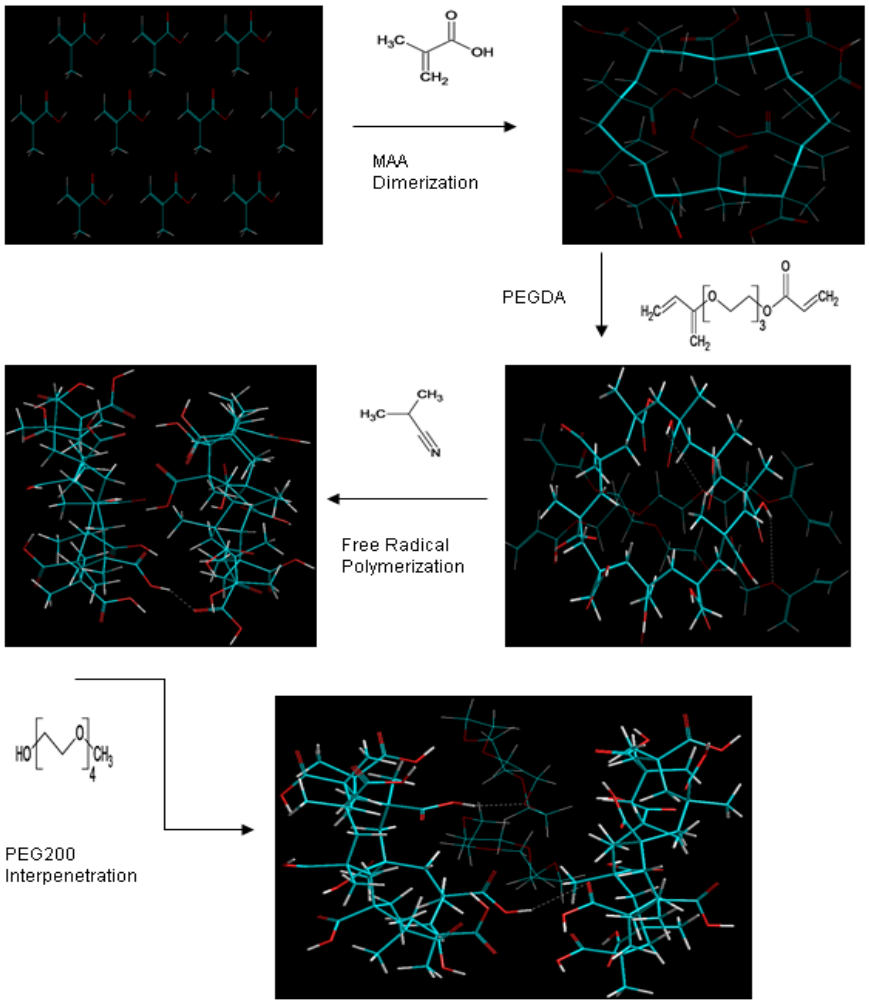

Figure 4.3: Polymerization schematics generated using HyperChem for molecular modeling.

4.3.4. Molecular weight determination of the synthesized hydrogel

Molecular weight of a hydrogel can be used to estimate the mechanical strength. Polymer solutions can be characterized as either being dilute, semi-dilute, or concentrated. When shear stress is applied on polymer solutions, polymer concentration has an impact on the change in viscosity. When chain entanglement occurs during shearing, the bulk viscosity deviates from linearity, due to the added viscoelastic effects of chain slippage and polymer interactions. The molecular weight of the H2 was determined as 125kDa from the intercept of the plot (Figure 4.4). H2 was selected based on porosity analysis and rheological properties. Second virial coefficient was determined as 5×10^{-6} mol mg/g^2 from the slope of Kc/R_θ versus c. The negative value of A_2 showed that there was an attractive overall net interactive force between polymer

chains, whereas, the positive value of the second virial coefficient indicated polymer chain interpenetration which led to steric stabilization (Tessier et al., 2004). The charge was due to MAA pH response which indicated that at high pH values (attraction), the hydrogel can shrink while at low it can swell (repulsion). The resulting stabilization could be the result of positive or negative enthalpy, where positive enthalpy reflects the release of bound solvent and negative entropy reflects the loss of configurationally freedom as the polymer chains interpenetrate. In this condition the dispersion is sterically stabilized (Priyadarshini et al., 2013).

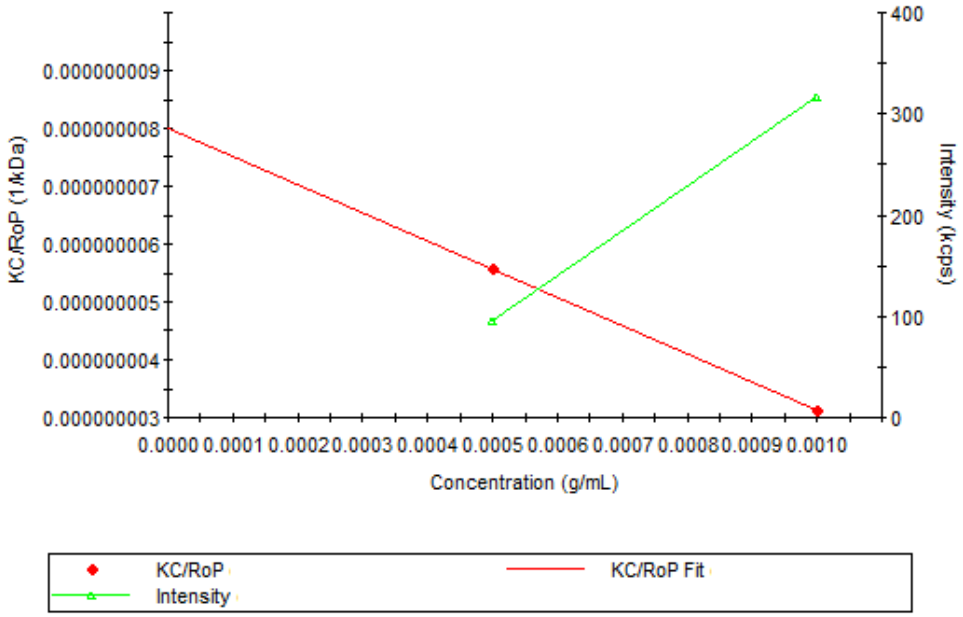

Figure 4.4: Debye plot of viscoelastic hydrogel indicating molecular weight.

4.3.5. Rheological analysis of hydrogels for determination of shear response

4.3.5.1. Formulated hydrogel flow behavior characterization

Rheological analysis was used to characterize the impact of crosslinker and plasticizer concentration. Decreases in viscosity indicate shear thinning, whilst an increase would indicate shear thickening (η vs. τ). Figure 4.5 indicated both shear thickening and thinning. Shear thickening was due to network reorganization which led to network reinforcement (Xu and Craig, 2010). This can be seen around a strain of less than 30Pa for H1-H5. In terms of H2, the rapid drop in viscosity indicated that the sample had varying viscoelastic properties. Due to high crosslinker concentration, this caused high shear thickening as the chains coiled under high strain before aligning. It was then followed by shear thinning which was due to; fast de-crosslinking kinetics, shear induced disentanglement of rapidly association and dissociation of

network chains (Seiffert and Sprakel, 2012). The onset and degree of shear thinning varies among materials and qualitatively correlates to the molecular weight distribution. H4 had higher viscosity indicating high molecular weight due to increased crosslink density caused by a high crosslinker concentration.

H4's viscosity was followed by H5, which had more cross-linker, but less MAA. H1, H2 and H3 had high viscosities because of high PEG200 concentration. The flow behavior indicated that the hydrogels had a pseudoplastic flow (H1, H2 and H3). The viscosity of a pseudoplastic substance decreased with increasing rate of shear ($\dot{\gamma}$ vs. τ curve). Apparent viscosity was obtained at any rate of shear from the slope of the tangent to the curve at a specified point. The most satisfactory representation for a pseudoplastic material, however, was probably a graphic plot of the entire consistency curve. The curve for pseudoplastic materials resulted from a shearing action on long-chain molecules of materials such as linear polymers. As shearing stress was increased, normally disarranged molecules begin to align their long axes in the direction of flow. This orientation reduced internal resistance of the material and allowed a greater rate of shear at each successive shearing stress (Erk et al., 2012). H4 and H5 had a Newtonian flow behavior due to high crosslinker concentration. This indicated that the chained aligned during shearing without coiling, causing flow at every given strain. In comparison to H1-H3, this indicates that H1-H3 are entangled hydrogels whereas H4 and H5 are branched. In addition, some of the solvent associated with the molecules may have been released, resulting in an effective lowering of both the concentration and the size of the dispersed molecules. This mode of behavior was indicated by H2 which has improved viscosity due to plasticizer and enhanced elasticity due to high crosslinker ratio.

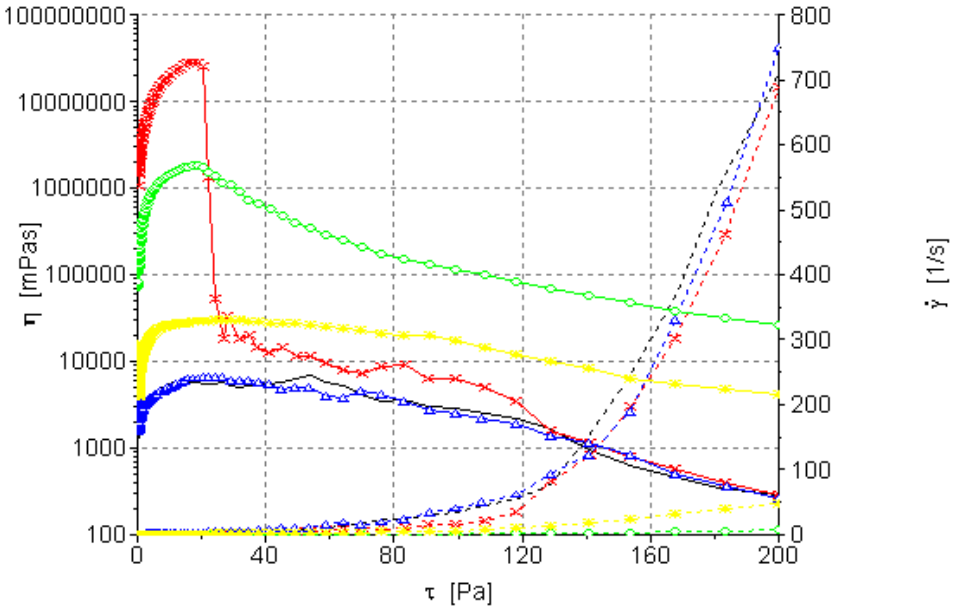

Figure 4.5: Yield stress test showing a plot of viscosity (η) versus strain (τ) versus shear rate ($\dot{\gamma}$). H1 (−), H2 (x), H3 (Δ), H4 (○) and H5 (∗).

The hydrogels appearance indicated to have undergone both shear thinning and thickening during analysis. A yield test was conducted to analyze their flow behaviors (Figure 4.6). Three forces have been recognized to play a role in controlling the response of a strained entanglement network (Wang et al., 2007). During flow, intermolecular locking forces f_{iml} arose and caused conformational deformation in each load-bearing strand between entanglements (H1-H3). The chain deformation built up a retractive force $f_{retract}$ within each strand that caused shear thickening. During continuous breakdown, cohesive force f_{ent} played a role in stabilizing the strands. The entangled hydrogels then yielded during continuous deformation when the declining f_{iml} could not sustain the elevated$f_{retract}$, thus causing shear thinning. A viscosity versus shear rate linear graph was plotted to determine if it fitted the Bingham equation (4.14). After the data fitted linear regression was then performed on the data. When a curvature occurred, the data then plotted on a logarithmic basis, which promoted the use of the power-law where consistency and the power-law index were used for flow determination when a straight line forms. The Cross model (4.13) was also used for flow determination when a curvature occurred. The overall flow indicated pseudoplastic flow as the curve (Figure 4.5 $\dot{y}$ vs. τ) and plot (Figure 4.6) did not start from the origin. The data indicated that H1 was different from H2-H5. This was due to a balance effect of PEGDA with PEG200. When PEGDA was high, the addition of PEG200 reduced imposed viscous behaviors, whilst high PEG200 was imposed by PEGDA

strong elastic forces. Due to H1 not consisting of PEG200, the elastic properties was more favorable.

The Cross model:

$$\frac{\eta-\eta_\infty}{\eta-\eta_\infty} = \frac{1}{1+(K\dot{\gamma})^m} \tag{4.13}$$

Bingham model:

$$\eta = \eta_\infty + \frac{\eta_0}{(K\dot{\gamma})^m} \tag{4.14}$$

Power-law liquid model:

$$\eta = k\dot{\gamma}^{n-1} \tag{4.15}$$

Where η indicate viscosity and $\dot{\gamma}$ indicates shear rate.

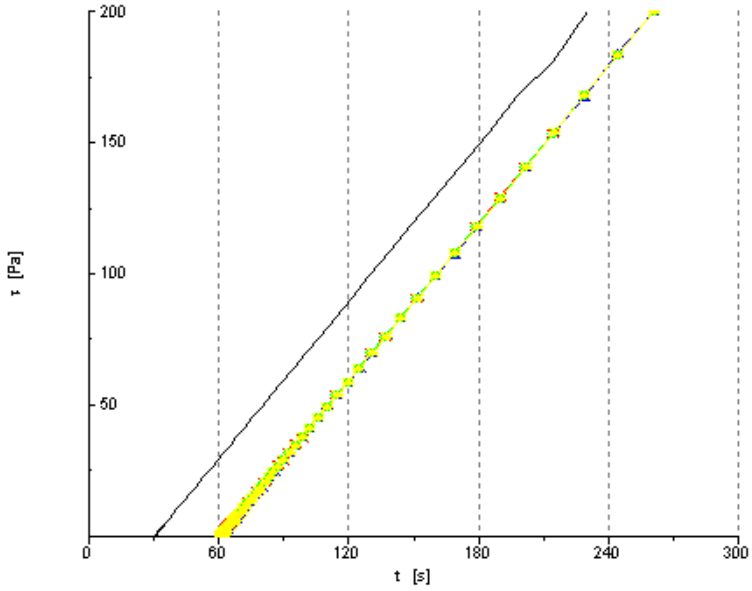

Figure 4.6: Characterization of viscoelastic polymer flow based on Newtonian and non-Newtonian flow. H1(−), H2 (x), H3 (Δ), H4 (○) and H5 (∗). H2, H3, H4 and H5 overlap.

4.3.5.2. Characterization of viscoelastic behavior

For viscoelastic analysis, solids and lipids are either elastic or viscous and some can be both as seen in Figure 4.7. These can then follow different forms of rheological behaviors such as Newtonian or Hookean. In rheology, a solid material can neither does not undergo deformation nor has a limited deformation gradient when a certain amount of stress is exerted on it. On the contrary a liquid will change shape when a stress is applied. Based on the Newtonian (viscous) and Hookean (elastic) laws, viscoelastic materials will harbor both behaviors (H1-H4). Polymer chain branches tend to vary in number, length and distribution along the main chain by means of changing number, size or the flexibility of the branches. Thus, entangled polymer chains with few branches exhibit higher viscosity at low shear frequency than that of a corresponding linear polymer of the same molecular weight (H5>H4>H2>H1>H3) .This behavior was due to long branched polymers' viscosity being more shear dependent and their relaxation time being longer that than linear polymers. H5 did not show viscoelastic properties but only exhibited a high storage modulus (dilute polymer solutions, relaxation time lower than 1, and *G''* always predominates) which was due to the high crosslink percentage and no plasticizer. This indicated that PEGDA had a major impact on the increase in mechanical properties of polymers. H4 showed no glassy state where storage and loss moduli crossover due to relaxation time being approximately equal to 1; and the viscous and transition-to-flow regions can only be seen.

Contrary to H4, H1 showed a relaxation time greater than 1 where only the rubbery region can be seen, in combination with the glassy region. This indicated low level of mechanical strength due to low concentration of PEGDA. This indicated the existence of branches/crosslinks between the two polymers. Polymer blends are compositions of chemically different polymers and are regarded as homogeneous if the components are compatible and mix at a molecular level (Kurniawan et al., 2012). Blends are heterogeneous or incompatible if the components are present in separate phases. If blends are incompatible, mechanical energy is needed to disperse the minor phase (mixing) and coalescence occurs if the blend morphology is not stabilized. Moreover, the elastic properties of non-compatible blends depend on energy storage mechanisms at the interphase. The relaxation of the dispersed phase itself is often much longer than the relaxation of the polymer chains of the individual components (Franck, 2005). The viscous regions indicated a point where *G'* predominates and viscous behavior prevails. Transition-to-flow point indicated a point where the two moduli cross and elastic behavior dominates. The rubbery region is where elastic behavior dominates. The leathery point is where crossover occurs again and the value of *G''* is higher rate than *G'* and the glassy region is the

area that occurs at high frequencies where *G''* continues to predominate (Barnes, 2000). This indicated that H2 had optimum viscoelastic properties.

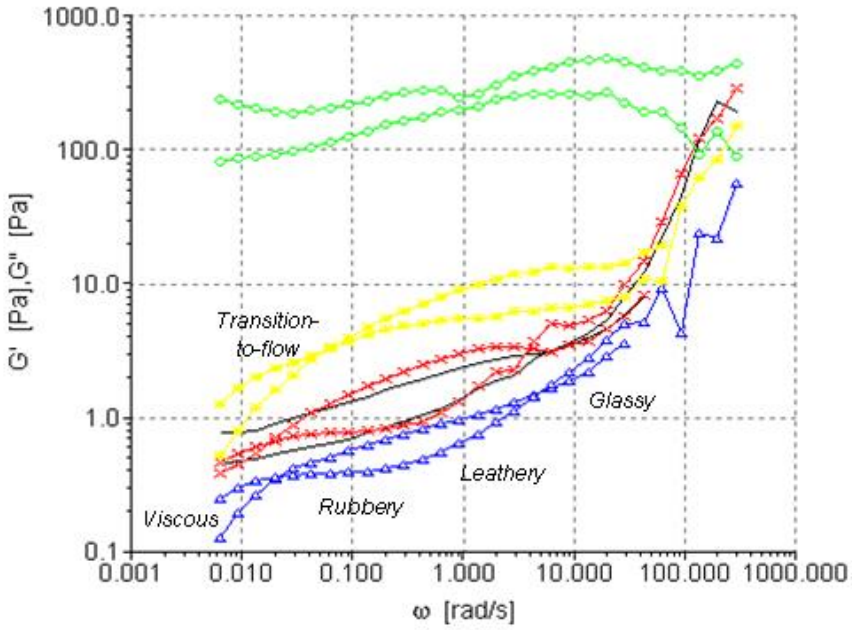

Figure 4.7: Frequency sweep showing storage (G") and loss (G') modulus versus frequency (ω). H1 (–), H2 (x), H3 (Δ), H4 (○) and H5 (∗).

Furthermore, based on these observations, H1-H4 indicated changes in molecular weight as seen by the deepening of the *G''* valley with increase in molecular weight due to molecular weight dependency on relaxation time (Jackson et al., 1994). The main and important property of viscoelastic materials is to able to withstand or even contribute to the continuous stretching/relaxing motion. Taking into consideration their swelling dynamics (volume changes) and changes in large force exertion combined with favorable time response scaling curves, this makes them more suitable for application in microsensors and microactuators of MEMS devices (De et al., 2002). Due to their diffusion-driven responses, these types of hydrogels can be used as valves to regulate the flow of fluids in microchannels (Baldi et al., 2003; Eddington and Beebe, 2005). PEG 200 acted as filler as it interpenetrates the PEGDA and MAA polymer chains causing the polymers to have a higher viscosity at low shear rates.

4.3.5.3. Evaluation of hydrogel elastic strength and structural recovery under constant strain

To determine if there would be structural recovery due to fluctuation of hemodynamic forces, a creep test was conducted. The creep compliance was determined from the 1-s creep curve using Equation 4.16.

$$J(t) = \frac{\gamma(t)}{\tau} \tag{4.16}$$

Since some of the hydrogels showed a linear viscoelastic behavior, the recovery curve can be predicted using Equation 4.17.

$$\gamma_{recoverable}(t) = \tau J(t) - \tau J(t-1) \tag{4.17}$$

The recovery curve at any given time t can be calculated by the superposition of the strain from the positive creep stress at time t = 0 to time t = t seconds and negative creep stress from time t = 1s to t = t seconds. The retardation curve can be divided into three parts. The first part was the instantaneous compliance representing the instantaneous elastic component of the material. The viscoelastic nature of the material was represented by the second part and characterized by one or more Voigt units. The last part of the curve, during which strain was increasing linearly with time, characterizes the zero shear viscosity of the material. When there was high shear stress the shear stress was high enough to break down the bonds responsible for the elastic behavior. The strain increased enormously and the behavior of the material was purely viscous. The absence of elastic components allowed the material to flow freely which means that the yield value would have been exceeded and the shear rate would start to increase (Ceulemans et al., 1999).

Prior to creep test, a stress sweep was required in order to obtain the strain value to be used in creep test (Figure 4.8). The shear thinning behavior of hydrogels means that viscosity will remain constant for some time as a result of the pseudoplastic nature of the materials. Under small shear rates, the hydrogels behave like Newtonian fluids whereby viscosity is not affected by shear rate. Once high shear rates are reached, hydrogel polymer chains start to untangle and align in the direction of flow. This causes the hydrogel to start behaving like a non-Newtonian fluid whose viscosity changes with the change in shear rate. The point where the viscosity starts to drop, was then taking as the yield point to be used for deformation and

recovery test. The modulus has similar behavior to viscosity, as its changes are influenced by the shear rate. Deformation was conducted for 180 seconds and then followed by structure recovery time of 360 seconds. Creep analysis was then analyzed by plotting compliance (J) versus time (t). The creep analysis application was used to determine immediate elastic response, delayed elastic response and steady-state viscous response.

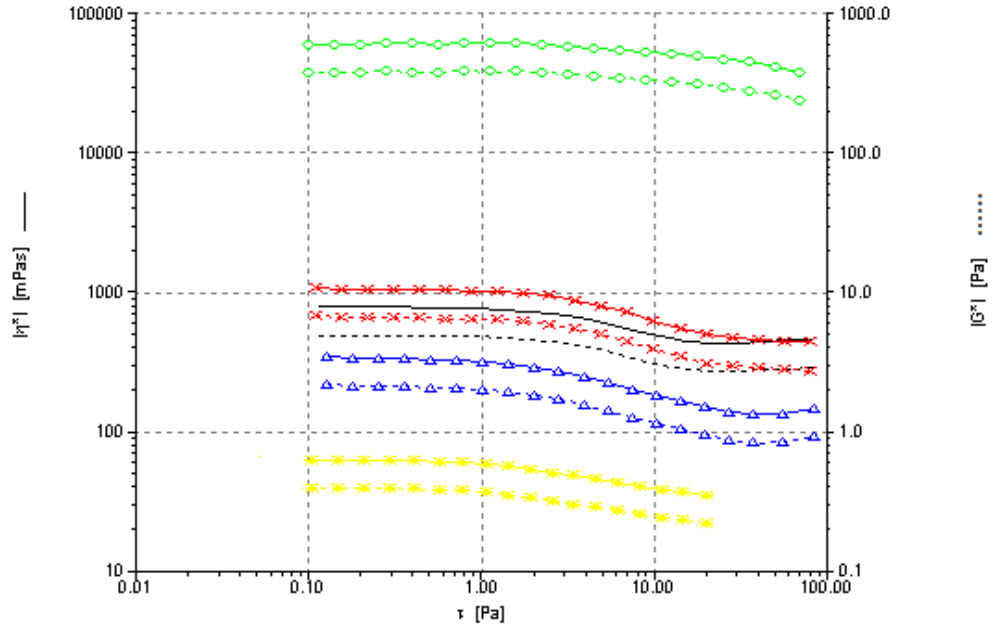

Figure 4.8: Stress Sweep of H1(−), H2 (x), H3 (Δ), H4 (○) and H5 (∗).The linear viscoelastic limits are defined as the strains and stresses at which the complex modulus decreases to 95 % of its value. ($|\eta^*| -$ complex dynamic viscosity and $|G^*| -$ complex modulus).

H4 had a high viscosity due to high concentration of PEGDA. This was due to high crosslink density playing a role in increasing viscosity and causing hydrogels to become very rigid or glassy. H5 had the lowest crosslinking density due to reduced elastomeric properties. Because of high PEG200 concentration in H3, viscosity was greatly reduced since the plasticizer decreased the interaction energy of the polymer chains. However, in comparison of H1 and H2, the plasticizer allowed the polymer chains to develop into a more extended conformation, thus causing a slight increase in viscosity in H2. Zero shear viscosity was determined, as the viscosity measured in shear deformation at a shear rate approaching zero. Zero shear viscosity can be used to characterize the stiffness and resistance to permanent deformation under long term loading of the hydrogels. Table 4.6 shows zero shear viscosity (η_0), equilibrium compliance (J_{e0}), relaxation time (λ_0) and elastic modulus (G_0) for the H1, H2, H3 and H5. H4 was excluded

from creep analysis at it was glassy and rigid. The high value of equilibrium compliance illustrated the level of elasticity of polymers. This was used to determine the percentage of structural recovery (J-r) which demonstrated that the addition of PEG200 delayed structural recovery due to lowered crosslink density. The data indicated that addition of the plasticizer reduced structural recovery due to reduced interaction energies resulting in impaired elastic modulus of PEGDA due to reduced retraction forces.

Table 4.6: Creep test analysis of viscoelastic hydrogel for structural recovery evaluation.

Formulation	η_0 (Pas)	J_{e0} (1/Pa)	λ_0 (s)	G_0 (Pa)	J-r (%)
H1	176.0±1.2	1.736±0.3	305.6±4.6	0.5761±0.11	38.56
H2	4.230±0.2	4.164±0.3	17.61±2.3	0.2402±0.05	9.738
H3	54.83±3.5	2.854±1.6	156.4±8.3	0.3504±0.03	7.56
H5	105.9±2.1	2.782±1.1	294.5±11.2	0.3595±0.9	21.57

η_0 - Zero shear viscosity, J_{e0} - equilibrium compliance, λ_0 - relaxation time, G_0 - elastic modulus and J-r - percentage of structural recovery.

4.3.6. Swelling behavior and kinetics of formulated hydrogels

Swelling studies were conducted to assess level of swelling which was influenced by the amount of plasticizer and crosslinker. Swelling will also play a role in implant fabrication. The hydrogel's swelling decreased with increasing amount of crosslinking, since the number of crosslinks inside the network per volume unit increased and free spaces for water molecules decreased. This created a more elastic and less rigid hydrogel network. The number of hydrophilic amide groups between two crosslinks decreased (the hydrophilic properties of the network decreases) so, water uptake decreased. Kinetics of the swelling process was determined by the n value. This indicated the process where water penetrated the network of the hydrogel when immersed in water. Degree of crosslinking affected the swelling equilibrium. Swelling equilibrium was achieved when the energy and entropy losses due to stretching and organization of polymeric chains became equal to gains in energy due to secondary molecular forces (Jagur-Grodzinski, 1999). This was governed by the change in free energy of mixing, energy of elastic deformation and electrostatic interactions (Melekaslan and Okay, 2000). Table 4.7 shows the swelling equilibrium and swelling exponent. This indicated that the plasticizer could impair the swelling kinetics due to PEG-200 interacting with water between PEGDA-MAA polymer chains.

Table 4.7: Equilibrium swelling ratio, equilibrium water content and swelling exponent.

Formulation	n_p	SR	EWC (%)
H1	0.304±0.02	3.71±0.3	78.8
H2	0.125±0.02	3.2±0.9	76
H3	0.435±0.04	1.56±0.5	60
H4	0.883±0.1	4.81±1.2	82.8
H5	0.071±0.01	2.18±0.9	68.5

n_p- Swelling exponent, SR - swelling ratio and EWC - swelling equilibrium

Swelling kinetics of hydrogels can be classified as diffusion-controlled (Fickian) or relaxation-controlled (non-Fickian). Fickian kinetics is characterized by the *n*=0.5 (H1, H2, H3 and H5), whereas, a value of *n* between 0.5 and 1.0 this indicates a non-Fickian process (or Case II transport) where the relaxation of polymeric chains of the hydrogel determines the rate of water sorption (H4). Swelling will reach maximum point when elastic restoring force of the network balances the osmotic forces. Peppas and co-workers stated that with non-Fickian diffusion behavior, the network would change from glassy to rubbery state during swelling due to a low relaxation rate (Barati et al., 2010). The value of the swelling exponent increased as the structure would become more rigid when the amount of crosslinker was increased. Therefore, the diffusion behavior would follow anomalous diffusion as the network relaxation rate reduces. When diffusion into the hydrogel occurs much faster than the relaxation of the polymer chains, the swelling kinetics is said to be diffusion controlled (Suzuki et al., 1996). H2 indicated to consist of the lowest Fickian kinetics values, which made it an applicable hydrogel for allowing Fickian diffusion. This hydrogel also remained stable during tests without degrading. In terms of hydrolytic degradation, H3 had rapid degradation as it had dissolved within 3 hours of swelling studies. This was due to high plasticizer concentration increasing hydrolytic degradation due to high concentration of COOH groups. Other formulations were stable for more than a week reaching swelling equilibrium without mass loss.

4.4.7. Hydrogel mechanical analysis for matrix resilience and rigidity

Texture analysis was used to characterize resilience and rigidity to differentiate between brittle and elastic hydrogels. PEG is a hydrophilic, water soluble and biocompatible polymer that can be used in a variety of biomedical applications. This polymer shows little immunogenicity and is non-toxic. Its polyether backbone cannot be enzymatically degraded and offers resistance to protein adsorption when covalently crosslinked. The physical and mechanical properties of hydrogels made of PEG biomaterials can be readily manipulated via alterations in selected polymerization conditions which have been shown to directly influence hydrogel crosslink

density, swelling, and the elastic modulus resulting in scaffolds with rigidities ranging from those found in soft tissues such as the liver and skin up to rigidity values of articular cartilage and bone (Nemir et al., 2010)). PEGDA hydrogels have been shown to be highly tunable. The mechanical properties PEGDA hydrogels can be controlled by varying the molecular weight or concentration of the polymer, with an increase in elastic modulus with increasing polymer concentration or decreasing polymer molecular weight (Nemir and West, 2010). The data in Table 4.8 correlates with rheology analysis. An increase in PEG200 concentration was shown to impair resilience, as the hydrogels do not regain their complete initial structure after removal of the applied strain. PEG has also been shown to impair viscoelastic properties of the hydrogel by shifting the rheological behavior more into viscous behavior. An increase in PEGDA improved the hydrogel's resilience and rheology compliance. When used for implant application, it is required that hydrogels withstand physicochemical changes such as fluctuation in temperature, pressure and pH. For intravenous application, hemodynamic forces exerted on the hydrogel would lead to impairment of the implant-programmed function as the changes would lead to the leaching of drugs and destruction of the implant. This may cause thrombosis as the mechanically degraded polymer could block blood vessels. H4 had reduced resilience due to lack of viscoelastic properties that prevented retraction forces and intermolecular force interaction, thus causing the hydrogel to fracture under strain. The amount of deformation and resilience by H1 and H2 correspond with rheological analysis. This indicated that both an increase in plasticizer impairs level of recovery, whereas high crosslinker makes the hydrogels more rigid due to a high mesh network.

Table 4.8: Mechanical analysis of polymer strength and structural recovery.

Formulation	Rigidity ($N.mm^{-1}$)	Deformation ($N.m^{-1}$)	Resilience (%)
H1	3.83±0.8	0.53±0.01	95.1
H2	3.77±0.6	0.268±0.03	76.3
H3	3.62±1.2	0.146±0.03	60.5
H4	0.69±0.2	0.11±0.01	15.2
H5	1.42±0.5	0.314±0.02	63.7

4.3.8. Evaluation of structural changes after polymerization

FTIR analysis of the viscoelastic hydrogel indicated successful polymerization of MAA and PEGDA, and interpenetration of PEG200 within the cross-linked network (Figure 4.9). The figure represents evaluation of H2. The 3383.44-3377.45cm^{-1} peak is shared between the plasticizer and the final product which indicated an alcohol/phenol O-H stretch, 1550.39cm^{-1} was distinct in the final product indicating an aromatic C=C bending, 701.11cm^{-1} was also distinctive to the final

product indicating an aromatic C-H bending. The hydrogel was formed by methacrylic acid forming poly methacrylic acid which is represented by peak 1634.10cm^{-1} (vinyl unsaturation) disappearing due to a homopolymerization process (Garcia et al., 2011). This was later bound with polyethylene glycol diacrylate (cross-linker) and then polyethylene glycol 200 (plasticizer) which binds the PEGDA: MAA together. From the FTIR spectrum, the 1982cm^{-1} represented phenyl ring substitution overtones. The presence of aromatic compounds was confirmed by the pattern of the weak overtones and combination tone bands found from 2000 to 1600cm-1. The peak observed at 1165cm^{-1}, this was due by a shift from the 1188cm^{-1} of PEGDA represented an ester stretch. The 748cm^{-1} band lying in the 870-675cm^{-1} region indicated the presence of a phenyl ring substitution. This indicated successful polymerization of PEGDA-MAA and interpenetration by PEG-200.

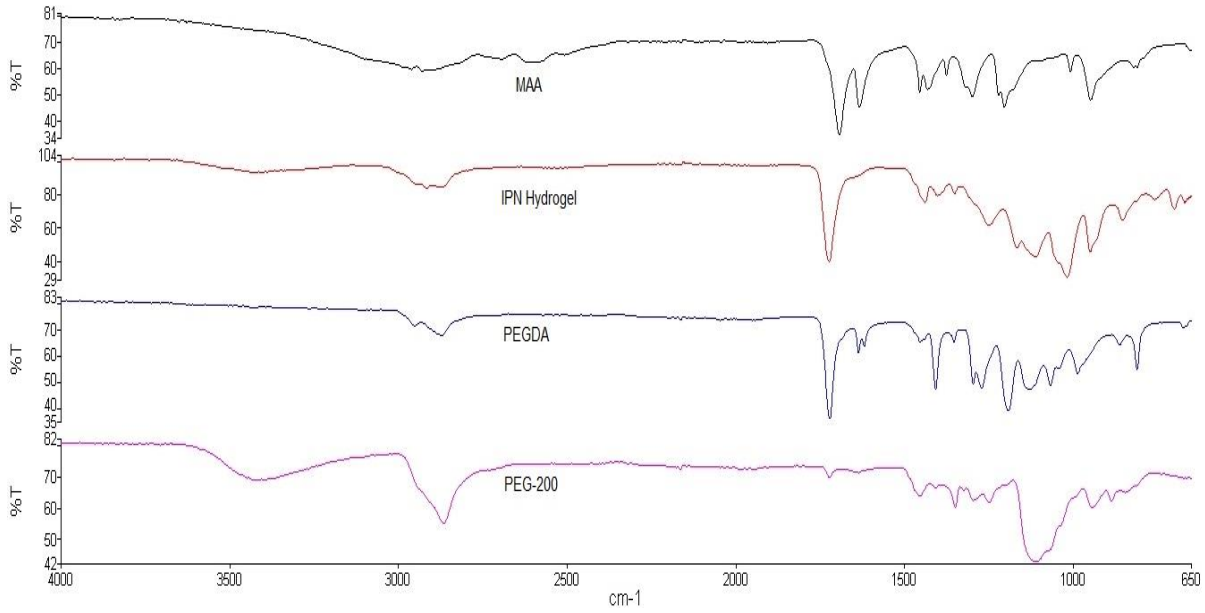

Figure 4.9: FTIR spectra of the viscoelastic hydrogel after polymerization.

4.3.9. Hydrogel thermodynamic analysis

4.3.9.1. Thermodynamic stability and molecular interaction analysis

Thermodynamic properties of hydrogel play a role in stability. Incompatible polymer blends show distinct glass transitions for each component. However, the value may change in relation to the pure components. Whilst, homogeneous blends exhibit only one glass transition. The evaluation of the glass transitions will provide information about miscibility, compatibility, and interphase effects. In most cases, heat flow rates obtained at relatively low cooling rates do not

have a smooth bell shape typical to polymer crystallization, but display some irregularities. Contrary to this, at high cooling temperatures, the DSC curves become smoother without any irregularities in the heat flow. These irregularities can occur due to different crystallinity factors which may include; (1) fractionated crystallization in the polymer blend or copolymer may lead to the appearance of crystallization exotherm with multiple peaks, (2) transient non-integral folding crystal that initially develop during crystallization then transform to integral folding crystal through isothermal thickening and thinning, (3) delay of crystallization due to homogeneous and heterogeneous nucleation and (4) non-monotonous development of latent heat during crystallization. Thus latent heat is extremely sensitive to every act of nucleation as well as to a space limitation during growth of spherulites.

This resulted in multiple peaks of the DSC signal at the corresponding time/temperature. The smoothed shape of crystallization indicated exotherm, indicating a large number of spherulites are nucleated at the same temperature range (Di Lorenzo et al., 2006). From Figure 4.10, it can be confirmed that there was transition with a loss of weight which was due to evaporation. This showed that even after drying the samples in a lyophilized, some DMSO was completely removed. During the repeat run, the peak was not present indicating complete evaporation and degradation of the hydrogel. However, crystallization was still present. The glass transition may shift in any direction as a result of the effect of the plasticizer and crosslinker used. Addition of a crosslinker and the polymerization process can increase the T_g temperature, while plasticizers reduce it. Glass transition was observed around 57°C. The polymer mix was homogenous as observed by presence of only one glass transition peak (reversible thermal expansion region). The broad peak of 140.87°C represented solvent evaporation; followed by cold crystallization (found in crosslinked polymers due to decrease in activation energy as temperature increases) at 423.17°C. This depicted irreversible shrinkage occurring due to reorganization, chain folding and recrystallization. Melting occurred at 320.65°C, followed by crystallization from the melt. The multiple melting peaks and recrystallization indicated reorganization of imperfect crystals during heating (Cheng and Jin, 2002).

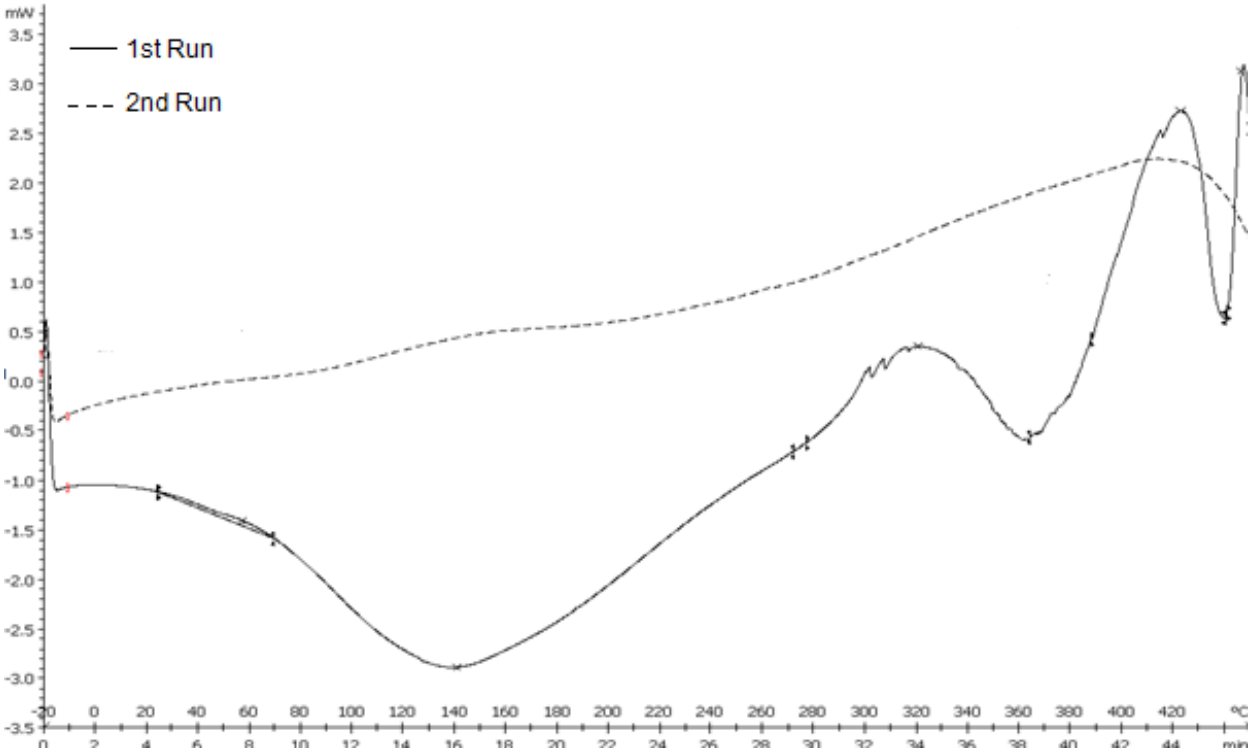

Figure 4.10: DSC curve of viscoelastic hydrogel showing glass transition, melting temperature and crystallization peaks.

Table 4.9 and 4.10 confirms that addition of a plasticizer does suppress the melting point as seen H1 and H2. Negative values indicate domination of potential energy due to covalent bonding. This occurred when shared electrons bind the atoms to each other. The positive values indicate domination of kinetic energy due to ionic bonds. This occurred when oppositely charged ions interact. From the values acquired, it indicated that increasing the crosslinker concentration increased the ionic strength of the polymer, which can be seen by formulation of brittle hydrogel, H5. Ionic bonds are the strongest bonds in relation to covalent bonds, thus increasing the mechanical strength of the viscoelastic polymers. This can aid in determining the flexibility of polymer chains in a solution. The interaction parameter accounts for the contribution of the non-combinatorial entropy of mixing and the enthalpy of mixing to the Gibbs energy of mixing. A negative value indicated that the polymer was miscible, while the positive value indicated that the enthalpy of mixing was unfavorable (Higgins et al., 2010). This was supported by rheological and molecular modeling indicating that the synthesized hydrogel components started as immiscible mixture. Due to polymerization, this results in a heterogeneous hydrogel whereby each the plasticizer interpenetrated the co-polymer network thus affecting the interaction energies and tuning both chemical and physical properties.

Table 4.9: Determination of heat of fusion and melting temperatures affected by plasticizer concentration.

Formulation	T_m/°C	ΔH_m/Jg^{-1}
H1	139.73±1.3	-226.39±12.3
H2	84.69±1.4	-187.57±9.8
H3	81.28±1.7	-290.92±13.2
H4	174.54±2.2	-220.68±11.1
H5	141.36±3.2	-132.58±13.2

T_m/°C represents melting temperature whilst ΔH_m/JG^{-1} represents Gibbs energy of mixing.

Table 4.10: Interaction energy and density changes caused by plasticizer concentration.

Crosslinker concentration	B/J cm^{-3}	χ_{12}
<2%	442.18±22.6	66.02±3.6
>2%	696.20±13.5	96.04±1.6

B/J cm^{-3} represents interaction parameter whilst X_{12} represents interaction density

4.3.9.2. Thermal degradation analysis of viscoelastic hydrogel at various heating rate

TGA allows rapid degradation studies by means of estimating rate of degradation based on the duration of storage and specific temperatures. Thermal degradation leads to transformation of the macromolecular network, whereby in most polymers these structural changes occur as regions near their glass transition. Once the temperature reaches above a polymer's glass transition temperature, this causes chemical and biochemical degradations to take place (Lucas et al., 2008). By means of estimating glass transition and activation energies, this allows pre-formulation of polymers which can have longer thermal and hydrolytic stability. Addition of a plasticizer has been shown to reduce glass transition of polymers, thus it will also reduce the activation of the polymers leading to reduced lifetime stability.

Figure 4.11 differential thermogravimetric (DTG) analyses obtained from the derivative reveal the rate of change of weight and are particularly useful in defining the temperature of the initial onset of decomposition for each weight loss event. Based on the DTG curve, we can find several major events of weight loss due to evaporation of occluded water at low temperature (free water evaporation, bound water evaporation), decomposition of organic components and burning of decomposed organic molecules (Zhong and Chu, 2012). The peak at 210°C indicates the evaporation of remaining DMSO from the polymer as it was hard to remove via lyophilzation. This is followed degradation of PEG200 and PEGDA between 250°C and 500°C. Within this region CO_2 and remaining bound water was released which caused variation in mass change due to chemical reactions (oxidation). Increasing heating rate (10°C/min-6°C/min)

increased degradation rate and activation energy as can be been seen in the figure. Three heating rates are shown in this figure as they were used for determination of decomposition kinetics. The heating rates become similar after 450°C due to decomposition of all carbon based materials.

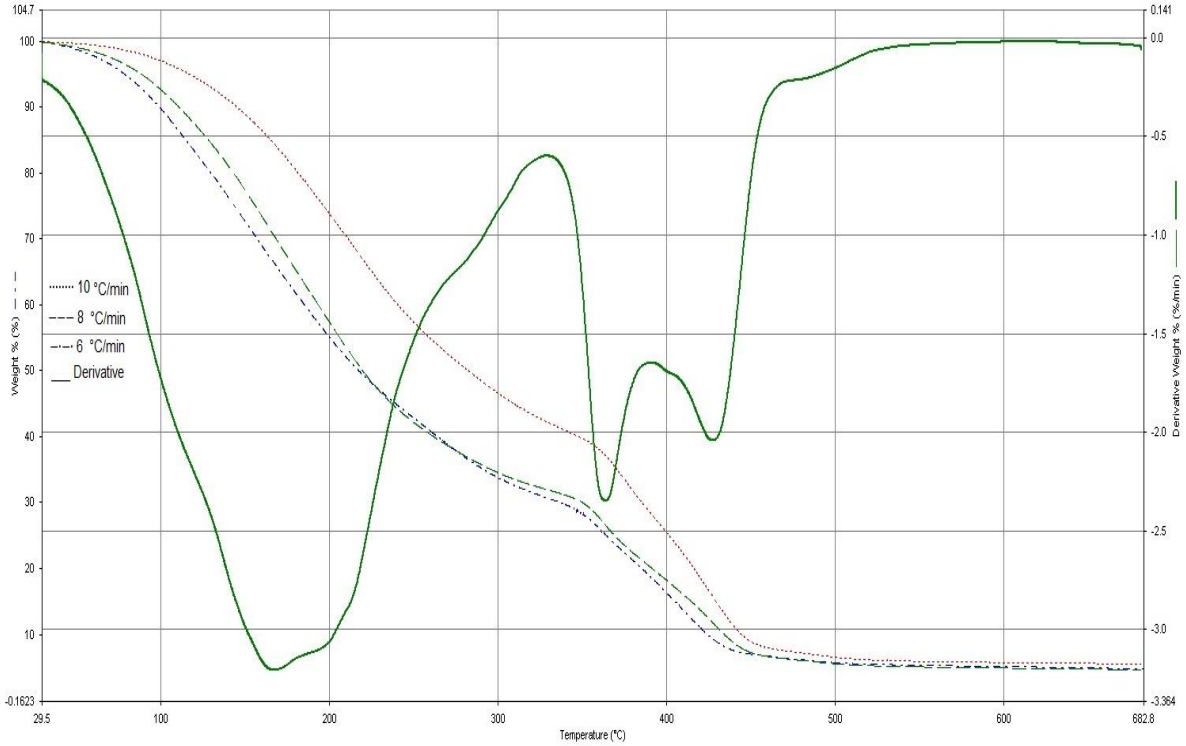

Figure 4.11: TGA characteristic of viscoelastic hydrogel showing different melting points of H2.

4.3.10. Lifetime prediction of hydrogel stability

TGA lifetime predictions studies were analyzed to assess the lifetime of the viscoelastic hydrogel when used for implant application. The slope of log heating rate versus temperature enabled the estimation of the activation energy (Table 4.11) for a mass loss greater than 5%. As the heating rate was increased, the activation energy also increased. This also correlated to the degradation rate of the hydrogel, whereby using low heating rates more time was given for interacting bonds to be broken. This was seen by high mass loss in low heating rates, which also allow increased mass change sensitivity. Due to different heating rates variation in time the intermolecular forces are exposed to thermal energy and the mass change, Table 4.12 indicate the time the hydrogel will fail at varying temperatures. At 30°C, the hydrogel is expected to last for 3.5 years as more activation energy is required to dissociate the hydrogel network. This indicates long-term stability of the hydrogel.

Table 4.11: Determination of activation energy for prediction of polymer lifetime under inert atmosphere.

Heating rate (°Cmin−1)	Atmosphere	*E*a.(kJmol−1)	$\mathbf{P(X_f)}$	E/RT
	Nitrogen			
6°C/min		88.55±6.2	16.32	30.66
8°C/min		109.56±11.4	19.32	37.21
10°C/min		149.11±12.7	23.87	47.24
Average		115.74±10.3	19.99	38.67

Viscoelastic hydrogel lifetime prediction was determined using H2 as it showed better rheological properties (i.e. similar rheology properties to those of H1). The high lifetime predicted relates to high mechanical strength. As indicated in DSC studies, the plasticizer impaired the glass transition of the hydrogel. When a hydrogel was stored at temperatures above the glass transition, chemical properties of the hydrogel will change which will lead to instability with the physical properties.

Table 4.12: Predicted viscoelastic hydrogel lifetime at varying temperatures.

Component	30°C	150°C	300°C	600°C
Viscoelastic Hydrogel	31298 hours	11.34 hours	5.03 hours	0.8 hours

4.4.11. Cytotoxicity analysis of viscoelastic hydrogel

Polymer biocompatibility has a major impact on the functionality of the implant. Cytotoxicity test was used for prediction of possible localized and systemic immune response. This was required as biocompatibility affects patient compliance (pain, fever and swelling) and drug release (thrombosis/biofouling). Biocompatibility may be categorized as either blood or tissue biocompatibility. If the biomaterial is expected to be exposed to blood, protein adsorption causes activation of adherent platelets that lead to formation of thrombi on the biomaterial surface. This adhesion may cause reduction of drug diffusion from the biomaterial and due to embolization. This can cause blockage of blood that may lead to stroke. In tissue biocompatibility, inflammation causes aggregation of neutrophils, eosinophils, macrophages and foreign body giant cells which leads to the formation of granulation tissue if the foreign body is not removed. This later leads to fibrous encapsulation that stops/reduce biomaterial function (Park and Park, 1996). The data obtained was plotted as “dead cell” and “live cell” signal versus the concentration of the viscoelastic hydrogel (Figure 4.12). At concentration higher than 80mg/mL the hydrogel occurred to be causing some level of toxicity. This however was clouded by the hydrogel making the media more viscous which could have interrupted with the cytotoxicity assay. Hemocompatability was not assessed in this study as the PEGDA has been shown to

prevent blood cell adhesion or activation at the surface of the materials. All the polymers that are used are FDA approved the requirement for cytotoxicity was to ascertain the removal of thermal initiator and unreacted monomers that may cause irritation.

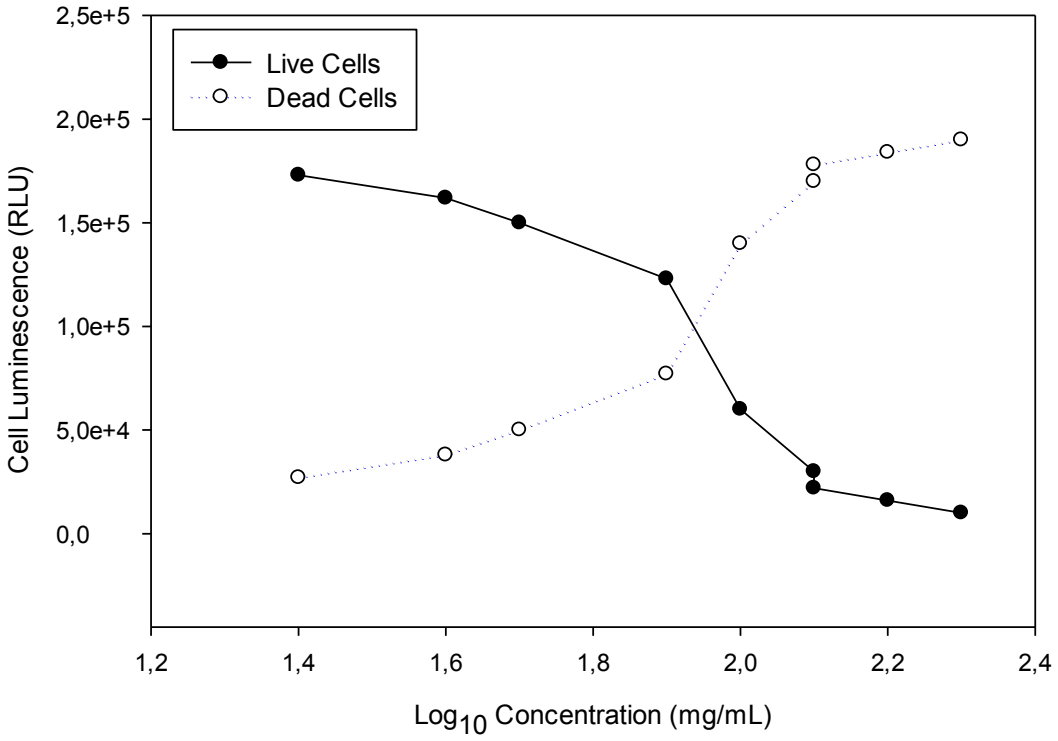

Figure 4.12: Logistic model determining cytotoxicity of viscoelastic hydrogel.

4.4. Concluding Remarks

Rheology and texture analysis has shown that the hydrogel can withstand low shear stress that are associated with atherogenic prone regions, whereas if the hydrogel was to be placed in high-shear thrombotic regions, there would be 76% structure recovery after reducing the stress. The hydrogel has also indicated to be biocompatible and had low swelling ratio. This is ideal to avoid thrombotic effect, which can be induced by change of flow after implantation. This indicates that application of this hydrogel in intravenous biomaterials can be beneficial by being able to withstand fluctuations in hemodynamic forces that can affect diffusion; the hydrogel will also offer the stable control of programmed/responsive drug release by healing after high shear rates. Turbulent and laminar flows have been shown to affect drug release from drug eluting stents (Chiu and Chien, 2011). The use of a viscoelastic hydrogel for formation of an antigen

responsive interpenetrating network (IPN) hydrogel can be beneficial in controlling the diffusion rate of osmotic pump. In the following chapter, antibody conjugated SLN are embedded within the viscoelastic IPN to form an antigen responsive hydrogel. This was used for controlling drug diffusion in correlation to LDL concentration.

CHAPTER FIVE

IMPLANT DESIGN PROCEDURE, CHARACTERIZATION, AND *EX VIVO* EVALUATION

5.1. Introduction

Numerous clinical trials and research have indicated that continuous monitoring of physiochemical changes holds great potential to provide early indication of various chemical imbalances signifying illness as well monitoring disease progression (Vaddiraju et al., 2010). The need to replace existing diagnostic tools, such as the use of; glucose test strips, chromatography, mass spectroscopy and enzyme linked immunosorbent assays (ELISA), with faster and cost effective diagnostic devices will aid in providing early signal of bio/chemical imbalances. This can also assist in the prevention and treatment of various disorders like diabetes, asthma, cancer and cardiovascular disorders. Implantable biosensors offer continuous biochemical imbalance monitoring without the need for human intervention. Implantable biosensors have many possible applications and real chance effectiveness when employed appropriately in medicine. Sensitivity of these implantable biosensors is vital, as it is required to detect specific molecules at very low concentrations in a pool of other molecules of varying sizes. Sensitivity is more important when there are a number of molecules, which are homologous. The design of implants has to be simplified as this can interfere with sensitivity and specificity. Although implantable systems have improved diagnostics, their reliability is commonly hampered by factors like biofouling and immune response (Gifford et al., 2006). To combat this problem, integration of polymer science and drug delivery system may aid in improving biocompatibility and reducing macromolecule/cell adhesion onto implant surfaces.

Foreign body immune response and tissue inflammation usually occur within a short period after implantation. This may cause implant instability as the clustering of the immune cells can interrupt the biosensors signaling and the confinement of the implant to fibrosis tissue can reduce detection of chemical imbalance (Onuki et al., 2008). The degree of the inflammatory and immune reaction depends on the properties of the device, such as shape, size, surface chemistry, roughness, design, morphology and porosity, composition, sterility issues, contact duration, degradation, the type of host specie, genetic inheritance, site of implantation and the microenvironment (Fournier et al., 2003). Biocompatibility is controlled by the cell–cell, cell–polymer, and polymer–protein interactions. Following implantation, a polymer–blood interface is immediately created and the first step of the tissue response is a non-specific adsorption of

blood and tissue fluid proteins on the whole surface of the foreign material by walling off the foreign material in a fibrous 10-100 μm thick layer (Turner et al., 1991). However, when there is integration of biosensors with drug delivery systems, modification of the implant surface can aid in the reduction of the fibrous wall formation which can affect implant functionality. Polymeric materials such as Pellethane™, polyallylamine, horseradish peroxidase derivatives and polyethylene glycol can be used to improve biocompatibility of biosensor by reducing biofouling and the foreign body immune response (Wang et al., 2013).

Selection of a controlled drug delivery technology suitable for each drug depends on many factors, including physicochemical properties of the drug, duration of release and the release kinetics (Dey et al., 2008). Controlled release mechanisms involved may be broadly classified into physical and chemical mechanisms. The physical mechanisms include diffusion of drug molecules through a polymer layer, dissolution or degradation of polymer matrix thus controlling the drug release rate, osmotic pressure and occurrence of ion exchange for ionized drugs (Siegel and Rathbone, 2012). Chemical mechanisms involve breaking of covalent bonds that connect drug molecules to a delivery vehicle, such as polymer chains through chemical or enzymatic degradation (Joshi and Patel, 2012). Diffusion controlled drug release usually occurs in two mechanisms that involve reservoir controlled and matrix controlled devices. In the reservoir devices, the drug reservoir is covered with a thin polymer layer which functions as a rate-controlling membrane. At steady state, drug release rate remains constant resulting in zero-order drug release kinetics (Siegel and Rathbone, 2012). The main objective of the drug delivery system would be to have drug concentration in the blood maintained between the maximum safe concentration (C_{max}) and the minimum effective concentration (C_{min}) (Acharya and Park, 2006). In this study, drug delivery systems were designed to function by means of physical mechanism. The anti-LDL SLN and viscoelastic hydrogels are used in this chapter to design an antigen responsive interpenetrating network (IPN) hydrogel. The hydrogel was then used to coat a hydrophobic porous polymeric tube to control drug infusion rate. An alternative drug delivery system was designed for infusion of anti-LDL SLN via an 18 gauge catheter tube. An osmotic pump would then be attached to the tube to allow sustained infusion of fenofibrate as a model cholesterol-lowering lipophilic drug.

5.2. Material and Methods

5.2.1. Materials

Glutaraldehyde, ethyl cellulose, polyethylene oxide, cyanoacrylate, castor oil, mannitol, methanol, Ethylenediaminetetraacetic acid (EDTA), Traut's reagent (2-Iminothiolane), Ellman's reagent (5, 5'-dithiobis-(2-nitrobenzoic acid), TEMED, ammonium persulfate (APS) and phosphate buffered saline pH 7.4 (PBS) were purchased from Sigma (Sigma-Aldrich, Missouri, USA). Gelatin capsules were purchased from Gel-U-Cap (Gel-U-Cap S.A. (Pty) Ltd, Pretoria, SA). Anti-LDL SLN was synthesized as described in Chapter 3. Catheters: 18Ga. x 2-1/2" (6.35 cm) radiopaque over 20Ga. and RW Introducer Needles were purchased from Arrow International (Tefelex Inc., Pennsylvania, USA). In the present study, all the chemical agents were analytic grade and used without further purification.

5.2.2. Reservoir fabrication from gelatin capsule

Due to requirement of biocompatible and/or biodegradable materials for implantation, gelatin capsule were employed in this study. However due to high solubility of gelatin in warm water, the capsules required a hydrophobic coating (ethyl cellulose) to allow long-term stability. The modification of gelation capsule was conducted using coacervation phase separation technique as described by Atyabi and colleagues with modifications (Atyabi et al., 2004). Briefly, empty gelatin capsules were dispersed in 1.3%$^{w/}_{v}$ ethyl cellulose and 6%$^{v/}_{v}$ glutaraldehyde in ethanol solution at room temperature for 5 minutes. The solution was sonicated for 30 minutes, followed by overnight stirring at room temperature. Hexane was added at 1mL/min for coacervation phase separation. The solution was stirred for 60 min to complete the process of clear gelatin capsule coating. Coated gelatin capsules were then washed with an excess of n-hexane, filtered and dried at room temperature.

5.2.3. Characterization of modified gelatin capsule hardness and resilience

The strength and degree of flexibility of the reservoir (capsule) was analyzed using the Texture analyzer (TA.XT Plus, Stable Micro System Ltd, Surrey, UK). Texture analysis was conducted using a P/2 - 2 mm diameter stainless cylinder probe and 10mm cylindrical delrin probe for testing membrane resilience, deformation energy and membrane. Equation 5.1 shows the procedure used for measuring membrane resilience. Testing dry and wet samples helped in determining mechanical properties changes before and after implantation. Each test was conducted in triplicated. Briefly, the capsule was filled with a drug suspension and sealed with

cyanoacrylate. The sample was then placed on the texture analyzer platform to perform compression tests. The speed was set to 2mm/sec for each test using a load of 1kg.

$$Membrane\ Resilence\ (\%) = \frac{AUC\ (Anchors\ 2-3)}{AUC\ (Anchors\ 1-2)} \times 100 \quad (5.1)$$

Where, AUC represent area under curve

5.2.4. Antigen responsive hydrogel synthesis and characterization

The detection of atherosclerosis biomarkers oxidized LDL (oxLDL) and excess LDL required embedding of anti-LDL SLNs within the viscoelastic hydrogel. Prior to incorporation of anti-LDL SLN (Chapter 3) into the viscoelastic hydrogel (Chapter 4), the avidin coated SLN and LDL particles were thiolated before adding antibodies. Thiolation was conducted by immersing the avidin coated SLN into PBS containing 2mM EDTA at pH 8.0 as per the Pierce Chemical Co. biotinylation protocol (Thermo Fisher Scientific Inc, Massachusetts, USA). A four-fold molar excess of Traut's reagent to protein was added and incubated at room temperature for 2 hours with continuous stirring. The beaker containing the solution was covered with aluminum foil during the incubation period. To remove excess Traut's reagent from the SLN, a desalting column was used. Thiolation was conducted to add the thiol group (R–SH) onto avidin coated SLN surface. This will enable thiolated antibody conjugated SLN to bind to acrylate groups found of polyethylene glycol diacrylate of the viscoelastic hydrogel. N, N, N9, N9-tetramethylethylenediamine (TEMED) and ammonium persulphate (APS) were used to preserve structure of avidin and antibodies in the polymerization process as a substitute for AIBN (thermal initiator) which requires temperature above 40°C heat to initiate polymerization. The method reported by Miyata et al was used for polymerization of anti-LDL SLN-LDL complex on the acrylate groups (Miyata et al., 1999). Briefly, appropriate amounts of PEGDA, MAA, SLN-LDL complex and PEG-200 were added together with 0.01mL of 0.1M aqueous APS and 0.01mL of 0.8M aqueous TEMED as redox initiators. The copolymerization was performed at room temperature for 3 hours to synthesize the interpenetrating network (IPN). After the polymerization, the resultant antigen responsive IPN hydrogels were immersed in phosphate buffer to remove any residual chemicals and unreacted monomers. For determining the responsive behaviour, the antigen responsive hydrogel and the control hydrogel consisting of no SLN-LDL complex were swelled till equilibrium was reached using 0.2M phosphate buffer solution (pH 7.4). The hydrogels were of equal length and weight. To the swollen hydrogels, 100mg/mL LDL particles were added into the swollen hydrogels. The swelling ratios were determined every 30 minutes for 3 hours.

5.2.5. Antigen responsive hydrogel viscoelasticity determination

Rheological analysis was conducted using cone and plate rheometer (Haake Mars, Modular Advanced Rheometer systems, Thermo Fisher Scientific, Massachusetts, USA) fitted with a D=35mm/1° Tan cone. The viscoelastic properties were determined by performing frequency sweep test. When performing a frequency sweep, a cover was used to prevent sample drying and evaporation due to long running duration. A Stress sweep test was conducted in order to determine the stress value to be used in the creep test. This value was taken from the point where the loss of modulus started to decrease. The value indicates the critical stress and a point where the hydrogel strength correlates with its yield point (G' vs. τ). This test was run to determine the deformation energy and flow. The yield stress was also determined to capture the starting point of flow and type of flow of the hydrogel. For all the tests, the temperature was set to 37°C to correlate with the human body temperature.

5.2.6. Porous polymeric tube synthesis

Due to the antigen responsive hydrogel swellability and hydrophilic nature, the hydrogel required a platform to stabilize the antigen responsive hydrogel. Without the stabilizer, the hydrogel will not mold into a tubule capable of withstanding hemodynamic force. This will also prevent the hydrogel from collapsing during drug release and swelling. The inner tube was synthesized from 6%$^{w}/_{v}$ ethyl cellulose, 4%$^{v}/_{v}$ castor oil and 2%$^{w}/_{v}$ methyl cellulose dissolved in ethanol at 50°C for 5 minutes. The methyl cellulose was used to act as a porogen, the castor oil as a plasticizer and the ethyl cellulose for hydrophobic properties. The solution was poured onto a glass plate (100x15mm) and dried in a vacuum oven for 6 hours at 50°C. The dried sheath polymer was then molded into a tubule using 18 gauge spinal needles. The coiled sheath was held together using cyanoacrylate bioadhesive.

5.2.7. Mechanical analysis of polymeric tube

Mechanical properties of the dried sheath polymer were evaluated in order to assess the ability of the tube to be formed to withstand mechanical changes *in vivo*. The tubule will be inserted into the jugular vein in order to deliver fenofibrate intravenously. Four mechanical properties; tensile strength, percentage elongation at break, elastic modulus and work of failure, were computed from the load-strain profile and film dimension using the equations below (5.2-5.5). This test will provide estimation long life durability and structural integrity. The strips were cut into equal length and width 35x20mm. They were then attached onto the cardboard sample holders using a double sided tape. A small amount of glue (cyanoacrylate) was also applied to

firmly attach the strips to the sample holders. Each sample was assessed in triplicated. The tests were done using a nanotensile tester (nanoTensile 500, Hysitron, Minnesota, USA) as described by Boppa (2009). A 100N load cell was used. A samples prepared as described earlier were aligned and mounted in the upper clamp, the gauge length adjusted to 15mm, and then the other end of the sample was mounted in the lower clamp. The edges of the frame were cut with a pair of sharp scissors. The load was set to zero and the weight of the sample was measured. Then the machine was started and the sample stretched at the rate of 15mm/min until the sample ruptured. The load-elongation data was stored digitally. After the stress versus strain curve was generated. A line tangent to the stress-strain curve and parallel to the line joining origin and peak point was drawn to estimate ultimate strength, toughness, elasticity and deformation.

$$\tau = Lmax/A_i \quad (5.2)$$

$$\varepsilon = \Delta l_i/A_i \quad (5.3)$$

$$EM = dL/dm\ /A_i \quad (5.4)$$

$$\omega = AUC \times \delta/A_i \quad (5.5)$$

Where; τ is the tensile strength, $Lmax$ the maximum load, A_i the initial cross-sectional area of the sample, ε the percent elongation at break, Δl_b theincrease in length at break point, l_i the initial gauge length, EM the elastic modulus,dL/dm the slope of the linear potion of the elastic deformation, ω the work of failure, AUC the area under the curve and δ the cross-head speed.

5.2.8. Osmotic pump fabrication

The osmotic pump was designed to be able to fit into the modified gelatin capsule and to prevent backward flow of drug suspension against intravenous force. The osmotic pump consisted of two layers. The top layer was ethyl cellulose which would make a hydrophobic layer preventing the drug from leeching into the implantation site. Leeching of the drug could lead to rhabdomyolysis. The second layer was made of mannitol which will act as an osmotic agent. Mannitol was mixed with polyethylene oxide (PEO) which will generate the osmotic pressure to push the drug suspension into the blood stream. The pump was designed following Ning et al method with modification (Ning et al., 2011). A Carver standard bench top laboratory

press was used for formation of the hydrophobic disc (ethyl cellulose) and osmotic pump (mannitol: PEO) at 2 tons of force (Model 3851, Carver, Inc., Indiana, USA). Ethyl cellulose, polyethylene oxide and mannitol were added into a 5/16C pellet die. The PEO and mannitol mixture was added first before adding ethyl cellulose to form a hydrophobic layer. The weight and hardness of the pumps were kept within similar ranges of 100±1.2mg and 100N (TA.XT Plus, Stable Micro System Ltd, Surrey, UK), respectively.

5.2.9. Implant fabrication and characterization

Two different drug delivery devices were designed using a catheter for infusion of anti-LDL SLNs into the blood stream. The second device consisted of an antigen responsive hydrogel coated polymeric tube for antigen responsive system. An 18Ga. x 2-1/2" (6.35cm) radiopaque catheter was removed from a 20Ga. RW introducer needle to form the catheter infusing drug delivery system. The syringe docking port was removed to allow easy catheter attached onto the hollowed gelatin capsule. The gap between the capsule and the catheter was sealed using cyanoacrylate. The other side of the capsule was filled with the osmotic pump with the hydrophobic disc facing the catheter end. The osmotic agent side was placed in such a way that it faced opposite the tube to allow the hydrophobic layer (ethyl cellulose) to prevent drug leaching towards the osmotic pump region. For the antigen responsive polymeric tube, the tube was also inserted in a similar manner as the catheter. This was followed by coating the polymeric tube with the antigen responsive hydrogel as indicated in Figure 5.1. Briefly, the antigen responsive hydrogel was allowed to polymerize on the surface of the polymeric tube as discussed in 5.2.4. This resulted in a coat of 0.2mm thickness. Each coated polymeric tube was allowed to dry in a sterile fume hood for 4 hours prior further use.

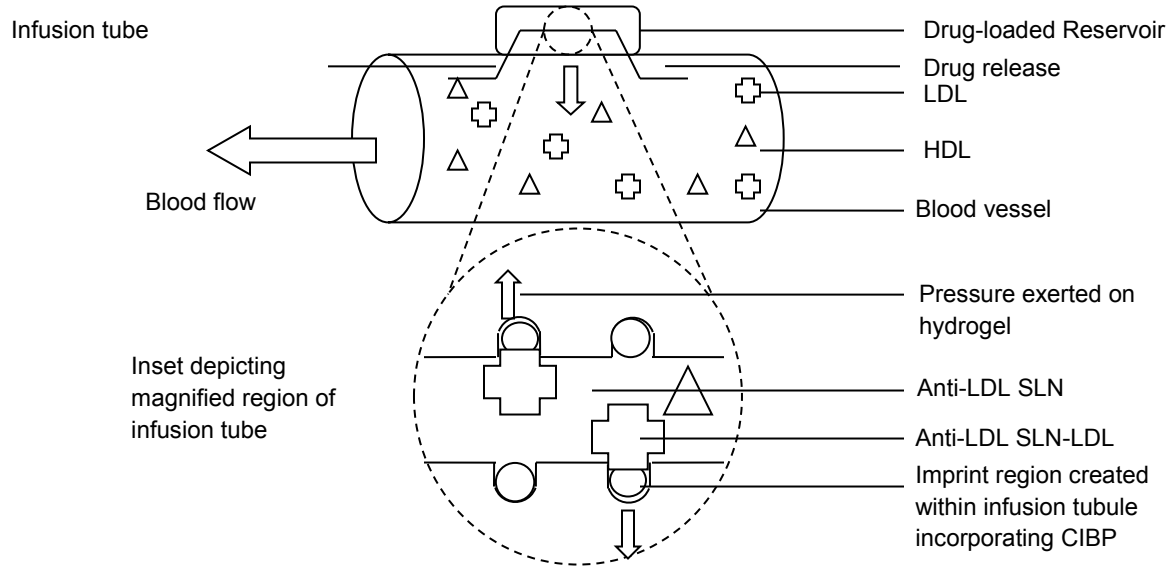

Figure 5.1: A lateral view (with magnification) of the intravascular implantable sensor and drug delivery device.

5.2.10. Implant Optimization using Design of Experiments

Design of experiments was conducted to determine the optimum formulation for antigen responsive polymeric tube. Minitab version 16 was used using Box-Behnken design method (Minitab Inc, Pennsylvania, USA). Briefly, varying concentration of anti-LDL SLN ranging from lower limit of 20mg/mL and upper limit of 35mg/mL was embedded into the viscoelastic hydrogel. The polymeric tube also consisted of constant varying concentration of methyl cellulose ranging from lower limit of 0.1g to upper limit of 1.0g. The ethyl cellulose (3g) and castor oil (3mL) were kept constant. The polymeric tube limits were in relation to porosity analysis and mechanical properties tests. The surface area relates to the size of the final antigen responsive polymeric tube that was exposed to LDL particles in the blood stream. Surface area affected the level of LDL that interacted with anti-LDL antibodies which in turn affected level of porous change. The low limit was found to be 485mm^2 relating to a tube of 30X2mm length, whilst the upper limit was determine to 824mm^2 relating to a tube approximately 50X2mm in length. The various formulations are illustrated in Table 5.1. Each formulation was tested for change in pore size and amount of drug release in triplicate.

Table 5.1: Design of Experiments for antigen responsive polymeric tube.

Formulation	Surface Area (mm^2)	Anti-LDL SLN (mg/mL)	Methyl Cellulose (mg)
F1	654.5	20.0	1
F2	824.0	27.5	0.5
F3	824.0	20.0	0.5
F4	485.0	35.0	0.1
F5	485.0	27.5	1
F6	824.0	35.0	0.1
F7	654.5	35.0	0.1
F8	654.5	27.5	0.5
F9	485.0	27.5	0.5
F10	654.5	27.5	1
F11	654.5	35.0	0.5
F12	654.5	27.5	0.1
F13	485.0	20.0	0.5
F14	654.5	20.0	0.5
F15	824.0	27.5	1

5.2.11. Porosity analysis on Design of Experiments formulations

Porosity studies were conducted to assess the pore structure of polymeric tube and modified gelatin capsules. The presence of pores on the polymeric tube will allow determining the diffusion rate, whilst the pore on the capsule will make the capsule semipermeable. Prior to porosity analysis the polymeric tube and modified gelatin capsules were immersed in PBS pH 7.4 for 48 hours to open up the pores. They were then dried overnight at 40°C in a vacuum oven. The pore sizes of hydrated and prior hydration samples were compared. Samples were cut into small strips of size range of 0.001g to 500g, which were then degassed for 16 hours at 40°C for analysis. This was then followed by analysis in nitrogen gas and liquid nitrogen for 6 hours. The isothermal log plot was used to characterize pore distribution uniformity (ASAP 2020, Micrometrics, Georgia, USA).

5.2.12. *In vitro* dissolution tests on Design of Experiments formulations

Dissolution tests were performed by using the flow through dissolution method (USP Apparatus 4, Erweka, Heusenstamm, Germany). The equipment was fitted with 22.6mm cells (internal diameter) at 37 ± 0.1°C. A ruby ball (Ø 5mm) and 1g of glass beads (Ø 1mm) were placed at the bottom of the cone to ensure laminar flow of the jet of fluid entering the cell. Phosphate buffer (250mL) at pH 7.4 was used and purged at a flow rate of 35mL/min. The drug reservoir was also assessed to remove all possibilities of drug leaching which when the system was to be used *in vivo* would lead to drug toxicity. The uncoated polymeric tube was also loaded with a drug and this was used to determine drug diffusion gradient. The polymeric tube was later

coated with a sensing layer. Different concentrations of anti-LDL SLN per mm^3 area of polymeric tube were used. The dissolution media was spiked with different concentrations of low density lipoprotein (lipoprotein). The drug delivery was assessed based on drug release models described in Table 5.2. For catheter infusion of anti-LDL SLN, the release was investigated by putting the pumps with the orifice in sideward position into a 100mL glass vial, filled with 15mL of PBS buffer (pH 7.4) consisting of 2%$^{v}/_{v}$ Tween® 80. All tests were conducted at a period of 25 days.

Table 5.2: Mathematical models to be used to describe drug dissolution curves.

Kinetics	Equation
Zero-order	$\mathrm{Q_t} = \mathrm{Q_0} + \mathrm{K_0 t}$
First-order	$\ln Q_t = \ln Q_0 + K_1 t$
Hixson-Crowell	$Q_0^{1/3} - Q_t^{1/3} = K_s t$
Higuchi	$Q_t = K_H \sqrt{t}$
Korsmeyer-Peppas	$Q_t / Q_\infty = K_k t^n$

Q_t is the amount of drug dissolved in time t, Q_0 is the initial amount of drug in the solution, Q_∞ is the drug released at an infinite time, K_0 is the zero-order kinetics, K_1 is the first-order kinetics, K_s is the constant incorporating the surface-volume relation, K_H is the Higuchi dissolution constant, and K_t is the Korsmeyer-Peppas dissolution constant and n is the drug release mechanism.

5.2.13. Swellability studies and hydrolysis degradation studies

Swelling kinetics and dynamics were analyzed by immersing optimized coated polymeric tube, antigen responsive hydrogel and modified capsules in PBS pH 7.4. This will allow determining rate of hydrolytic degradation and diffusion kinetics. The dispersed samples were then incubated in an orbital shaker at 37°C until swelling remained constant. Each sample was tested in triplicate. The weight of hydrogels was measured every 30 minutes after blotting them on filtering paper. Swelling rate was calculated using Equation 5.6.

$$SR = \frac{W_t - W_0}{W_0} \tag{5.6}$$

Where; SR, W_t and W_0 are the swelling weight ratio, weight of swollen hydrogel at time t and weight of the hydrogel before swelling, respectively. To determine kinetics of the swelling process, the equation below can determine the rate law where the swelling exponent *n* provides insights into the water sorption mechanism that is in operation. The analysis of the diffusion mechanism in all networks is described by the following Equation 5.7.

$$SR = Kt^n \quad (5.7)$$

Where *K* is the swelling ratio front factor and *n* represents the swelling exponent. A straight line was obtained by plotting ln (SR) versus ln (t) for the initial 60% of swelling. The gradient of this line gave n value while the intersection was ln (K)**.** Equilibrium water was calculated from Equation 5.8.

$$EWC\ (\%) = \frac{W_\infty - W_0}{W_\infty} \times 100 \quad (5.8)$$

Where; W_∞ was the weight of the water that diffused into the gel at equilibrium state and W_0 was the weight of initially dried hydrogel.

5.2.14. Evaluation of implant components thermal stability under various heating rates

The thermogravimetric analysis (TGA) of Perkin-Elmer was carried out to evaluate the stabilities of the samples as the function of temperature in nitrogen atmosphere under a flow of 30mL/min. TGA was used in combination with Evolved gas analysis (EGA) after pyrolysis was carried out using a TGA 4000 thermogravimetric analyzer (PerkinElmer Inc., Massachusetts, USA) combined with infrared spectrometry (TG-IR) through the TL 8000 transfer line. The Pyris 6 software was used to perform the thermal analysis and to trigger the IR software. The heating was conducted from 30°C to 600°C at a heating rate of 10°C/min, 8°C/min and 6°C/min. TimeBase software was used for IR data interpretation for designing Gram-Schmidt plot. The formulation which showed stability was evaluated by gridding the hydrogel, capsule and polymeric tube into fine powder. The thermogravimetric test was conducted in triplicate. Each test consisted of a powder weighing approximately 20mg.

5.2.15. Kinetics and lifetime prediction of implant components

Thermal degradation kinetics and lifetime prediction were determined using Thermogravimetric Analysis (TGA) (PerkinElmer Inc., Massachusetts, USA). TGA provides a method for accelerating the lifetime testing of polymers so that short-term experiments can be used to predict in-use lifetime. From the resultant thermal curves, the temperatures for constant decomposition level were determined. The kinetic activation energy was then determined from a plot of the logarithm of the heating rate versus the reciprocal of the temperature. This activation energy was then used to calculate the estimated lifetime at a given temperature. A sample with

mass of 10 mg was inserted into ceramic crucible and the temperature was increased from 30° to 600°C under both air and nitrogen flowing at (30mL/min) using three heating rates of; 6, 8 and 10°C/min. The conversion rate of reaction was determined as the ratio of actual mass loss to the total mass loss corresponding to the degradation process using Model Free kinetics software (Equation 5.9).

$$\alpha = \frac{M_0 - M}{M_0 - M_f} \tag{5.9}$$

Where; M, M_0 and M_f were the actual, initial and final masses of the sample, respectively. The rate of degradation, (dα/dt), can be expressed as functions of temperature and mass of the sample. Using the selected value of conversion, the temperature (in kelvin) at that conversion level was measured for each thermal curve. A plot of the logarithm of the heating rate versus the corresponding reciprocal temperature at constant conversion was prepared. The plotted data produced a straight line. The next step in the process was the calculation of activation energy (E) from the slope using the method of Flynn and Wall equation (Equation 5.10).

$$E = \frac{-R}{b}\left[\frac{d\log\beta}{d(1/T)}\right] \tag{5.10}$$

Where E was the activation energy (J/mol), R is the gas constant (8.134 J/molK), T was the temperature at constant conversion (K), β was the heating rate (°C/min) and b was the constant (0.457). The value of the derivative term (d log β)/ [d (1/T)] was represented by the slope of the line. To calculate the estimated time to failure (Equation 5.11 & 5.12), the value for the temperature at the constant conversion point was first selected for a slow heating rate (β). This value, along with the activation energy (E) was used to calculate E/RT. This value was then used to select a value for log $P(X_f)$ from the numerical integration table given in Appendix 1. This value was calculated by taking the antilogarithm.

$$\ln t_f = \frac{E}{RT_f} + \ln\left[\frac{E}{\beta R}.P(X_f)\right] \tag{5.11}$$

$$T_f = \frac{E/R}{\ln T_f - \ln\left[\frac{E}{\beta R}.P(X_f)\right]} \tag{5.12}$$

t_f is the Estimated time of failure (min), E is the activation energy (J/mol), T_f is the failure temperature (K), R is the gas constant (8.134 J/molK), P(X_f) is the function whose values depend on E at the failure temperature and β is the heating rate (°C/min). The estimated lifetime t_f of a polymer to failure was determined using the time when the mass loss reached 5wt%, i.e. α = 0.05.

5.2.16. Thermodynamic evaluation of implant components

DSC was used to characterize thermal stability of the capsule and polymeric tube. Dried samples were analyzed using a Differential Scanning Calorimeter (Mettler Toledo, Ohio, USA) to check their thermal and thermodynamic properties. Mettler STARe software system, version 9.x, was used for data acquisition and indium was used to calibrate the instrument. The polymers were mildly pulverized into powder prior to loading into aluminum pans using little pressure as high pressure during grinding could lead to destruction of crystal lattice. The samples (10 mg) were then transferred into 40μL DSC standard aluminum pans, which were then sealed. The samples were analyzed by conventional method involving heating over the temperature range from 0 to 500 °C at a rate of 10 °C/min under an 8kPa nitrogen atmosphere. Each experiment was repeated twice where the first run was performed to remove thermal history.

5.2.17. Structural transformations analysis of implant components

Attenuated Total Reflectance-FTIR (ATR-FTIR) analysis of native polymeric tube and its components, castor oil, ethyl cellulose and methyl cellulose and the fabricated capsule components were undertaken to evaluate, ascertain and compare the structural transformations. ATR-FTIR spectra were recorded on a Perkin Elmer Spectrum 2000 FTIR spectrometer with a MIRTGS detector (PerkinElmer Spectrum 100, Wales, UK), using an ATR-FTIR cell and a diamond crystal internal reflection element. Samples were analyzed at a wavenumber range of 650-4000cm^{-1} with a resolution of 4cm^{-1} and 100 scans per spectrum.

5.2.18. Implant *Ex vivo* experimentation for evaluation of intravascular stability

Ex vivo studies were conducted using a peristaltic pump (Minipuls 3, Gilson, Lasec, Cape Town, SA) indicated in Figure 5.2(a). This was used to determine drug release from the antigen coated polymeric tube and to assess the adhesion of cells of the surface of the tubule, which may impair porosity. The flow rate was set to 22mL/min prior to introduction of blood. Total cholesterol; HDL and LDL were analyzed using EnzyChrom AF HDL and LDL/VLDL assay kits

(E2HL-100, Abcam®, Cambridge, UK). Colorimetric procedure was used by firstly centrifuging a mixture of 20µL serum and 20µL precipitation reagent at 9,500g for 5 minutes. 24µL of the supernatant were then mixed with 96µL of assay buffer. This was used for HDL analysis. The pellet was mixed with 40µL PBS (pH 7.4) and 24µL of the pellet mix was mixed with 20µL assay buffer to be used for analysis of LDL/VLDL. Serum (12µL) was also mixed with 108µL assay buffer and used to calculate total cholesterol. The optical density (OD) values were measured at 570nm using the Victor X3 Luminometer (PerkinElmer Inc., Massachusetts, USA). The optimized antigen coated polymeric tube implant was inserted in a tube as depicted in Figure 5.3(b). Drug release was analyzed using ultra-performance liquid chromatography (UPLC).

A flask containing sheep blood was immersed in liquid paraffin and maintained at 37±0.5°C for the entire duration of the study (Figure 5.2 (c)). All blood samples were immediately transferred into heparinized vacutainers (BD Vacutainers®, Franklin Lakes, NJ, USA) and stored at (4°C). Blood (5mL) was removed for analysis every 10 minutes for 1 hour, whilst 5mL drug free blood was injected to maintain dissolution sink conditions. Nicotinic acid (50µL, 1mg/mL) was added into the drawn out blood to serve as a standard during UPLC analysis. The experiment was conducted for 1 hour, thus to avoid a situation where the anticoagulant becomes deactivated which normally would occur after an hour. The samples were thereafter centrifuged at 2000g for 20 minutes yielding a clear plasma supernatant, which was pipetted with an adjustable calibrated micropipette (Boeco GmbH, Hamburg, Germany). All clear plasma samples were stored at -70°C until further analysis.

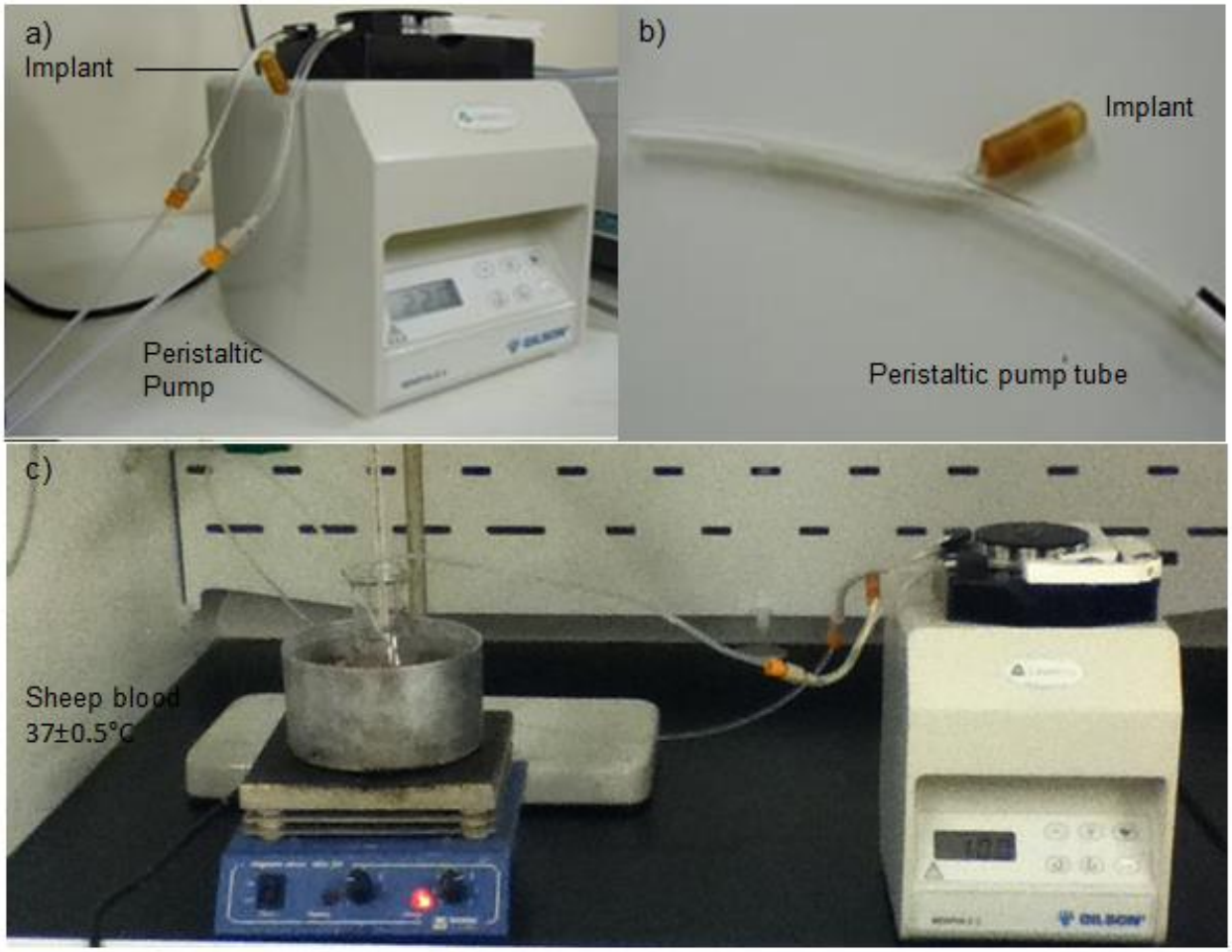

Figure 5.2: *Ex vivo* studies setup using peristaltic pump (a) *Ex vivo* step on the peristaltic apparatus, (b) Insertion of the implant into a peristaltic tube, (c) sheep's blood maintained at 37±0.5°C.

5.2.19. Quantitative determination of fenofibrate in plasma from *ex vivo* studies

Analysis was performed on Waters Acquity UPLC^{TM} system (Waters Corporation, Massachusetts, USA) consisting of a binary solvent manager, a sample manager and a photodiode array (PDA) detector. The mobile phase used was a mixture of methanol and 20mM ammonium acetate in the ratio of 70:30($\%^{v}/_{v}$) employing gradient elution. The detector was set at a sampling rate of 20 points s^{-1} and filter time constant of 0.2 seconds. System control, data collection and data processing were accomplished using Waters Empower 2 chromatography data software. The analytical column used was Waters Acquity UPLC BEH C-18 column, 1.7µm, 2.1x100mm (Waters Corporation, Massachusetts, USA). The optimized conditions were as follows: injection volume: 5.0µL, flow rate: 0.6mL/min at a column temperature of 25°C, sample temperature of 37°C and detection wavelength: 254nm at 1.2nm. A plasma sample (500µL) was mixed with 3mL ethyl acetate for extraction of the drug. This mixture was

centrifuged and the supernatant separated and dried using nitrogen. The dried drug was then suspended in 250µL of methanol and injected into ANSI-2mL UPLC vials from which 5µL sample of the suspended drug was injected into the C18 column using a gradient method that involved elution of methanol and ammonium acetate buffer (pH 4.7; 0.01M) at flow rate of 0.6mL/min. Table 5.3 shows the parameters used during the UPLC drug detection and quantification.

Table 5.3: UPLC instrumental settings for the determination of Fenofibrate in plasma samples.

Parameters	Values/Conditions
Strong wash	90% ($^{v}/_{v}$) acetonitrile : 10% ($^{v}/_{v}$) water
Weak wash	10%($^{v}/_{v}$) water : 90%($^{v}/_{v}$) acetonitrile
Mobile phase	20mM ammonium acetate
Column specification	BEC C18 1.7µM, 2.1x50mm
Injected volume	5µL
Run time	10 minutes
Column temperature	25°C
Sample temperature	37°C
Wavelength of absorption	254nm

5.3. Results and Discussion

5.3.1. Implant design and characterization

The drug reservoir was 22.75mm in length with a width of 8.00mm and a circumference of 25.50mm. This reservoir had a surface area of 1.37mm^2 and a volume of 0.0037mm^3 that carried the drug in its semisolid form. The implant was designed so that the drug would be pushed into the 7cm long and 2mm (6 French) wide infusion tube consisting of hydrophobic inner layer to prevent tube collapse and a hydrophilic layer imprinted with anti-LDL SLN (Figure 5.3(a & b)). Interaction of anti-LDL SLN with LDL particles will induce shear stress on the tubule which facilitated drug diffusion into the blood stream. The tubule was flexible, had a high tensile strength of over 2MPa, had a low friction coefficient because of the hydrophilic sensing layer, was stable for implantation and could resist biofilm deposition. *Ex vivo* studies indicated no biofilm formation due to PEGDA effects. This was based on observation of no impairment of drug release rate. Pumps are normally filled with a solution of the drug of interest and implanted subcutaneously in the animal. Following an equilibration time, this was estimated to be 30 minutes for the hydration of the polymeric tube. The drug was delivered at a constant rate to the site of interest driven by the osmotic pressure generated inside the pump (Cooper et al., 2007). Figure 5.3 (c) indicates the alternative drug delivery system designed using an 18Ga. catheter. This will be used for infusion of anti-LDL SLN, which will interact with increasing LDL

concentration. The SLN-LDL complex will then be cleared from the blood stream during nanoparticle phagocytosis. The complex will then be degraded in their liver, which will lead to burst drug release.

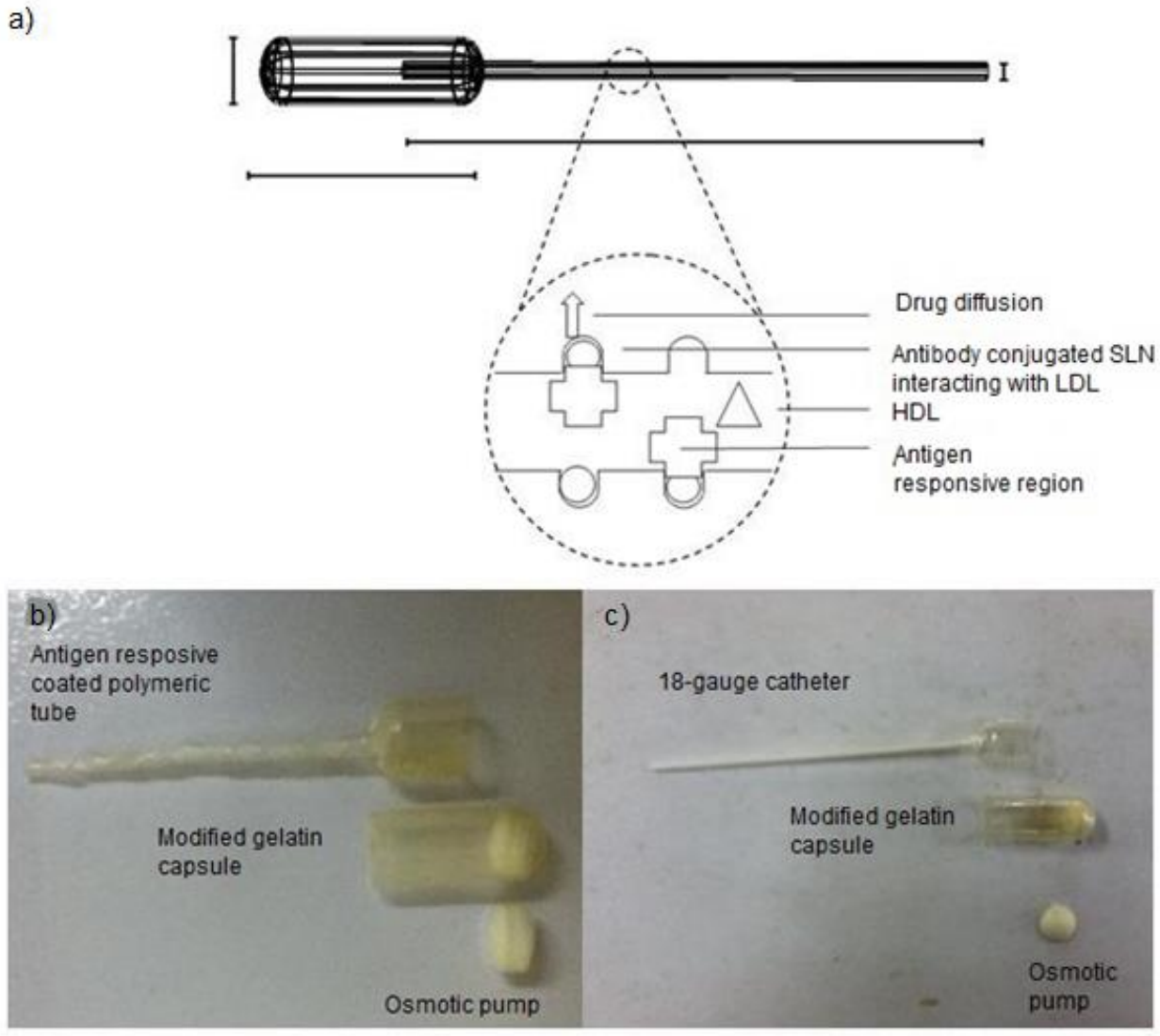

Figure 5.3: Schematic of the IVISDDD. (a) Indicates the layout of coating of the porous polymeric tube with the antigen responsive IPN (b) indicates formation of the IVISDDD using osmotic pump, modified gelatin capsule and coated polymeric tube and (c) indicates the assembled IVISDDD using an 18Ga. catheter for infusion of anti-LDL SLN.

5.3.2. Determination of antigen responsiveness

Antigen responsiveness of the antigen responsive IPN was assessed to quantify the change in swelling ratio in response to presence of LDL particles. Figure 5.4 indicates the swelling ratios of the antigen responsive IPN (Antibody (+)) and the antibody-antigen free control viscoelastic

hydrogel (Antibody (-)). The swelling ratio of the hydrogels was determined by the ratio of their changing diameters. This indicated that the swelling ratio of antigen responsive IPN increased abruptly following the addition of free LDL particles. This furthermore indicated that the swelling ratio of antigen responsive IPN was dependent on LDL concentration as the control remained constant. The change in the antigen responsive IPN was induced by the change in crosslinking density between the conjugated anti-LDL SLN-LDL. Competitive binding of the free LDL particles was shown to trigger a change in gel volume owing to breaking of non-covalent crosslinks. The conjugated LDL particles then dissociated the unconjugated antibody bound LDL to reverse the gel into is initial conformation. This action indicated a reversible swelling mechanism, which is ideal for increasing dosage of therapeutic in response to antigen concentration. In addition, this demonstrated that the IPN displayed shape-memory behavior, and that stepwise changes in antigen concentration can induce pulsatile permeation of a therapeutics through the network (Miyata et al., 1999).

On the forefront of imprinting gel systems, are intelligent and stimuli-sensitive imprinted hydrogels that can transform their swelling behavior and in turn modulate their analyte binding abilities (Byrne et al., 2002). In molecular imprinted hydrogels, the analytes are polymerized with the polymers, and later removed. This could not be done with the current study, as LDL particles are not of similar size. In molecular imprinted polymers, size and orientation play a role in the sensing of analytes. Interpenetrating hydrogels are required for sensing of molecules with varying structures. Unlike IPN, molecular imprinted hydrogels have an increased functionality lifespan. The use of macromolecules limits sensing duration as the half-life of the macromolecules affects the sensing process. However, IPN hydrogels have an increase sensing activity compared to molecular imprint hydrogels. Therefore, to improve IPN activity, modified macromolecules with increased half-life are required. This study shows that the IPN can be used for coating the polymeric tube in order to fabricate an intravenous drug delivery device capable of detecting antigen and releasing drugs in response to level of antigen. *Ex vivo* studies and *in vitro* studies were conducted to assess the implant drug release.

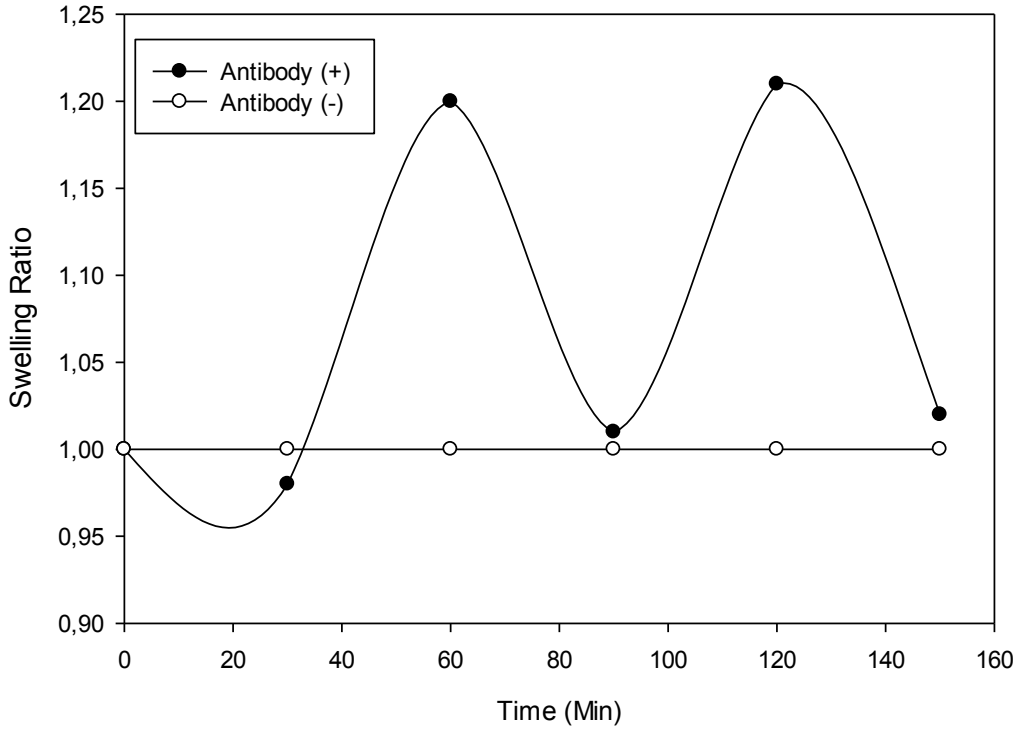

Figure 5.4: Scatter plot showing the effects of the free antigen concentration on the hydrogel swelling ratio.

5.3.3. Determination of the Infusion rate from the osmotically driven implant

Drug release rate from osmotically driven devices is normally directly proportional to the drug solubility. The drug release rate from the osmotically driven implant was directly proportional to the osmotic pressure and was defined by the Equation 5.13.

$$\frac{dv}{dt} = \frac{A}{h} L_p \sigma \pi C \qquad (5.13)$$

Where dv/dt was the rate of water influx into the device, A was the surface area of the membrane, L_p was the diameter of the orifice, σ was a reflection coefficient and C was the concentration of the released drug. The reservoir showed low level porosity, when hydrated making an ideal storage compartment for viscous liquid suspensions. Lipophilic drugs such as fenofibrate have a low aqueous solubility of 92µg/mL in water (Jamzad and Fassihi, 2006). Since the drug aqueous solubility is low its plasma, solubility was also low hence the inherent osmotic pressure within the device was low. The addition of mannitol improved the osmotic pressure thus enhancing the rate of drug release (Patra et al., 2013). Polyethylene oxide (PEO)

was used because of its high hydrodynamic pressure (Nyström et al., 1991). The ethyl cellulose layer acted as a hydrophobic barrier that prevented the drug from interacting with the pump system. Mannitol was been used, as it is a known osmotic agent that causes osmotic pressure approximately equal to 38atm pressure (Khan et al., 2012). This low pressure indicates that the drug release will be slow in relation to substance such as sodium chloride and lactose which have 150atm and 356 at pressure, respectively (Emara et al., 2012). Figure 5.5 shows the swelling of the osmotic pump and the stability of the hydrophobic layer (methyl cellulose) during swelling. The insert shows the swelling pump with the hydrophobic methyl cellulose layer remaining intact during swelling. Infusion varied in different formulation based due to the antigen responsive IPN as discussed in porosity analysis. This was due to the drug delivery device being a multi-compartment where the hydrophobic layer had its own diffusion gradient different from the IPN diffusion gradient.

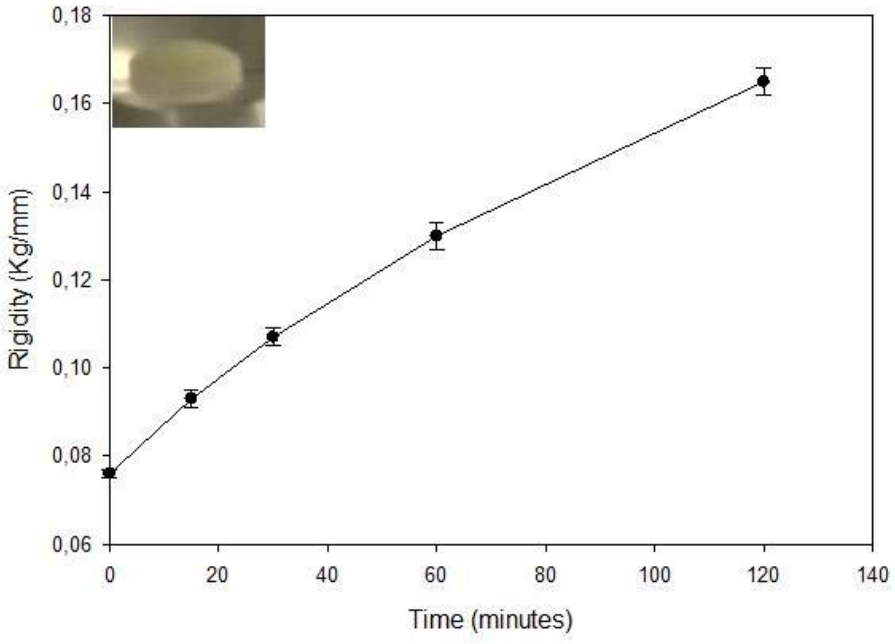

Figure 5.5: Graphical depiction of the increasing rigidity of the osmotic pump with swelling (photographic image of osmotic pump as inset at 60 minutes).

The use of the osmotically driven drug delivery device enables delivery of therapeutic agents at a controlled rate. Pump used on the catheter infusion of anti-LDL SLN, indicated to have a constant infusion of 120mg/day, which is equivalent to 108mg of fenofibrate eluded from anti-

LDL per day. The release from polymeric tube varied between 4.9-98mg/day due to the double layer diffusion system. Initially it was determined that it took 30 minutes to hydrate and solubilize the contents of the core before generating sufficient osmotic pressure to start drug release from the capsule when it was evaluated separately from the catheter and tube. The orifice of the catheter (0.8mm) and polymeric tube (1.6mm) varied causing different infusion rates. For intravenous application, the osmotic pressure was required to prevent backflow of blood which may cause orifice blockage due to blood clotting. The hydrodynamic pressure produced by the pump ensured that the drug was released at a controlled rate and allowed the removal of biofilm deposition on the orifice surface. The hydrodynamic pressure caused by the swelling of PEO will counteract resistance and prevent backflow of the drug solution into the drug delivery system thus ensuring efficient and controlled drug release. As the swelling increased, an increase in resilience was observed.

5.3.4. Optimized formulation responses

5.3.4.1. Influence of pore size changes on drug release

Porosity analyzer and dissolution apparatus (USP 4) were used for analyzing pore size and drug release, respectively. The amount of drug released correlated with the size of the pores and the anti-LDL SLN distribution as an increase in pores size was proportional to increase in release rate. Design of Experiments generated 15 formulations (Table 5.4). The ratio of ethyl cellulose (EC) to methyl cellulose (MC) affected the porosity of the polymeric tube, whilst the amount of the anti-LDL SLN used determined the amount of drug released in relation to circulating LDL particles. High porosity caused an increase in drug release as seen by F2, F9 and F10 which had high porogen methyl cellulose concentration and surface area. This differs to F1 which had lower limit anti-LDL SLN indicating that the responsive layer also controlled level of diffusion which correlates to the previous chapter (Chapter 4, $n<0.125$). The low porogen formulations: F5, F7 and F15 had lower drug release. In relation to polymeric tube size and anti-LDL SLN, the nanoparticle concentration indicates to be proportional to amount of drug release.

F14, however had high drug release albeit the low SLN concentration and the low porogen concentration. The high release and high porosity could be have been induced by level of pore distribution and possibly erosion of the antigen responsive hydrogel from the polymeric tube. However, in some formulations with low anti-LDL SLN concentrations drug release was low even though porosity was high i.e. F6 and F13 indicating an intact antigen responsive hydrogel.

Furthermore, the surface area of the tube exposed to LDL particles also played a role in F4, whereas in F3 the anti-LDL SLN dictated rate of release. The polymeric tube was designed such that it would prevent the collapse of the sensing layer. This indicated that main drug release-controlling factor was the anti-LDL SLN concentration in the sensing layer and the pore change in the antigen responsive hydrogel. The amount of porogen acted as the limiting factor by controlling diffusion into the antigen responsive layer. This correlation is depicted in Figure 5.6. It was evident that when porosity increased, drug release increased. F8 showed that porosity was directly proportional to drug release as the release and pore size curve intersect. Circulation of free LDL caused changes in the pore structure of the implant resulting in responsive drug release integration with the constant drug release through diffusion and that modulated by the osmotic pump. This indicates that the drug delivery was functional.

Table 5.4: Design of Experiments response, in vitro drug release correlation to change in porosity.

Formulation	Drug release (mg/day)	Porosity (A)
F1	17.9±2.1	39.0647±4.6
F2	89.0±4.6	126.529±11.2
F3	20.4±4.2	45.591±9.2
F4	5.76±1.2	36.463±6.3
F5	10.88±1.3	39.0647±2.3
F6	16.1±1.3	46.761±5.6
F7	11.2±2.2	47.627±3.4
F8	38.5±3.5	36.057±7.2
F9	98.0±2.4	126.529±4.6
F10	92.0±2.0	72.483±6.7
F11	9.8±0.9	47.627±5.6
F12	9.8±1.1	47.627±3.5
F13	11.5±2.1	65.284±13.3
F14	87.0±6.2	72.483±12.3
F15	4.9±0.8	45.591±2.4

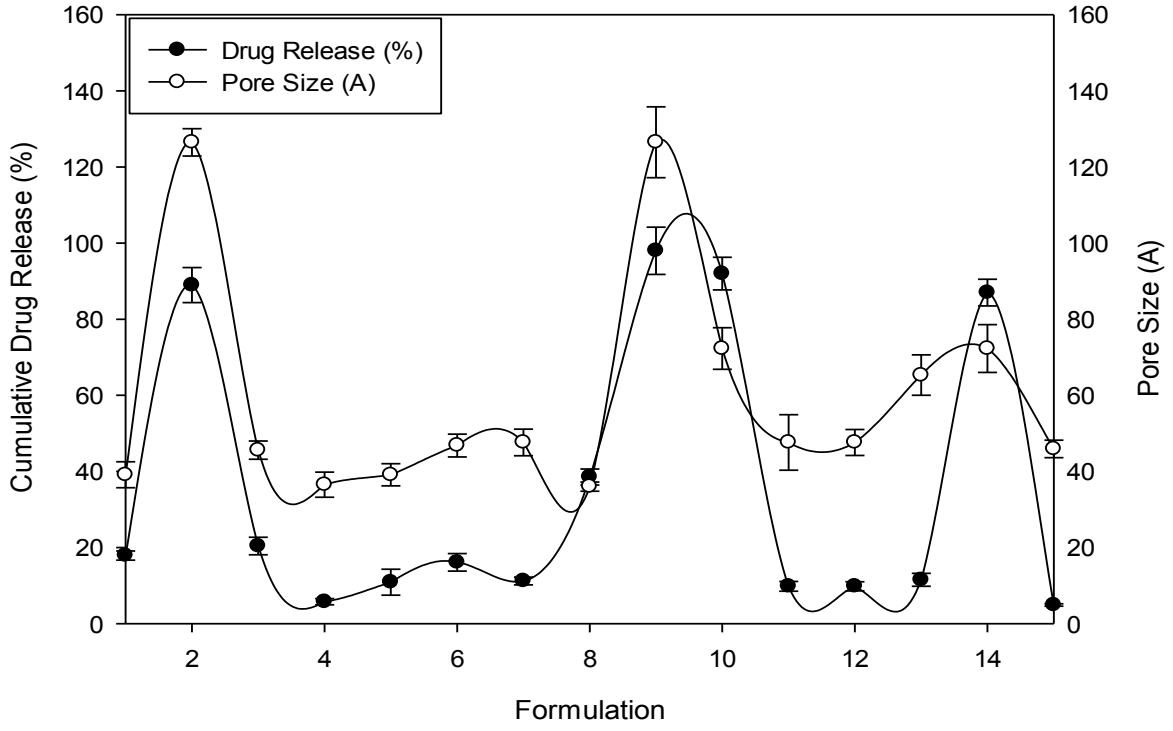

Figure 5.6: Correlation of cumulative drug release to pore size of the IVISDDD.

5.3.4.2. Optimized drug delivery system characterization

The final optimized formulation was generated to have a surface area of 485.37mm^2 and a concentration of 20mg of anti-LDL SLN as indicated in Figure 5.7. The polymeric tube methyl cellulose concentration was established to be 0.48g for making pores. The ethyl cellulose and castor oil will remain constant. The concentration of the viscoelastic hydrogel also remained constant as the anti-LDL SLN concentration will dictate the amount of porous changes during interaction with free LDL particles. Prior to implantation, mechanical properties of the implant are required. For insertion into the vein, the tube has to flexible so that it does not damage arterial wall.

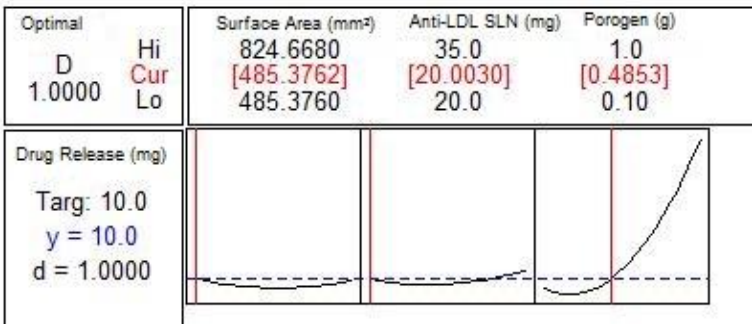

Figure 5.7: Optimized antigen responsive drug delivery system.

5.3.5. Polymeric tube mechanical strength analysis

Nanotensile machine was used to characterize the mechanical strength of the polymeric tube. The Young's modulus of rubber materials has been shown to fall under the range of 0.01-0.1GPa. The Young's modulus is a measure of the stiffness of the elastic material. The modulus of 25.2MPa indicated that the structure would become rigid structure when hydrated. The modulus is smaller than the expected 75 to 300MPa for commercial catheters (Shoa et al., 2008). This means that the polymeric tube will not be able to be flexible enough not to damage the arterial wall. However the modulus indicates a bending radius of 10mm and also indicates the tube will not face buckling during insertion and yet enabling passage through highly curve regions. This will be due to hydrophobic chains of ethyl cellulose aligning thus preventing flexibility. Table 5.5 shows the estimated values of the polymeric tube mechanical strength. Mechanical toughness was found to be low due to the reduction in crystallinity of the polymer caused by the porogen (methyl cellulose) which made the polymeric tube brittle. From the measured Young's modulus value, it can be hypothesized that the polymeric tube would be able to withstand hemodynamic and motion torsions (Maximum of 100 dynes/cm^2). The yield and ultimate strength indicate the force strain required to break the tube.

The implant may be able to tolerate hemodynamic force but not mechanical force during movement. However, the level of toughness indicated not to be sufficient to withstand constraint from neck muscles during *in vivo* studies. This level of toughness, 0.11 J/cm^3 indicates that under high constraint, the tubule brittle state will make it break. An increase in methyl cellulose indicated to affect the toughness of the polymeric tube to high distribution of pores that affected the structural integrity of the tubule. However, the plasticizer castor oil played a role in improving the elasticity of the tube. The 1.55MPa ultimate strength indicates that during stretching of the tubule, the tubule will break even fewer than 8% of strain. This is due to high distribution of pores. Due to these mechanical drawbacks, the catheter infusion of anti-LDL SLN is the more

viable option. This alternative method (antibody conjugated SLN catheter infusion) retains the novelty of the device.

Table 5.5: Nanotensile tests to determine mechanical strength of polymeric tube strands.

Measurements	Polymeric Tube
Young Modulus	25.2MPa
Yield Stress	1.21
Ultimate Strength	1.55MPa
Strain	0.08
Toughness	0.11J/cm^3

5.3.6. Thermal degradation measurements of polymeric tube and modified capsule at various heating rates

Thermal degradation measurements were carried out at different linear heating rates and the temperatures at which a set percentage of mass loss occurred was noted. The second derivative of the thermograms of modified gelatin capsule indicated that there are two degradation points, 100°C and 340°C (Figure 5.8(a)). The gradual decrease in mass until 100°C indicates the presence of moisture. Ethyl cellulose has been shown to have a thermal decomposition point of 280°C (Aggour, 2000). Gelatin undergoes gradual degradation between 300°C and 500°C (Sampath and Babu, 2006). A peak degradation point of inflection shift of gelatin to 340°C indicates improved thermal stability and an improvement in the lifetime of the polymer when cross-linked to gelatin. In Figure 5.8(b), this shows the degradation of the polymeric tube that also had three differential peaks. The first peak indicated decomposition of castor oil at 215°C. At 350°C, this relates to degradation of ethyl cellulose. This is then followed by degradation of methyl cellulose at 430°C. Lifetime prediction on antigen responsive hydrogels was not conducted as the protein denatures above 40°C.

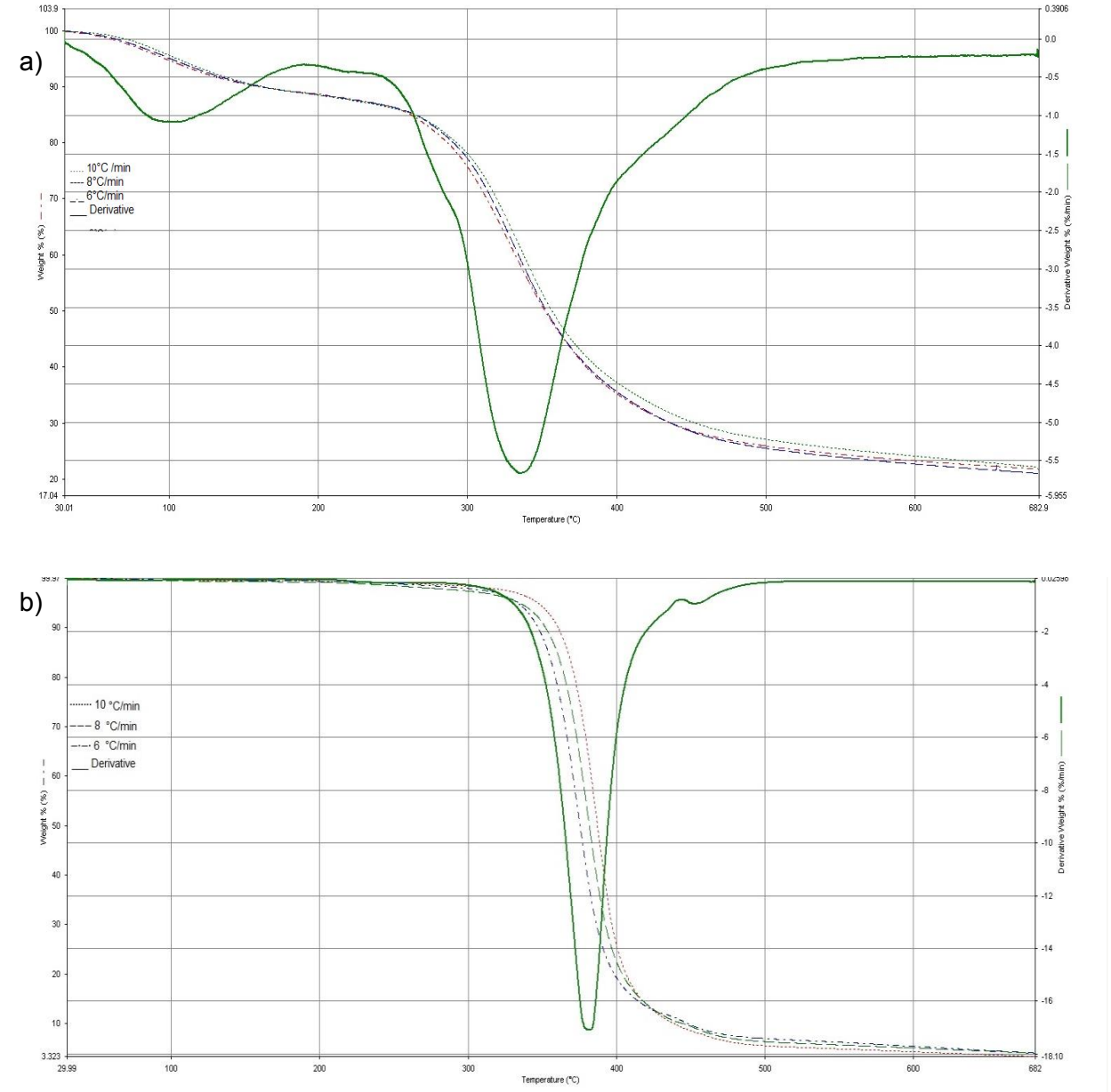

Figure 5.8: TGA and DTG curves under 6°C, 8°C and 10°C heating rate for modified gelatin capsule (a) and polymeric tube (b).

5.3.7. Analysis of thermal decomposition of polymeric tube and modified capsule

The combined TG/IR was used for the determination of decomposition by-products due to depolymerizing by determining if the polymers yield their parent monomers during decomposition. The onset of mass loss may be used to define the upper limit of thermal stability for the implant (Price et al., 2006). Polymer degradation can be categorized according to six main mechanisms (Jankovic, 2013). However, cyclization and cross-linking rarely cause a

change in sample mass, unless they occur in conjunction with; main-chain scission, side group scission, elimination and/or depolymerization. Figure 5.9 shows that during decomposition, the monomers were formed and evolved as gas detectable by IR. The greatest peak was due to immersion of carbon dioxide as indicated in capsule, hydrogel and polymeric tube. Thus is due to all the implant components consisting of carbon based materials. Peaks depicted between 2000 cm^{-1} and 1500 cm^{-1} indicate the presence of carbonyl and secondary amine groups in the evolved gas. Peaks observed above 3000 cm^{-1} represent the breaking of primary and secondary amino causing the release of nitrogen based products. Peaks observed between 1000 cm^{-1} and 600 cm^{-1} indicate immersion of alkene group from polyethylene group of PEGDA and PEG-200. Other reported volatile compounds produced by ethyl cellulose include H_2O, CO, CO_2, C_2H_4, C_2H_6, C_2H_5OH, CH_3CHO and unsaturated aliphatic compounds which are conserved between the capsule and the polymeric tube (Brown and Tipper, 1978).

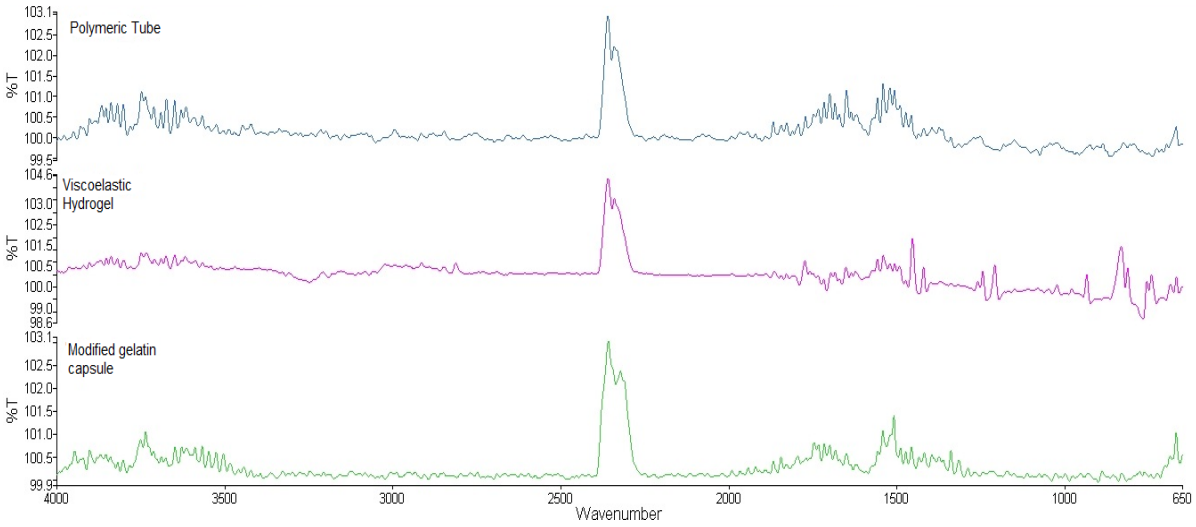

Figure 5.9: Timebase FTIR spectrum showing immergence of carbon dioxide due to carbon based materials.

5.3.8. Thermal degradation kinetics analysis

Degradation kinetics was conducted to determine the lifetime of the implant components. For meaningful correlation of thermal stability with polymer structure, it was essential that the experiments be carried out under similar experimental conditions. Figure 5.10 was generated by using temperature at which degradation begins to occur for the polymeric tube, i.e. for which 5% of the polymer mass is lost. It was observed that the activation energy increases with increase in heating rate.

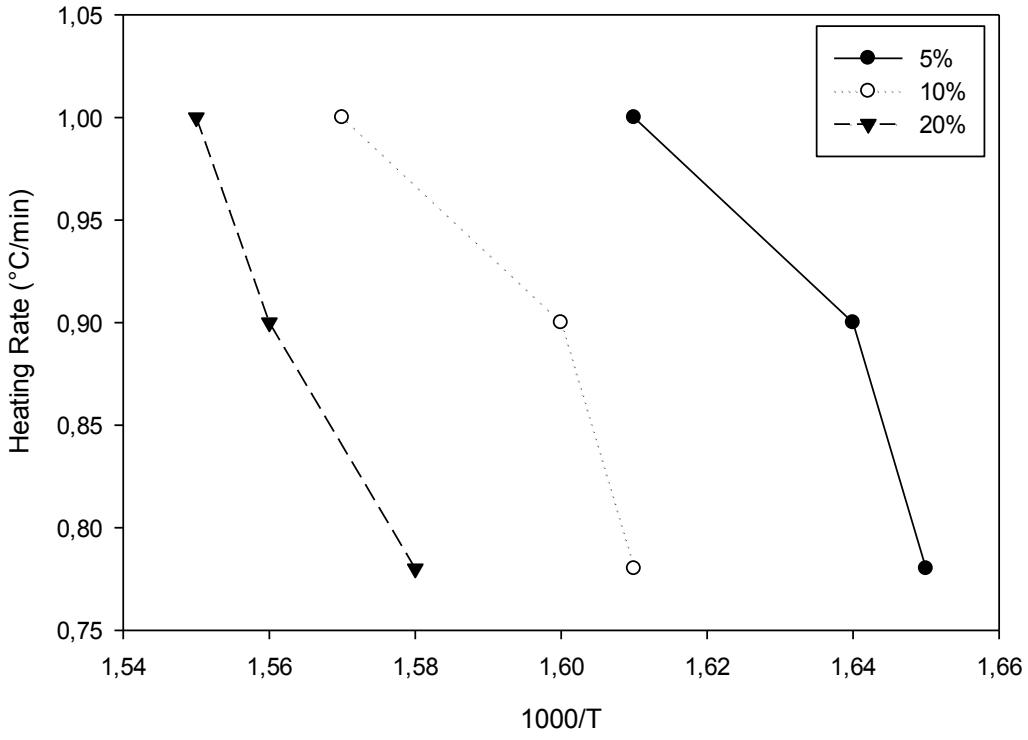

Figure 5.10: Kinetic analysis to determine activation energy of polymeric tube. (▼-20% (y = -5.75x+9.86 [R^2 = 0.9944]), ○ -10% (y = -5.1923x + 9.1631[R^2 = 0.8784]) and ● - 5% (y = -5.1923x+9.3708[R^2 = 0.8784]).

The activation energy was calculated using the slope of the line of log heating rate (°C/min) versus temperature (K), (d log b)/ [d (1000/T)]. The given decomposition reaction for the values of E/RT were required to be between 29 and 46 for b value to be within 1% of 0.457. $P(X_f)$ values have to lie between 10 and 50 (a function whose values depend on E_a at the failure temperature). The E_a value is expected to approximately remain constant over the relatively short-range mass loss from 0-20% after which it would decrease, reaching a minimum of about 50% mass before increasing steadily during further degradation. The lower activation energy reaction was expected to dominate the kinetics at slow heating rates followed by high activation energy being involved in fast heating rates and high temperatures (Katsikas and Popović, 2003). As the heating rate was increased, the onset of decomposition was pushed to higher temperatures. This phenomenon highlighted the time and temperature dependency of the decomposition reaction. Figure 5.11 indicates degradation of the capsule. In relation to polymeric tube degradation, the capsule indicated to be thermal stable due to high E/RT values. Polymeric tube stability was affected by the unstable crystalline structure produced by the

porogen as indicated during nanotensile studies. Table 5.6 shows the calculated value of activation energy to be used in estimation of thermal lifetime span of the synthesized implant components.

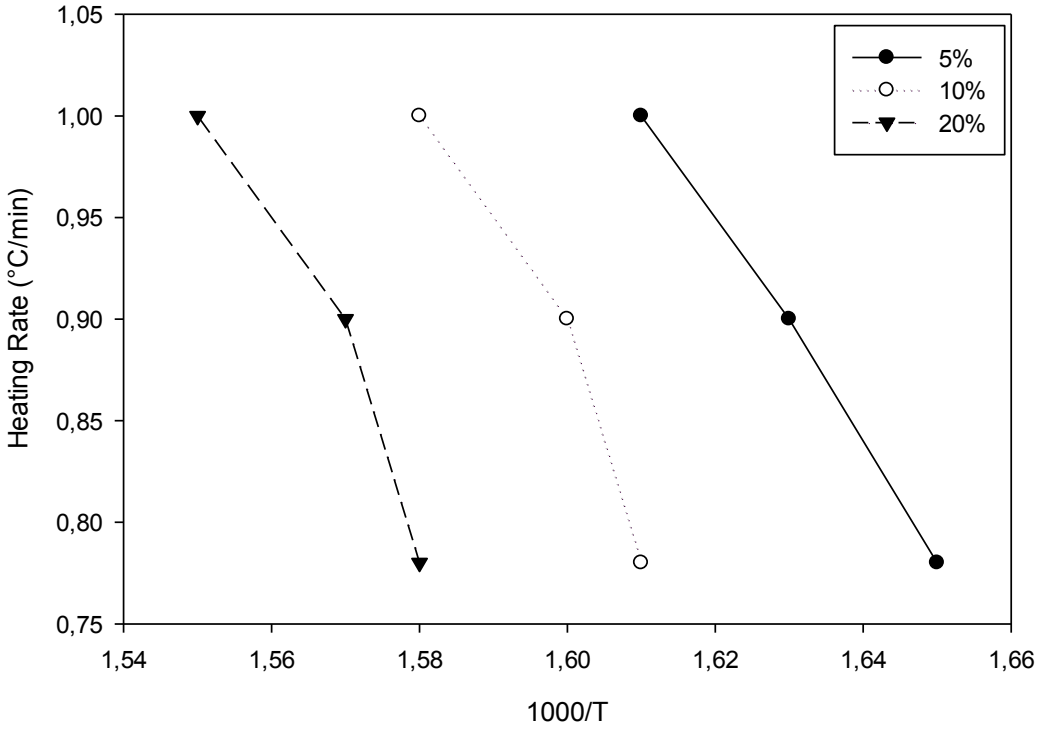

Figure 5.11: Kinetic analysis to determine activation energy of modified gelatin capsule. (▼-20 %(y=-7x+11.86 [R² = 0.9423]), ○ -10% (y = -7x + 12.07 [R² = 0.9423]) and ● - 5% (y = -5.5x +9.8583 [R² = 0.9973])). It was observed that the activation energy increased with increase in heating rate.

Table 5.6: Thermal degradation kinetic parameters of a modified gelatin capsule (reservoir) and a polymeric tube at a mass loss of 5%.

Heating rate (°Cmin^{-1})	**Implant Component**	***E*a.(kJmol^{-1})**	$\mathbf{P(X_f)}$	**E/RT**
	Reservoir			
6°C/min		100.05±4.6	11.24	34.93
8°C/min		127.34±6.2	13.67	43.25
10°C/min		127.34±5.3	13.44	40.20
Average		*118.3*		
	Polymeric tube			
6°C/min		117.55±9.2	13.12	23.81
8°C/min		132.55±6.4	14.49	26.76
10°C/min		133.12±11.2	14.28	26.39
Average		*127.34*		

5.3.9. Activation energy of polymeric tube and modified capsule

Activation energy can be used in determining the decomposition kinetics of the polymer. Polymeric tube and modified gelatin capsules were analyzed. Activation energy has been reported to decrease at the initial stage and gradually increase when mass loss goes above 30% (Wang et al., 2004). Figure 5.12 corroborates the expected behavior of degradation. The initial mass loss indicated the first step of degradation where the reaction was accelerated once the decomposition started owing to the decrease in the activation energy. During that stage, chemical modifications such as oxidation of the polymer occurred. Since the tests were conducted under inert conditions, the initial loss could was due to evaporation of residual solvents or polymerization. The decomposition reaction went into the second stage whereby mass percentage starts to increase.

Based on single step degradation model, activation usually remains constant during increasing temperature as seen by capsule activation kinetics. The higher values obtained may in polymeric tube can be caused by computational errors of the method as well as by physical properties of the polymer (Peterson et al., 2001). Due to polymeric tube high carbon density due to methyl cellulose and ethyl cellulose, oxidative chemical reaction increase mass during decomposition that affects activation energy. In a highly crosslinking network, each molecular bond has an activation energy (broken energy). Therefore, this activation energy will depend of which kind of bond is being broken as a result of an increase in temperature (Gracia-Fernández et al., 2005). This indicated high activation energy of the polymeric tube in comparison to the capsule. The increased lifetime was linked to increased cellulose compounds concentrations that normally require more energy for pyrolytic degradation. The variation in activation energies and lifetime predictions could be due to change in activation energy based on the degree of mass loss.

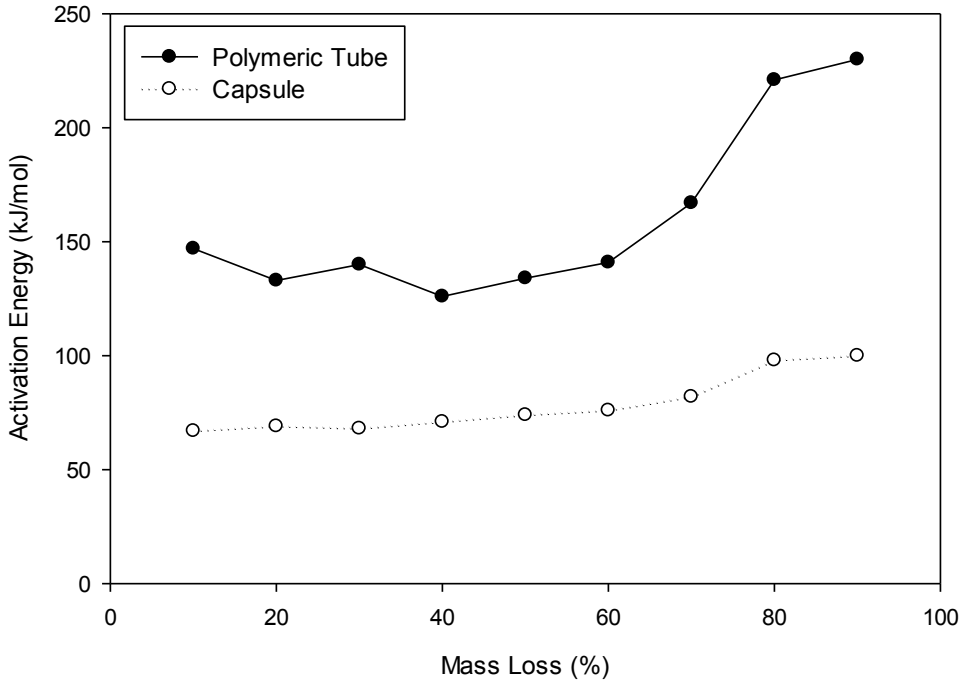

Figure 5.12: Scatterplot depicting the change in E_a with mass loss.

Based on the activation energy, the estimated lifespan of the capsule and the polymeric tube was estimated in Table 5.7 at varying temperatures. This indicated the time required for complete degradation of the individual components.

Table 5.7: Lifetime prediction of capsule and polymeric tube at varying temperatures.

Component	30°C	100°C	200°C	400°C
Capsule	7.06×10^{12} min	9.69×10^{7} min	8.8×10^{5} min	8.3×10^{2} min
Polymeric Tube	9.74×10^{15} min	1.26×10^{22} min	3.5×10^{7} min	1.7×10^{5} min

5.3.10. Hydrolytic degradation of modified capsule, antigen responsive hydrogel and polymeric tube

Hydrolysis is another way by which polymers can undergo chemical degradation and for hydrolysis to occur the polymer must contain hydrolysable covalent bonds such as the ones prevalent in chemical groups that include esters, ethers, anhydrides, amides, carbamides (urea) and ester amides (urethane). Hydrolysis is dependent on parameters that include; water molecule presence and activity, temperature, pH and time. The design of materials with a controlled life span needs the choice of specific monomers to obtain a copolymer with the optimum hydrophilic characteristics. Well organized molecular frameworks (crystalline domains)

prevent the diffusion of O_2 and H_2O, thus limiting chemical degradation. Oxidative and hydrolytic degradation on a given material easily take place within disorganized molecular regions (amorphous domains) (Lucas et al., 2008). Figure 5.13 shows the hydrolytic degradation of the polymeric tube, the modified gelatin capsule and the antigen responsive hydrogel. Due to presence of polyethylene glycol in the in the hydrogel, the change in mass was more rapid due to leaching of the plasticizer into the buffer and the increase in hydrogel solubility due to plasticizer effects. The initial high mass indicates point of swelling equilibrium. The delay in hydrogel degradation was dependent on the level of crosslinking and the amount of plasticizer. The capsule and tube had reduced hydrolytic degradation due to the presence of ethyl cellulose. In correlation to antibodies half-life, this indicates that the device can also be viable for 30 days before both the antibodies and the IPN starts to fail. However, the tube and capsule are capable of remaining stable for more than 3 months.

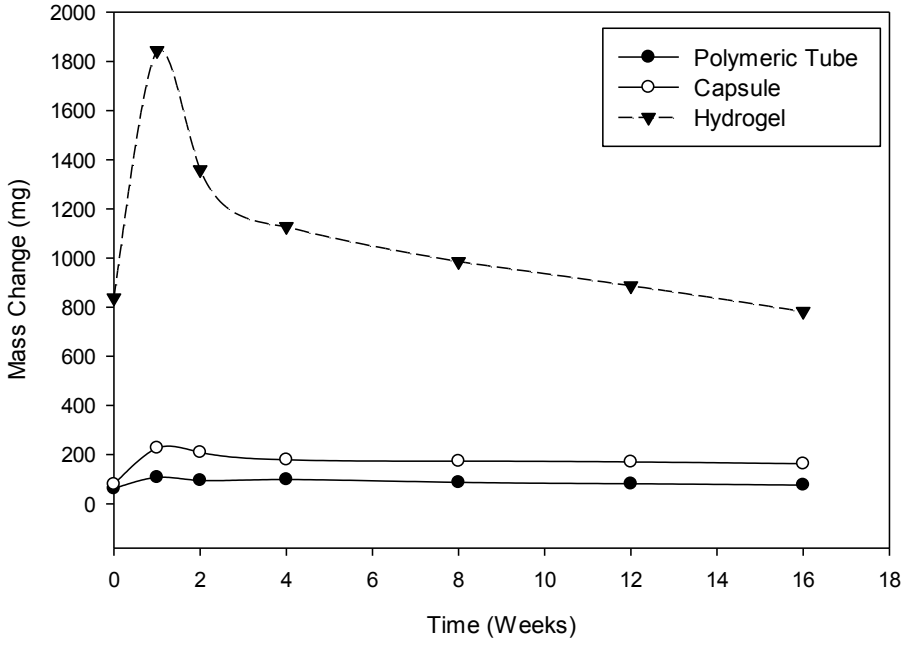

Figure 5.13: Hydrolytic degradation of the gelatin capsule, the polymeric tube and the hydrogel.

5.3.11. Mechanical properties of polymeric tube and modified capsule

Textural analysis was carried out to measure rigidity and deformation energy of the implant components, coated polymeric tube and modified gelatin capsule. For drug reservoir (gelatin capsule), the main property that was determined was the amount of force that was required to rupture the reservoir leading to drug leakage and dose dumping and hence toxicity if the implant

was used *in vivo* (Table 5.8). The tests also evaluated the force that would cause extrusion of the drug because of body movements since it would affect the programmed drug release rate. The data indicated that it would require a force of 1kg to cause the capsule to rupture and release the drug content. This amount of force can only be exerted *in vivo* on the animals to be used by means of external force not relating to movement. Due to pigs to be used in this study, the large amount of neck muscle is hypothesized to be sufficient to absorb any force before the capsule is affected. In terms of the polymeric tube, 0,78kg of force is unlikely to be exerted intravenously. The only issue is the limitation of a bending radius of 10mm and the low Young's modulus of 25MPa that may break. Evaluation of the flexibility of the polymeric tube and capsule enabled the assessment of possible damage that may occur to the implant during movement. Knowing the extent of the tube's flexibility also helps in ruling out the possibility of vascular damage during movement. If the tube were not flexible, there would be damage to the vascular wall resulting in the formation of thrombosis and if flexibility becomes too high, the tube might recoil under hemodynamic force. The flexibility of the tube relates to the nanotensile studies, which indicate that the hydration of ethyl cellulose will cause the polymeric tube to be rigid whilst the porogen affect the elongation of the tube by weakening the structure due to pore distribution.

Table 5.8: Textural analysis for determination of mechanical strength of the reservoir and polymeric tube.

Measurements	Polymeric Tube	Reservoir
Crush Resistance	0.73±0.1kg	1.054±0.9kg
Resilience	20±4.7%	47.3±3.6%
Rigidity	16.47±2.6N/mm	1.63±0.03N/mm
Extensibility	1.57±0.2mm	-
Deformation energy	0.018±0.003N/m	0.006±0.001N/m

5.3.12. Analysis of the implant intermolecular properties

FTIR was conducted to analyze intermolecular properties of the drug delivery system components. Figure 5.14 is a the FTIR spectra of the components making up the implant and in Figure 5.14(a) the peak at 3383.44-3377.45cm^{-1} was observed in both plasticizer and the final product thus indicating the presence of an alcohol/phenol O-H stretching vibration, 1550.39cm^{-1} was distinct in the final product which indicated presence of aromatic C=C bending vibrations, 701.11cm^{-1} was also distinct to the final product and it represented aromatic C-H bending

vibrations. The hydrogel (Figure 5.14(b)) was synthesized by methacrylic acid forming poly methacrylic acid of which process can be confirmed by the disappearance of the peak at 1634.10cm^{-1} (vinyl unsaturation) due to the homopolymerization process. Poly methacrylic acid was then combined with polyethylene glycol diacrylate (cross-linker) and then later polyethylene glycol 200 (plasticizer) which bound the PEGDA: MAA together. Figure 5.13(c) confirms the successful crosslinking of ethyl cellulose. Hydrolytic degradation was reduced because of the modification with ethyl cellulose.

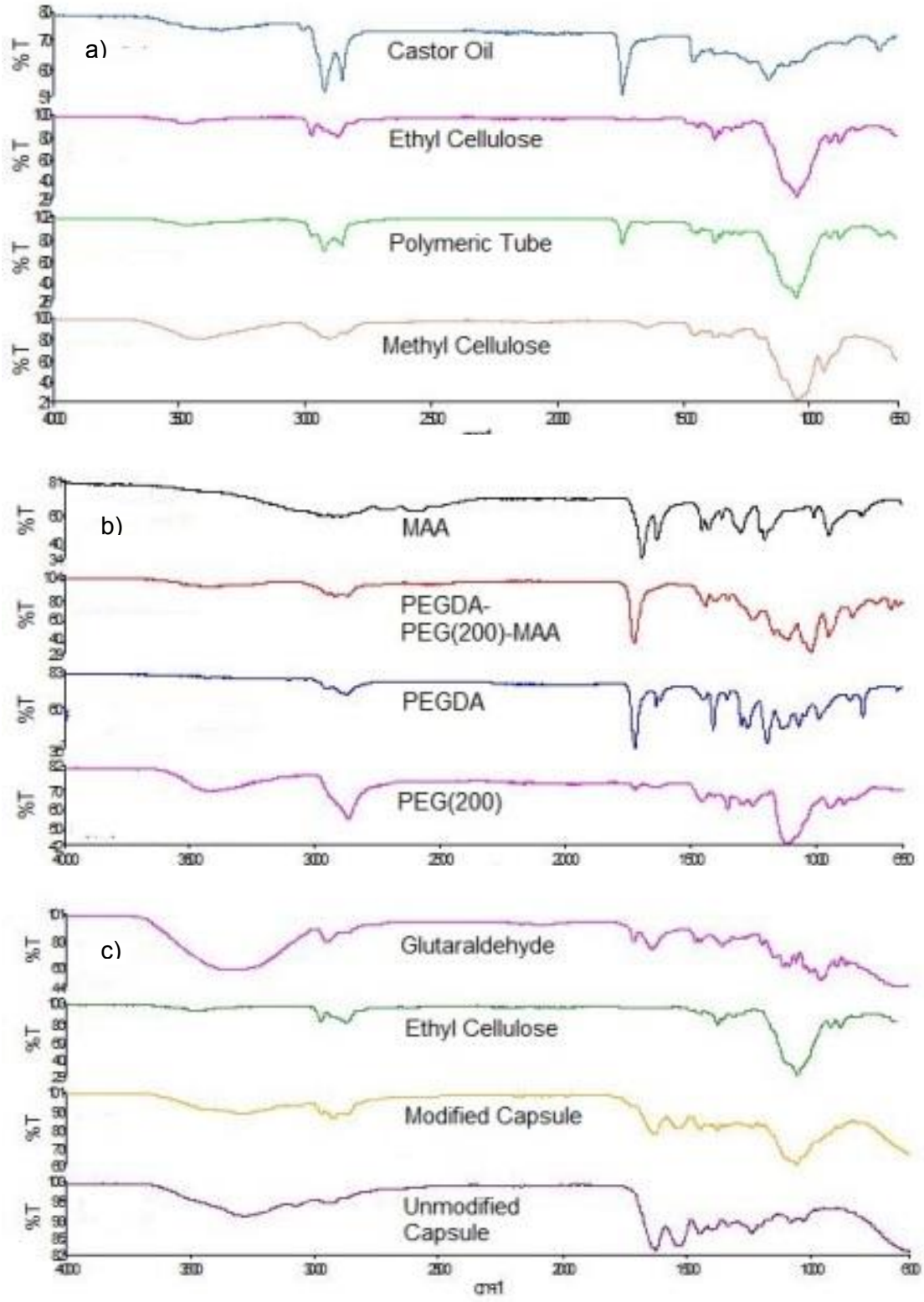

Figure 5.14: FTIR spectra of the (a) polymeric tube, (b) antigen responsive IPN and (c) modified gelatin capsule.

5.3.13. *In vitro* dissolution of optimized antigen responsive drug delivery system

Drug release studies were conducted on the optimized antigen responsive implant and the catheter infusion of anti-LDL SLN implant. Osmotic pump driven drug delivery systems usually follow zero-order kinetics due to the constant infusion rate. The implant kinetics was hypothesized to also follow zero-order kinetics and a combination of another kinetic models favoring change in porosity of the implant surface. Table 5.9 shows that zero-order is favored, followed by Hixson-Crowell, First-order, Korsmeyer-Peppas, Higuchi and then Baker-Lonsdale. Zero-order was favored due to constant drug release from the porous polymeric tube and sensing layer. Hixson-Crowell follows due to non-disintegration of the diffusion matrix whereby drug solubility plays a role in release. First-order drug release kinetics occurred because of the antigen responsive layer. Korsmeyer-Peppas, Higuchi and then Baker-Lonsdale kinetics occurred because of drug release from porous matrix. The mean dissolution time of a drug depends on the dose/solubility ratio (Ranaki et al., 2003). A higher MDT computed was a reflection of slow release rate, low solubility of the drug and higher drug-retarding ability of the sensing layer. MDT was determined using the first 3 days of dissolution experimentation.

Table 5.9: Determination of the most favorable drug release kinetics of IVISDDD.

Kinetics	R^2
Zero-order	0.9917
First-order	0.9899
Hixson-Crowell	0.9908
Higuchi	0.9752
Baker-Lonsdale	0.9706
Korsmeyer-Peppas	0.9804
Mean Dissolution Time	1273.141±12.3

In terms of the catheter infusion of anti-LDL SLN, the release kinetic indicated to follow zero-order kinetics based on the adjusted R^2 value. However, due to high viscosity of the nanosuspension, there was also sign of Korsmeyer-Peppas drug release influence by means of diffusion (n=0.26). This release correlated to Alzet® osmotic pump delivery of fenofibrate nanoparticles (Hill et al., 2012).

5.3.14. Implant mechanical stability in circulating plasma

Ex vivo studies were required to assess implant stability in plasma. This would allow detection of protein/cell adhesion on the surface of the antigen responsive system that causes disruption of the drug release rate. Method development was begun with the optimization of chromatographic conditions including mobile phase composition and wavelength adjustment.

The mobile phase comprising of methanol and ammonium acetate (70:30; $\%^{v/}_{v}$) was shown improved signal-to-noise ratio and thus found to be suitable for the chromatographic separation of the analyte. The use of acetonitrile with ammonium acetate caused undifferentiated peak. Due to high solubility of fenofibrate in methanol, the peak under methanol: ammonium acetate led to clear distinctive peaks as seen in Figure 5.15. Under these chromatographic conditions employed, *ex vivo* study samples showed sharp peaks of fenofibrate and nicotinic acid with good resolution (Figure 5.15). The retention time of the drug was found to be 1.9±0.016min, whilst the retention time of the internal standard was 0.2±0.023min.

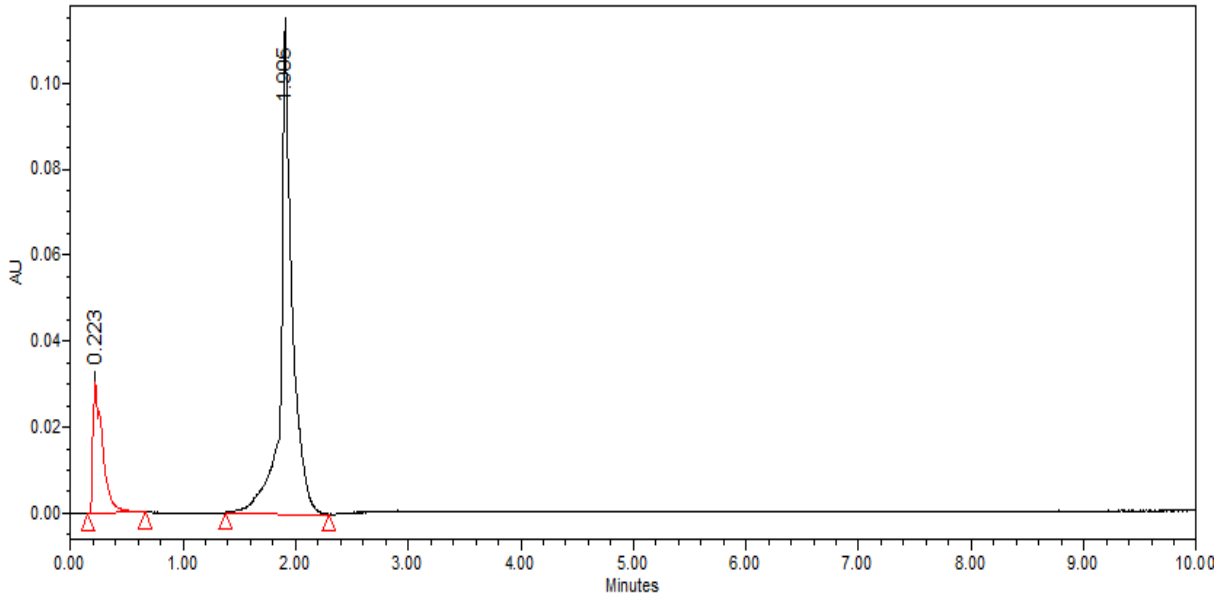

Figure 5.15: A typical UPLC chromatogram indicating the separation and retention time of fenofibrate (1.905 min) and the internal standard nicotinic acid (0.233 min).

The linearity of the developed methods was assessed by analysing series of different concentrations (0.0-1800µg/mL) of fenofibrate solution. Under the above described experimental conditions, the calibration curve of chromatographic peak area versus fenofibrate concentration has shown good linear dynamic range (Figure 5.16). Linearity was maintained primarily within the concentration range of 250-1800µg/mL of fenofibrate. Slope, intercept, correlation coefficient (R^2), standard deviation of slope and intercept obtained by the linear least squares treatment of the results were 0.0115, 0.7357 and 0.99 respectively.

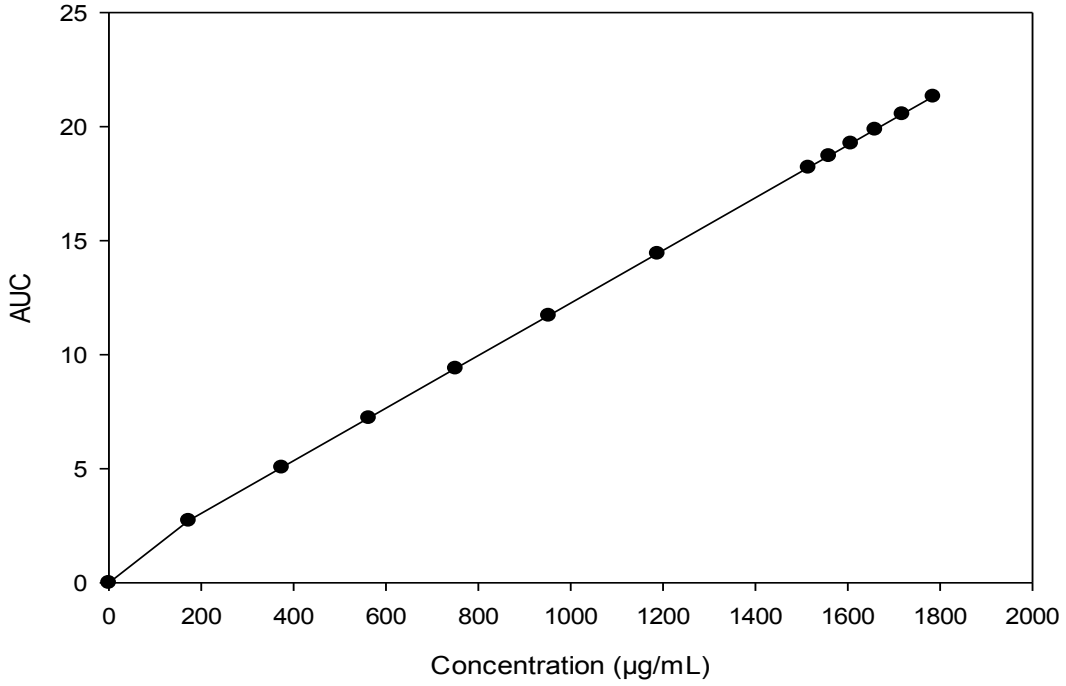

Figure 5.16: Standard calibration curve generated for quantifying fenofibrate in plasma samples employing a UPLC (N=3, S.D = 0.3).

Circulating blood is fluid that has the capacity to clot (form a thrombus) at sites of injury, when a foreign material is introduced or where blood flow is slowed or irregular (stasis or turbulence). Therefore, it is important to fabricate implants in such a way that they do not induce thrombosis. Preventing thrombosis can be done by fabricating suitably flexible ('soft') implants which cause low surface friction to minimize vessel trauma and thrombosis. Selecting materials with low thrombogenicity can also minimize thrombus formation on the catheter surface. In Figure 5.17, this indicates the drug release from the antigen responsive polymeric tube. The curve did not follow zero-order kinetic models during initial stages of drug release due to diffusion of the drug from the porous layers. Korsmeyer-Peppas model (R^2 = 0.9656) was favored when as the porogen eroded (methyl cellulose) from the implant surface. This differed from *in vitro* studies were there was combination of Korsmeyer-Peppas was favored after Zero-order, First-order and Hixson-Crowell. Korsmeyer-Peppas release kinetics was supported which indicated that after erosion, drug diffusion was occurring. Evaluation of the polymeric tube microscopically indicated no bioadhesion of blood cells. This is due to PEGDA prevent adhesion of proteins on the surface of the tubule which alternately recruits blood cells and immune cells on the surface of intravenous devices. The absence of biofilm adhesion correlates to no evidence of drug release

impairment. The catheter infusion was not assessed *ex vivo* as the device has is FDA approved for animal use without causing any biofilm adhesion on the surface of the tube. Furthermore, the high osmotic force generated by the osmotic pump will prevent clotting of the orifice.

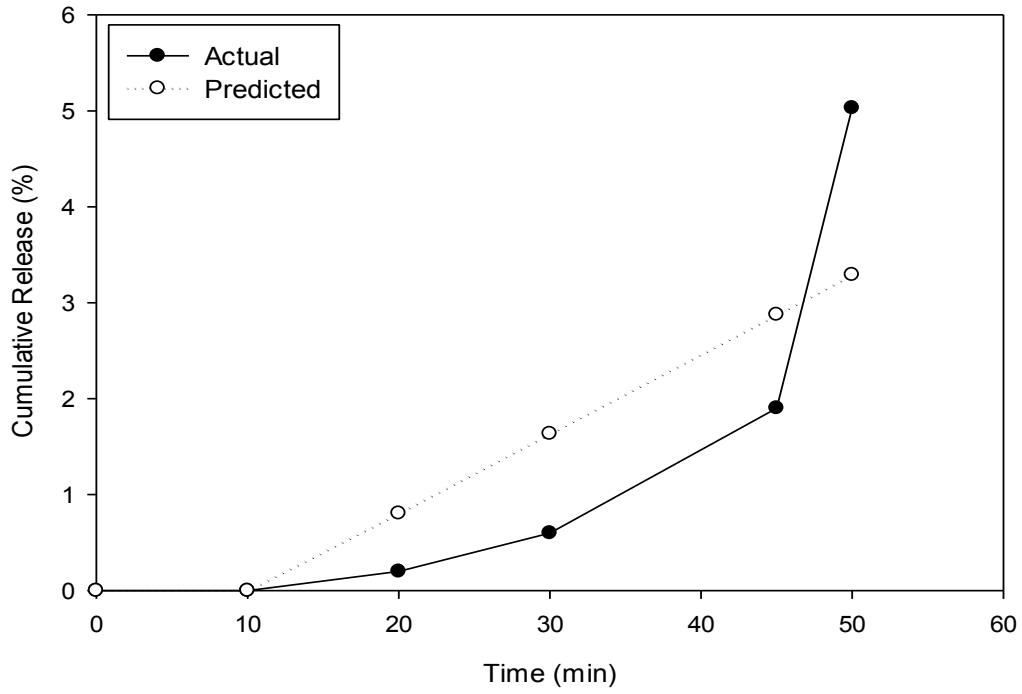

Figure 5.17: *Ex vivo* drug release from implant (N=3).

5.4. Concluding Remarks

The use of polyethylene glycol in the design of IVISDDD showed no signs of adhesion of blood cells to the antigen responsive IPN layer due to no evidence of drug release impairment. Physical properties such as high tensile strength, resistance to compression which maintains patent lumen, optimum flexibility, and a low friction coefficient were affected. The polymeric tube synthesized from ethyl cellulose and methyl cellulose failed to fulfill efficient mechanical strength as brittleness was observed. This would lead to thrombosis if the tube fractured inside the lumen. The amount of plasticizer was also indicated to affect the solubility of the IVISDDD as the antigen responsive IPN was shown to degrade faster than the polymeric tube and modified capsule over a period of 16 weeks. Rapid hydrolytic reduces the life-spam of the implant. Furthermore, the drug release rate of the antigen responsive coated polymeric tube indicated to have varying releases kinetics due to delayed pore formation due to the hydrophobic layer. Due

to mechanical limitations of the polymeric tube, the catheter infusion of anti-LDL SLN was selected as the viable device that can withstand forces exerted *in vivo*. Albeit the drawbacks in mechanical strength, the responsive component of the device was proven to be functional and novel. The dependence of the swelling ratio on antigen concentration indicated the device could be used for detection of analytes in various environments. This can also be applied in detection of mutated protein and circulating pathogens. Future studies will require refinement of the mechanical properties by usage of a more elastic polymer such as elastomer as a platform for the antigen responsive hydrogel. Overall, the antigen responsive polymeric tube device indicates to be viable for operation for duration of 30 days based on the limitation of usage of antibodies which has short lifespan and the rate of hydrolytic degradation. The following chapter, Chapter 6 encompasses the infusion of anti-LDL SLN as an alternative device for *in vivo* studies due to the nature of the polymeric tube weak mechanical properties. For *in vivo* studies, the drug reservoir was filled with drug loaded anti-LDL SLN to bind to circulating LDL particles. This is proposed to aid plasma clearance of LDL particles due to macrophage engulfment and elution of drug circulation of the anti-LDL SLN.

CHAPTER SIX

IN VIVO EVALUATION OF THE CLINICAL EFFICACY OF THE DRUG DELIVERY DEVICE

6.1. Introduction

Infusion pumps used for the continuous infusion of pharmacological compounds *in vivo* can be divided into two types based on the level to which may impair animal movement and the possibility to alter the infusion solution and the infusion rate (Abe et al., 2009).The design of the syringe pumps allows easy alteration of the infusion rate and the changing of the infusion solution. This however may negatively affect animal movements (Turner et al., 2011). An implantable device would reduce animal stress, as there are no extruding attachments that may hinder animal movements. However, the quantity of the solution to be infused and the rate of infusion cannot be altered, as it would require surgery to remove, modify and place the implant back (Cooper et al., 2007). Alzet® pumps (DURECT Corporation, California, USA) are examples of implantable infusion pumps whose infusion solution and infusion rate cannot be changed during the experiment/treatment. The iPRECIO™ infusion pump (Primetech Corporation, Tokyo, Japan) is a combination of an implantable and a syringe pump (Tan et al., 2011). It is refillable, therefore allows the alteration of the infusion solution and the infusion rate. Although these pumps are invasive, they offer the ability to ensure a constant infusion of drugs at a required and predetermined concentration during the duration of treatment. Bypassing physiological barriers such as the epidermis, the gastrointestinal and blood brain barrier allows targeted drug delivery of therapeutics that cannot be delivered via oral, intravenous or transdermal routes (Meng and Hoang, 2012).

Drug bioavailability can be affected by dosing, physiochemical changes and type of disease being treated (chronic or acute). Chronic diseases caused by glucose and cholesterol imbalances require constant drug administration as chemical imbalances can fluctuate throughout the day. Since it is not easy to alter the infusion rate after the device is implanted, the integration of a component that can modify the amount of the drug released in response to the physicochemical imbalances would enable the design of a self-regulatory delivery system. There are a number of responsive devices that are thermo-responsive, electro-responsive, pH responsive and antigen responsive (Murdan, 2003). Antigen responsiveness enables the detection of chemical imbalances that may signify the occurrence and the progression of a disease.

The use of macromolecules that are normally utilized in biosensors such as antibodies, enzymes, ligands and receptors allows identification and quantification of disease biomarkers (Miyata et al., 2002). A glucose self-regulatory device that comprises an antigen responsive polymer was designed to release insulin when glucose levels went above optimum levels. Antigen responsive hydrogels was fabricated with concanavalin A (ConA) as a receptor molecule for competitive binding of glucose against dextran, α-methyl mannoside or glycated protein, (Oliver et al., 2009). These hydrogels can undergo reversible swelling during the competitive binding of glucose. Competitive binding of the targeted biomarker causes structural changes that involve the breaking of non-covalent links between the hydrogel conjugated competitor and hydrogel monomers (Miyata et al., 1999). The shape of the hydrogel will change in relation to the concentration level of the concerned biomarker. Low concentration of the biomarker would result in reversible swelling of the hydrogel whilst high concentration of the biomarker would cause the hydrogel to swell until it reaches the equilibrium point. However, hydrogels have limitation on the level of application. Application in intravenous application would lead to impairment of hemodynamic force as the hydrogel swells. Furthermore, breakage of the hydrogel can cause thrombosis. Therefore, in this study, the use of an antigen responsive hydrogel was substituted with antigen responsive nanoparticles.

An anti-LDL antibody was conjugated to SLN for detection of LDL in pigs fed on and atherogenic diet. The implant was made to function as both a syringe and an infusion pump. The osmotic pump would cause constant drug release even when LDL concentrations are low. The aim of the animal study was to provide information on the risks and benefits the use of the implant *in vivo* as a way of correlating *in vitro* studies. Pigs naturally develop atherosclerosis as aortic fatty streaks have been observed in young pigs after being fed diets high in fat (particularly saturated fat) and cholesterol within a few weeks (Vilahur et al., 2011). Pigs were used in the *in vivo* study because familial hypercholesterolemia (FHC) in swine resembles human familial combined hyperlipidemia (Suzuki et al., 1996). Familial combined hyperlipidemia is a complex lipid and lipoprotein disorder associated with the development of severe coronary lesions similar to those occurring in advanced human coronary disease (Hasler-Rapacz et al., 1996). Recent studies on humans, pigs, rhesus monkeys and baboons showed that the physiological characteristics of pigs LDL most closely resemble those of human as compared to baboons and rhesus monkey (Chapman and Goldstein, 1976). *In vivo* studies using the pig as the animal model allows the optimization of the implant before progressing to human trials.

Among different breeds of pigs, Large White pigs have shown to have higher levels of LDL (Yang et al., 2011).

6.2. Material and Methods

6.2.1. Materials

Fenofibrate, cholesterol, lard and nicotinic acid were purchased from Sigma (Sigma Aldrich, Missouri, USA). A cholesterol kit consisting of a cholesterol reaction buffer, 2X LDL/VLDL precipitation buffer, a lyophilized cholesterol probe, lyophilized enzyme mix, lyophilized cholesterol esterase and standard cholesterol (2µg/µL) were purchased from (ab65390, Abcam®, Cambridge, UK). Methanol and acetonitrile were purchased from Merck (Merck KGaA, Darmstadt, Germany), whilst pig growth and sow was purchased from Epol® (Rainbow Farms, Westville, SA). An 18Ga. x 2-1/2" (6.35 cm) catheter was also used for infusion of anti-LDL SLN. In the present study, all the chemical agents were analytic grade and used without further purification.

6.2.2. Use of experimental animals

Large White female pigs weighing 35kg at the beginning of the study were used. The animal experiments were approved by the Animal Ethics and Control Committee (AECC) of the University of the Witwatersrand (2011/52/05). The guideline for the use and care of animals in experimental education and other scientific procedures was used (AESC guideline). The animals used in this study represent a pilot study.

6.2.3. Experimental procedures conducted on Large White pig model

Experimental procedure entitled the feeding routine, monitoring behaviour of animals, monitoring recovery after surgical procedure and histopathological analysis after euthanization. The pigs were fed daily with a mixture of the normal and atherogenic diet during meal times (9am and 3pm). This was done to reduce chances for the pig to deny feeding only on the atherogenic diet because of the taste difference to the normal diet. The control diet did not constitute of lard and cholesterol. The appropriate amount of lard and cholesterol were added into the normal diet to make atherogenic diet. The amount of food given to the pigs was increased with every 4% increase in body weight of the pigs. The animals had free access to water through the nose push drinkers.

Table 6.1: Atherogenic swine diet composition.

Protein	**150 g/kg**	**Min**
Total lysine	7.5 g/kg	Min
Total methionine	12 g/kg	Min
Moisture	120 g/kg	Max
Fat	25 g/kg	Min
Fiber	80 g/kg	Max
Calcium	10 g/kg	Max
Phosphorus	6 g/kg	Min
Lard	200 g/kg	Max
Cholesterol	20 g/kg	Max

Observations of the pigs were conducted simultaneously while blood samples were being withdrawn as illustrated in Figure 6.1. The blood samples were withdrawn from the intrajugular catheter placed in the jugular vein. Sampling of 5mL blood was conducted at 0, 1, 3, 5, 7, 9, 11, 13, 15, 18, 21 and 24 days after implantation. Blood (5mL) was collected in BD Vacutainer tubes (BD Vacutainers®, Franklin Lakes, New Jersey, USA). The tubes were stored at -80° C. For analysis, the blood samples were centrifuged, and the supernatant was then used to determine the drug concentration and the quantity of LDL. For accurate analysis of the cholesterol level, pigs were required to fast overnight prior to blood sampling.

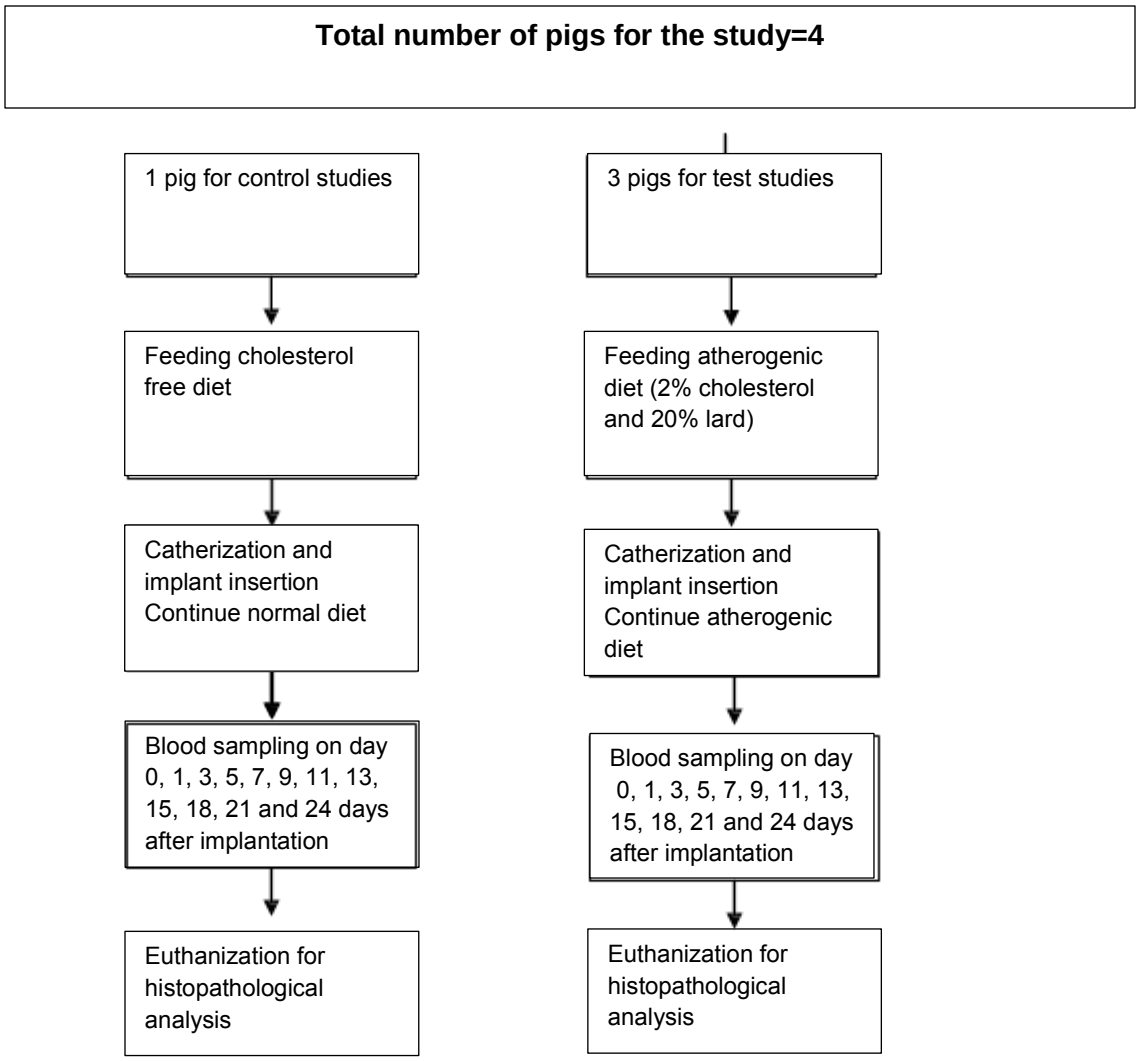

Figure 6.1: A schematic illustrating the study design for the *in vivo* experimentation in the Large White pig model.

At the end of the study, the animals were euthanized which was induced by an overdose of sodium pentabarbitone (200mg/kg). Blood vessel and surrounding tissue were then excised for histochemical tests to ascertain tolerance to the drug delivery system by evaluating through the localized inflammation. The inflammatory response was analyzed by preparing histological slides for determining the development of inflammatory cell infiltrates. The samples were sent to IDEXX Laboratories (Onderstepoort, Pretoria, SA) for histopathological testing. Briefly, the specimens were fixed in 10% buffered formalin. The specimens were the cut into sections and processed in an automated tissue processor according to the IDEXX Laboratories standard operating procedure PTA-his-SOP-27. After tissue processing, wax blocks were produced and

sections of 5-6µm were cut using PTA-his-SOP-30 standard operating procedure. A routine Haematoxylin and Eosin (H/E) was also done before microscopical examination using PTA-his-SOP-205 standard operating procedure. Cell proliferation, exudates, stromal reaction, fibrosis and signs of inflammation were analyzed. The thickness of the epithelial cell layer, type of vaginal cell layer, degree of inflammation, ulceration, fibrosis, neutrophil and mononuclear inflammatory infiltration as well as tissue necrosis and fibrosis were examined and scored. Due to the implants being similar in chemical nature, histopathology analysis was conducted to assess if the pigs tolerated the device. The aim was not to differentiate the immune response between the control and experiment control. The information from pathological analysis was used as a collective assessment of immune tolerance of the implant.

6.2.4. Catheter and Implant implantation

Catheter and drug delivery system implantation into the jugular vein (once off surgery) involved having an intrajugular catheter implant placed into the jugular vein of each pig for use in the administration of sedatives and blood sample withdrawal. Each pig was anaesthetised using ketamine (HCl 11mg/kg), midazolam (0.3mg/kg), topical procaine HCl (0.5%) and maintained under medical oxygen (12%) and isoflurane gas (2%) for about 30 to 60 minutes during the surgical procedure to insert of a catheter into the jugular vein with minimal stress to the pig(Hodgson, 2007). Buprenorphine (0.05mg/kg I.M.) and carpofen (4mg/kg I.M.) where then administered for analgesia and inflammation. The implantation procedure involved the insertion under aseptic conditions of a 7-gauge double lumen 35cm catheter (CS-28702) (Arrow Deutschland GmbH, Erding, Germany) into the left jugular vein. The jugular vein was exposed by an incision made dorsal to the jugular groove on the left lateral aspect of the neck (Figure 6.2(a)). The jugular vein was then isolated by blunt dissection and 10cm of the catheter was inserted into the lumen of the vein then fastened to the wall of the vein by a purse suture technique (Figure 6.2(b)). The remaining 25cm of catheter was tunneled subcutaneously to a cranial exit point at the dorsal aspect of the scapula with the use of a trocar (Figure 6.2(c)). The external injection ports of the catheter were sutured to the skin of the pig (Figure 6.2(e)). The catheter was cleaned by the withdrawal of blood followed by flushing with heparinized saline (1000IU/L of 0.9% saline) twice daily.

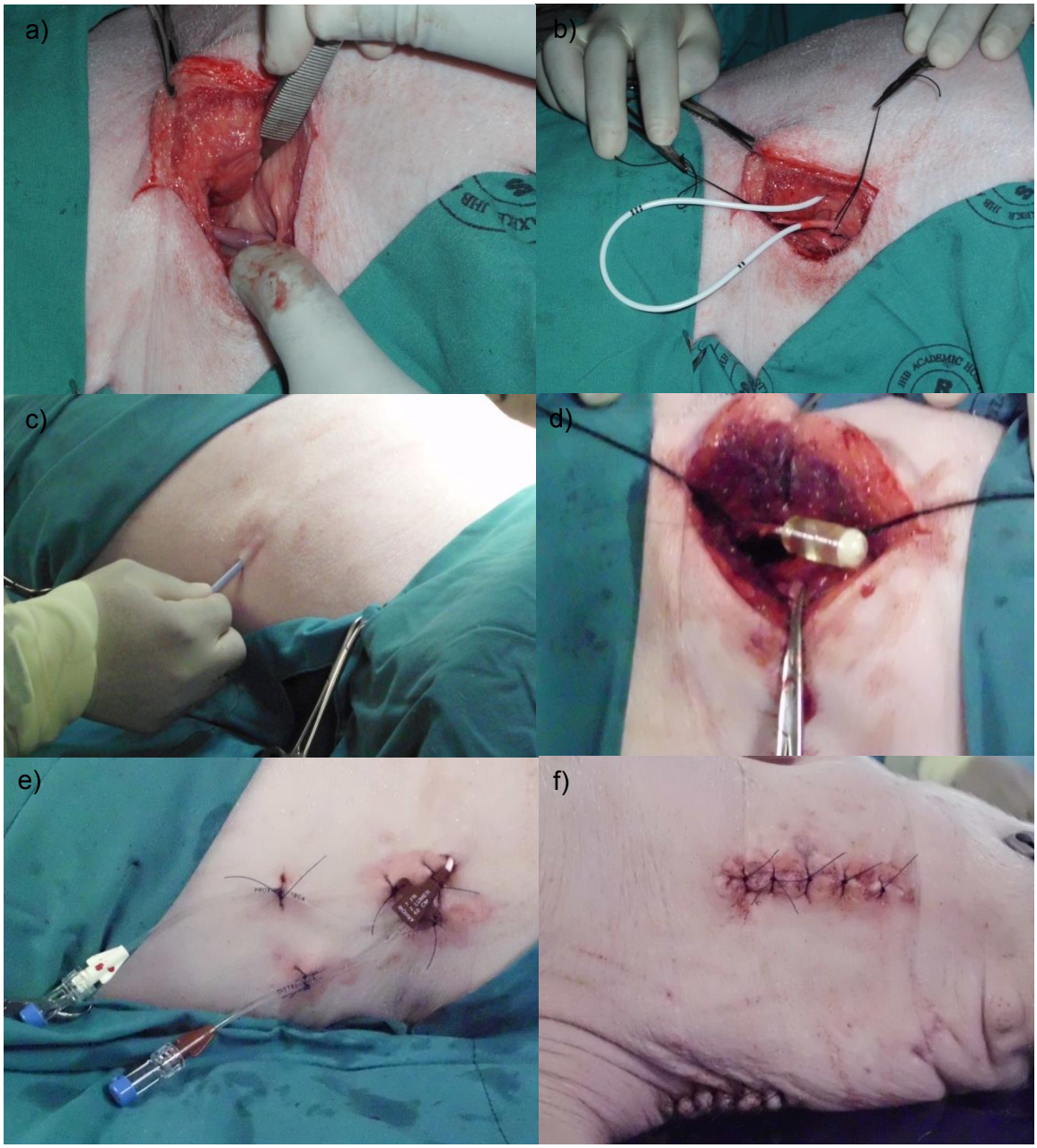

Figure 6.2: Catheterization and implant insertion surgical procedure. (a) The surgical procedure for the jugular vein catheterization of experimental pigs depicting surgical incision into the jugular area, (b) insertion of the catheter, (c) subcutaneous tunneling, (d) insertion of the drug delivery device, (e) suturing of the catheter external injection ports and site of implantation sutured.

The mode of drug delivery system implantation followed the Usvald and colleagues' procedure, where an incision was made in caudal part of *sulcus jugularis sin (*Usvald *et al., 2008)*. The subcutaneous tissue was blunt prepared up to *musculus cutaneus colli*. The muscle was then cut through and two lower located muscles, *m. brachiocephalicus* and *m. sternocephalicus* were

separated. A retractor was inserted into the incision site and *v.jugularis externa* was then prepared. Two 4M silk fixation ligatures were set around the vein, proximally and distally from the point of cannulation, about 5cm apart, and the vein was drawn into the operation site. To prevent vasoconstriction, the vein was moistened with 2% lidocain. The vein was then punctured using a hypodermic needle and the needle tip was used to guide the insertion of the drug delivery system tube into the lumen. Anti-LDL SLN was positioned in a region inside the lumen to enable them to interact with the plasma LDL particles. Penetration of the needle into lumen of the vein was checked by the aspiration of blood. Around the region of the tubule insertion site, a 4M silk fixation ligatures were set to prevent bleeding (Figure 6.2(d)). The site of insertion was then covered by the fascia of *m. brachiocephalicus* and *m. sternocephalicus* and both muscles were sutured together (Figure 6.2(f)). The animals were monitored using the score sheet (Appendix C) was taken daily for the duration of the study to monitor changes in vital signs to determine the IVISDDD tolerance level during recovery stage.

6.2.5. Chromatographic qualitative assay of fenofibrate concentration in Large White pig model

Analysis was performed on Waters Acquity UPLC^{TM} system (Waters Corporation, Massachusetts, USA) consisting of a binary solvent manager, a sample manager and a photodiode array (PDA) detector. The mobile phase used was a mixture of methanol and 20mM ammonium acetate in the ratio of 70:30%$^{v/}_{v}$ employing gradient elution. The detector was set at a sampling rate of 20 points s^{-1} and filter time constant of 0.2 seconds. System control, data collection and data processing were accomplished using Waters Empower 2 chromatography data software. The analytical column used was Waters Acquity UPLC BEH C-18 column, 1.7µm, 2.1x100mm (Waters Corporation, Massachusetts, USA). The optimized conditions were as follows: injection volume: 5.0µL, flow rate: 0.6mL/min at a column temperature of 25°C, sample temperature of 37°C and detection wavelength: 254nm at 1.2nm. Stock solutions of fenofibrate (mg/mL) and nicotinic acid (mg/mL) which was used as the internal standard were prepared in methanol. Sheep blood was mixed with different concentrations of fenofibrate to generate calibration standards, which also included quality control standards. To 500µL of plasma 50µL of nicotinic acid was added and vortexed. The drug was extracted using 3mL ethyl acetate followed by centrifugation at 2000 for 15 minutes. The supernatant was then withdrawn and dried using a stream of nitrogen and re-suspended using 250µL of the mobile phase. For validation, specificity was tested using the lowest concentration to show separation of

fenofibrate from impurities in plasma. Linearity was determined by plotting concentrations against peak area ratios of fenofibrate to nicotinic acid.

Table 6.2: UPLC analysis parameters.

Elution Time (min)	Ammonium Acetate ($\%^{v}/_{v}$)	Methanol ($\%^{v}/_{v}$)
Initial	50	50
0.5	60	40
1	10	90
1.5	50	50
3	50	50

6.2.6. Total cholesterol and Lipoprotein levels quantification and characterization

Quantitative colorimetric/fluorimetric determination of HDL, LDL/VLDL and total cholesterol was determined using a HDL and LDL/VLDL assay kit (ab65390, Abcam®, Cambridge, UK). Serum (100µL) was mixed with 100µL of precipitation reagent in a 1.5mL centrifuge tube. The tube was vortexed and centrifuged on a TableTop high-speed centrifuge for 10 minutes at 2000g (TG16-WS, Hunan Xiangyi Laboratory Instrument Development Co., Ltd, Changsha, China). The supernatant was transferred into a clean tube. This was labeled HDL. After removal of all supernatant, the pellet was mixed with 200µL PBS. The mixture was transferred into a new tube and labeled LDL/VLDL. Serum (12µL) was transferred into a new tube and mixed with 108µL assay buffer for analysis of total cholesterol. A standard was made by mixing 5µL of 300mg/dL cholesterol with 145µL assay buffer. A blank was made from 50µL assay buffer. A 96 well plate was used, where 50µL of blank, standard, HDL, LDL/VLDL and total cholesterol was transferred into wells in duplicate. To each well a 50µL of working reagent (44µL assay buffer, 2µL enzyme mix, 2µL cholesterol esterase and 2µL cholesterol probe per well) was added. The plate was tapped to mix the solutions and left at room temperature for 30 minutes. A standard curve was made by diluting the Cholesterol Standard to 0.25µg/µL by adding 20µL of the Cholesterol Standard to 140µL of Cholesterol Assay Buffer. 0, 4, 8, 12, 16, 20µL was added into a series of wells in a 96-well plate. The volume was adjusted to 50µl/well with Cholesterol Assay Buffer to generate 0, 1, 2, 3, 4, 5µg/well of the Cholesterol Standard. The optical density was measured using Victor X3 Luminometer at 570nm wavelength (PerkinElmer Inc., Massachusetts, USA).

6.2.7. Data statistical analysis

All results are presented as mean±SD. Statistical analysis was performed by repeated-measures ANOVA and by t test for paired and unpaired observations. Statistical significance was accepted for $p<.05$.

6.3. Results and Discussion

6.3.1. Post-surgical examination

Post-surgery analysis was conducted to assess implant tolerance, feeding behavior in relation to new atherogenic diet, weight changes, animal wellbeing and maintenance of the catheters. Pigs are increasingly being used as animal models in the area of cardiovascular research because of the similarities of their anatomy and physiology to that of humans, specifically the comparative hemodynamic and coagulation properties (Fudge et al., 2002). The use of the pig model for testing of the responsive implantable osmotic pump was conducted to assess the implant's tolerance and to validate its functionality *in vivo*. The pigs initially weighed 35kg at the onset of the study and at the end of the study, atherogenic pigs weighed 57±2kg whilst the control pig weighed 50kg. Increase in body mass and muscle growth may result in the catheter being pulled out of the vein. To avoid catheter pullout, the study was conducted for a limited duration of 25 days. This experimental timeframe also took into consideration the implant's half-life of 30 days, which is the half-life of the antibodies used for sensing (Apo-B100). Assessment of IVISDDD tolerance indicated no impairment of comfort, as the animals appeared awake, were interested in their surroundings, recumbent or eating after surgery and during the entire study. Feeding behavior was affected neither by the surgery nor by the atherogenic diet. The Incision site on all pigs was kept clean during the study by application of an antiseptic at the site.

6.3.2. Implant induced inflammatory response analysis

Histopathological analysis on the tolerance of the implant was analyzed as a collective characterization of the immune tolerance amongst the animals due to animals immune system exposed to the same implant. An inflammatory response was caused by tissue injury that resulted from the implantation of the device as well as the continual presence of the device in the body. When the tissue was injured by device implantation, a wound healing response was initiated through a series of complex events. The main stages in this process included acute inflammation, chronic inflammation, and the formation of granulomatous tissue. Chronic inflammation characterized by the presence of macrophages, monocytes, and lymphocytes, as

well as the proliferation of blood vessels and connective tissue to restructure the affected area occurred mainly because the implant was not removed but stayed *in situ* for the 25 day study. Morphological evaluation of the implantation site confirmed chronic inflammation of severe degree where macrophages and lymphoplasmacytes predominate with some epithelioid macrophages and multinucleated giant cells also present based on the scoring indicated in Table 6.3. The scoring between the control and experiment pigs was similar due to the implant physiochemical properties being similar.

The chronic inflammatory response is a normal process whereby the multi-nucleated foreign body giant cells and macrophages are required around the implant region to isolate the implant from surround tissue by means of fibrosis. This response has also been reported to occur in response to vascular grafts, pacemaker leads, prostheses, neural probes, glucose biosensor and orthopedic joint prostheses (Bridges et al., 2010). Focal cystic spaces surrounded by the inflammatory cells and the multinucleated cells were evident in this analysis. Focal areas of necrosis as well as small areas of acute inflammation with neutrophil infiltrates were also observed scattered in the implantation site. Scattered eosinophils were also present in between the acute inflammatory infiltrates. Within the necrosis mineralization (dystrophic calcification) was present. Fibrosis was also indicated to be severe with mature dense collagen also evident encapsulating some of the inflammatory infiltrates around the implantation site. This encapsulation has also been reported to occur around glucose biosensor effecting biosensor activity by cutting of the sensors from analytes and also inducing degradation of the implant (Wisniewski et al., 2000). In this study, degradation of the gelatin capsule was also evident.

Table 6.3: Histological analysis of implantation sites based on grading immune response (Scaling 1-5).

Immune Response	**Grading score**
Acute inflammation	2+
Chronic inflammation	3+
Eosinophil	2+
Stromal reaction	3+
Fibrosis	2+

Figure 6.3 indicates the immune response against the implant in both control and experimental pigs. This indicates that after acute inflammation which occurred after surgical intervention, the tissues surrounding the implant started healing. The healing process led to recruitment of immune cells in the implantation site to aid in the healing process. However, due to the

presence of a foreign body, the microphages and multinucleated cells began surrounding the capsule via cell-cell interaction. This caused formation of stromal reaction with vascularization and granulation tissue as well as the collagenous-rich fibrous encapsulation. Moderate neutrophil and eosinophil infiltrates were also present in the inflammatory tissue. Minor necrosis was also observed. This was due to degradation of the capsule via increase in temperature around the insertion site and recruitment of ions. While the former was caused by the tissue injury that resulted from implantation of the device as well as the continual presence of the device in the body, the latter is a result of the body's natural response to the fibrotically confined implanted device that prevents it from interacting with the surrounding tissue (Bhardwaj et al., 2010).

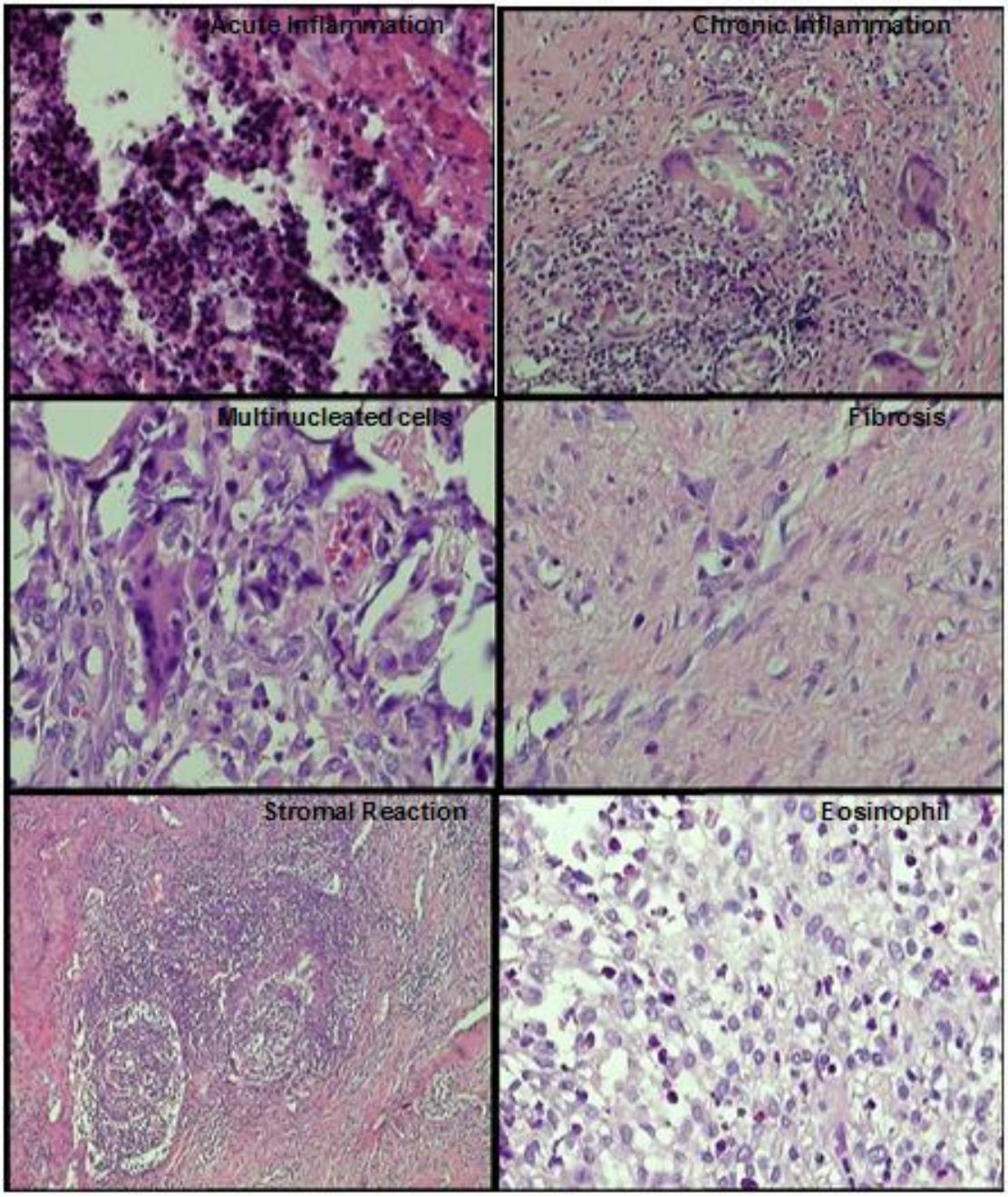

Figure 6.3: Histological micrographs showing representative sections of subcutaneous tissue following implantation of the gelatin reservoir.

6.3.3. Cholesterol level evaluation

Lipoprotein metabolic abnormalities such as LDL often manifest themselves as an increase in number or composition (Checovich et al., 1991). Increase in LDL, HDL and total cholesterol level concentrations were evaluated in this study. Although an elevation in plasma LDL particle number places an individual at increased risk of coronary heart disease, it has been shown that

it is the correlation between a predominance of smaller, denser LDL particles that mostly increased the risk of coronary heart disease (Austin and Krauss, 1986). The anti-LDL SLN used in this study were directed towards binding apolipoprotein B (apoB) which is the major protein constituent of LDL (varying in size and composition). The antibodies have been already been shown to be selective against both unmodified LDL and oxLDL particles in Chapter 3. Genetic variation in the apoB protein causes accumulation of LDL in the plasma because of reduced plasma clearance. Normal LDL half-life in the circulation has been shown to be in the order of 3-4 days (Shepherd, 2003). When plasma clearance does not occur, there is modification of the apoB protein. In this study, the sampling was also conducted every 3 days in order to assess the inclusion of newly synthesized LDL particles when mature LDLs have not been removed from the circulatory system.

In vivo studies expect glycation and oxidation of proteins and lipids to take place which have been shown to contribute to atherogenesis. Glycation is a non-enzymatic process, whereby binding of glucose to apoB protein increases the atherogenic activity of low-density lipoprotein (LDL). In diabetic patients, glycation of LDL is significantly increased in comparison to normal subjects. Metabolic abnormalities associated with glycation of LDL include; diminished recognition of LDL by the classic LDL receptor; increased covalent binding of LDL in vessel walls, enhanced uptake of LDL by macrophages, thus stimulating foam cell formation, increased platelet aggregation, formation of LDL-immune complexes and generation of oxygen free radicals resulting in oxidative damage to both the lipid and protein components of LDL and any nearby macromolecules (Lyons, 1993). The designed implant is applicable for people susceptible to atherosclerosis such as those suffering from diabetes and familial hypercholesterolemia by targeting synthesized LDL before oxidation occurs. Immunodiffusion also indicated that the anti-LDL SLN could also bind to oxidized LDL which indicates that they can also be used in patients who are already suffering from atherosclerosis. Figure 6.4 Indicates the generated standard curve for cholesterol which will be utilized for determine LDL, HDL and total cholesterol levels. Slope, intercept, correlation coefficient (R^2), standard deviation of slope and intercept obtained by the linear least squares treatment of the results were 0.0015, 0.0021 and 0.992 respectively.

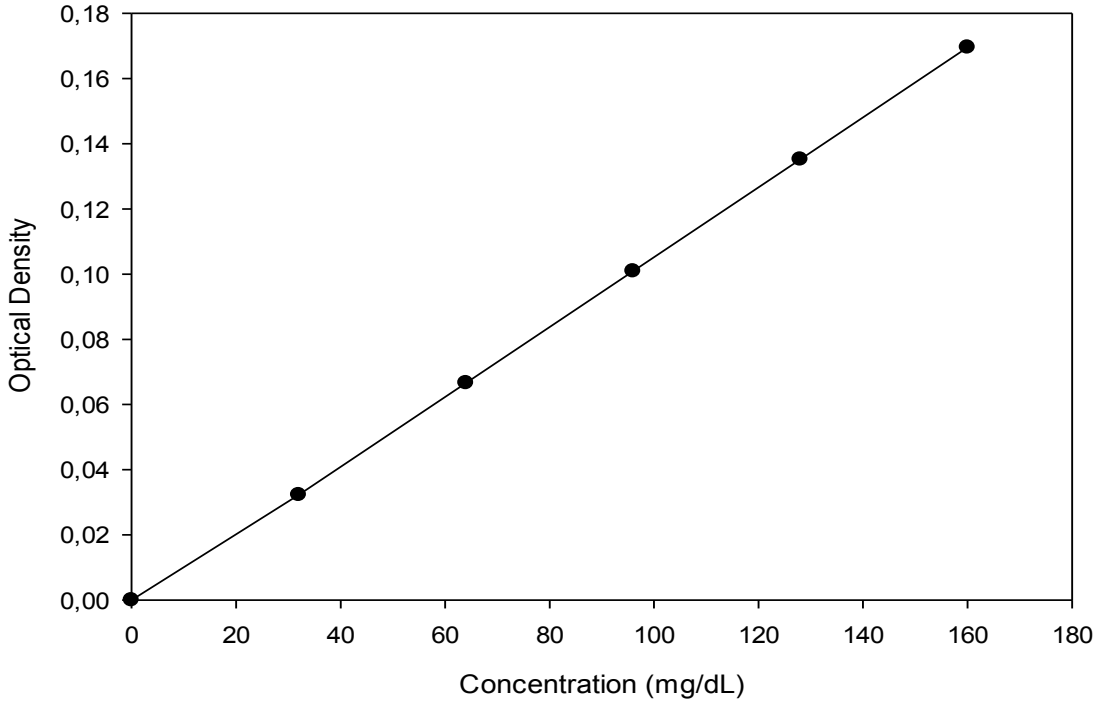

Figure 6.4: Cholesterol standard curve.

Due to elevated levels of serum LDL cholesterol being an important biomarker that indicates the progression of atherogenesis. Similar atherosclerosis development in animals and humans that results from deficiencies in functional LDL receptors mean that there exists alternative pathways for LDL uptake. LDL has been shown to undergo oxidative modification when incubated *in vitro* and exposed to copper ions as shown in Chapter 3 (Steinberg et al., 1989). The oxidized LDLs then cause formation of foam cells. A large fraction of the plasma cholesterol in cholesterol-fed large white pigs was found to be present in LDL, suggesting that cholesterol-fed pigs may represent a suitable model to study the role of LDL and oxidized LDL in the progression of atherosclerosis. Triglyceride levels were not measured, as they did not change significantly in the pigs fed on the atherogenic diet. Figure 6.5 indicates LDL profiles obtained during atherogenic diet and drug delivery testing. The control group had a slightly constant high LDL profile due to the absence of antibodies on the SLN. In terms of the atherogenic pigs, an increase in LDL caused an increase in Apo-B100 protein which was a target for anti-LDL SLN. The decrease in LDL concentration was associated with fenofibrate drug release and increase LDL uptake during anti-LDL SLN-LDL complex clearance. Fenofibrate altered LDL subclass distribution by reducing small dense LDL subclass by causing formation of large buoyant LDL

subclass. This greatly reduces atherosclerosis by removing small dense LDL particles which are more susceptible to oxidation (Davidson et al., 2006). Therefore, the obtained data indicates a 30-42±6.2% decrease in buoyant LDL subtraction, which is known to be atherogenic in atherogenic pigs. In the control group, the level was reduced by 15-20%. The study correlates with previous studies which have shown that miniature pigs fed a 4% cholesterol diet had elevated LDL cholesterol levels; 27+/-3.5mg/dL (mean±SEM, n=36) to 250±28mg/dL (n=10), 260±15mg/dL (n=6), and 260±17mg/dL (n=10) at 6, 14, and 24 weeks, respectively (Holvoet et al., 1999).

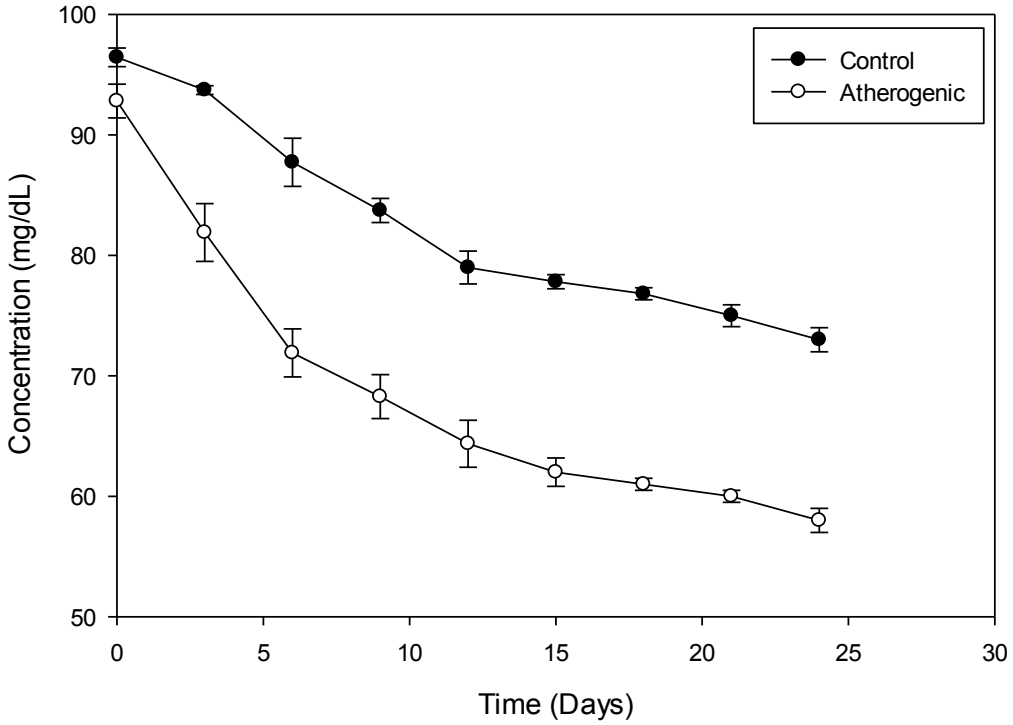

Figure 6.5: LDL concentration profiles for the 25-day study (N=3).

Fenofibrate mainly increase HDL concentration. These particles serve as an anti-atherogenic molecule. Figure 6.6 indicates increase in HDL concentration. In control group, the level of HDL was increased by 40%, whilst in experiment there was about 35-42% increase. The concentration had a slow increased due to dietary induced cholesterol. Without a change in diet, cholesterol levels will continue to be elevated despite use of therapeutics. Studies on fenofibrate activities usually show a reduction in plasma cholesterol and TG levels of 10% to 30% and 30% to 67%, respectively; while VLDL-C and LDL-C are decreased by 30% to 70% and 2% to 29%,

respectively, whereas HDL-C is increased by up to 26% in an 8-week study (Guérin et al., 1996). There have also been observations whereby a reduction of 10% to 37% in apoB concentrations has been reported (Farnier et al., 1994). This indicated that apart from therapeutic intervention, the inclusion of dietary change could play a role in improving levels of HDL elevation and LDL decrease.

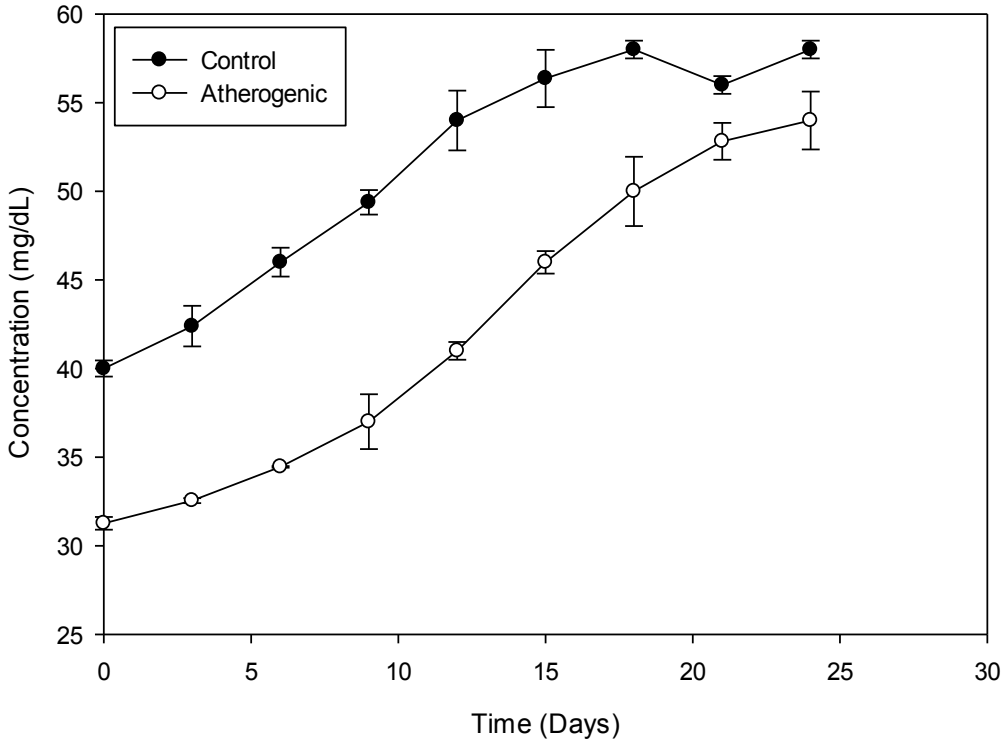

Figure 6.6: HDL concentration profiles obtained in 25-day (N=3).

Due to Large White pigs having been shown to exhibit higher levels of triglycerides, cholesterol, HDL-cholesterol and LDL-cholesterol at any given time, independent of the time after feeding them an atherogenic diet (Freire et al., 1998). Cholesterol has been shown to increase after feeding as the increase in both HDL and LDL cholesterol levels could be associated with the postprandial stimulation of bile secretion (Rector et al., 2004). The higher serum cholesterol level in Large White pigs could be further explained by its positive correlation with body weight gain which may be demonstrated by the high correlation between serum cholesterol at 8 weeks of age and body weight at 4 and 8 weeks of age. This indicates that there is physiological relationship of cholesterol with growth. Due to this feature, the control pig can also be used as a

control for atherogenic diet induced hypercholesterolemia without anti-LDL antibodies as they gain weight. As animals grow the amount of cholesterol in their tissues generally increases (Rauw et al., 2007; Werdi-Pratiwi et al., 2006). Figure 6.7 indicates the obtained data indicating that total cholesterol was reduced and maintained at 130mg/dL during the study. Cholesterol was shown to increase in the control experiment possible because of the increase in body weight and lack of anti-apo-B100 anti-LDL SLN. Total cholesterol level was reduced by 16% in control pig due to degradation of drug loaded nanoparticles during liver uptake causing a burst drug release. In relation to experimental pigs, there is a significant reduction due to increased uptake of the LDL due to anti-LDL SLN-LDL complex and burst drug release that can occur during degradation. Therefore, this indicates that the inclusion of the anti-LDL antibodies on the surface of the SLN led to significant reduction in total cholesterol by 35%, whilst in control pigs; the cholesterol was reduced by 16% and maintained around 129mg/dL.

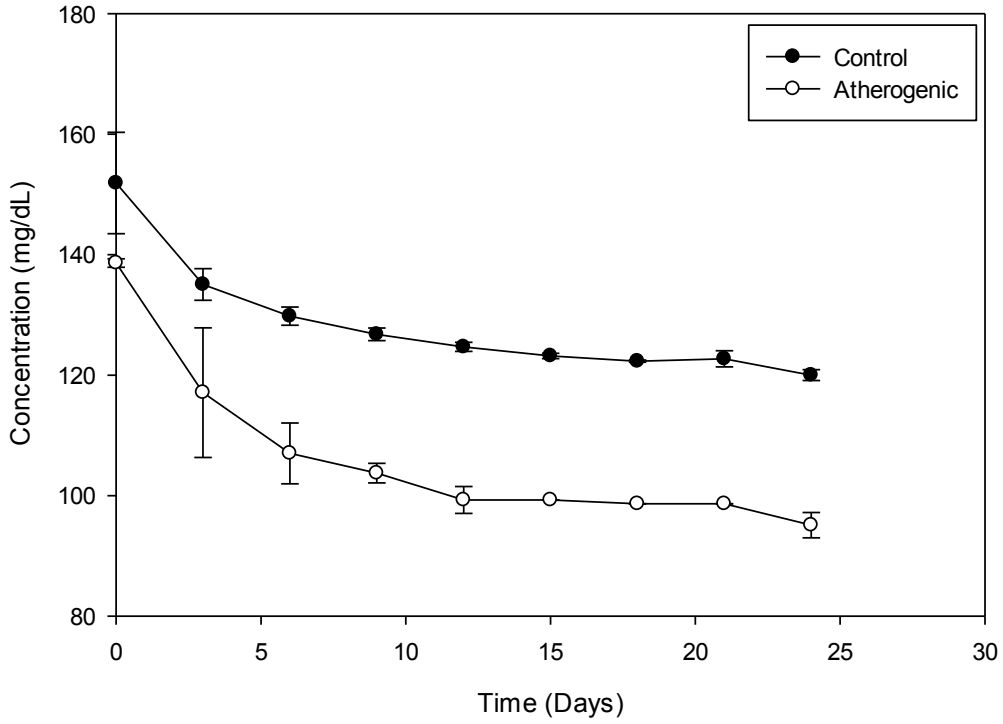

Figure 6.7: Diet induced hypercholesterolemia, reduction of total cholesterol (N=3).

6.3.4. Validation of fenofibrate concentration chromatographic assay

For drug release analysis, a standard curve of fenofibrate was generated. Linearity was maintained primarily within the concentration range of 250-1800µg/mL of fenofibrate as indicated in Chapter 5. Slope, intercept, correlation coefficient (R^2), standard deviation of slope and intercept obtained by the linear least squares treatment of the results were 0.0115, 0.7357 and 0.99 respectively. Fenofibrate was selected as a lipophilic drug model in this study. It has been shown that fenofibrate acts by increasing HDL level, which was proven in Figure 6.6. When baseline HDL-C was <35mg/dL, the increase was much more pronounced and may even reached 40% to 50% (Després, 2001). In relation to LDL-C, fenofibrate has been shown to reduce LDL-C by 25% independent of the HDL-C baseline. Thus, this shows that fenofibrate can be used to increase low levels of HDL-C when there are elevated levels of LDL-C those ranges from 100 to 129mg/dL (Balfour et al., 1990).

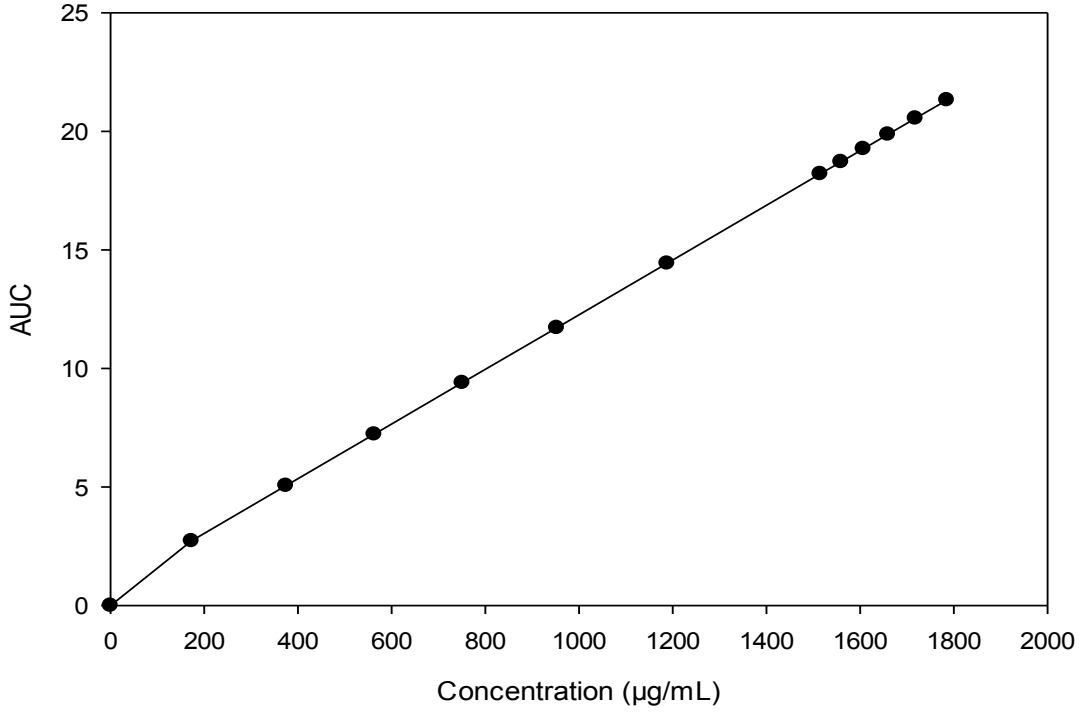

Figure 6.8: Standard curve of fenofibrate obtained by UPLC (N=3, S.D=0.03).

Cumulative drug release of the antibody free SLN in control group was compared to antibody conjugated SLN in atherogenic diet induced hypercholesterolemia pigs. The fluctuations and decrease for drug released in Figure 6.9 indicates a balance between an increase in newly

synthesized LDL concentration induced by diet and the reduction of circulating LDL due to enhanced LDL uptake. The uptake of the SLN-LDL led to burst release of fenofibrate when the SLNs were degraded in the liver. Therefore the drug release indicates that increased uptake of LDL particles by Kupffer cells can play a role in increasing drug release from nanoparticles. In relation to control group, the drug level is lower in control due to the absence of anti-apo-B100 antibodies on the surface of SLN. This indicates that there was no enhancement of LDL uptake which correlated with higher total cholesterol, HDL and LDL levels. There were no major fluctuations in cholesterol and lipoprotein concentration (HDL, LDL and total cholesterol) as their synthesis was independent of drug release rate. The gradual decrease of LDL and total cholesterol was due to the presence of fenofibrate reducing synthesis of LDL and its clearance from the plasma via LDL-receptor activity. This was then followed a gradual increase in HDL cholesterol. Based on the drug release kinetics, the data indicates that the release does not follow the expected zero-order kinetics that has been reported for osmotic pumps. This was due to drug loaded nanoparticles burst release during degradation combining with drug elution during circulation. The high drug release in atherogenic pigs is dependent on increasing LDL concentration, whilst in control is independent. This can aid in increasing therapeutic dose in relation to increase in LDL concentration. The more the anti-LDL SLN bind to LDL particles, the more there is an increase in drug concentration. The fluctuation seen is hypothesized to relate to synthesis of new LDL particles and their half-life. When LDL concentration is high, this led to increase in drug release due to increase LDL uptake, and thus cause burst release during lysosome degradation of anti-LDL SLN-LDL complex.

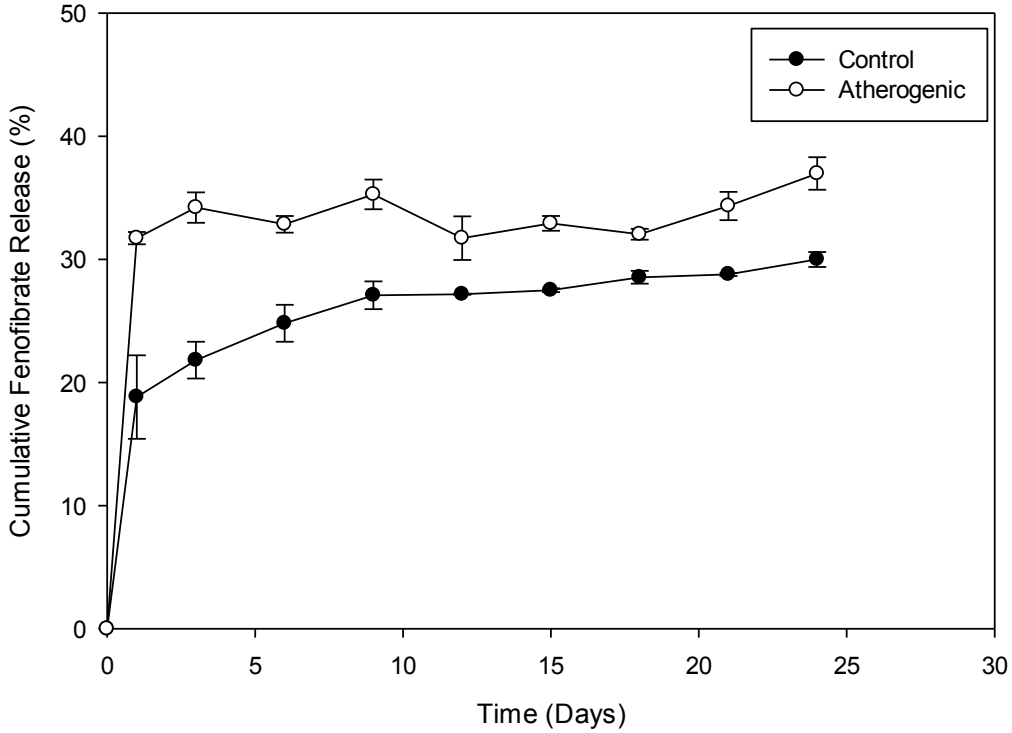

Figure 6.9: *In vivo* drug release profiles in all experimental pigs obtained using UPLC (N=3).

Each drug delivery system is known to have specific drug release kinetics. In this study, the *in vivo* drug release data followed Korsmeyer-Peppas release kinetics based on adjusted R^2 values (Figure 6.10). Zero-order kinetics is a process of constant release based on the observation of the drug dissolution of several types of modified release pharmaceutical dosage forms, as in the case of some transdermal systems, as well as matrix tablets with low soluble drugs (release the drug slowly) in coated forms, osmotic systems and dosage forms that do not disaggregate (Costa and Sousa Lobo, 2001). Zero-order release was observed on antibody free SLN in this study due to drug release being from drug eluting anti-LDL SLN being proportional to amount of LDL synthesized and the rate of anti-LDL SLN-LDL uptake and degradation. Osmotic pumps such as Alzet® pumps have been shown to have zero-order release kinetics (Ghosh and Ghosh, 2011). IVISDDD demonstrated a fluctuation in drug release due to degradation of biodegradable nanoparticles that caused burst release during degradation by the liver, thus causing an increase in dosage during increase in apo-B100 (LDL). First-order kinetics which describes absorption and/or elimination of water-soluble drugs in porous matrices was also observed due to fenofibrate low solubility (lipophilic); Higuchi was slightly favored which describes the drug release from a matrix system where initial drug concentration in the

matrix is much higher than drug solubility, where drug diffusion takes place only in one dimension, drug particles are much smaller than system thickness, matrix swelling and dissolution are negligible, drug diffusivity is constant and perfect sink conditions are always attained in the release environment (Shoaib et al., 2006). This could be linked to the burst release of fenofibrate during degradation.

Hixson-Crowell was partially favored during drug eluting phase prior uptake by liver cells. Hixson-Crowell is described as the process whereby dissolution occurs in planes that are parallel to the drug surface if the drug delivery device dimensions diminish proportionally, in such a manner that the initial geometrical form remains constant all the time. The geometrical form was changed during degradation of the anti-LDL SLN-LDL complex. Based on the adjusted R squared values, the implant indicates to follow Korsmeyer-Peppas drug release which relates to *in vitro* studies. However due to degradation of nanoparticles by liver cells leading to burst release, this caused Fickian diffusion to occur was represented by n values of 0.2 and 0.03 for control and experiment, respectively unlike super case II due to erosion. Baker-Lonsdale was also not favored as it showed that drug release was not dependent on the diffusion coefficient, drug solubility and porosity of the system (Costa and Sousa Lobo, 2001). Overall, in relation to *in vitro* and *ex vivo* studies, Korsmeyer-Peppas release kinetics was always favored during drug release.

In relation to anti-apo-B100 free SLN, conjugations of antibodies on SLN for targeted delivery seem to have offered controlled drug release and increased LDL clearance. Due to fenofibrate reduction of total cholesterol, LDL cholesterol, apo-B, total TG and TG-rich lipoprotein (VLDL), the drug release fluctuations are induced by continuous atherogenic diet whereby more LDL particles (more apoB) are required to carry dietary cholesterol. In terms of the effects on LDL and HDL by fibrates correlated to reported data whereby LDL has been shown to be reduced by 20%–35% and HDL increase by 10%–25% (Chang et al., 2012). This study also supports that management of cholesterol also requires lifestyle modifications, such as weight loss, increasing physical activity and dietary changes (Chang et al., 2012).

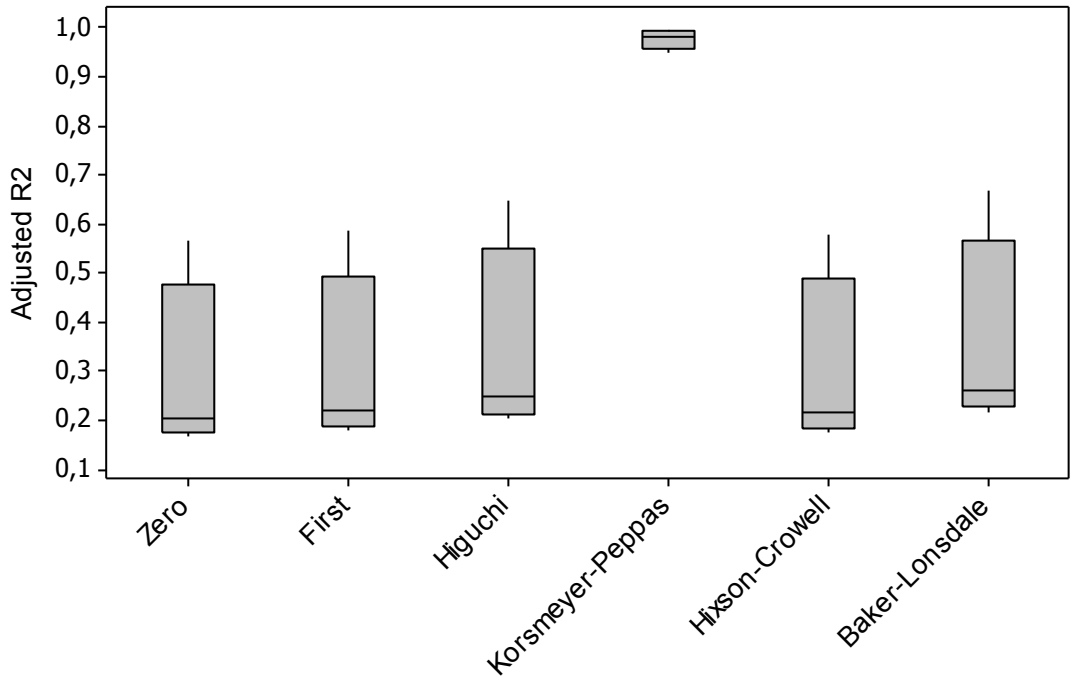

Figure 6.10: Adjusted R^2 of drug release for determination of drug release.

6.4.5. Capsule *in vivo* biodegradation

In vivo biodegradation of the capsule was assessed in relation to hydrolytic and pyrolytic degradation. Implant biodegradation can affect implant function if the degradation kinetics of the polymers *in vivo* does not remain constant to maintain sustained drug release. In this study, biodegradation of the capsule was evaluated at the end of the study in correlation to hydrolytic and pyrolytic degradation. The capsules were found have undergone degradation and absorbed by the surrounding tissue. There was no sign of laceration around capsule region as indicated by histopathological analysis. This indicated that the degradation products were biocompatible. Factors such as temperature and pH also have an effect on the implant degradation kinetics and they may increase or decrease the implant degradation rate. During hydrolytic degradation, the capsule was shown to be stable for more than 16 weeks without evidence of degradation or erosion. Erosion can cause the surface area to change over time. Recent experiments have revealed that a lower gelatin concentration results in a higher degree of degradation strongly suggesting that the observed degradation of the gelatin samples was not due to the action of proteases as, according to the Michaelis–Menten equation, whereby enzyme-catalyzed

degradation would increase with gelatin concentration (Arifin et al., 2006). At the end of the *in vivo* studies, the capsule indicated degradation was occurring.

Protein stability is important, as gelatin chains with a more unfolded conformation are more accessible to the solvent and, as a consequence, more prone to degradation by hydrolysis. In this study it was evident that gelatin degradation involved breaking of the pentosidine and pyridinoline cross-links and the cleavage of peptide bonds (van den Bosch and Gielens, 2003). During acute inflammatory response which occurred for a relatively short duration, permeation of salts, proteins and water through the endothelial tight junctions of the capillary walls was increased and this resulted in edema. This was supported by the histopathological analysis which indicated that the capsules were encapsulated. The presence of salt ions indicated that the type of salt ions, their concentration and the pH of the solution have an influence on the degree of degradation. Salt ions have been shown to assist in cleavage peptide bonds and cross-links. The data indicated that the capsule induced inflammatory responses which cause an increase in degradation of the gelatin due to formation of the fibrotic encapsulation. This problem was also seen in glucose biosensor as previously stated. The immune response was expected as the tissue around the implant was undergoing regeneration. This caused attraction of immune cells to aid in restructuring of the tissue. Due to the implant being a foreign object, a fibroblast was generated generating a microenvironment whereby there was an increase in salt ions and macrophage to combat the implant. This indicates that a more biocompatible device such as Alzet® osmotic pump can be used as an alternative reservoir.

6.3.6. Pharmacokinetics analysis

Pharmacokinetics-Pharmacodynamics was assessed to assess to evaluated impact of fenofibrate. Lipophilic drug are difficult to administer intravenously because of their low aqueous solubility. Addition of solvents may aid solubility but most of the solvents that would work would also have detrimental effects. In this study, the use of pharmacokinetics helped in assessing the efficacy and toxicity of a patient's drug therapy. Table 6.4 indicates the pharmacokinetics parameters, AUC, Mean Residence Time (MRT) and drug elimination time. Lambda-z, the first-order rate constant associated with the terminal (log-linear) portion of the curve was estimated via linear regression of time vs. log concentration. MRT extrapolated to infinity for infusion models was calculated. The high AUC and AUC of fenofibrate delivered by antibody conjugated SLNs demonstrate longer circulation property of anti-LDL SLN. This indicates improved bioavailability of fenofibrate by anti-LDL SLN. The low elimination constant was also supported

by the enhanced half-life and AUC, AUC and AUMC. The lower elimination rate by anti-LDL SLN indicates retention of nanoparticle. This was due to engulfment endocytosis of the LDL-SLN complex by cells with LDL receptors and localization of SLN targeted to different organs, which correlates to drug fluctuations. The elimination time can also vary among different individual due to pharmacogenomics variations. Fibrates are metabolized by the hepatic cytochrome P450 (CYP) 3A4 and genetic variation in this enzyme causes variation in fenofibrate metabolism (Miller and Spence, 1998). Future studies are requiring to access tissue distribution of nanoparticles and correlation of elimination time with pharmacogenetic data. Overall, the infusion anti-LDL SLN improved lowering LDL and increase of HDL by enhancing the circulation time of fenofibrate.

Table 6.4: Pharmacokinetic parameters of anti-LDL SLN and antibody free SLN.

	$AUC_{0\rightarrow t}$(mg/mL h)	$AUC_{0\rightarrow\infty}$(mg/mL h)	$k_{el}(\lambda)$(h^{-1})	MRT(h)	$t_{1/2}\lambda$(h)
Native SLN	103.09±9.1	842.41±12.6	0.12±0.001	7.37±2.5	5.48±1.4
Anti-LDL	98.520±1.190	2366.645±96.895	0.036±0.012	23.110±5.51	16.300±3.7

$AUC_{0\rightarrow t}$: Area under the concentration–time curve for time 0 to time t;k_{el} : terminal elimination rate constant;$AUC_{0-\infty}$: area under the concentration–time curve for time 0 to infinity (∞); $t_{1/2}$: terminal half-life; MRT: mean residence time.

6.4. Concluding Remarks

In this study *in vivo* drug release was shown to follow Korsmeyer-Peppas kinetics, which correlated to *in vitro* studies. In experimental animals whereby the SLN consisted of anti-apo-B100 antibodies, this showed fluctuations of fenofibrate overtime. The fluctuations were hypothesized to have been caused by interaction with newly synthesized LDL particles induced by diet. Interaction with newly synthesized LDL particles caused increased uptake during drug elution phase, which was followed by burst release during degradation. The cholesterol levels correlated to this hypothesis based on the level of reduced total cholesterol and LDL particles and also increased HDL levels. In relation to control animals, the drug and cholesterol levels were maintained at a constant level overtime. Whereas in experimental animals that were placed on an atherogenic diet, dietary cholesterol was significantly decreasing overtime.. However, the immune response indicated the reservoir required refinement as the encapsulation can affect the device function by reducing osmotic rate and rapid degradation of the device. Furthermore, future studies will require assessment of SLN distribution *in vivo*. In conclusion, the presence of the anti-apo-B100 SLN can prevent binding of LDL to scavenger receptors on macrophages present in plaques which leads to activation and release of proteins

such as monocyte chemo-attractant protein 1 (MCP-1) from the macrophages, which recruit new monocytes into the plaque that subsequently become activated, leading to an aggravated state of inflammation (Kamath et al., 2012). This indicates that the infused anti-apo-B100 SLN can function as controlled/responsive drug delivery vehicles and offer immune protection/management against formation of atherogenic plaque.

CHAPTER SEVEN
CONCLUSION AND RECOMMENDATIONS

7.1 Conclusion

A variety of illnesses requires continuous monitoring in order to have efficient therapeutic intervention. Proper selection of biomarkers is vital, as this is the key to diagnosis and activation of the responsive drug delivery system. By detecting an illness before it manifests, therapeutic dosing would relate to the severity of disease change. In this study, designing anti-apo-B100 anti-LDL SLN made of solid lipid nanoparticles enabled detection of both oxidized and native LDL particles which are biomarkers for atherosclerosis. The purpose of embedding anti-LDL SLN in IPN viscoelastic hydrogel was to design a system that changes in pore structure during interaction with antigens to produce an antigen responsive drug delivery system. Due to LDL variation in particles size, molecular imprint hydrogel could not be designed due to imprint region specificity for size and orientation during interaction. A responsive system was then made by conjugating thiolated LDL-SLN complex to acrylate groups of the hydrogel. This allowed change in swelling ratio of the hydrogel, thus allowing increase pore size. However, due to hydrophilic nature of the hydrogel, it required attachment onto a hydrophobic porous tube to prevent collapse when exposed to aqueous environment. The designed polymeric porous tube was successful during *in vitro* and *ex vivo* studies, however due to high mechanical strength; the tube was removed from the study. Torsion of the polymeric tube would cause damage to the pig's arterial wall and damage onto the drug delivery system. An 18Ga. catheter was used for infusion of anti-apo-B100 anti-LDL SLN for *in vivo* studies as an alternative means of designing a responsive drug delivery system.

The "Large White" pig model was used for *in vivo* studies after induction of high cholesterol by feeding the pigs an atherogenic diet consisting of lard and cholesterol. IVISDDD reduced total cholesterol and LDL concentration. Drug release followed zero-order kinetics in anti-LDL SLN free control group. This correlated with osmotic pumps currently on the markets. This type of kinetics however has a limitation due to inability to change infusion rate in relation to dosage required. This was due to constant drug release from nanoparticles. However, in anti-LDL SLN group pigs, fluctuation of drug release correlated with LDL half-life and increase in dietary cholesterol. An increase in LDL concentration led to increased uptake of LDL-anti-LDL SLN complex, which lead to degradation of the complex, leading to burst release. This followed the

Korsmeyer-Peppas release order kinetics. Reduction in LDL concentration was beneficial in reducing chances of LDL oxidation that can cause atherosclerosis. In conclusion, the present study shows great potential for detecting biomarkers for disease prevention and treatment. However, future studies require analysis of anti-LDL SLN tissue distribution which aid in pharmacodynamics analysis. . For confirmation of liver uptake of anti-apo-B100, future imaging studies are required. Due to degradation of the gelatin capsule serving as reservoir, osmotic pump inflammatory response could be improved by means of using Alzet® pump or iPRECIO™ infusion pump as a substitute. This will aid in longer operation of the device. However, for longer infusion periods, changes of total volume of the drug reservoir and infusion rates have to be made. In conclusion, all objectives in this were studies were met. Furthermore, in relation to other osmotic pumps on the market, the IVISDDD indicates to be the only responsive osmotic pump capable of changing dosage of the therapeutic by means of burst release in relation to number of LDL-HDL complex. This device can also be used in detecting pathogens and mutagens.

7.2 Recommendations

The use of osmotic pumps has been shown to offer a chance to increase bioavailability of lipophilic drugs and reduce side effects profile. The use of antibody-conjugated nanoparticles has also shown to be able to enhance LDL plasma clearance. However, the osmotic driven system indicated to have limitation. Osmotic pumps have been shown to have a setback after the pump has reached its maximum swelling or the osmotic reagent has been depleted, thus the device has to be removed and replaced. It is therefore recommended to use peristaltic system for infusion of therapeutics, as this will offer a better control on drug release rate and allow for a refillable system. Based on the location of the implant, continuous implantation can affect compliance. In this study, the device is not ready for human application but veterinary application based on size, location of implantation and lifetime of the implant. However, in relation to Alzet® pumps, the system can be competitive to osmotic system already on the market. Thus, refillable peristaltic driven system can improve compliance.

In relation to the activity of antibody-conjugated nanoparticles, pharmacodynamics analysis is required to assess the organ distribution of the nanoparticle. This will aid in correlating the burst release effect from the nanoparticles during nanoparticle-LDL complex degradation. The implant also indicated to require rescaling in size to allow easy positioning for human trials. However, the reduction in reservoir size will affect the amount of drug stored. This can be corrected by

means of using a more potent drug that would be released at a slower rate, whilst refillable implants would offer better patient compliance. The use of macromolecules (i.e. antibodies) for sensing of chemical imbalance has shown to have better efficacy and sensitivity in comparison to enzyme, but reduced device duration of functioning due macromolecules' short half-life. Genetically modified macromolecules and molecular imprints can aid in increasing device functional duration.

References

Abe, C., Tashiro, T., Tanaka, K., Ogihara, R., Morita, H., 2009. A novel type of implantable and programmable infusion pump for small laboratory animals. J. Pharmacol. Toxicol. Methods 59, 7-12.

Aggour, Y.A., 2000. Thermal decomposition behaviour of ethyl cellulose grafted copolymers in homogeneous media. J. Mater. Res. 35, 1623-1627.

Ahn, K.W., Sampson, N.S., 2004. Cholesterol oxidase senses subtle changes in lipid bilayer structure. Biochemistry. 43, 827-836.

Alvarez, M., Lechuga, L.M., 2010. Microcantiliver-based platforms as biosensing tools. Analyst. 135, 827–836.

Aoun, S.B., Dursun, Z., Koga, T., Bang, G.S., Sotomura, T., Taniguchi, I., 2004. Effect of metal ad-layers on Au (111) electrodes on electrocatalytic oxidation of glucose in an alkaline solution. J. Electroanal. Chem. 567, 175-183.

Aranovich, G., Donohue, M., 1997. Determining Surface Areas from Linear Adsorption Isotherms at Supercritical Conditions. J. Colloid. Interface Sci. 194, 392-397.

Arifin, D.Y., Lee, L.Y., Wang, C.-H., 2006. Mathematical modeling and simulation of drug release from microspheres: Implications to drug delivery systems. Adv. Drug Delivery Rev. 58, 1274-1325.

Arya, S.K., Datta, M., Malhotra, B.D., 2008. Recent advances in cholesterol biosensor. Biosens. Bioelectron. 23, 1083-1100.

Athyros, V.G., Papageorgiou, A.A., Athyrou, V.V., Demitriadis, D.S., Kontopoulos, A.G., 2002. Atorvastatin and micronized fenofibrate alone and in combination in type 2 diabetes with combined hyperlipidemia. Diabetes Care. 25, 1198-1202.

Austin, M.A., Krauss, R.M., 1986. Genetic control of low-density-lipoprotein subclasses. Lancet. 2, 592-595.

Backmann, N., Zahnd, C., Huber, F., Bietsch, A., Plückthum, A., Lang, H., Güntherodt, H., Hegner, M., Gerber, C., 2005. A label free immunosensor array using single-chain antibody fragments. Proc. Natl. Acad. Sci. 102, 14587–14592.

Badia, A., Carlini, R., Fernandez, A., Battaglini, F., Mikkelsen, S.R., English, A.M., 1993. Intramolecular electron-transfer rates in ferrocene-derivatized glucose oxidase. J. Am. Chem. Soc. 115, 7053–7060.

Bae, J., Kim, T., Kim, M., Park, J., Ahn, Y., 2010. Transcriptional Regulation of Glucose Sensors in Pancreatic β-Cells and Liver: An Update. Sensors. 10, 5031-5053.

Bajpai, A.K., Shukla, S.K., Bhanu, S., Kankane, S., 2008. Responsive polymers in controlled drug delivery. Prog. Polym. Sci. 33, 1088-1118.

Baldi, A., Yuandong, G., Loftness, P.E., Siegel, R.A., Ziaie, B., 2003. A hydrogel-actuated environmentally sensitive microvalve for active flow control. J. Microelectromech. Syst. 12, 613-621.

Barati, A., Norouzi, S., Sharafoddinzadeh, S., Davarnejad, R., 2010. Swelling Kinetics Modeling of Cationic Methacrylamide-Based Hydrogels. World Appl. Sci. J. 11, 1336-1341.

Barnes, H.A., 2000. Linear viscoelastic and time effects, in: Barnes, H.A. (Ed.), A Handbook of elementary rheology. Fluid Mechanics, Aberystwyth, pp. 81-106.

Battaglini, F., Koutroumanis, M., English, A.M., Mikkelsen, S.R., 1994. Targeting glucose oxidase at aspartate and glutamate residues with organic two-electron redox mediator. Bioconjugate Chem. 5, 430–435.

Bawarski, W.E., Chidlowsky, E., Bharali, D.J., Mousa, S.A., 2008. Emerging nanopharmaceuticals. Nanomedicine. 4, 273-282.

Bayer, C.L., Peppas, N.A., 2008. Advances in recognitive, conductive and responsive delivery systems. J. Control. Release. 132, 216-221.

Beiler, B., Sáfrány, Á., 2007. Polymer monoliths synthesized by radiation co-polymerization in solution. Radiat. Phys. Chem. 76, 1351-1354.

Belluzo, M., Ribone, M., Lagier, C., 2008. Assembling Amperometric Biosensors for Clinical Diagnostics. Sensors. 8, 1366-1399.

Beltowski, J., Wojcicka, G., Mydlarczyk, M., Jamroz, A., 2002. The effect of peroxisome proliferator-activated receptors alpha (PPARalpha) agonist, fenofibrate, on lipid peroxidation, total antioxidant capacity, and plasma paraoxonase 1 (PON 1) activity. J. Physiol. Pharmacol. 53, 463-475.

Bergmann, N.M., Peppas, N.A., 2008. Configurational Biomimetic Imprinting for Protein Recognition: Structural Characteristics of Recognitive Hydrogels. Ind. Eng. Chem. Res. 47, 9099-9107.

Berna, A., 2010. Metal oxide sensors for electronic noses and their application to food analysis. Sensors. 10, 3882–3910.

Bhardwaj, U., Sura, R., Papadimitrakopoulos, F., Burgess, D.J., 2010. PLGA/PVA hydrogel composites for long-term inflammation control following s.c. implantation. Int. J. Pharm. 384, 78-86.

Bhattacharya, A., Misra, B.N., 2004. Grafting: a versatile means to modify polymers: Techniques, factors and applications. Prog. Polym. Sci. 29, 767-814.

Bhattacharyya, A., Klapperrich, C.M., 2007. Design and testing of a disposable microfluidic chemiluminescent immunoassay for illness biomarkers in human serum samples. Biomed. Microdevices. 9, 245-251.

Bhattarai, N., Ramay, H.R., Gunn, J., Matsen, F.A., Zhang, M., 2005. PEG-grafted chitosan as an injectable thermosensitive hydrogel for sustained protein release. J. Control. Release. 103, 609-624.

Blaha, M., Masin, V., Stransky, P., Blaha, V., Cermanova, M., Maly, J., Belada, D., 2005. Optimization of the therapeutic procedure during LDL-apheresis--a computerized model. Transfus. Apher. Sci. 32, 149-156.

Bondi, M.L., Azzolina, A., Craparo, E.F., Lampiasi, N., Capuano, G., Giammona, G., Cervello, M., 2007. Novel cationic solid-lipid nanoparticles as non-viral vectors for gene delivery. J. Drug Target. 15, 295-301.

Braunecker, W.A., Matyjaszewski, K., 2007. Controlled/living radical polymerization: Features, developments, and perspectives. Prog. Polym. Sci. 32, 93-146.

Bridges, A.W., Whitmire, R.E., Singh, N., Templeman, K.L., Babensee, J.E., Lyon, L.A., García, A.J. 2010. Chronic inflammatory response to microgel-based implant coatings. J. Biomed. Mater. Res. A 94, 252-258.

Brown, W.P., Tipper, C.F.H., 1978. The pyrolysis of cellulose derivatives. J. Appl. Polym. Sci. 22, 1459-1468.

Buenger, D., Topuz, F., Groll, J., 2012. Hydrogels in sensing applications. Prog. Polym. Sci. 37, 1678-1719.

Byrne, B., Stack, E., Gilmartin, N., O'Kennedy, R., 2009. Antibody-based sensors: Principles, problems and potential for detection of pathogens and associated toxins. Sensors. 9, 4407–4445.

Byrne, M.E., Park, K., Peppas, N.A., 2002. Molecular imprinting within hydrogels. Adv. Drug Delivery Rev. 54, 149-161.

Çağlayan, M.O., Sayar, F., Demerel, G., Garipcan, B., Otman, B., Celen, B., Piskin, E., 2009. Stepwise formation approach to improve ellipsometric biosensor response. Nanomedicine. 5, 152–161.

Calara, F., Dimayuga, P., Niemann, A., Thyberg, J., Diczfalusy, U., Witztum, J.L., Palinski, W., Shah, P.K., Cercek, B., Nilsson, J., Regnstrom, J., 1998. An animal model to study local oxidation of LDL and its biological effects in the arterial wall. Arterioscler. Thromb. Vasc. Biol. 18, 884-893.

Caldorera-Moore, M., Peppas, N.A., 2009. Micro- and nanotechnologies for intelligent and responsive biomaterial-based medical systems. Adv. Drug Delivery Rev. 61, 1391-1401.

Cao, X., Lai, S., Lee, L.J., 2001. Design of a self-regulated drug delivery device. Biomed Microdevices. 3, 109–118.

Carmena, R., Duriez, P., Fruchart, J.C., 2004. Atherogenic lipoprotein particles in atherosclerosis. Circulation. 109, III2-7.

Cass, A.E.G., Graham, D., Francis, G.D., Hill, H.A., 1984. Ferrocene-mediated enzyme electrode for amperometric determination of glucose. J. Am. Chem. Soc. 56, 667-671.

Cecchi, E., Giglioli, C., Valente, S., Lazzeri, C., Gensini, G.F., Abbate, R., Mannini, L., 2011. Role of hemodynamic shear stress in cardiovascular disease. Atherosclerosis. 214, 249-256.

Ceulemans, J., Van Santvliet, L., Ludwig, A., 1999. Evaluation of continuous shear and creep rheometry in the physical characterisation of ointments. Int. J. Pharm. 176, 187-202.

Chambers, A.F., Vanderhyden, B.C., 2006. Ovarian Cancer Biomarkers in Urine. Clin. Cancer Res. 12, 323-327.

Chambin, O., Jannin, V., Champion, D., Chevalier, C., Rochat-Gonthier, M.H., Pourcelot, Y., 2004. Influence of cryogenic grinding on properties of a self-emulsifying formulation. Int. J. Pharm. 278, 79-89.

Chang, C.N., How, C.H., Tavintharan, S., 2012. Beyond low-density lipoprotein cholesterol: why, who and when. Singapore Med. J. 53, 566-568.

Chapman, M.J., Goldstein, S., 1976. Comparison of the serum low density lipoprotein and of its apoprotein in the pig, rhesus monkey and baboon with that in man. Atherosclerosis. 25, 267-291.

Charles, P., Stubbs, V., Soto, C., Martin, B., White, B., Taitt, C., 2009. Reduction of Non-Specific Protein Adsorption Using Poly(ethylene) Glycol (PEG) Modified Polyacrylate Hydrogels In Immunoassays for Staphylococcal Enterotoxin B Detection. Sensors. 9, 645-655.

Chaubey, A., Malhorta, B.D., 2002. Mediated biosensors. Biosens. Bioelectron. 17, 441-456.

Checovich, W.J., Aiello, R.J., Attie, A.D., 1991. Overproduction of a buoyant low density lipoprotein subspecies in spontaneously hypercholesterolemic mutant pigs. Arterioscler. Thromb. 11, 351-361.

Cheng, S.Z.D., Jin, S., 2002. Chapter 5 Crystallization and melting of metastable crystalline polymers, in: Stephen, Z.D.C. (Ed.), Handbook of Thermal Analysis and Calorimetry. Elsevier Science B.V., pp. 167-195.

Chiu, J.J., Chien, S., 2011. Effects of disturbed flow on vascular endothelium: pathophysiological basis and clinical perspectives. Physiol. Rev. 91, 327-387.

Chiu, M.H., Prenner, E.J., 2011. Differential scanning calorimetry: An invaluable tool for a detailed thermodynamic characterization of macromolecules and their interactions. J. Pharm. Bioall. 3, 39-59.

Colburn, W.A., 2000. Optimizing the use of biomarkers, surrogate endpoints, and clinical endpoints for more efficient drug development. Journal of clinical pharmacology 40, 1419–1427.
Condon, J.B., 2006. Chapter 1 - An Overview of Physisorption, Surface Area and Porosity Determinations by Physisorption. Elsevier Science, Amsterdam, pp. 1-27.

Cooper, J.D., Heppert, K.E., Davies, M.I., Lunte, S.M., 2007. Evaluation of an osmotic pump for microdialysis sampling in an awake and untethered rat. J. Neurosci. Meth. 160, 269-275.

Costa, P., Sousa Lobo, J.M., 2001. Modeling and comparison of dissolution profiles. Eur. J. Pharm. Sci. 13, 123-133.

Davidson, M.H., Bays, H.E., Stein, E., Maki, K.C., Shalwitz, R.A., Doyle, R., 2006. Effects of fenofibrate on atherogenic dyslipidemia in hypertriglyceridemic subjects. Clin. Cardiol. 29, 268-273.

De Jong, W.H., Borm, P.J., 2008. Drug delivery and nanoparticles:applications and hazards. Int. J. Nanomedicine. 3, 133-149.

De, S.K., Aluru, N.R., Johnson, B., Crone, W.C., Beebe, D.J., Moore, J.S., 2002. Equilibrium Swelling and Kinetics of pH-Responsive Hydrogels: Models, Experiments, and Simulations. J. Microelectromech. Syst. 11, 544–555.

Deligkaris, K., Tadele, T.S., Olthuis, W., Berg van den, A., 2010. Hydrogel-based devices for biomedical applications. Sens. Actuators B Chem. 147, 765-775.

Denkbas, E.B., Odabasi, M.J., 2000. Chitosan microspheres and sponges: Preparation and characterization. J. Appl. Polym. Sci. 76, 1637-1643.

Deo, S.K., Moschou, E.A., Peteu, S.F., Bachas, L.G., Daunert, S., Eisenhardt, P.E., Madou, M.J., 2003. Peer Reviewed: Responsive Drug Delivery Systems. Anal. Chem. 75, 206 A-213 A.

Dey, N., Majumdar, S., Rao, M., 2008. Multiparticulate drug delivery systems for controlled release. Trop. J. Pharm. Res. 7, 1067-1075.

Dhakar, R.C., Maurya, S.D., Sagar, B.P.S., Prajapati, S.K., Jain, C.P., 2010. Variables influencing the drug entrapment efficiency of microspheres: a pharmaceutical review. Der Pharmacia Lettre. 2, 102-116.

Di Francesco, F., Fuoco, R., Trivella, M.G., Ceccarini, A., 2005. Breath analysis: trends in techniques and clinical applications. Microchem. J. 79, 405-410.

Di Lorenzo, M.L., Sajkiewicz, P., La Pietra, P., Gradys, A., 2006. Irregularly shaped DSC exotherms in the analysis of polymer crystallization. Polym. Bull. 57, 713-721.

Di Natale, C., Macagnano, A., Martinelli, E., Paolesse, R., D'Arcangelo, G., Roscioni, C., Finazzi-Sgro, A., D'Amice, A., 2003. Lung cancer identification by means of analysis of breath by means of an array of non-selective gas sensors. Biosens. Bioelectron. 18, 1209–1218.

Dzyadevych, S.V., Arkhypova, V.N., Soldatkin, A.P., El'skaya, A.V., Martelet, C., Jaffrezic-Renault, N., 2008. Amperometric enzyme biosensors: Past, present and future. IRBM. 29, 171-180.

Eddington, D., Beebe, D., 2005. Development of a Disposable Infusion System for the Delivery of Protein Therapeutics. Biomed. Microdevices. 7, 223-230.

El-Hamed, F., Dave, N., Liu, J., 2011. Stimuli-responsive releasing of gold nanoparticles and liposomes from aptamer-functionalized hydrogels. Nanotechnology. 22, 0957-4484.

Emara, L.H., Taha, N.F., Mursi, N.M., 2009. Investigation of the effect of different flow-through cell designs on the release of diclofenac sodium SR tablets. Dissolut. Technol. 16, 23-31.

Emara, L.H., Taha, N.F., Badr, R.M., Mursi, N.M. 2012. Development of an osmotic pump system for controlled diclofenac sodium. Drug Discov. Ther. 6, 269-277.

Erickson, D., Mandal, S., Yang, A.J., Cordovez, B., 2008. Nanobiosensors: optofluidic, electrical and mechanical approaches to biomolecular detection at the nanoscale. Microfluid Nanofluid. 4, 33-52.

Erk, K.A., Martin, J.D., Hu, Y.T., Shull, K.R., 2012. Extreme Strain Localization and Sliding Friction in Physically Associating Polymer Gels. Langmuir. 28, 4472-4478.

Fernández-Garcia, M., Martinez, J.J., Madruga, E.L., 1998. Solvent effects on the free-radical polymerization of methyl methacrylate. Polym. J. 39, 991-995.

Foerstendorf, H., Benda, C., Gärtner, W., Storf, M., Scheer, H., Siebert, F., 2001. FTIR Studies of Phytochrome Photoreactions Reveal the CO Bands of the Chromophore: Consequences for Its Protonation States, Conformation, and Protein Interaction†. Biochemistry. 40, 14952-14959.

Fournier, E., Passirani, C., Montero-Menei, C.N., Benoit, J.P., 2003. Biocompatibility of implantable synthetic polymeric drug carriers: focus on brain biocompatibility. Biomaterials. 24, 3311-3331.

Franck, A., 2005. Creep recovery measurements of polymers, 77th Annual Meeting of the American Society of Rheology. TA Instruments, Vancouver, pp. 1-7.

Frasco, M., Chaniotakis, N., 2009. Semiconductor Quantum Dots in Chemical Sensors and Biosensors. Sensors 9, 7266-7286.

Freitas, C., Müller, R.H., 1998. Effect of light and temperature on zeta potential and physical stability in solid lipid nanoparticle (SLN™) dispersions. Int. J Pharm. 168, 221-229.

Fudge, M., Coleman, R.E., Rlat, B.S., Parker, S.B., 2002. A minimally invasive percutaneous technique for vein catherization in pigs. J Am Assoc Lab Anim Sci. 21, 38-42.

Garcia, J., Zhang, Y., Taylor, H., Cespedes, O., Webb, M.E., Zhou, D., 2011. Multilayer enzyme-coupled magnetic nanoparticles as efficient, reusable biocatalysts and biosensors. Nanoscale. 3, 3721-3730.

Gaziano, T.A., Pagidipati, N., 2013. Scaling up chronic disease prevention interventions in lower- and middle-income countries. Annu. Rev. Public Health. 34, 317-335.

Gerard, M., Chaubey, A., Malhotra, B.D., 2002. Application of conducting polymers to biosensors. Biosens. Bioelectron. 17, 345-359.

Ghaffari, M.A., Ghiasvand, T., 2010. Kinetic study of low density lipoprotein oxidation by copper. IJCB. 25, 29-36.

Ghosh, T., Ghosh, A., 2011. Drug delivery through osmotic systems-an overview. J. App. Pharm. Sci. 1, 38-49.

Gifford, R., Kehoe, J.J., Barnes, S.L., Kornilayev, B.A., Alterman, M.A., Wilson, G.S., 2006. Protein interactions with subcutaneously implanted biosensors. Biomaterials. 27, 2587-2598.

Gil, E.S., Hudson, S.M., 2004. Stimuli-responsive polymers and their bioconjugates. Prog. Polym. Sci. 29, 1173-1222.

Giljohann, D.A., Mirkin, C.A., 2009. Drivers of biodiagnostic development. Nat. 462, 461-464.

Gokce, E.H., Ozyazici, M., Souto, E.B., 2010. Nanoparticulate strategies for effective delivery of poorly soluble therapeutics. Ther Deliv. 1, 149-167.

Gonzalo-Ruiz, J., Mas, R., de Haro, C., Cabruja, E., Camero, R., Alonso-Lomillo, M.A., Muñoz, F.J., 2009. Early determination of cystic fibrosis by electrochemical chloride quantification in sweat. Biosens. Bioelectron. 24, 1788-1791.

Goppert, T.M., Muller, R.H., 2003. Plasma protein adsorption of Tween 80- and poloxamer 188-stabilized solid lipid nanoparticles. J Drug Target. 11, 225-231.

Gracia-Fernández, C.A., Gómez-Barreiro, S., Ruíz-Salvador, S., Blaine, R., 2005. Study of the degradation of a thermoset system using TGA and modulated TGA. Prog Org Coat. 54, 332-336.

Grayson, A.C., Shawgo, R.S., Johnson, A.M., Flynn, N.T., Li, Y., Cima, M.J., Langer, R., 2004. A BioMEMS review: MEMS technology for physiologically integrated devices. Proceeding of the IEEE. 92, 6-21.

Hancock, B., Shamblin, S., Zografi, G., 1995. Molecular Mobility of Amorphous Pharmaceutical Solids Below Their Glass Transition Temperatures. Pharm. Res. 12, 799-806.

Hasler-Rapacz, J., Kempen, H.J., Princen, H.M., Kudchodkar, B.J., Lacko, A., Rapacz, J., 1996. Effects of simvastatin on plasma lipids and apolipoproteins in familial hypercholesterolemic swine. Arterioscler. Thromb. Vasc. Biol. 16, 137-143.

Hickey, T., Kreutzer, D., Burgess, D.J., Moussy, F., 2002. *In vivo* evaluation of a dexamethasone/PLGA microsphere system designed to suppress the inflammatory tissue response to implantable medical devices. J. Biomed. Mater. Res. 61, 180-187.

Higgins, J.S., Lipson, J.E.G., White, R.P., 2010. A simple approach to polymer mixture miscibility. Phil. Trans. R. Soc. A. 368, 1009-1025.

Hill, A., Geibler, S., Weigandt, M., Mader, K., 2012. Controlled delivery of nanosuspensions from osmotic pumps: Zero order and non-zero order kinetics. J. Controll Release. 158, 403-412.

Hirsch, J.D., Eslamizar, L., Filanoski, B.J., Malekzadeh, N., Haugland, R.P., Beechem, J.M., Haugland, R.P., 2002. Easily reversible desthiobiotin binding to streptavidin, avidin, and other biotin-binding proteins: uses for protein labeling, detection, and isolation. Anal. Biochem. 308, 343-357.

Hoare, T.R., Kohane, D.S., 2008. Hydrogels in drug delivery: Progress and challenges. Polymer. 49, 1993-2007.

Hock, B., Seifert, M., Kramer, K., 2002. Engineering receptors and antibodies for biosensors. Biosens. Bioelectron. 17, 239-249.

Hodgson, D.S., 2007. Comparison of isoflurane and servoflurane for short-term anesthesia in piglets. J Vet. Ana. 2, 117-124.

Hoffman, A.S., 2002. Hydrogels for biomedical applications. Adv. Drug Delivery Rev. 54, 3-12.

Holvoet, P., Collen, D., Van de Werf, F., 1999. Malondialdehyde-modified LDL as a marker of acute coronary syndromes. JAMA. 281, 1718-1721.

Hopkins, P.N., 2010. Defining the challenges of familial hypercholesterolemia screening: Introduction. J Clin Lipidol. 4, 342-345.

Huang, J.T., Leweke, F.M., Oxley, D., Wang, L., Harris, N., Koethe, D., Gerth, C.W., Nolden, B.M., Gross, S., Schreiber, D., Reed, B., Bahn, S., 2006. Disease biomarkers in cerebrospinal fluid of patients with first-onset psychosis. PLoS Med 3.

Hussain, M., Wackerlig, J., Lieberzeit, P., 2013. Biomimetic Strategies for Sensing Biological Species. Biosensors. 3, 89-107.

Boppa, V, 2009. Characterization of Structure and Tensile Properties of Electrospun. Master of Science. North Carolina: North Carolina State University pp. 94-97

Inzelt, G., Pineri, M., Scheltze, J.W., Vorotyntsev, M.A., 2000. Electron and proton conducting polymers: Recent developments and prospects. Electrochimica Acta. 45, 2403-2421.

Ivnitski, D., Abdel-Hamid, I., Atanasov, P., Wilkins, E., 1999. Biosensor for detection of pathogenic bacteria. Biosens. Bioelectron. 14, 599–624.

Jackson, J.K., De Rosa, M.E., Winter, H.H., 1994. Molecular Weight Dependence of Relaxation Time Spectra for the Entanglement and Flow Behavior of Monodisperse Linear Flexible Polymer. Macromolecules. 27, 2426-2431.

Jagur-Grodzinski, J., 1999. Biomedical application of functional polymers. React Funct Polym. 39, 99-138.

Jamzad, S., Fassihi, R., 2006. Role of surfactant and pH on dissolution properties of fenofibrate and glipizide—A technical note. AAPS PharmSciTech 7, E17-E22.

Jankovic, B., 2013. Thermal characterization and detailed kinetic analysis of Cassava starch thermo-oxidative degradation. Carbohydr Polym 95, 621-629.

Jean-Francois, J., Fortier, G., 1996. Immobilization of L-asparaginase into a biocompatible poly(ethylene glycol)-albumin hydrogel: I: Preparation and *in vitro* characterization. Biotechnol Appl Biochem 23, 221-226.

Jeong, B., Gutowska, A., 2002. Lessons from nature: stimuli-responsive polymers and their biomedical applications. Trends Biotechnol. 20, 305-311.

Joshi, J.R., Patel, R.P., 2012. Role of biodegradable polymers in drug delivery. nternational J.Curr. Pharm. Res. 4, 74-81.

Kabiri, K., Omidian, H., Zohuriaan-Mehr, M.J., 2003. Novel approach to highly porous superabsorbent hydrogels: synergistic effect of porogens on porosity and swelling rate. Poly. Int. 52, 1158-1164.

Kamath, A.V., Williams, S.P., Bullens, S., Cowan, K.J., Stenberg, Y., Cherry, S.R., Rendig, S., Kukis, D.L., Griesemer, C., Damico-Beyer, L.A., Bunting, S., 2012. Pharmacokinetics and Biodistribution of a Human Monoclonal Antibody to Oxidized LDL in Cynomolgus Monkey Using PET Imaging. PLoS ONE 7, e45116.

Katsikas, L., Popović, I.G., 2003. Improvement to the Flynn−Wall Method of Determining Apparent Activation Energies of the Thermal Degradation of Polymers†. J. Phys. Chem B. 107, 7522-7525.

Keck, C.M., Muller, R.H., 2006. Drug nanocrystals of poorly soluble drugs produced by high pressure homogenisation. Eur. J. Pharm. Biopharm. 62, 3-16.

Khan, Z.A., Tripathi, R., Mishra, B. 2012. Design and evaluation of enteric coated microporous osmotic pump tablet (ECMOPT) of quetiapine fumarate for the treatement of psychosis. Acta Pol Pharm. 69, 1125-1136.

Killard, A.J., Deasy, B., O'Kennedy, R., Smyth, M.R., 1995. Antibodies: Production, function and application in biosensors. Trend. Anal. Chem. 14, 257–266.

Kim, S., Kim, J.-H., Jeon, O., Kwon, I.C., Park, K., 2009. Engineered polymers for advanced drug delivery. Eur. J. Pharm. Biopharm. 71, 420-430.

Korshunov, V.A., Schwartz, S.M., Berk, B.C., 2007. Vascular remodeling: hemodynamic and biochemical mechanisms underlying Glagov's phenomenon. Arterioscler Thromb Vasc Biol. 27, 1722-1728.

Korsmeyer, R.W., Gurny, R., Doelker, E., Buri, P., Peppas, N.A., 1983. Mechanisms of solute release from porous hydrophilic polymers. Int. J. Pharm. 15, 25-35.

Kumar, P., Mishra, B., 2007. An overview of recent patents on oral osmotic drug delivery systems. Recent Pat. Drug Deliv. Formul. 1, 236-255.

Kurniawan, N.Y., Enemark, S., Rajagopalan, R., 2012. The role of structure in the nonlinear mechanics of cross-linked semiflexible polymer networks. J. Chem. Phys. 136, 1-9.

Kutchta, F., Van Herk, A., German, A.L., 2000. Propagation Kinetics of Acrylic and Methacrylic Acid in Water and Organic Solvents Studied by Pulsed-Laser Polymerization. Macromolecules 33, 3641-3649.

Kwon, Y.M., Kim, S.W., 2005. Thermosensitive Biodegradable Hydrogels for the Delivery of Therapeutic Agents, in: Kwon, G.S. (Ed.), Polymeric Drug Delivery Systems (DRUGS AND THE PHARMACEUTICAL SCIENCES). PharmaceuTech, Inc, Carolina, pp. 251-264.

Laboria, N., Fragoso, A., Kemmer, W., Latta, D., Nilson, O., Botero, M.L., Drese, K., O'Sullivan, C.K., 2010. Amperometric immunosensors for carcinoembryonic antigen in colon cancer samples based on monolayers of dentritic bipodal scaffolds. Anal. Chem. 82, 1712–1719.

Langer, K., Coester, C., Weber, C., von Briesen, H., Kreuter, J., 2000. Preparation of avidin-labeled protein nanoparticles as carriers for biotinylated peptide nucleic acid. Eur. J. Pharm. Biopharm. 49, 303-307.

Lapin, N.A., Chabal, Y.J., 2009. Infrared Characterization of Biotinylated Silicon Oxide Surfaces, Surface Stability, and Specific Attachment of Streptavidin. J Phys Chem. B. 113, 8776-8783.

Lastoskie, C.M., Gubbins, K.E. 2001. Characterization of Porous Materials Using Molecular Theory and Simulation. Adv Chem Eng. 28, 203-250.

Lee, C.H., Moturi, V., Lee, Y., 2009. Thixotropic property in pharmaceutical formulations. J. Control Release. 136, 88-98.

Levicky, R., Horgan, A., 2005. Physicochemical perspectives on DNA microarray and biosensor technologies. Trends Biotechnol. 23, 143–149.

Li, C., Han, J., Ahn, C.H., 2007. Flexible biosensors on spirally rolled micro tube for cardiovascular *in vivo* monitoring. Biosens. Bioelectron. 22, 1988–1993.

Lin, J., Wei, Z., Mao, C., 2011. A label-free immunosensor based on modified mesoporous silica for simultaneous determination of tumor markers. Biosens. Bioelectron. 29, 40–45.

Lu, C.J., Kao, H.L., Sun, Y., Liu, H.M., Jeng, J.S., Yip, P.K., Lee, Y.T., 2003. The hemodynamic effects of internal carotid artery stenting: a study with color-coded duplex sonography. Cerebrovasc Dis. 15, 264-269.

Lucas, N., Bienaime, C., Belloy, C., Queneudec, M., Silvestre, F., Nava-Saucedo, J.-E., 2008. Polymer biodegradation: Mechanisms and estimation techniques – A review. Chemosphere. 73, 429-442.

Lyons, T.J., 1993. Glycation and oxidation: A role in the pathogenesis of atherosclerosis. Am. J. Cardiol. 71, B26-B31.

Lyu, S., Untereker, D., 2009. Degradability of Polymers for Implantable Biomedical Devices. Int. J. Mol. Sci. 10, 4033-4065.

Machado, R.F., Laskowski, D., Deffenderfer, O., Burch, T., Zheng, S., Mazzone, P.J., Mekhail, T., Jennings, C., Stoller, J.K., Pyle, J., Duncan, J., Dweik, R.A., Erzurum, S.C., 2005. Detection of lung cancer by sensor array analyses of exhaled breath. Am. J. Respir. Crit. Care Med. 171, 1286–1291.

Malam, Y., Loizidou, M., Seifalian, M., 2009. Liposome and nanoparticles: Nanosized vehicles for drug delivery in cancer. Trends Pharmacol. Sci. 30, 592-599.

Malek, A.M., Alper, S.L., Izumo, S., 1999. Hemodynamic shear stress and its role in atherosclerosis. JAMA. 282, 2035-2042.

Martin-Palma, R.J., Manso, M., Torres-Costa, V., 2009. Optical biosensor based on semiconductor nanostructures. Sensors. 9, 5149–5172.

Maximov, V.D., Reukov, V.V., Barry, J.N., Cochrane, C., Vertegel, A.A., 2010. Protein-nanoparticle conjugates as potential therapeutic agents for the treatment of hyperlipidemia. Nanotechnology. 21, 0957-4484.

Mayeux, R., 2004. Biomarkers: potential uses and limitations. NeuroRx. 1, 182-188.

McNally, H., Pingle, M., Lee, S.W., Guo, D., Bergstrom, D.E., Bashir, R., 2003. Self-assembly of micro- and nano-scale particles using bio-inspired events. Appl. Surf. Sci. 214, 109-119.

Meilander, N.J., Yu, X., Ziats, N.P., Bellamkonda, R.V., 2001. Lipid-based microtubular drug delivery vehicles. J. Control Release. 71, 141-152.

Melekaslan, D., Okay, O., 2000. Swelling of strong polyelectrolyte hydrogels in polymer solutions: effect of ion pair formation on the polymer collapse. Polymer. 41, 5737-5747.

Meng, E., Hoang, T., 2012. MEMS-enabled implantable drug infusion pumps for laboratory animal research, preclinical, and clinical applications. Adv. Drug Delivery Rev. 64, 1628-1638.

Merisko-Liversidge, E.M., Liversidge, G.G., 2008. Drug nanoparticles: formulating poorly water-soluble compounds. Toxicol Pathol. 36, 43-48.

Miekisch, W., Schubert, J.K., Vagts, D.A., Geiger, K., 2001. Analysis of volatile disease markers in blood. Clin Chem. 47, 1053-1060.

Mishra, R., Datt, M., Banthia, A., 2008. Synthesis and Characterization of Pectin/PVP Hydrogel Membranes for Drug Delivery System. AAPS PharmSciTech. 9, 395-403.

Missirlis, D., Hubbell, J.A., Tirelli, N., 2006. Thermally-induced glass formation from hydrogel nanoparticles. Soft Matter. 2, 1067-1075.

Miyata, T., Asami, N., Uragami, T., 1999. A reversibly antigen-responsive hydrogel. Nature. 399, 766-769.

Miyata, T., Jikihara, A., Nakamae, K., Hoffman, A.S., 1996. Preparation of poly(2-glucosyloxyethyl methacrylate)-concanavalin A complex hydrogel and its glucose-sensitivity. Macromol Chem Physic. 197, 1135-1146.

Miyata, T., Uragami, T., Nakamae, K., 2002. Biomolecule-sensitive hydrogels. Adv. Drug Delivery Rev. 54, 79-98.

Mochalin, V.N., Sagar, A., Gour, S., Gogotsi, Y., 2009. Manufacturing nanosized fenofibrate by salt assisted milling. Pharm Res. 26, 1365-1370.

Muller, R.H., Mader, K., Gohla, S., 2000. Solid lipid nanoparticles (SLN) for controlled drug delivery - a review of the state of the art. Eur J Pharm Biopharm. 50, 161-177.

Muller R.H., Ruhl D., Runge S. 1996. Biodegradation of solid lipid nanoparticles as a function of lipase incubation time. Int. J Pharm. 144,115–21.

Munoz, A., Guichard, J.P., Reginault, P., 1994. Micronised fenofibrate. Atherosclerosis. 110, S45-48.

Murata, M., Matsubara, Y., Kawano, K., Zama, T., Aoki, N., Yoshino, H., Watanabe, G., Ishikawa, K., Ikeda, Y., 1997. Coronary artery disease and polymorphisms in a receptor mediating shear stress-dependent platelet activation. Circulation. 96, 3281-3286.

Murdan, S., 2003. Electro-responsive drug delivery from hydrogels. J Control Release. 92, 1-17.

Nadeau, J., 2009. Editorial: nanotechnological advances in biosensors. Sensors 9, 8907-8910.
Nakamae, K., Miyata, T., Jikihara, A., Hoffman, A.S., 1994. Formation of poly(glucosyloxyethyl methacrylate)-concanavalin A complex and its glucose-sensitivity. J Biomater Sci Polym Ed 6, 79-90.

Nemir, S., Hayenga, H.N., West, J.L., 2010. PEGDA hydrogels with patterned elasticity: Novel tools for the study of cell response to substrate rigidity. Biotechnol Bioeng. 105, 636-644.

Nemir, S., West, J., 2010. Synthetic Materials in the Study of Cell Response to Substrate Rigidity. Ann Biomed Eng. 38, 2-20.

Ning, M., Zhou, Y., Chen, G., Mei. 2011. Preparation and I*n Vitro/In Vivo* evaluation of Vinpocetine elementary osmotic pump system. Adv Pharm Sci. 2011, 1-7.

Nyström, B., Olafsen, K., Roots, J., 1991. Effect of pressure on hydrodynamic properties of poly(ethylene oxide) in deuterated and in non-deuterated solvents. Polymer. 32, 904-908.

Oliver, N.S., Toumazou, C., Cass, A.E., Johnston, D.G., 2009. Glucose sensors: a review of current and emerging technology. Diabet Med. 26, 197-210.

Onuki, Y., Bhardwaj, U., Papadimitrakopoulos, F., Burgess, D.J., 2008. A review of the biocompatibility of implantable devices: current challenges to overcome foreign body response. J Diabetes Sci Technol. 2, 1003-1015.

Ou, S.H., Wu, M.C., Chou, T.C., Liu, C.C., 2004. Polyacrylamide gels with electrostatic functional groups for the imprinting of lysozyme. Anal Chim Acta. 504, 163–166.

Papavasiliou, G., Sokic, S., Turturro, M., 2012. Synthetic PEG hydrogels as extracellular matrix mimics for tissue engineering applications, in: Sammour, R. (Ed.), Biotechnology-Molecular studied and novel applications for improved quality of human life. Intec, Croatia, pp. 111-134.

Park, H., Park, K., 1996. Biocompatibility Issues of Implantable Drug Delivery Systems. Pharm Res. 13, 1770-1776.

Parmpi, P., Kofinas, P., 2004. Biomimetic glucose recognition using molecularly imprinted polymer hydrogels. Biomaterials. 25, 1969-1973.

Parveen, S., Misra, R., Sahoo, S.K., 2012. Nanoparticles: a boon to drug delivery, therapeutics, diagnostics and imaging. Nanomedicine. 8, 147-166.

Patel, S., Solanki, A., Parikh, J., 2010. Enhancement of rate of dissolution of fenofibrate by ternary solid dispersion. J. Pharm. Cosm. 1, 1-11.

Patra, C.N., Swain, S., Sruti, J., Patro, A.P., Panigrahi, K.C., Beg, S., Rao, M.E., 2013. Osmotic drug delivery systems: basics and design approaches. Recent Pat. Drug Deliv. Formul. 7, 150-161.

Pedersen, N., Hansen, S., Heydenreich, A.V., Kristensen, H.G., Poulsen, H.S., 2005. Solid lipid nanoparticles can efffectively bind DNA, streptavidin and biotinylated ligands. Eur. J. Pharm. Biopharm. 62, 155-162.

Peterson, J.D., Vyazovkin, S., Wight, C.A., 2001. Kinetics of the Thermal and Thermo-Oxidative Degradation of Polystyrene, Polyethylene and Poly(propylene). Macromol. Chem. Physic. 202, 775-784.

Phillips, M., Cataneo, R.N., Ditkoff, B.A., Fisher, P., Greenberg, J., Gunawardena, R., Kwon, C.S., Tietje, O., Wong, C., 2006. Prediction of breast cancer using volatile biomarkers in the breath. Breast Cancer Res. Treat. 99, 19-21.

Phillips, M., Glesson, K., Hughes, J.M.B., Greenberg, J., Cataneo, R.N., Baker, L., McVay, W.P., 1999. Volatile organic compounds in breathe as markers of lung cancer: A cross-sectional study. Lancet. 353, 1930–1933.

Pierigè, F., Serafini, S., Rossi, L., Magnani, M., 2008. Cell-based drug delivery. Adv. Drug Delivery Rev. 60, 286-295.

Pietzsch, J., Lattke, P., Julius, U., 2000. Oxidation of apolipoprotein B-100 in circulating LDL is related to LDL residence time. *In vivo* insights from stable-isotope studies. Arterioscler. Thromb. Vasc. Biol. 20, E63-67.

Podczeck, F., 1993. Comparison of *in vitro* dissolution profiles by calculating mean dissolution time (MDT) or mean residence time (MRT). Int J Pharm. 97, 93-100.

Prestwich, G.D., Marecak, D.M., Marecek, J.F., Vercruysse, K.P., Ziebell, M.R., 1998. Controlled chemical modification of hyaluronic acid: synthesis, applications, and biodegradation of hydrazide derivatives. J. Control Release. 53, 93-103.

Price, D.M., Hourston, D.J., Dumont, F., 2006. Thermogravimetry of Polymers, Encyclopedia of Analytical Chemistry. John Wiley & Sons, Ltd. pp 13-36.

Priyadarshini, N., Sampath, M., Kumar, S., Mudali, U.K., 2013. Particle Size Variation and Prediction of Molecular Weight of Bi(III) Hydrolyzed Polymer Using Light Scattering Technique. ISRN Inorg. Chem. 2013, 5.

Pundir, C.S., Narang, J., Chauhan, N., Sharma, P., Sharma, R. 2012 An amperometric cholesterol biosensor based on epoxy resis membrane bound cholesterol oxidase. Inidan J Med Res. 136, 633-640.

Qin, S., Van der Zeyden, M., Oldenziel, W.H., Cremers, T.I.F.H., Westerink, B.H.C., 2008. Microsensors for *in vivo* measurements of glutamate in brain tissue. Sensors. 8, 6860-6884.

Qiu, Y., Park, K., 2001. Environment-sensitive hydrogels for drug delivery. Adv. Drug Delivery Rev. 53, 321-339.

Qiu, Y., Park, K., 2012. Environment-sensitive hydrogels for drug delivery. Adv. Drug Delivery Rev. 64, Supplement, 49-60.

Rabbani, N., Godfrey, L., Xue, M., Shaheen, F., Geoffrion, M., Milne, R., Thornalley, P.J., 2011. Glycation of LDL by methylglyoxal increases arterial atherogenicity: a possible contributor to increased risk of cardiovascular disease in diabetes. Diabetes. 60, 1973-1980.

Ramirez, N.B., Salgado, A.M., Valdman, B., 2009. The evolution and development of immunosensors for health and environmental monitoring: Problems and perspectives. Braz. J. Chem. Eng. 26, 227–249.

Ranaki, E., Dokoumentzi, A., Macheras, P., 2003. The mean dissolution time depends on the dose/solubility ratio. Pharm. Res. 20, 406-408.

Rao, E., Ranpise, A., Borate, S., Thanki, K. Mechanistic evaluation of the effect of sintering of Compritol 888 ATO matrices. AAPS PharmSciTech. 10, 355-360.

Rinaki, E., Dokoumetzidis, A., Macheras, P., 2003. The Mean Dissolution Time Depends on the Dose/Solubility Ratio. Pharm. Res. 20, 406-408.

Ripp, S., Jegier, P., Johnson, C., Moser, S., Sayler, G.S., 2008. Bioluminescent bioreporter assays for targeted detection of chemical and biological agents. P Soc Photo-Opt Ins. 6945, 1–6.

Ronkainen, N.J., Halsall, H.B., Heineman, W.R., 2010. Electrochemical biosensors. Chem. Soc. Rev. 39, 1747–1763.

Roy, D., Cambre, J.N., Sumerlin, B.S., 2010. Future perspectives and recent advances in stimuli-responsive materials. Prog Polym Sci. 35, 278-301.

Ruggeri, Z.M., Orje, J.N., Habermann, R., Federici, A.B., Reininger, A.J., 2006. Activation-independent platelet adhesion and aggregation under elevated shear stress. Blood. 108, 1903-1910.

Sampath, S.S., Babu, B.V., 2006. Kinetic parameter estimation of gelatin waste by thermogravimetry. Proc Natl Con Env Cons. 2006, 473-579.

Schwarz, C., Mehnert, W., 1997. Freeze-drying of drug-free and drug-loaded solid lipid nanoparticles (SLN). Int. J. Pharm. 157, 171-179.

Seiffert, S., Sprakel, J., 2012. Physical chemistry of supramolecular polymer networks. Chem. Soc. Rev. 41, 909-930.

Sershen, S., West, J., 2002. Implantable, polymeric systems for modulated drug delivery. Adv. Drug Delivery Rev. 54, 1225–1235.

Sethi, R.S., 1994. Transducer aspects of biosensors. Biosens. Bioelectron. 9, 243-264.

Shan, G., Lipton, C., Gee, S.R., Hammock, B.D., 2003. Immunoassay, Biosensors and other Non-chromatographic Methods, in: Lee, P.W., Aizawa, H., Barefoot, A.C., Murphy, J.J. (Eds.), Handbook of Residue Analytical Methods for Agrochemicals. John Wiley and Sons, Ltd, Chichster, UK, pp. 623–679.

Sharma, J., Puri, S., 2001. Kinetics of phase separation in polymer-solvent mixtures. Phys. Rev. 64, 021513.

Shepherd, J., 2003. Combined lipid lowering drug therapy for the effective treatment of hypercholesterolaemia. Eur. Heart J. 24, 685-689.

Shoa, T., Madden, J.D., Fekri, N., Munce, N.R., Yang, V.X.D. 2008. Conducting polymer based active catheter for minimally invasive interventions inside arteries. Conf. Proc. IEEE Eng. Med. Biol. Soc. 2008, 2063-2066.

Shoaib, M.H., Tazeen, J., Merchant, H.A., Yousuf, R.I., 2006. Evaluation of drug release kinetics from ibuprofen matrix tablets using HPMC. Pak. J. Pharm. Sci. 19, 119-124.

Siegel, R., Rathbone, M., 2012. Overview of Controlled Release Mechanisms, in: Siepmann, J., Siegel, R.A., Rathbone, M.J. (Eds.), Fundamentals and Applications of Controlled Release Drug Delivery. Springer US, pp. 19-43.

Sijja, H.K., East, M.P., Mao, H., Wang, Y.H., Nie, S., Yang, L., 2009. Development of multifunctional nanoparticles for targeted drug delivery invasive imaging of therapeutic effect. Curr Drug Discov Technol. 6, 43-51.

Sonoki, K., Yoshinari, M., Iwase, M., Iino, K., Ichikawa, K., Ohdo, S., Higuchi, S., Iida, M., 2002. Glycoxidized low-density lipoprotein enhances monocyte chemoattractant protein-1 mRNA expression in human umbilical vein endothelial cells: relation to lysophosphatidylcholine contents and inhibition by nitric oxide donor. Metabolism. 51, 1135-1142.

Souto, E.B., Mehnert, W., Muller, R.H., 2006. polymorphic behaviour of compritol 888 ATO as bulk lipid and as SLN and NLC. J. Microencapsulation. 23, 417-433.

Steinberg, D., Parthasarathy, S., Carew, T.E., Khoo, J.C., Witztum, J.L., 1989. Beyond cholesterol. Modifications of low-density lipoprotein that increase its atherogenicity. N. Engl. J. Med. 320, 915-924.

Stuart, M.A., Huck, W.T., Genzer, J., Muller, M., Ober, C., Stamm, M., Sukhorukov, G.B., Szleifer, I., Tsukruk, V.V., Urban, M., Winnik, F., Zauscher, S., Luzinov, I., Minko, S., 2010. Emerging applications of stimuli-responsive polymer materials. Nat. Mater. 9, 101-113.

Suzuki, A., Ishii, T., Maruyama, Y., 1996. Optical switching in polymer gels. J Appl Phys. 80, 131-136.

Szepes, A., Makai, Z., Blümer, C., Mäder, K., Kása Jr, P., Szabó-Révész, P., 2008. Characterization and drug delivery behaviour of starch-based hydrogels prepared via isostatic ultrahigh pressure. Carbohydr. Polym. 72, 571-578.

Tan, T., Watts, S.W., Davis, R.P., 2011. Drug Delivery: Enabling Technology for Drug Discovery and Development. iPRECIO Micro Infusion Pump: Programmable, Refillable, and Implantable. Front Pharmacol. 2, 00044.

Tessier, P.M., Sandler, S.I., Lenhoff, A.M., 2004. Direct measurement of protein osmotic second virial cross coefficients by cross-interaction chromatography. Protein Sci. 13, 1379-1390.

Thévenot, D.R., Toth, K., Durst, R.A., Wilson, G.S., 2001. Electrochemical biosensor: Recommended definitions and classification. Biosens. Bioelectron. 16, 121–131.

Tiwari, R., Pathak, K., 2011. Statins therapy: a review on conventional and novel formulation approaches. J. Pharm. Pharmacol. 63, 983-998.

Tokarev, I., Minko, S., 2009. Multiresponsive, Hierarchically Structured Membranes: New, Challenging, Biomimetic Materials for Biosensors, Controlled Release, Biochemical Gates, and Nanoreactors. Adv. Mat. 21, 241-247.

Tothill, I.E., 2009. Biosensors for cancer markers diagnosis. Sem Cell Dev Bio. 20, 55-62.

Traitel, T., Cohen, Y., Kost, J., 2000. Characterization of glucose-sensitive insulin release systems in simulated *in vivo* conditions. Biomaterials. 21, 1679-1687.

Tsai, H.-K.A., Moschou, E.A., Daunert, S., Madou, M., Kulinsky, L., 2009. Integrating Biosensors and Drug Delivery: A Step Closer Toward Scalable Responsive Drug-Delivery Systems. Adv. Mat. 21, 656-660.

Turner, P.V., Pekow, C., Vasbinder, M.A., Brabb, T., 2011. Administration of substances to laboratory animals: equipment considerations, vehicle selection, and solute preparation. JAALAS. 50, 614-627.

Turner, R.F., Harrison, D.J., Rajotte, R.V., 1991. Preliminary *in vivo* biocompatibility studies on perfluorosulphonic acid polymer membranes for biosensor applications. Biomaterials. 12, 361-368.

Tymoczko, J.L., Stryer, L., Berg, J.M., 2002. The Complex Regulation of Cholesterol Biosynthesis Takes Place at Several Levels, in: JM, B., JL, T., L, S. (Eds.), Biochemistry, 5th edition ed. W H Freeman, New York. Chapt 26, pp 1-8.

Uner, M., Yener, G., 2007. Importance of solid lipid nanoparticles (SLN) in various administration routes and future perspectives. Int. Nanomedicine. 2, 289-300.

Usvald, D., Hlucilova, J., Strnadel, J., Prochazka, R., Motlik, J., Marsala, M., 2008. Permanent jugular catherization in miniature pig: treatment, clinical and pathological observations. Vet Med. 53, 365-372.

Uzum, O.B., Karadag, E., 2012. Behavior of Semi IPN Hydrogels Composed of PEG and AAm/SMA Copolymers in Swelling and Uptake of Janus Green B from Aqueous Solutions. J Appl Polym Sci. 125, 3318-3328.

Vaddiraju, S., Tomazos, I., Burgess, D.J., Jain, F.C., Papadimitrakopoulos, F., 2010. Emerging synergy between nanotechnology and implantable biosensors: a review. Biosens. Bioelectron. 25, 1553-1565.

van den Bosch, E., Gielens, C., 2003. Gelatin degradation at elevated temperature. Int J Biol Macromol. 32, 129-138.

Vasan, R.S., 2006. Biomarkers of cardiovascular disease: molecular basis and practical considerations. Circulation. 113, 2335-2362.

Vaughan, C.J., Murphy, M.B., Buckley, B.M., 1996. Statins do more than just lower cholesterol. Lancet. 348, 1079-1082.

Vestergaard, M., Kerman, K., Tamiya, E., 2007. An overview of label free electrochemical protein sensors. Sensors. 7, 3442–3458.

Vilahur, G., Padro, T., Badimon, L., 2011. Atherosclerosis and thrombosis: insights from large animal models. J Biomed Biotech. 2011, 907575.

Vo-Dinh, T., 2008. Nanosensing at the single cell level. Spectrochimica Acta Part B. 63, 95-103.

Vollmer, F., Arnold, S., 2008. Whispering-gallery-mode biosensing: Label-free detection down to single molecules. Nat. Met. 7, 591–596.

Wang, H., Tao, X., Newton, E., 2004. Thermal degradation kinetics and lifetime prediction of a luminescent conducting polymer. Polym. Int. 53, 20-26.

Wang, J.H., Wang, K., Bartling, B., Liu, C.C., 2009. The detection of alkaline phosphatase using an electrochemical biosensor in a single-step approach. Sensors. 9, 8709-8721.

Wang, S.-Q., Ravindranath, S., Wang, Y., Boukany, P., 2007. New theoretical considerations in polymer rheology: Elastic breakdown of chain entanglement network. J. Chem. Physic. 127, 064903-064914.

Wang, Y., Papadimitrakopoulos, F., Burgess, D.J., 2013. Polymeric “smart” coatings to prevent foreign body response to implantable biosensors. J. Control Release. 169, 341-347.

Wilson, G.S., Hu, Y., 2000. Enzyme-based biosensors for *in vivo* measurements. Chem. Rev. 100, 2693-2704.

Wisniewski, N., Moussy, F., Reichert, W.M. 2000. Characterization of implantable biosensor biofouling. J Anal Chem. 366, 611-621.

Wong, D.T., 2006. Salivary diagnostics powered by nanotechnologies, proteomics and genomics. J. Am. Den. Ass. 137, 313-321.

Wong, J., Brugger, A., Khare, A., Chaubal, M., Papadopoulos, P., Rabinow, B., Kipp, J., Ning, J., 2008. Suspensions for intravenous (IV) injection: a review of development, preclinical and clinical aspects. Adv. Drug. Deliv. Rev. 60, 939-954.

Wu, Y., Gupta, C., Shannon, M.A., 2008. Effect of solution concentration, surface bias and protonation on the dynamic response of amplitude-modulated atomic force microscopy in water. Langmuir. 24, 10817–10824.

Wu, Y., Zheng, J., Li, Z., Zhao, Y., Zhang, Y., 2009. A novel reagents amperometric immunosensor based on gold nanoparticles/TMB/Nafion-modified electrode. Biosens. Bioelectron. 24, 1389–1393.

Xu, D., Craig, S.L., 2010. Multiple Dynamic Processes Contribute to the Complex Steady Shear Behavior of Cross-Linked Supramolecular Networks of Semidilute Entangled Polymer Solutions. J. Physic. Chem. Lett. 1, 1683-1686.

Yang, B., Bassols, A., Saco, Y., Perez-Enciso, M., 2011. Association between plasma metabolites and gene expression profiles in five porcine endocrine tissues. GSE. 43, 28.

Yavuz, H., Denizli, A., 2005. Immunoadsorption of cholesterol on protein A oriented beads. Macromol Biosci. 5, 39-48.

Zhang, Y., Huo, M., Zhou, J., Zou, A., Li, W., Yao, C., Xie, S., 2010. DDSolver: an add-in program for modeling and comparison of drug dissolution profiles. AAPS. 12, 263-271.

Zhao, H.Y., Zheng, W., Meng, Z.X., Zhou, H.M., Xu, X.X., Li, Z., Zheng, Y.F., 2009. Bioelectrochemistry of hemoglobin immobilized on a sodium alginate-multiwall carbon nanotubes composite film. Biosens. Bioelectron. 24, 2352-2357.

Zhao, Z., Lei, W., Zhang, X., Wang, B., Jiang, H., 2010. ZnO-Based Amperometric Enzyme Biosensors. Sensors. 10, 1216-1231.

Zhong, C., Chu, C.C., 2012. Biomimetic mineralization of acid polysaccharide-based hydrogels: towards porous 3-dimensional bone-like biocomposites. J. Mat. Chem. 22, 6080-6087.

Zhu, T., Ansquer, J.C., Kelly, M.T., Sleep, D.J., Pradhan, R.S., 2010. Comparison of the gastrointestinal absorption and bioavailability of fenofibrate and fenofibric acid in humans. J. Clin. Pharmocol. 50, 914-921.

Appendix A: TGA lifetime kinetics Toop's table

TABULATION OF $-\log p(x') = -\log\left[\frac{1}{x'e^{x'}} - \int_{x'}^{\infty}\frac{dx}{xe^{x}}\right]$

		0.1	0.2	0.3	0.4	0.5	0.6	0.7	0.8	0.9
10	6.4157	0.0515	0.1030	0.1544	0.2057	0.2569	0.3081	0.3591	0.4101	0.4611
11	6.9276	0.0508	0.1015	0.1522	0.2028	0.2533	0.3038	0.3542	0.4046	0.4549
12	7.4327	0.0502	0.1003	0.1504	0.2004	0.2504	0.3004	0.3502	0.4001	0.4499
13	7.9323	0.0497	0.0993	0.1489	0.1985	0.2480	0.2975	0.3469	0.3963	0.4456
14	8.4273	0.0493	0.0985	0.1477	0.1968	0.2459	0.2950	0.3440	0.3930	0.4420
15	8.9182	0.0489	0.0978	0.1466	0.1954	0.2441	0.2929	0.3415	0.3902	0.4388
16	9.4056	0.0486	0.0971	0.1456	0.1941	0.2425	0.2910	0.3393	0.3877	0.4360
17	9.8900	0.0483	0.0965	0.1448	0.1930	0.2411	0.2893	0.3374	0.3855	0.4336
18	10.3716	0.0480	0.0960	0.1440	0.1919	0.2399	0.2878	0.3356	0.3835	0.4313
19	10.8507	0.0478	0.0956	0.1433	0.1910	0.2387	0.2864	0.3341	0.3817	0.4293
20	11.3277	0.0476	0.0951	0.1427	0.1902	0.2377	0.2852	0.3326	0.3801	0.4275
21	11.8026	0.0474	0.0948	0.1421	0.1895	0.2368	0.2841	0.3314	0.3786	0.4259
22	12.2757	0.0472	0.0944	0.1416	0.1888	0.2359	0.2831	0.3302	0.3773	0.4244
23	12.7471	0.0471	0.0941	0.1411	0.1881	0.2351	0.2821	0.3291	0.3760	0.4230
24	13.2170	0.0469	0.0938	0.1407	0.1876	0.2344	0.2813	0.3281	0.3749	0.4217
25	13.6855	0.0468	0.0935	0.1403	0.1870	0.2338	0.2805	0.3272	0.3739	0.4205
26	14.1527	0.0467	0.0933	0.1399	0.1865	0.2331	0.2797	0.3263	0.3729	0.4194
27	14.6187	0.0465	0.0931	0.1396	0.1861	0.2326	0.2791	0.3255	0.3720	0.4184
28	15.0836	0.0464	0.0928	0.1393	0.1857	0.2320	0.2784	0.3248	0.3711	0.4175
29	15.5474	0.0463	0.0926	0.1390	0.1853	0.2315	0.2778	0.3241	0.3704	0.4166
30	16.0103	0.0462	0.0925	0.1387	0.1849	0.2311	0.2773	0.3235	0.3696	0.4158
31	16.4722	0.0461	0.0923	0.1384	0.1845	0.2306	0.2768	0.3229	0.3689	0.4150
32	16.9333	0.0461	0.0921	0.1382	0.1842	0.2302	0.2763	0.3223	0.3683	0.4143
33	17.3936	0.0460	0.0920	0.1379	0.1839	0.2299	0.2758	0.3217	0.3677	0.4136
34	17.8532	0.0459	0.0918	0.1377	0.1836	0.2295	0.2754	0.3212	0.3671	0.4130
35	18.3120	0.0458	0.0917	0.1375	0.1833	0.2292	0.2750	0.3208	0.3666	0.4124
36	18.7701	0.0458	0.0916	0.1373	0.1831	0.2288	0.2746	0.3203	0.3661	0.4118
37	19.2276	0.0457	0.0914	0.1371	0.1828	0.2285	0.2742	0.3199	0.3656	0.4112
38	19.6845	0.0457	0.0913	0.1370	0.1826	0.2282	0.2739	0.3195	0.3651	0.4107
39	20.1408	0.0456	0.0912	0.1368	0.1824	0.2280	0.2735	0.3191	0.3647	0.4102
40	20.5966	0.0455	0.0911	0.1366	0.1822	0.2277	0.2732	0.3187	0.3642	0.4098
41	21.0519	0.0455	0.0910	0.1365	0.1820	0.2274	0.2729	0.3184	0.3638	0.4093
42	21.5066	0.0455	0.0909	0.1363	0.1818	0.2272	0.2726	0.3181	0.3635	0.4089
43	21.9609	0.0454	0.0908	0.1362	0.1816	0.2270	0.2724	0.3177	0.3631	0.4085
44	22.4148	0.0454	0.0907	0.1361	0.1814	0.2268	0.2721	0.3174	0.3628	0.4081
45	22.8682	0.0453	0.0906	0.1359	0.1812	0.2265	0.2718	0.3171	0.3624	0.4077
46	23.3212	0.0453	0.0906	0.1358	0.1811	0.2264	0.2716	0.3169	0.3621	0.4074
47	23.7738	0.0452	0.0905	0.1357	0.1809	0.2262	0.2714	0.3166	0.3618	0.4070
48	24.2260	0.0452	0.0904	0.1356	0.1808	0.2260	0.2712	0.3163	0.3616	0.4067
49	24.6779	0.0452	0.0903	0.1355	0.1806	0.2258	0.2709	0.3161	0.3612	0.4064
50	25.1294	0.0451	0.0903	0.1354	0.1805	0.2256	0.2707	0.3159	0.3610	0.4061

Example of use: 12 7.4327
0.3 0.1504
0.04 0.0200
7.6031

$\log p(12.34) = -7.6031$
$p(12.34) = 2.494 \times 10^{-8}$

Appendix B: Animal Ethics Clearance Certificate

AESC3

STRICTLY CONFIDENTIAL

ANIMAL ETHICS SCREENING COMMITTEE (AESC)

CLEARANCE CERTIFICATE NO. 2011/52/05

APPLICANT: **Mr M Ngoepe**

DEPARTMENT: **School of Pharmacy and Pharmacology**

PROJECT TITLE: **An implantable sensor for disease prevention and treatment**

Number and Species

4 large white pigs

Approval was given for to the use of animals for the project described above at an AESC meeting held on **29 November 2011**. This approval remains valid until **30 November 2013**.

The use of these animals is subject to AESC guidelines for the use and care of animals, is limited to the procedures described in the application form and to the following additional conditions:

Approved subject to:
Approved with the following conditions:

- The study animal is included in the title.
- The applicant provides details on the make-up on the high cholesterol diet and how food volumes change with body mass and growth of the animals.
- The applicant discusses with Dr G Candy how *in vitro* measures could provide valuable insights into the functionality of the sensor.

Signed: _____ (Chairperson, AESC) Date: 13/12/2011

I am satisfied that the persons listed in this application are competent to perform the procedures therein, in terms of Section 23 (1) (c) of the Veterinary and Para-Veterinary Professions Act (19 of 1982)

Signed: _____ (Registered Veterinarian) Date: 13/12/2011

cc: Supervisor:
Director: CAS

Appendix C: Score sheet for Implant Tolerance

Table A: Score sheet template used for each pig during the study to determine welfare assessment and tolerance to the implant

Evaluation parameter	Score and behavioral description
1. COMFORT 0 = awake, interested in surroundings, recumbent, eating 1 = awake, not interested in surroundings, recumbent, reduced appetite 2 = lethargic, depressed appearance, anorexic 3 = head down, lethargic, anorexic, bruxism 4 = recumbent, fixed look and staring, eyes half closed, little response when prodded, bruxism	
2. AGITATION 0 = asleep or calm 1 = mild agitation 2 = moderate agitation 3 = hysterical	
3. FEEDING BEHAVIOR 0 = normal – at feed trough 1 = mild changes 2 = moderate changes 3 = severe changes – anorexic	
4. RESPIRATORY RATE 0 = normal 1 = noticeable increase 2 = hyperventilation 3 = hyperventilation with mouth breathing	
5. PALPATION SORENESS & RANGE OF MOTION SORENESS	

0 = none

1 = mild pain (occasional vocalization)

2 = moderate pain (frequent vocalization)

3 = severe pain (vociferous vocalization,

bites, tries to escape)

6. SOFT TISSUE SWELLING & HEAT

(AROUND SURGICAL AREA)

0 = none

1 = slight

2 = mild

3 = moderate

4 = severe

7. APPEARANCE OF INCISION SITE

0 = clean, no redness

1 = redness, suture intact

2 = incision open

3 = incision infected (redness, swelling,

purulent drainage)

Score

0-3 total score or <1 score in a category: No intervention

4-9 total score or >1 score in a category: Administer buprenorphine – 2 doses (0.05 mg/kg), at 12-hour intervals for 24 hours, and re-evaluate pain score.

10 – 11: Administration of buprenorphine - 1 dose (0.05 mg/kg) and re-evaluation of pain score in 1 hour. If pain is controlled, pain score will be re-evaluated at 6 and 12 hours and administer second dose of buprenorphine at 8 hours. Re-evaluation of pain score at 12 hours after second dose. If pain is controlled, continue with 2 or more doses over 24 hours. Discontinuation at 24 hours after first dose and re-evaluation of pain score. If no changes occur, the pig will be removed from the study.

Appendix D: Abstracts of Papers Published from this Dissertation

Abstracts

Review Paper

Abstract: Recent advances in biosensor design and sensing efficacy need to be amalgamated with research in responsive drug delivery systems for building superior health or illness regimes and ensuring good patient compliance. Varieties of illnesses require continuous monitoring in order to have efficient illness intervention. Physicochemical changes in the body can signify the occurrence of an illness before it manifests. Even with the usage of sensors that allow diagnosis and prognosis of the illness, medical intervention still has its downfalls. Late detection of illness can reduce the efficacy of therapeutics. Furthermore, the conventional modes of treatment can cause side effects such as tissue damage (chemotherapy and rhabdomyolysis) and induce other forms of illness (hepatotoxicity). The use of drug delivery systems enables the lowering of side effects with subsequent improvement in patient compliance. Chronic illnesses require continuous monitoring and medical intervention for efficient treatment to be achieved. Therefore, designing a responsive system that will reciprocate to the physicochemical changes may offer superior therapeutic activity. In this respect, integration of biosensors and drug delivery is a proficient approach and requires designing an implantable system that has a closed loop system. This offers regulation of the changes by means of releasing a therapeutic agent whenever illness biomarkers prevail. Proper selection of biomarkers is vital, as this is key for diagnosis and a stimulation factor for responsive drug delivery. By detecting an illness before it manifests by means of biomarkers levels, therapeutic dosing would relate to the severity of such changes. In this review, various biosensors and drug delivery systems are discussed in order to assess the challenges and future perspectives of integrating biosensors and drug delivery systems for detection and management of chronic illness.

Paper 1

Abstract: Cardiovascular biomarkers such LDL overproduction can serve as indicators of physiochemical changes signifying manifestation and progression of a disease. Antibody-conjugated solid lipid antibodies can aid in site directed drug delivery system, biosensing technology and facilitate plasma clearance of excess LDL particles. An oil-in-water emulsion technique and ultra-sonication were used to synthesize solid lipid nanoparticles of 140nm in

size, with a zeta potential of -43.1 mV. The SLN consisted of Compritol 888 ATO as the lipid core, Pluronic F68 as the stabilizer and fenofibrate as a model lipophilic drug. The biotinylated anti-β LDL antibodies were then conjugated with avidin coated SLN. Drug entrapment efficiency was found to be 86%, drug loading capacity of 14%, while the drug release was 6mg/day due to erosion mode of release (super case II transport). Slow release of lipophilic drugs such as statins and fibrates can reduce myopathy side effects. The study also indicates that antibody conjugated solid lipid nanoparticles could be beneficial in detecting/imaging of atherosclerotic lesion and delivery of drugs with low water solubility over extended period. Furthermore they are ideal for β-LDL plasma clearance during nanoparticle excretion and reduce excess LDL absorption/binding to LDL receptors.

Paper 2

Abstract: Some hydrogels used in tissue engineering are often highly susceptible to hydrolytic degradation (to allow long term tissue regeneration) and have not been shown to mimic the viscoelastic (firmness and resistance to shear under high strains) behavior of the native tissue when subjected to dynamic loading conditions. A viscoelastic hydrogel with tunable mechanical and degradation properties was synthesized from PEGDA-MAA-PEG200. Whereby, PEGDA concentration affected level of viscoelastic behavior and PEG200 changed the solubility of the polymer, thus making it more prone to hydrolytic degradation. Rheology, texture analysis, FTIR, porosity and microscopy were used for characterization of physical and chemical properties. Rheology indicated that the hydrogels undergo shear thinning as shear stress and frequency increase, whilst changes in PEGDA and PEG200 can affect structural recovery, which is a property that is desirable for designing injectable biomaterials for controlled drug delivery and tissue engineering applications. A changed in PEG200 was shown to allow tuning of pore size, surface chemistries (degradation and swelling) and reduced mechanical (viscoelastic) properties due to interpenetration of PEG200 decreased the interaction energy of the polymer chains of PEGDA-MAA. This indicates that the plasticizer, PEG200 can be used for tuning viscoelastic properties of PEGDA-MAA polymers and affect pore size as it can act as a porogen.

Paper 3

Abstract: Hypercholesterolemia is a condition associated with atherosclerosis due to elevated levels and oxidation of low density lipoproteins (LDLs). Due to engulfment of LDL particles by

macrophages and low LDL metabolism that lead to formation of atherogenic plagues, it is hypothesized that anti-LDL nanosuspension can enhance LDL metabolism during nanoparticles clearance by Kupffer cells. Furthermore, drug eluting nanoparticles can further reduce cholesterol synthesis and increase uptake of dietary cholesterol by LDLs. Solid lipid nanoparticles (~130nm in diameter) were coated with avidin to allow conjugation of biotinylated anti-Apo-B100 antibodies. *In vitro* studies showed a constant drug release of 10mg/day, whilst *in vivo* studies showed controlled drug release with zero-order kinetics. This correlated to the crystallinity of the formulation, which was analyzed by differential scanning calorimetry (DSC) and X-ray diffraction (XRD). This indicated that infusion of target specific drug eluting nanosuspension can be effective in management of metabolic disorders whereby a disease is manifested by overproduction of biochemical compounds. Although infusion pumps infusion rate cannot be altered, the use of nanosuspension allows a combination of constant drug release due to osmotic drive and burst release due to targeted nanosuspension.